X-ray Binary Evolution and the Connection to Star Formation in Nearby Galaxies with the *Chandra* Local Volume Survey

Breanna Arlene Binder

A dissertation submitted in partial fulfillment of
the requirements for the degree of

Doctor of Philosophy

University of Washington

2013

Reading Committee:

Scott Anderson, Chair

Eric Agol

Benjamin Williams

Program Authorized to Offer Degree:
Astronomy

University of Washington

Abstract

X-ray Binary Evolution and the Connection to Star Formation in Nearby Galaxies with the *Chandra* Local Volume Survey

Breanna Arlene Binder

Chair of the Supervisory Committee:
Dr. Scott Anderson
Department of Astronomy

X-ray binaries, especially those with a massive stellar companion, provide a unique probe through which one can study the end-points of high-mass stellar evolution while simultaneously tracing recent star formation. In this thesis, I analyze the high-mass X-ray binary populations of five nearby galaxies using matched observations from the *Chandra X-ray Observatory* and the *Hubble Space Telescope*. The global X-ray properties of the X-ray binary populations of these galaxies is correlated with the star formation histories of the host galaxies. Unlike previous studies of the X-ray–star formation connection, which corrects for contamination by background sources only in a statistical sense, I have developed a source classification scheme utilizing the resolved stellar populations from *Hubble* imaging to separate X-ray binary candidates from contaminating X-ray sources. This thesis validates the statistical corrective approach typically applied to more distant galaxies, where it is not possible to resolve individual stars. Additionally, the X-ray binary populations of these nearby galaxies is used to constrain models of massive star evolution. This includes an estimate of the fraction of massive evolved binaries that undergo an X-ray luminous phase, the characteristic timescale of the X-ray luminous phase, and the mass distribution of stellar companions in X-ray binaries.

TABLE OF CONTENTS

Page

List of Figures iii

List of Tables v

Glossary vii

Chapter 1: Introduction 1
1.1 A Brief History of X-ray Astronomy 1
1.2 Overview of Single Star Evolution 2
1.3 Compact Object Formation 5
1.4 Binary Star Evolution 11
1.5 X-ray Emission from Normal Galaxies 18
1.6 Thesis Outline 19

Chapter 2: The *Chandra* Local Volume Survey 21
2.1 The Galaxy Sample 22
2.2 Observations and Data Reduction 26
2.3 Image Alignment 28
2.4 `ACIS-Extract` 31
2.5 Sensitivity Maps 54

Chapter 3: X-ray Source Characteristics 57
3.1 Comparison Overall Catalog Properties 57
3.2 Individual Source Properties 73

Chapter 4: Multiwavelength Observations and Source Classification 107
4.1 Optical Counterparts from *HST* 107
4.2 Multiwavelength Observations 108
4.3 Source Classification 138

Chapter 5: X-ray Luminosity Functions and Implications for Binary Evolution . . 162
5.1 X-ray Luminosity Functions 162
5.2 Star Formation Histories 168
5.3 Observed Correlations with Star Formation 171
5.4 X-ray Binary Formation and Evolution 180

Chapter 6: Individual X-ray Sources of Interest 190
6.1 The NGC 404 Central Engine 190
6.2 SN 2010da: The "Supernova Impostor" in NGC 300 205
6.3 NGC 300 X-1: a Wolf Rayet + Black Hole Binary 215

Chapter 7: Summary and Future Work 229
7.1 The Impact of the *Chandra* Local Volume Survey 229
7.2 Future Research 230

LIST OF FIGURES

Figure Number Page

2.1 Observations of the CLVS galaxies . . . 51
2.2 The fraction of point sources recovered by `wavdetect` . . . 54

3.1 Cumulative distributions of CLVS catalog properties . . . 58
3.2 X-ray color-color diagram of all CLVS X-ray sources . . . 68
3.3 The percentage of source classifications based on hardness ratios . . . 69
3.4 Radial source distributions . . . 71
3.5 X-ray vs. optical scale lengths . . . 73
3.6 Spectra of bright sources in NGC 404 . . . 94
3.7 Spectra of bright sources in NGC 55 . . . 95
3.8 Spectra of bright sources in NGC 2403 . . . 97
3.9 Spectra of bright sources in NGC 4214 . . . 101

4.1 Optical *HST* images of NGC 300 X-ray sources. . . . 110
4.2 Optical *HST* images of NGC 404 X-ray sources. . . . 112
4.3 Optical *HST* images of NGC 55 X-ray sources. . . . 113
4.4 Optical *HST* images of NGC 2403 X-ray sources. . . . 116
4.5 Optical *HST* images of NGC 4214 X-ray sources. . . . 120
4.6 Source classification flowchart, without *HST* imaging . . . 139
4.7 Optical and X-ray color-magnitude diagrams used to classify X-ray sources. . . 141
4.8 Source classification flowchart, with *HST* imaging . . . 142
4.9 Final source classification fractions by galaxy . . . 161

5.1 The differential 2-8 keV XLFs for each galaxy . . . 165
5.2 The XLF normalization versus SFR . . . 167
5.3 The SFHs of the five CLVS galaxies . . . 169
5.4 The SFR as a function of the birthrate parameter . . . 170
5.5 Cumulative distributions of the M_* and SFR from the CLVS and the literature 172
5.6 The slope of the XLF as a function of SFR . . . 174
5.7 The number of luminous X-ray sources as a function of the SFR . . . 176

5.8 The L_X–SFR relation . . . 177
5.9 The 90% and 50% X-ray luminosities as a function of SFR . . . 181
5.10 The number of *Chandra* HMXBs as a function of *HST* OB stars . . . 183
5.11 Duty cycle upper limits for HMXBs . . . 188

6.1 Smoothed *Chandra* image of the NGC 404 nuclear region . . . 193
6.2 Soft and hard X-ray emission from the NGC 404 nucleus . . . 194
6.3 Hardness map of the NGC404 nuclear X-ray emission . . . 195
6.4 Hα-*I* color map with HR contours superimposed . . . 196
6.5 Cumulative arrival time of NGC 404 nucleus counts . . . 197
6.6 Power law photon index and Eddington ratio for LLAGNs and XRBs . . . 203
6.7 Raw and smoothed RGB imaging of SN 2010da . . . 208
6.8 The 0.5-6 keV spectrum of SN 2010da. . . . 211
6.9 The cumulative arrival time distribution of counts for SN 2010da . . . 212
6.10 Long-term X-ray luminosity of SN 2010da . . . 213
6.11 *Chandra* image of NGC 300 X-1 . . . 217
6.12 NGC 300 X-1 light curve . . . 218
6.13 NGC 300 X-1 periodogram . . . 220
6.14 PDF of NGC 300 X-1 . . . 220
6.15 Long-term light curve of NGC 300 X-1 . . . 221
6.16 The 0.5-5 keV spectrum of NGC 300 X-1 . . . 225
6.17 X-ray luminosities vs. photon indices for HMXBs with BH primaries . . . 228

LIST OF TABLES

Table Number Page

1.1 End Products of Stellar Evolution 12

2.1 Summary of CLVS Galaxy Properties 23
2.2 Prior X-ray Surveys of the CLVS Galaxies 24
2.3 Summary of *Chandra* Observations 27
2.4 Alignment of *Chandra* and *HST* Images 30
2.5 Number of X-ray sources at each `AE` iteration 33
2.6 *Chandra* Local Volume X-ray Source List 33
2.7 Fraction of CLVS Sources Recovered by `wavdetect` 55
2.8 Limiting Fluxes (erg s^{-1} cm^{-2}) and Luminosities (erg s^{-1}) of Merged Observations 56

3.1 Hardness Ratio Source Classification Scheme 60
3.2 Hardness Ratios of the CLVS X-ray Sources 61
3.3 Percentage (%) of Preliminary Classifications Based on Hardness Ratio Analysis 70
3.4 X-ray Radial Source Distribution Scale Lengths 72
3.5 Best-Fit Spectral Models for X-ray Sources with More Than 50 Counts . . . 75
3.6 Rapid and Long-Term Source X-ray Variability 102

4.1 Multiwavelength Observations of CLVS X-ray Sources 121
4.2 X-ray Point Source Classifications 143

5.1 X-ray Luminosity Function Fits 164
5.2 Galaxy Sample, Star Formation Rates, and Birthrate Parameters 171
5.3 HMXB-SFR Relation Data 178

6.1 NGC 404 Temporal Variability as a Function of Energy 198
6.2 Best-Fit Spectral Models for the NGC 404 Central Engine 200
6.3 AGN and XRB Properties of NGC 404 204
6.4 SN 2010da Spectral Fits 210
6.5 NGC 300 X-1 0.5-5 keV Spectral Fitting 224
6.6 Spectral and Timing Characteristics of NGC 300 X-1 226

7.1 Summary of X-ray Transient Properties 232

GLOSSARY

AGB: asymptotic giant branch

AGN: active galactic nucleus

BH: black hole

CE: common envelope

CV: cataclysmic variable

GC: globular cluster

HMXB: high mass X-ray binary

HR: hardness ratio

HST: Hubble Space Telescope

ISM: interstellar medium

LMXB: low mass X-ray binary

MS: main sequence

MW: Milky Way

NS: neutron star

PSF: point-spread function

RG: red giant

RLOF: Roche lobe overflow

SFH: star formation history

SFR: star formation rate

SN: supernova

SSS: super-soft sources

ULX: ultraluminous X-ray source

WD: white dwarf

XLF: X-ray luminosity function

XRB: X-ray binary

ACKNOWLEDGMENTS

I'd like to start with my sincere appreciation to the entire University of Washington Astronomy Department. Special thanks go to Benjamin Williams for giving me the opportunity to work on this data set, for reading endless paper drafts, and for pushing me outside my comfort zone. Thank you to my "administrative" advisor, Scott Anderson, for the endless supply of encouragement. Thank you to Eric Agol for teaching the high energy course and making sure I knew the physics of X-ray emission, and, of course, my GSR Toby Burnett from the physics department.

Thank you to the *Chandra* Local Volume Survey collaboration for all your invaluable input, discussions, and guidance: Julianne Dalcanton, Mike Eracleous, Paul Plucinsky, Evan Skillman, Mike Garcia, Anil Seth, Albert Kong, Terry Gaetz, and Dan Weisz. Thank you to Maren Halvorsen, Nancy Hertzsprung, and everyone at the Robinson Center for Young Scholars for the opportunity to teach astronomy to Seattle's highly capable youth, and reminding me why I wanted to become an astronomer in the first place.

Last, but certainly not least, thank you to my family. My parents, Carl and Karen Binder, have been the best cheerleaders I could have asked for. I spent the majority of my graduate school years truly believing I would never make it far enough to be writing this now, but you always knew better. Without your unshakable faith in me, I would not have gone far. And, of course, thank you to Eddie Schwieterman for all the love, comfort, and support you have brought to my graduate school experience and into my life. I can't wait for our future together.

DEDICATION

To my parents, Carl and Karen, who have always been my biggest fans.

Chapter 1

INTRODUCTION

X-ray binaries (XRBs), especially those with high-mass stellar companions (high-mass X-ray binaries, or HMXBs), are both a unique probe through which the end-points of massive star evolution can be studied and useful tracers of recent star formation. In a single XRB, the physics of mass transfer that occurs between a compact object and its stellar companion directly influences the quantity of X-rays produced over time. Determining how the star formation history of a galaxy correlates with its overall XRB population in the nearby universe sheds light on binary star evolution and is critical for understanding galaxy evolution at high redshift.

In this thesis, I examine the XRB populations (in particular, HMXBs) of five nearby galaxies. This sample is used to constrain massive binary evolution models, and to explore the relationship between HMXBs and star formation.

1.1 A Brief History of X-ray Astronomy

Humans have pondered the mysteries of the heavens for thousands of years. The advent of telescopes, first pointed at the sky hundreds of years ago by Galileo, allowed humans to peer beyond what is readily accessible to our eyes. Indeed, for most of human history, astronomy was comprised entirely of such optical observations, utilizing wavelengths that the human eye has evolved to detect. Observations at different wavelengths, however, are relatively new to astrophysics research. The emission of X-rays from astronomical sources was first detected during a rocket flight in 1962 [148]. Although the significance of X-ray emission as a probe of the universe at cosmological distances was immediately appreciated, it was not until several years later that substantial progress was made in understanding the origin of X-rays.

The first satellite devoted entirely to the study of cosmic X-rays was *Uhuru* [149], which

launched into orbit on 1970 December 12. *Uhuru* was designed to search for X-ray-emitting sources in an energy range of 2-20 keV, to determine their locations to a precision of a few square arcminutes (for bright sources), to study the structure of extended X-ray sources with a resolution of $\sim 30'$, to detect X-ray spectral features and variability and, whenever possible, to perform coordinated X-ray observations with multiwavelength facilities [149]. The X-ray fluxes measured corresponded to luminosities of up to 10^{38} erg s^{-1}, more than 10^4 times the total energy output of the Sun.

More than four decades have now passed since the era of *Uhuru*, and what began in the early 1970s as detailed individual studies of a small number of X-ray sources has blossomed into numerous mature, rich subjects: X-ray emission from active galactic nuclei (AGN) and their evolution over the history of the universe; supernovae explosions and gamma-ray bursts; and the evolution and collective properties of X-ray binaries (XRBs), starting with the discovery of Cen X-3 [149]. Much of the development in these fields has been made possible by continually improving X-ray satellites. Today, X-ray astronomy continues to be carried out using data from a host of satellites that were active from the 1980s to the early 2000s: the HEAO series, *EXOSAT*, *Ginga*, *RXTE*, *ROSAT*, *ASCA*, as well as *BeppoSAX*, which detected the first afterglow of a gamma-ray burst (GRB). NASA's current X-ray flagship mission is the *Chandra* X-ray Observatory, launched in 1999 along with the European Space Agency's *XMM-Newton*.

In order to understand how XRBs form, evolve, and how they can be used as tracers of star formation in nearby and distant galaxies, it is important to first understand the basics of *single* star evolution. I will next provide and overview of single star evolution, with an emphasis on massive stars. Then I will discuss how the evolution of massive binaries differs from that of single stars.

1.2 Overview of Single Star Evolution

Detailed studies in the 1970s of a small handful of oXRBs and early work on binary evolution models [232, 325, 92] have developed into a mature field, and a "standard picture" of XRB formation and evolution has emerged [417, 418]. The evolution of binary stars differs from that of single stars only if the stars are in a close enough orbit to interact with one another.

To understand how neutron stars and black holes can be formed in binary systems, and how the evolution of binary stars differs from that of single stars, we must first have a strong knowledge of *single* star evolution.

All stars begin their lives as interstellar clouds, whose cores contract under the influence of gravity. The subsequent evolution of the star is driven by the radiative loss of energy, which causes the gas to contract. Due to the release of gravitational potential energy, the temperature of the gas increases – a self-gravitating gas in hydrostatic equilibrium has a 'negative heat capacity.' The more the star radiates to cool itself, the more it will contract, the hotter it gets, and the more it is forced to go on radiating. This cycle is clearly an unstable situation over the long-term, and explains why the star, which starts out as an interstellar gas globe, *must* end its life as a compact object.

Stars spend the vast majority of their lives in a stage of hydrostatic equilibrium called the main-sequence (MS), where outward pressure generated by the fusion of hydrogen into helium balances against the inward pull of gravity. Hydrostatic equilibrium requires that the pressure within the star (a combination of radiation, gas pressure, and later on partially degenerate electrons) obey the relation

$$\frac{\mathrm{d}P}{\mathrm{d}r} = -\frac{GM(r)\rho(r)}{r^2}, \tag{1.1}$$

where $M(r)$ and $\rho(r)$ are the stellar mass and density interior to the radius r. There are three fundamental timescales of MS stellar evolution. When the hydrostatic equilibrium of a star is disturbed (e.g., because of sudden mass loss), the star will restore this equilibrium on a so-called dynamical timescale:

$$\tau_{\rm dyn} = \sqrt{R^3/GM} \approx 30 \text{ min } \left(R/R_\odot\right)^{3/2} \left(M/M_\odot\right)^{-1/2}. \tag{1.2}$$

When the thermal equilibrium of a star is disturbed, it will restore this equilibrium on a thermal timescale (also called the Kelvin-Helmholtz timescale), which is the time it would take for the star to emit all of its thermal energy at its present luminosity:

$$\tau_{\rm th} = GM^2/RL \approx 30 \text{ Myr } \left(M/M_\odot\right)^{-2}. \tag{1.3}$$

The third timescale is the nuclear one, which is the time needed for the star to exhaust its nuclear fuel reserve (proportional to M) at its present fuel consumption rate (proportional to L):

$$\tau_{\rm nuc} \approx 10 \text{ Gyr } (M/M_\odot)^{-2.5} . \tag{1.4}$$

The above timescales were approximated assuming a MS mass-luminosity relation of $L \propto M^{3.5}$ and a mass-radius relation of $R \propto M^{1/2}$. Both these relations are good approximations for $M \geq M_\odot$ MS stars [113, 62, 458], and are therefore appropriate when discussing the progenitor stars in a primordial HMXB.

Once a star has exhausted its initial hydrogen fuel, it begins its post-MS evolution. Without support from fusion, the core begins to contract and, therefore, the temperature increases, which can induce hydrogen shell fusion in the regions of the star outside the core. The final end-product of this evolution depends on the initial mass of the star (and, by extension, the star's core mass). The helium cores of low-mass stars (with initial stellar masses $M \leq 2.3\ M_\odot$) become degenerate during hydrogen shell burning, and when the core reaches $0.45\ M_\odot$ the temperature is hot enough to begin helium fusion. The ignition of helium in a degenerate core results in a "helium flash." Although energetic, the helium flash is not violent enough to disrupt the star.

Helium fusion produces carbon and oxygen as nuclear products. Stars with initial masses in the range 2.3–8 $M_\odot$ will eventually ignite carbon. Observations of white dwarfs in Galactic clusters that still contain stars as massive as $\sim 8 M_\odot$ [342, 437] suggest that even these higher-mass stars still terminate their lives as white dwarfs.

Massive stars ($M \geq 10\ M_\odot$) experience episodes of fusion alternating with stages of exhaustion of nuclear fuel, until their cores are composed of iron. Fusion of iron requires, rather than releases, energy; when the core mass exceeds the $\sim 1.4\ M_\odot$ Chandrasekhar limit (the maximum possible mass for an electron-degenerate configuration), the core implodes to form a neutron star or a black hole. The gravitational energy released during this implosion ($\sim 4 \times 10^{53}$ erg) is far greater than the binding energy of the stellar envelope, triggering a violent explosion which ejects the outer layers of the star with speeds up to 10^4 km s^{-1}. Such

catastrophic explosions are referred to as supernovae (SNe), and result in the formation of a compact object (either a neutron star or a black hole).

I will next provide a brief overview of the current understanding of supernovae, and the properties of neutron stars (NSs) and black holes (BHs).

1.3 Compact Object Formation

There is general agreement that most stellar-mass compact objects are formed during the collapse of a massive star, which powers a supernova explosion. In order to produce an explosion, the star must eject its outer layers. Instabilities play a key role in increasing the efficiency with which the gravitational energy from the collapsing star is tapped to drive an explosion. Just before collapse, the star's core is composed of iron covered by silicon and oxygen layers. The initial core collapse is halted when a proto-NS with $\sim$1 $M_\odot$ forms, and the infalling material "bounces" off the suddenly rigid core on a thermal timescale. The outgoing shock runs into the rapidly infalling outer layers of the star, stalling the explosion [53]. After the bounce, this dense proto-NS accretes from the turbulent atmosphere at extremely high rates (up to $\sim$1 $M_\odot$ s^{-1}; [53]). Depending on the delay time before the explosion, the mass of the proto-NS may increase via this post-bounce accretion by up to $\sim$1 $M_\odot$.

1.3.1 Instabilities

Some tiny fraction of a strong flux of neutrinos from the proto-NS is absorbed and heats the "turbulent atmosphere" in between the proto-NS and the stalled shock. A SN is successful only if this energy can be utilized to revive the shock, allowing it to overcome the pressure of the infalling material. For sufficiently strong convective motions, the infalling layers may be pushed out and the explosion can be restarted. However, an initial jolt is required to start convection [175, 52, 202, 138, 139]. The "turbulent atmosphere" region plays a crucial role in accumulating the energy from the collapse, and an instability must then trigger the convective engine leading to a SN explosion [175, 139, 40, 54, 137, 358, 51, 264, 296, 397].

The precise mechanism for the instability and shock revitalization are areas of active research. Two models have emerged, which can be characterized by their growth times:

the Rayleigh-Taylor (the "rapid" instability model, with a characteristic time of ∼10–20 ms) and the standing accretion shock instability (the "delayed" instability model, with a characteristic time of ∼100–150 ms). The Rayleigh-Taylor instability is encountered just above the surface of the proto-NS. Neutrinos heat the turbulent atmosphere from below, creating a temperature gradient [28], while the infalling gas from above created a pressure gradient. As a result, low entropy gas finds itself on top of high entropy material, and a violent displacement of layers follows. Once the movement of the plasma is initiated, it turns into a convective engine. The Rayleigh-Taylor instability may appear quickly, ∼20 ms after the initial bounce [137]; however, the convective engine needs ∼100 ms to build up sufficient strength to launch the explosion. In simulations, if this instability does not launch the explosion within the first 200–300 ms, it means the Rayleigh-Taylor mechanism has failed and the star will not explode.

The standing accretion shock appears where the initial bounce stalls and gives rise to additional instabilities [54]. Outer stellar material is essentially in free fall as the star collapses. This material can acquire significant momentum by the time it hits the standing shock, and the "pounding" that results causes the plasma trapped in the turbulent atmosphere to vibrate and create pressure waves [129]. Interference in these waves transfers momentum to the plasma, which triggers the convective engine. The growth time for these "acoustic" instabilities is considerably longer than the Rayleigh-Taylor case: strong standing accretion shock instabilities require ∼500 ms to develop [40], and may result in a SN explosion as late as one second after the bounce.

As the proto-NS and turbulent atmosphere cool, energy stored in this region begins to decline. The amount of energy that can be extracted from the turbulent atmosphere, therefore, depends on how long it takes before the convective engine turns on. The Rayleigh-Taylor instability appears first; if it strong enough to start the convection, and there is enough energy accumulated in the turbulent atmosphere, the outer layers of the star can be ejected and a rapid expansion follows on a timescale of ∼200–300 ms. For stars in the 8–12 $M_{\odot}$ mass range [198, 48, 456, 294], a strong flux of neutrinos heats the material above the proto-NS, and the resulting pressure is sufficient to drive the explosion. The Rayleigh-Taylor instability therefore *enhances* the explosion, resulting in strong SN explosions. Even

during strong explosions, some degree of fallback is expected ($\sim$0.2–0.3 $M_\odot$). Thus, stars in the $\sim$8–12 $M_\odot$ mass range experience strong SN explosions and produce low-mass NSs, in the range of $\sim$1–1.5 $M_\odot$. For example, there are some indications that the Crab supernova progenitor star was in the 8–11 $M_\odot$ range [295, 293, 67, 91, 220].

For stars in the range of $\sim$12–20 $M_\odot$, the SN explosions are still strong due to the density of infalling material, which can hold off the explosion for long enough to allow significant energy build up in the turbulent region. The delay in the explosion allows for significant post-bounce accretion to occur. However, the infalling material does not hold off the explosion long enough for energy in the turbulent region to begin to decline, allowing the Rayleigh-Taylor instability to trigger the convective engine on a "rapid" timescale. As a consequence, $\sim$12–20 $M_\odot$ stars form more massive NSs, $\sim$1.5–3 $M_\odot$.

Stars up to $\sim$40 $M_\odot$ undergo significantly weaker SNe, if there is an explosion at all. Infalling silicon and oxygen layers prevent the convective engine from launching the explosion, allowing the star to collapse first to a proto-NS and to continue to collapse into a BH. Even if standing shock instabilities develop prior to the silicon/oxygen layers finishing their infall, the explosion will be weak and a signifiant amount of fallback will occur. The resulting BH has a mass of $\sim$3–10 $M_\odot$, depending largely on the star's initial stellar mass and the strength of the stellar winds.

For the most massive stars (>40 $M_\odot$), neither the Rayleigh-Taylor nor the standing shock instabilities can launch a convective engine energetic enough to overcome the high pressure of the infalling material [sometimes called an "unnovae," 222, 241]. Even if a weak explosion manages to occur, all of the ejected material is subject to fallback, and the entire star is accreted onto the newly formed massive BH ($\sim$5–15 $M_\odot$).

It is widely accepted that there are two main varieties of SN events [454, 177]: the thermonuclear run-away in white dwarfs approaching the Chandrasekhar mass and the direct core collapse of massive stars. Since the former SN explosion mechanism is not responsible for the creation of compact objects, I will focus the remainder of the discussion of SNe on two types of core collapse SN: the less luminous electron-capture SNe that occurs for lower-mass stars, and direct collapse of an iron core.

1.3.2 Core-Collapse Supernovae

Direct collapse of an Fe core, often referred to simply as "core-collapse SN" [CCSN 7, 75, 52, 54, 50, 138], are some of the most energetic events in the Universe, producing several times 10^{53} erg in neutrinos and several 10^{51} erg of kinetic energy in ejected material – as much energy as the Sun will produce over its entire lifetime. Stars more massive than $\sim$10 $M_\odot$ will eventually form iron cores, which implode under the pressure of infalling material until the electron degeneracy pressure is exceeded and a proto-NS forms.

Electron capture supernovae (ECSNe) are a distinct class of core-collapse supernovae (CCSN). Stars with initial masses of $\sim$8–10 $M_\odot$ are the high-mass equivalents to AGB stars [172], often called "super" AGB stars, and form an electron-degenerate core consisting of oxygen, neon, and magnesium (O-Ne-Mg) during the final stages of their evolution (instead of an iron core, as is the case for more massive stars). High rates of mass loss due to strong stellar winds [up to 10^{-4} $M_\odot$ yr^{-1} 455] mean that only a handful of these stars actually experience a SN explosion and form compact objects [279, 278]. Most of these stars end their lives as O-Ne-Mg white dwarfs. However, a handful of stars at the very upper end of this mass range [e.g., the top $\sim$4%; 378, 317] will have collapse induced by electron capture when the core mass grows to 1.38 $M_\odot$ and the central density reaches 4×10^9 g cm^{-3}, and explode via an ECSN [220, 55]. ECSNe are powered by neutrino heating, and result in a low energy explosion typically on the order of 10^{50} erg [176, 430, 203, 331], with energies of up to 10^{51} erg possible in some scenarios [267].

1.3.3 Neutron Stars

Neutron stars represent the strongest gravitational environment in which matter can stably exist. The state of stable matter at ultra-high densities remains an open question in subatomic physics. With the addition of strong magnetic fields and intense radiation, NSs provide a unique view into a density-temperature regime that cannot be explored in any laboratory setting. The birth properties of NSs also provide one of the most important constraints on SN theories.

The characteristic physical timescales – the free-fall time, fastest stable orbital period,

and stellar spin period – near a NS are measured in milliseconds. These timescales encode fundamental physical properties of the NS: its mass, radius, and angular momentum. The high characteristic temperature of matter in the vicinity of a NS (or BH) leads to a principal electromagnetic window in the X-rays. With the advent of X-ray astronomy, NSs themselves could be detected through their thermal emissions, and X-ray timing remains the most direct way of probing NS structure and dynamics.

The interior structure of a NS is described in a global sense by the equation of state (EOS), which relates the star's mass to its radius. The EOS of bulk nuclear matter is still highly uncertain. While most EOSs predict that R will decrease as M (and therefore the self-gravitational force) increases, different assumptions about the interior composition of the NS produce different detailed mass-radius relations [237, 221, 245]. The two outstanding issues surrounding NSs are therefore simple to state: what is the maximum mass of a NS, and what is a characteristic NS radius?

Observations of NS in evolved binary systems – XRBs, or the even more evolved binary pulsar systems – represent the only practical way of directly constraining either the mass or radius of individual NSs. A few dozen NSs have had masses reliably determined [some to $\pm 0.001\ M_{\odot}$; 351, 31, 135, 251] from binary pulsar timing, with all measured masses having a maximum value of 1.5–1.65 $M_{\odot}$ [consistent at the 4σ level; 136, 104, 30, 102]. Other NS mass measurements from XRB observations have resulted in an average mass of $1.35 \pm 0.04\ M_{\odot}$ [401]. Measurements of NS radii from observations of LMXBs are $\sim$11.5 km [387], consistent with the theoretical range of 10-15 km [173, 388]. Most importantly, no single NS has had *both* its mass and radius determined independently of emission models.

The identification of thermal radiation from NSs in XRBs has provided an additional breakthrough in understanding NS structure. NSs in quiescent XRBs likely have weak magnetic fields, and in some cases a known composition (a nearly pure hydrogen atmosphere from accretion from the companion star). When the XRB is actively undergoing mass transfer, reactions deep in the NS crust heat the interior. When accretion onto the NS star stops, the increased heat is radiated away from the surface. Spectral fitting of this thermal radiation can determine the radius,

$$r_{\rm rad} = \left(\frac{R}{D}\right)\left(1 - \frac{2GM}{Rc^2}\right)^{-1/2}, \tag{1.5}$$

where R and M are the NS radius and mass, respectively. Although both *Chandra* and *XMM-Newton* have been used to constrain the NS radius, the accuracy of this measurement is not yet sufficient to constrain the EOS.

1.3.4 Black Holes

Black holes are observed to span a large range of masses, from the stellar mass remnants of massive stars ($\sim$3–10 $M_\odot$) to supermassive (10^{6-9} $M_\odot$) BHs at the cores of galaxies. XRBs provide some of the best opportunities for obtaining mass constraints on stellar-mass BHs. Roughly 50 stellar mass BHs [470] have been observed in the local universe [248], including about 20 BHs with direct mass measurements.

A defining property of BHs is the event horizon, an immaterial surface that separates the interior region of space-time that cannot communicate with the external universe. For a Schwarzschild BH (e.g., non-spinning), the radius of the event horizon is given by

$$r_{\rm Sch} = \frac{2GM}{c^2} \approx 30 \text{ km} \left(\frac{M}{10M_\odot}\right). \tag{1.6}$$

For an extreme Kerr BH (e.g., rapidly spinning), the event horizon radius can move inwards by up to a factor of 2.

Black holes provide a key laboratory for testing general relativity. The immediate environs of BHs provide a unique laboratory where the properties of strong gravity can be directly observed. Near the event horizon of a BH, frame-dragging and gravitational redshift effects become important and stable circular orbits disappear. Merging BHs are expected to be a powerful source of detectable gravitational radiation. BHs additionally exhibit other exotic behaviors, such as plasma jets which accelerate matter to relativistic speeds and whose energy spectrum peaks near $\sim$1 Gev [436]. Newborn BHs are invoked as an explanation of gamma ray bursts [314].

1.4 Binary Star Evolution

The realization that neutron stars and black holes could exist in close binary systems initially came as a surprise. It was anticipated that the energy imparted during the SN explosion would act to disrupt the binary [38]. Later studies revealed that the effects of large-scale mass transfer prior to the SN was responsible for the survival of XRBs like Cen X-3 [419, 410], and that accreting neutron stars and black holes could serve as the energy source for the strong Galactic X-ray sources [464, 372].

To understand the formation and evolution of XRBs, it is essential to understand the interactions between the stellar components of a binary star system. Such interactions may include spin-orbit tidal interactions, mass transfer, and loss of angular momentum. XRBs can be formed through two main channels: as the direct result of a primordial binary star system, or through dynamical interactions in dense stellar environments (i.e., globular clusters). LMXBs are thought to form primarily through dynamical channels [163, 425]. It has been proposed that globular clusters are the principle (or sole) birth places of LMXBs in early-type galaxies [443], with natal kicks from compact object formation or evaporation of the parent cluster being responsive for LMXBs observed in the field [231, 206, 428]. HMXBs, meanwhile, are believed to form primarily from primordial binaries. In this thesis, I focus on the evolution of HMXBs from primordial binaries in the disks of galaxies, where the stellar density is too low for dynamical interactions to play a significant role.

For a primordial binary of two massive stars, the more massive component exhausts its hydrogen core faster, and will rapidly expand into a giant on a timescale of $\sim 10^{6-7}$ yr. The giant overflows its Roche lobe and begins transferring its hydrogen envelope to its lower-mass companion. At this point, there are two possible evolutionary pathways for the system, depending on the mass ratio of the two stars. If the stars are of comparable mass to one another (i.e., a high-mass XRB, or HMXB, progenitor system), the lower-mass star can accept the entire mass of the companion's hydrogen envelope. This leaves behind an He core, and the previously lower-mass companion has now become the more massive component. The He core finishes the remainder of its evolution quickly, on the order of $\sim 10^{5-6}$ yr. It explodes as a SN and leaves behind a compact object (most likely a neutron

star), which will become the main X-ray emitter in the HMXB. The massive companion now has an accelerated main sequence evolution due to its higher mass, and within $\sim 10^6$ yr expands into a supergiant.

X-rays can be produced in the system in one of two ways: stellar winds driven by the giant companion are accreted directly onto the compact object, or the giant can overflow its Roche lobe and begin transferring mass onto the compact object. The former case will produce lower-luminosity systems ($< 10^{36}$ erg s^{-1}), while Roche lobe overflow (RLOF) system are typically 2–3 orders of magnitude more luminous. The end product of a massive star's evolution depends on whether or not the star is in a binary system (see Table 1.1), with less massive progenitors able to produce higher mass remnants due to mass transfer from the companion.

Table 1.1: End Products of Stellar Evolution, as a Function of Mass, for Single and Binary Stars

		Final Product	
Initial Mass ($M_\odot$)	He-core mass ($M_\odot$)	Single Star	Binary Star
(1)	(2)	(3)	(4)
<2.3	<0.45	CO white dwarf	He white dwarf
2.3 – 6	0.5 – 1.9	CO white dwarf	CO white dwarf
6 – 8	1.9 – 2.1	O-Ne-Mg white dwarf	O-Ne-Mg white dwarf
8 – 12	2.1 – 2.8	neutron star	O-Ne-Mg white dwarf
12–25	2.8 – 8	neutron star	neutron star
>25	>8	black hole	black hole

I will next discuss the physics behind two important phases of binary star evolution: the common envelope (CE) phase, and the phase in which accretion onto the compact object occurs.

1.4.1 The Common Envelope Phase

It is generally accepted that a common envelope (CE) phase, in which the two binary components are orbiting about their center of mass within a shared, differentially rotating atmosphere, is essential for the formation of short-period binary systems containing compact objects [197, 396]. The CE phase of a binary star's evolution occurs if mass transfer between the two components of the binary proceeds more quickly than the accreting star can achieve equilibrium. A CE forms, and both stars begin to orbit one another through a combined atmosphere. Energy is transferred (via torques and frictional forces) from the binary components to the CE, which unbind the gases in the combined atmosphere. This process acts to harden the binaries (i.e., reduce the binary separation between the two components), and is thought to be the dominant mechanism for producing closely-interacting cataclysmic variables [305, 302] and XRBs [116, 12].

Despite widespread acceptance and recent advancements in computational capabilities, the detailed hydrodynamics and long-term evolution of the CE are still poorly understood. While trends observed in a handful of XRBs can be reproduced with existing computer models for a handful of sources [334, 353, 395, 345], accurately modeling entire populations of XRBs remains a challenge. The current approach to this problem is to parameterize the efficiency at which energy is transferred from the binary orbit into the ejection of the CE using a single parameter, $\alpha_{\rm CE}$ [435]. Using this efficiency parameter, the relation between the initial and final orbital separations of the binary component can be written as

$$\alpha_{\rm CE}\left[\frac{GM_cM_a}{a_f}-\frac{G(M_e+M_c)M_a}{a_i}\right]=|E_{\rm bind}|, \tag{1.7}$$

where G is the gravitational constant, a_i and a_f and the initial and final orbital separations, respectively, M_c is the mass of the donor star's core, M_e is the mass of the donor envelope, and M_a is the mass of the accreting star. $E_{\rm bind}$ is the energy required to unbind the CE, which includes both the gravitational binding energy and the thermal energy of the plasma gas, the ionization of H and He, and the dissociation of H_2 [168, 169]. One large source of uncertainty in the calculation of $|E_{\rm bind}|$ is the definition of the core-envelope boundary, which is typically assumed to be the radius at which the mass fraction of H drops below a

critical value [typically ∼10%, although model predictions are not very sensitive to changes in this parameter; 106, 252, 244].

Based on the widely accepted theory of XRB formation and the CE phase, one would expect that HMXBs containing a NS and a "naked He" star (He-HMXBs) would be common. These systems are thought to form when the stellar companion in the system evolves into a supergiant and forms a CE with the NS. Nearly two-thirds of all observed HMXBs contain a Be-type star (B stars with strong emission line spectra) in a wide orbit with a NS [P >30 days; 248], ideal candidates for He-HMXB progenitors. However, there is a puzzling lack of He-HMXBs in observations. At least 81 Galactic Be-HMXBs have been observed [333, 212, 22, 348, 347, 80], but after several decades of X-ray observations only one He-HMXB, Cyg X-3, has been found [422]

1.4.2 Accretion onto the Compact Object

Although accreting compact objects, including AGN, are relatively rare in the universe, they are so efficient at producing light (especially BHs) that their total emission, integrated over a Hubble time, is only an order of magnitude less than all of the stars in the universe [125].

I will next discuss two modes of accretion onto a compact object: accretion via a disk, and direct accretion from the winds of the companion star.

Disk Accretion

Perhaps the most famous model for accretion onto a compact object is the thin accretion disk, often called the α-disk model [325, 367, 297]. In this model, the companion star fills its Roche lobe and a narrow stream of gas escapes through the inner Lagrangian (L1) point. This escaping gas has a high specific angular momentum and cannot accrete directly onto the compact object; instead, it feeds into a thin disk of matter called an accretion disk. The α-disk model [367] parameterizes the disk viscosity, ν, as

$$\nu = \alpha a H, \tag{1.8}$$

where a is the sound speed in the accretion disk, H is the disk scale height (which can be a function of radius), and α is a dimensionless number $\leq$1. Typical disk models assume $\alpha \sim$0.01–0.1.

In the accretion disk, the gas moves in Keplerian orbits with an angular velocity,

$$\Omega_K = \left(\frac{GM}{R^3}\right)^{1/2}. \tag{1.9}$$

Viscous dissipation slowly drains energy from the bulk orbital motion, and viscosity transports angular momentum outward. As a result, the gas gets hotter as it sinks deeper into the gravitational potential well of compact object. In extreme gravitational fields, no stable particle orbits are possible close to the compact object [368]. The luminosity generated by thin disk accretion is given by

$$L_{\rm disk} = \frac{1}{2}\frac{GM\dot{M}}{R_*}, \tag{1.10}$$

where M is the mass of the compact object, $\dot{M}$ is the mass accretion rate, and R_* is the inner radius of the accretion disk. In other words, half of the gravitational energy to radius R_* is released as luminosity; the remaining gravitational energy goes into rotational energy and may be advected into the BH or deposited onto the surface of the NS.

For XRBs (and other accreting objects), it is often useful to discuss the luminosity in terms of the "Eddington luminosity" (or "Eddington limit"). This is the luminosity a source will achieve when the force of gravity pulling inwards balances the radiation pressure pushing out. For any accreting object, there is a luminosity beyond which radiation pressure will overcome gravity, and therefore a natural feedback process limits the accretion rate of the compact object.

Deriving the Eddington limit is straightforward: assuming spherical symmetry, the inward force of gravity is:

$$F_g = \frac{GMm}{R^2}, \tag{1.11}$$

which must balance the radiation force outward, given by

$$F_{\rm rad} = \frac{\kappa m}{4\pi R^2}\frac{L}{c}, \tag{1.12}$$

where κ is the opacity of the accretion disk material (here, a pure hydrogen disk is assumed). Since the accreting material in high-energy accretion disks is mostly composed of ionized hydrogen, the opacity is provided by Thomson scattering. It is useful to approximate that the radiation force on the disk will be felt almost entirely by electrons, while the mass of the disk lies almost exclusively in the protons. In other words, $\kappa = \sigma_T/m_p$, where σ_T is the cross-section for Thomson scattering and m_p is the mass of a proton.

Setting these two forces equal to one another and solving for L yields

$$L_{\rm Edd} = \frac{4\pi GMcm_p}{\sigma_T}. \tag{1.13}$$

For stellar-mass compact objects such as NSs and BHs, it is useful to write

$$L_{\rm Edd} = 1.3 \times 10^{38}\left(\frac{M}{M_\odot}\right) {\rm erg\ s^{-1}}. \tag{1.14}$$

When the accretion rate is greater than $\sim$1% of Eddington, the gas density can remain high, and the ionized gas is able to radiate efficiently and the accretion disk can remain geometrically thin [367, 242, 178].

If the gas density is low the gas may be unable to radiate energy efficiency, and the heat will be advected inwards with the flow. The disk becomes hot and "puffs up," forming a geometrically thick, but optically thin, and radiately inefficient advection-dominated accretion flow [ADAF; 242, 338, 291] XRBs, especially those containing BHs, are observed to cycle through different states [268] which are thought to correspond to transitions between α-disk accretion and more ADAF-like structures [121].

Wind Accretion

Early-type OB stars often possess strong line-driven winds [256], with mass loss rates of $\sim 10^{-10}$ $M_\odot$ yr^{-1} up to 10^{-6} $M_\odot$ yr^{-1} [304, 330]. In HMXBs, some fraction of this wind can be directly accreted by the compact object. Unlike the α-disk or ADAF models dis-

cussed above, this accretion mechanism is roughly spherical in nature, and as such is better described using the Bondi-Hoyle accretion model [44, 43].

The wind speed as a function of distance r from the compact object can be approximated as:

$$v(r) \sim v_\infty \left(1 - \frac{R_*}{r}\right)^\beta, \tag{1.15}$$

where R_* is the radius of the compact object, v_∞ is the ambient ISM velocity very far from the accreting object. Measurements of the ISM suggest typical values of $v_\infty \sim$2000 km s^{-1} and $\beta \sim$0.5–1 [186, 144, 329, 229, 230].

The material in the stellar wind will be captured when its kinetic energy is no longer able to overcome the gravitational pull of the compact object. This occurs when

$$\frac{1}{2} v_\infty^2 = \frac{GM}{r_{\rm acc}}, \tag{1.16}$$

where $r_{\rm acc}$ is the Bondi-Hoyle accretion radius and M is the mass of the compact object. This expression can be re-arranged to write:

$$r_{\rm acc} = \frac{2GM}{v_\infty^2}. \tag{1.17}$$

For Bondi-Hoyle accretion, the mass accretion rate onto the compact object is given by:

$$\dot{M} = \pi r_{\rm acc}^2 \rho_\infty v_\infty = \frac{4\pi G^2 M^2 \rho_\infty}{v_\infty^3}, \tag{1.18}$$

where ρ_∞ is the wind density. The wind density is, in turn, related to the mass loss rate of the donor star:

$$\rho_\infty = \frac{\dot{M}_w}{4\pi a^2 v_\infty}, \tag{1.19}$$

where $\dot{M}_w$ is the mass loss rate due to the stellar winds of the donor star and a is the distance between the donor star and the compact object.

In order to estimate the mass accretion rate onto the compact object, one must additionally take into consideration the orbital motion of the compact object itself. In other words,

$v_\infty^2 \sim v_{\rm wind}^2 + v_{\rm compact}^2$. Using the wind velocity profile from Equation 1.16 and assuming an orbital velocity of the compact object to be $(GM/a)^{1/2}$, Equation 1.18 becomes:

$$\dot{M} = \frac{G^2 M^2}{a^2 v_\infty \left(\frac{GM}{a} + v_\infty^2\right)^{3/2}} \dot{M}_w. \tag{1.20}$$

Equation 1.20 can be simplified in cases where the orbital velocity is much larger than the wind velocity, or vice versa:

$$\dot{M} = \begin{cases} \left(\frac{GM}{a v_\infty^2}\right)^{1/2} \dot{M}_w & \text{if } v_{\rm orbit} \gg v_\infty \\ \frac{G^2 M^2}{a^2 v_\infty^4} \dot{M}_w & \text{if } v_{\rm orbit} \ll v_\infty \end{cases}$$

In a realistic HMXB, the accreted material still possesses some angular momentum. As a result, a small accretion disk may still form, even in cases of wind-dominated accretion [254, 39, 371, 451]. Typical luminosities due to wind accretion are on the order of a few $\times 10^{36}$ erg s^{-1} [32, 366], roughly 2–3 orders of magnitude lower than for disk accretors [325].

1.5 X-ray Emission from Normal Galaxies

The X-ray emission from normal, non-active galaxies originates from a mixture of stellar sources and hot, diffuse gas. It is well known that the Milky Way hosts both HMXBs and LMXBs, reflecting the underlying ages of its stellar populations. In late-type galaxies, where the overall energy output is dominated by the light of massive stars, the X-ray emission is dominated by HMXBs, and the fast evolutionary timescale of massive stars ($\sim 10^7$ years) makes X-ray emission from HMXBs nearly simultaneous with their formation [375]. This provides a useful tracer of recent star formation, especially since X-ray emission is much less affected by interstellar extinction than conventional indicators [i.e., stellar population synthesis models; 213]. The use of X-ray emission as star formation indicator was first conceived in the late 1970's [393], and a correlation between X-ray emission from HMXBs and global far-IR emission from star-forming galaxies was first observed by *Einstein* [122]. However, it was not until the launch of *Chandra* that observers obtained the necessary angular resolution to study discrete X-ray point source populations.

Longer-lived LMXB systems trace older underlying stellar populations [225, 383, 406].

Early-type galaxies (E and S0 galaxies) contain relatively homogenous stellar populations, resulting in a more uniform population of XRBs that is dominated by LMXBs [354, 217]. Early-type galaxies show a relative lack of high-luminosity sources when compared to star-forming galaxies [216, 74, 124].

In the luminosity range detectable in most external galaxies with typical *Chandra* observations ($>10^{37}$ erg s^{-1}), Galactic X-ray emission is dominated by XRBs, while at lower luminosities other sources (accreting white dwarfs, supernova remnants, colliding wind binaries) are detected [434, 160, 442]. Populations of XRBs in the Milky Way and external galaxies are typically characterized by the shape of their X-ray luminosity functions (XLFs), which describe the number density of sources that exist at a given luminosity. Given the differences in evolutionary pathways, timescales, and environments which govern the formation of HMXBs and LMXBs, one should expect that the shape of a galaxy's XLF correlates with the SFH and age of the parent stellar population [161, 21, 120]. XLFs are typically parameterized as power laws or broken power laws, and are characterized by their slope, normalization, and (if present) the break luminosity at which the power law slope changed. In early-type E/S0 galaxies dominated by LMXBs, the normalization of the XLF is related to the stellar mass of the galaxy as would be expected for a passively evolving population of old stars [150, 218]. The XLFs of spiral and irregular-type galaxies, on the other hand, are dominated by HMXBs [174] and have a normalization that correlates with the recent star formation rate (SFR) of the host galaxy [465, 216, 161, 162].

1.6 Thesis Outline

In this thesis, *Chandra* and *HST* observations of five nearby galaxies are used to provide insight into the formation and evolution of XRBs and the X-ray luminosity function of galaxies. These results were also published in a series of papers: [36, 37, 35, 34, 33]. The remainder of this thesis is organized as follows:

- Chapter 2 describes the *Chandra* Local Volume Survey (CLVS) and the construction of the full X-ray point source catalogs.

- Chapter 3 presents the detailed X-ray analysis of the full CLVS source catalogs, in-

cluding hardness ratio analysis, spectral fitting, timing analysis, and the radial source distribution.

- Chapter 4 describes the multi-wavelength observations available for the full CLVS source catalogs. This includes both *Hubble Space Telescope* and publicly-available optical, infrared, radio, and ultraviolet observations. This chapter additionally describes the X-ray source classification scheme used to separate likely XRB candidates from background galaxies, foreground stars, supernova remnants, etc.

- Chapter 5 describes the construction and analysis of the X-ray luminosity functions for the XRB candidates found in each galaxy, and implications for binary star evolution models are also discussed.

- Chapter 6 presents a deeper analysis of three individual sources of interest observed as part of the *Chandra* Local Volume Survey. These sources are the NGC 404 central engine, the "supernova impostor" SN 2010da, and the black hole + Wolf-Rayet binary NGC 300 X-1.

- Chapter 7 is a summary of the impact the CLVS catalogs have had on our understanding of XRB populations, and presents directions for future research.

Chapter 2

THE *CHANDRA* LOCAL VOLUME SURVEY

The *Chandra* Local Volume Survey (CLVS) is a deep, volume-limited X-ray survey of five nearby galaxies. Overlapping *Hubble Space Telescope* (*HST*) imaging from the ACS Nearby Galaxy Survey Treasury additionally provides a wide-area multicolor census of stars down to $M_V \sim 0$ [87] and detailed star formation histories (SFHs) for at least 20% of each galaxy. When combined with the already well-studied disks of M 31 [224] and M 33 [449, 316, 407], these galaxies contain ∼99% of the stellar mass and ∼90% of the recent star formation out to a distance of ∼3.3 Mpc [402, 258, 133].

With its excellent angular resolution ($\sim 0\farcs5$) and positional accuracy, the *Chandra X-ray Observatory* [438] is the only X-ray telescope capable of separating the X-ray point source populations of nearby galaxies from diffuse emission. When combined with deep, optical *HST* imaging, reliable source identification and optical counterpart identification may be carried out even at distances of a few Mpc. The five galaxies targeted for the CLVS are nearby enough to perform resolved studies at both X-ray and optical wavelengths, with low background levels.

The CCD detectors present onboard *Chandra* (and, also *XMM-Newton*) provide a data hypercube of the observed field of view. Each individually detected photon is tagged with a two-dimensional position, energy, and time of arrival, providing observers simultaneously with an X-ray image and, for each detectable source, an X-ray spectrum and light curve. The X-ray CCD detectors are primarily composed of silicon, with a "gate" structure on one surface that defines pixel boundaries (each CCD is 1024×1024 pixels). Front illuminated (FI) CCDs have gate structures facing the incident X-ray beam, while back illuminated (BI) CCDs have their back sides facing incident X-ray radiation. BI devices possess better chip-average energy resolution than that of FI devices, and the response of the BI devices extends to energies inaccessible to the FI chips. The CCDs are arranged in two arrays: the I-array

(ACIS-I), containing 4 FI CCDs (I0-I3) in a square configuration spanning 16′.9×16′.9, and the S-array (ACIS-S), with 6 CCDs (S0-S5, with S1 and S3 being BI and the remaining four chips being FI) arranged in a linear array with a field of view of 8′.3×50′.6. Since CCDs are sensitive to optical radiation as well as X-rays, optical blocking filters are placed over the detectors.

I will next discuss the five galaxies targeted by this Survey: NGC 55, NGC 300, NGC 404, NGC 2403, and NGC 4214. This will be followed by a description of the observations used (both new and archival *Chandra* exposures), the data reduction techniques, and *Chandra*–*HST* image alignment. Then I will describe in detail how the X-ray point source catalogs were generated for each galaxy, and present the X-ray point source list for the total *Chandra* Local Volume Survey.

2.1 The Galaxy Sample

The five target galaxies of the CLVS span a representative sample of disk galaxies, with a range of stellar masses, metallicities, and morphologies. The basic properties of each of these galaxies, including their distance, morphology, inclination, stellar masses, and hydrogen column density $N_{\rm H}$ are summarized in Table 2.1. Table 2.2 summarizes prior X-ray surveys of all five galaxies, including the number of highly significant X-ray point sources detected and the limiting unabsorbed luminosity of each study.

2.1.1 NGC 55

NGC 55 is a member of the nearby Sculptor group of galaxies. Classified as an IAB(s)m type galaxy [98], NGC 55 is an edge-on analog of the Large Magellanic Cloud [362] and is the nearest bright edge-on galaxy [210]. The optical morphology of NGC 55 is asymmetric, with a bright region displaced from the geometrical center of the galaxy [346] interpreted as a bar viewed near- to end-on [97]. The edge-on orientation of NGC 55 offers excellent insight into the effect of disk-based star formation activity on extra-planar regions, and as such, NGC 55 has been a popular target for ISM studies [328, 127, 187, 303]. Ionized gas shells are observed to protrude well above the plane of the galaxy, and at least some of this

Table 2.1: Summary of CLVS Galaxy Properties

Property	NGC 55	NGC 300	NGC 404	NGC 2403	NGC 4214
(1)	(2)	(3)	(4)	(5)	(6)
Distance (Mpc)	2.1[a]	2.0[b]	3.05[b]	3.3[c]	2.9[c]
Morphology[d]	SB(s)m	SA(s)d	SA0	SAB(s)cd	IAB(s)m
R.A. (J2000)[e]	00:14:53.6	00:54:53.5	01:09:27.0	07:36:51.4	12:15:39.2
Decl. (J2000)[e]	-39:11:48	-37:41:04	+35:43:05	+65:36:09	+36:19:37
$m - M_0^e$	26.42	26.45	27.74	27.73	27.59
M_B^d	-17.76	-17.68	-16.63	-18.61	-17.39
Inclination[f] (°)	83	45	19	56	38
Position Angle[e] (°)	108	111	0	128	0
Major linear diameter[f] (kpc)	12.05	12.95	3.25	19.43	7.05
Stellar mass ($M_\odot$)	3×10^{10}[d]	4.3×10^{9}[h]	6.9×10^{8}[i]	1.9×10^{10}[j]	1.5×10^{9}[f]
$N_{\rm H}$ [k] (10^{20} cm^{-2})	1.37	4.19	5.13	4.36	1.99

[a][402], [b][87], [c][133], [d][98], [e]NED, [f][210], [g][284], [h][327], [i][400], [j][95], [k]Absorption through the ISM of the Milky Way, from [208]

gas appears to cool sufficiently to form new stars in the halo [409, 408]. The star formation rate derived from the total infrared luminosity of NGC 55 is 0.22 $M_\odot$ yr^{-1} [117].

NGC 55 was first observed at X-ray wavelengths by *ROSAT*, revealing 15 discrete X-ray sources and localized diffuse emission within the optical confines of the galaxy [337, 360, 85]. One of these sources has been established as a ULX and likely BH-XRB [390]. A detailed X-ray view of NGC 55 by *XMM-Newton* [391] revealed 137 X-ray sources detected within the field of view down to a flux of $\sim 5 \times 10^{-15}$ erg s^{-1} cm^{-2} in the 0.3-6 keV energy range. Of these sources, 42 are within the optical confines of the galaxy, and the authors find ∼20 X-ray sources to be consistent with an XRB origin, five SNRs, and seven candidate super soft sources (SSSs).

2.1.2 NGC 300

The first X-ray population studies of NGC 300 were performed with *ROSAT* between 1991 and 1997 [336], identifying 29 bright X-ray sources including NGC 300 X-1, a highly vari-

Table 2.2: Prior X-ray Surveys of the CLVS Galaxies

Galaxy	Observatory	# Detected Sources (within D_{25})	Limiting Unabs. Luminosity (10^{36} erg s^{-1})[a]	Reference(s)
(1)	(2)	(3)	(4)	(5)
NGC 55	*ROSAT*	22 (7)	16.8	[337, 360]
	XMM-Newton	137 (42)	2.9	[391]
NGC 300	*ROSAT*	47 (29)	7.7	[336]
	XMM-Newton	163 (86)	1.7	[60]
	Chandra	95 (77)	1.5	[34]
NGC 404	*Chandra*	0 (0)	1.2	[119]
	Chandra	72 (30)	0.6	[33]
NGC 2403	*Chandra*	58	0.5	[462]
	ASCA	3	$\sim 10^3$	[227]
	Chandra	41	320	[361]
	Einstein	6	260	[123]
NGC 4214	*Chandra*	20 (17)	1.0	[171]

[a]The limiting unabsorbed luminosities are reported for the 0.35-8 keV energy range. In cases where the original energy range was different, the expected 0.35-8 keV limiting unabsorbed luminosity assuming a power law with Γ =1.9 and the value of $N_{\rm H}$ for each host galaxy.

able supersoft source, and other bright sources coincident with known supernova remnants (SNRs) and H II regions. More recently, an *XMM-Newton* survey of the the X-ray source population of NGC 300 was presented by [60] down to a limiting luminosity of $\sim 3 \times 10^{35}$ erg s^{-1} in the 0.3-6 keV band. A total of 163 sources were detected in the energy range of 0.3-6 keV, and the 86 sources falling within the D_{25} optical disk were further characterized using hardness ratios, X-ray fluxes, and the available ground-based optical imaging.

In addition to the overall X-ray point source population, NGC 300 contains two highly interesting sources that are discussed further in Chapter 6: the "supernova impostor" SN 2010da [37] and the Wolf-Rayet + black hole binary NGC 300 X-1 [35].

2.1.3 NGC 404

At 3.05 Mpc [87], NGC 404 is the closest face-on [$i = 11°$, 101] S0 galaxy to the Milky Way. Although its optical morphology suggests NGC 404 is a classic "red and dead" early-type galaxy, the center appears to have a significant young component [45, 363, 400, 262] and may host an intermediate-mass, low-luminosity active nucleus [LLAGN, 36, 363, 263, 119]. Here, we focus on the non-nuclear X-ray point source population; the central source is included as part of the X-ray source catalog, but is not discussed in detail until Chapter 6.

2.1.4 NGC 2403

NGC 2403 is an outlying member of the M81 group. Although comparable in M_B, morphology, inclination, and dynamical mass to M 33, it lies more than four times farther away from M81 (the nearest large disk galaxy) than M33 is from the Milky Way [209], making it a far more isolated system. NGC 2403 lacks a central bulge, but like M33 hosts a luminous compact nuclear star cluster [90] containing a recently discovered X-ray transient source [461]. Additionally, NGC 2403 hosts a ULX [394], a recent SN Type IIp [SN 2004dj, 289, 459, 27], 35 spectroscopically confirmed or suspected SNRs [266], and 52 Wolf-Rayet candidates [110]. NGC 2403 has been observed multiple times with *XMM-Newton* [126, 392].

The dominant age of stars within the nuclear star cluster is $\sim$ 1.4 Gyr [461], while numerous stars within the inner disk show stellar ages of $\sim$100 Myr [90]. The youngest ($\sim 2 - 10$ Myr) and most massive H II regions are 0.7-1.6 kpc from the center [110]. The global star formation rate of NGC 2403 is $\sim 1.2\ M_\odot\ \mathrm{yr}^{-1}$ [213].

2.1.5 NGC 4214

Classified as an SB(s)m similar to the Large Magellanic Cloud [98], NGC 4214 is one of the nearest examples of a starburst galaxy [191, 355] with an abundant population of Wolf-Rayet stars. Despite its active star formation [$\sim$0.1 $M_\odot\ \mathrm{yr}^{-1}$ over the past 100 Myr; 446], only a small percentage of the stellar population is young (<1% formed in the past 50 Myr). Additionally, there is evidence from *HST* imaging and spectroscopy that suggests the stellar initial mass function (IMF) of NGC 4214 is steeper than that of [352] at high masses [>20

$M_\odot$, 411, 412]. However, the galaxy has formed very little of its stellar mass since $z \sim 1$, and the overall stellar populations of NGC 4214 are surprisingly similar to that of the nearby dwarf S0 galaxy NGC 404 [447].

NGC 4214 was the host of a Type Ia supernova [441] and a recent nova [193]. The most luminous X-ray source in NGC 4214, CXOU J121538.2+361921, is an XRB with a 3.62 hour period and is likely composed of a slightly evolved He-burning donor (of $\sim 2-3\ M_\odot$) and a NS [147, 105]. The X-ray point source population of NGC 4214 was investigated using both *Chandra* and *XMM-Newton* observations by [171], who demonstrated that the high energy properties of NGC 4214 were comparable to other dwarf starbursts down to a limiting luminosity of $\sim 10^{36}$ erg s^{-1}.

2.2 Observations and Data Reduction

The observations used for each of the five CLVS galaxies are summarized in Table 2.3. Data reduction was carried out with CIAO v4.3 and CALDB v4.4.2 using standard reduction procedures. We created images in the following energy bands (keV): 0.35-8.0, 0.35-1.0, 1.0-2.0, 2.0-8.0 with bin sizes of 1, 2, 3, and 4. To create exposure-corrected images, appropriate exposure maps were constructed using `fluximage` in CIAO. For galaxies with multiple exposures, images were combined using the CIAO tasks `merge_all` and `reproject_image`. For the instrument maps, spectral weights were computed assuming a power law spectrum with $\Gamma = 1.9$ (typical of XRBs and AGN). The average foreground column density $N_{\rm H}$ was used.

2.2.1 HST Star Catalogs

The *HST* star catalogs, and the SFHs derived from them, were presented and discussed in detail in numerous earlier works emphasizing the SFHs of each of the five CLVS galaxies. Here I present a brief overview of the *HST* fields and the construction of the good star catalogs; more details can be found in the following references: [87], [153], [445], [439]. The data were retrieved from the Multi-Mission Archive at STSci (MAST). All exposures were calibrated and flat-fielded using the standard *HST* pipeline.

Table 2.3: Summary of *Chandra* Observations

Galaxy	Observation ID	Date	Exposure Time (ks)	R. A. (J2000)	Decl. (J2000)	Detector
(1)	(2)	(3)	(4)	(5)	(6)	(7)
NGC 55	2255	11 Sep 2001	60	00 15 08.50	-39 13 13.30	ACIS-I
	4744	29 June 2004	9.7	00 14 54.00	-39 11 49.00	ACIS-I
	Total		70			
NGC 300	12238	25 Sep 2010	63	00 54 53.05	-37 38 42.10	ACIS-I
NGC 404	12239	21-22 Oct 2010	97	01 09 27.00	+35 43 04.00	ACIS-S
	870	19 Dec 2000	24	01 09 26.90	+35 43 03.40	ACIS-S
	384	30 Aug 1999	1.8	01 09 26.90	+35 43 03.00	ACIS-S
	Total		123			
NGC 2403	2014	17 Apr 2001	36	07 36 51.90	+65 36 00.60	ACIS-S
	4627	9 Aug. 2004	45	07 37 17.10	+65 35 58.30	ACIS-S
	4628	23 Aug. 2004	47	07 37 17.10	+65 35 58.30	ACIS-S
	4629	3 Oct. 2004	45	07 37 17.10	+65 35 58.30	ACIS-S
	4630	22 Dec. 2004	50	07 37 17.10	+65 35 58.30	ACIS-S
	Total		223			
NGC 4214	2030	16 Oct 2001	26	12 15 38.70	+36 19 41.90	ACIS-S
	4743	3 Apr. 2004	27	12 15 38.90	+36 19 40.00	ACIS-S
	5197	30 July 2004	29	12 15 38.90	+36 19 40.00	ACIS-S
	Total		82			

Advanced Camera for Surveys (ACS): Exposures were combined using `multidrizzle` task within PyRAF [223] to produce images, while photometry was performed using all individual exposures simultaneously. For photometry, DOLPHOT, a modified version of HSTphot[1] [108, 109] optimized for ACS, was used to fit the ACS point-spread function (PSF, calculated with TinyTim[2]) to all of the stars in the exposure, combine the results from all exposures, and convert the count rates to the Vega magnitude system using the Sirianni et al. zero-points for each filter [379]. All sources in the final catalog were classified as stars, not flagged as unusable (e.g., too many bad/saturated pixels, extending too far off the chip edge, etc.), have a signal-to-noise (S/N) ratio >4, and have $|\texttt{sharp}_{F606W} + \texttt{sharp}_{F814W}| < 0.274$. "Sharpness" indicates whether a star is too sharp (e.g., a cosmic

[1]See `http://purcell.as.arizona.edu/dolphot`.

[2]See `http://www.stsci.edu/software/tinytim/`.

ray) or too broad (e.g., a background galaxy). The star catalog is additionally cut on the crowding parameter, which is defined as how much brighter a star would have been if nearby stars had not been fit simultaneously. Stars with a high crowding parameter are more likely to have erroneous photometry, but a very strict cut has the effect of preferentially removing young stars (which are usually found in clusters). Stars are required to have $\texttt{crowd}_{F606W} + \texttt{crowd}_{F814W} < 0.6$ mag.

Wide-Field Planetary Camera 2 (WFPC2): The WFPC2 pipeline [184] was used with standard STScI baseline processing. Photometry was performed using HSTphot [108], which is optimized for WFPC2 images and adopts photometric calibrations given in [185][3] The WFPC2 photometric system is defined such that, in each WFPC2 filter, Vega has a magnitude corresponding to the nearest UBVRI filter. The different zero-points in the WFPC2 and ACS systems results in offsets of 0.02–0.04 mag between the two instruments. In all cases, magnitudes ware determined using the Vega mag system zeropoints.

2.3 Image Alignment

To classify optical counterparts to our *Chandra* X-ray sources, we place both the *Chandra* and *HST* frames onto the International Celestial Reference System (ICRS) by finding matches between stars or background galaxies in the Two Micron All Sky Survey (2MASS) Point Source Catalog [381] or the optical USNO-B1.0 catalog [282]. The offset between the 2MASS and USNO-B1.0 catalogs is $\sim 0\farcs05$[4]. We performed relative astrometry by individually aligning each *HST* and *Chandra* field to the same reference image frame and coordinate system.

All available *HST* fields for each galaxy were used to search for optical counterparts of each of the X-ray point sources. Typically, 3-6 bright 2MASS or USNO-B1.0 sources were found, per *HST* field, to match with either a *Chandra* X-ray source, a foreground star, or a background galaxy. The only galaxy to which we were unable to find a suitable number of matching reference stars was NGC 300. For NGC 300, we retrieved a publicly-available

[3]Updated with improved calibrations from `http://purcell.as.arizona.edu/wfpc2_calib/`.

[4]See `http://ad.usno.navy.mil/star/star_cats_rec.shtml`

ground-based R band image [see 233, for more details] from NED[5]. Foreground 2MASS stars with ground-based R-band counterparts were identified, and we used the IRAF task `ccmap` to compute the plate solution and update the image header with corrected WCS information.

We then aligned the *HST* images and *Chandra* image to the 2MASS-aligned ground-based R-band image by identifying matches between the ground-based R-band image and the $F814W$ frames. The plate solutions were again computed using `ccmap`, with $r.m.s.$ residuals typically less than a few hundredths of an arcsecond in both right ascension and declination. The *Chandra* field was searched for X-ray sources that matched the positions of foreground stars or background galaxies in 2MASS, resulting in five matched sources. The total alignment error for each field was computed by summing in quadrature the $r.m.s$ residuals in the individual fields and the ground-based R-band image. For frames with five or more matches from 2MASS, the plate solutions were computed using the `general` fit geometry, frames with four matches were fit using the fit geometry `rxyscale`, frames with three matches were fit using the geometry `rscale`. The results of our 2MASS/USNO-B1.0 astrometry are summarized in Table 2.4.

[5]See `http://ned.ipac.caltech.edu/`

Table 2.4: Alignment of *Chandra* and *HST* Images

Galaxy	Alignment Source	Field Name	Observation ID	R.A. (J2000)	Decl. (J2000)	# Sources Used For Alignment	*r.m.s.*, R. A.[b]	*r.m.s.*, Decl.[b]	# of X-ray Sources
(1)	(2)	(3)	(4)	(5)	(6)	(7)	(8)	(9)	
		ground-based *R*				4	0.″00773	0.″0225	
		Chandra	12238	00:54:53.05	-37:38:42.1	5	0.″1332 (0.″1330)	0.″2580 (0.″2570)	95
		WIDE-1	10915	00:54:21.37	-37:37:56.3	5	0.″0518 (0.″0512)	0.″0400 (0.″0327)	5
		WIDE-2	10915	00:54:34.7	-37:39:25.2	4	0.″0171 (0.″0152)	0.″0342 (0.″0258)	6
		WIDE-3	10915	00:54:47.7	-37:40:51.6	4	0.″0171 (0.″0152)	0.″0535 (0.″0485)	5
NGC 300[a]	2MASS	NGC 300-1	9492	00:55:35.66	-37:41:25.2	3	0.″0340 (0.″0331)	0.″0421 (0.″0356)	1
		NGC 300-2	9492	00:54:52.96	-37:38:59.8	6	0.″0772 (0.″0768)	0.″0435 (0.″0372)	2
		NGC 300-3	9492	00:54:55.33	-37:42:04.5	4	0.″0179 (0.″0162)	0.″0263 (0.″0137)	5
		NGC 300-4	9492	00:54:24.42	-37:34:20.8	5	0.″0528 (0.″0522)	0.″0449 (0.″0388)	2
		NGC 300-5	9492	00:54:26.89	-37:39:01.4	8	0.″0230 (0.″0217)	0.″0441 (0.″0379)	9
		NGC 300-6	9492	00:54:27.12	-37:44:23.2	4	0.″0253 (0.″0241)	0.″0400 (0.″0331)	7
		Chandra	merged	00:15:09.96	-39:13:12.9	5	0.″0297	0.″0942	154
		WIDE-1	11307	00:14:16.54	-39:09:45.0	4	0.″0783 (0.″0725)	0.″2265 (0.″2060)	2
		WIDE-3	11307	00:14:30.03	-39:10.18.8	4	0.″0533 (0.″0443)	0.″1174 (0.″0701)	1
NGC 55	USNO-B1.O	WIDE-4	11307	00:14:38.26	-39:10:41.9	4	0.″0401 (0.″0270)	0.″2437 (0.″0877)	3
		WIDE-5	11307	00:15:11.55	-39:12:58.3	4	0.″3832 (0.″3820)	0.″1197 (0.″0740)	4
		DISK	9765	00:15:31.06	-39:14:13.4	5	0.″0323 (0.″0126)	0.″1262 (0.″0840)	9
		FIELD	9765	00:14:53.73	-39:11:48.1	6	0.″0454 (0.″0343)	0.″1301 (0.″0898)	22
		Chandra	merged	07:37:12.85	+65:36:21.0	4	0.″0048	0.″0296	190
		HALO-1	10523	07:37:54.67	+65:31:29.2	4	0.″0127 (0.″0118)	0.″0636 (0.″0563)	1
NGC 2403	USNO-B1.O	HALO-6	10523	07:37:31.38	+65:40:29.5	6	0.″0569 (0.″0567)	0.″0412 (0.″0287)	8
		HALO-7	10523	07:38:01.5	+65:43:49.1	4	0.″0098 (0.″0086)	0.″0473 (0.″0369)	2
		X-1	10579	07:36:42.36	+65:35:36.3	4	0.″0069 (0.″0050)	0.″0419 (0.″0296)	18
		PR	10182	07:36:58.6	+65:36:10.9	3	0.″0702 (0.″0700)	0.″0487 (0.″0387)	37
		Chandra	merged	01:09:27.00	+35:43:04.00	3	0.″049	0.″087	74
NGC 404	2MASS	DEEP	10915	01:09:17.01	+35:44:46.3	3	0.″066 (0.″082)	0.″030 (0.″042)	3
		NE	11986	01:09:28.93	+35:45:44.6	4	0.″041 (0.″064)	0.″017 (0.″034)	5
		SW	11986	01:09:20.64	+35:42:16.3	4	0.″088 (0.″100)	0.″001 (0.″087)	3
		Chandra	merged	12:15:39.51	36:17:22.6	4	0.″0101	0.″0541	116
NGC 4214	USNO-B1.0	N4214	11986	12:15:32.63	36:21:40.7	3	0.″0147 (0.″0108)	0.″0541 (0.″0012)	4
		DEEP	10915	12:15:23.22	36:21:51.9	4	0.″0134 (0.″0088)	0.″0566 (0.″0166)	4

[a] Alignment errors show the uncertainties in each individual field and the ground-based *R*-band image added in quadrature.

[b] The error in parentheses is the uncertainty reported by `ccmap` for the individual field.

2.4 ACIS-Extract

To create the X-ray source catalogs for each of the CLVS galaxies, we utilize an iterative detection strategy using the source extraction and characterization tool `ACIS-Extract` [`AE`; 49]. The CIAO task `wavdetect` [134] was first used to create a list of potential source candidates, which was then used as input to `AE`. `AE` was used to determine various source properties (source and background count rates, detection significances, etc.) in multiple, user-defined energy bands, to extract spectra (with appropriate response matrices) and examine source light curves for temporal variability. The Poisson probability of not being a source (*prob_no_source*; hereafter *pns*) provided by `AE` for each source (which takes the local background uncertainty into account) was used as our source significance threshold criteria. Since numerous other studies involving the detection of X-ray sources have traditionally used simpler source detection algorithms when generating X-ray source lists, a quantitative comparison of the two methods was additionally conducted.

2.4.1 Iterative Source Detection

I will first describe the iterative approach to the X-ray source catalog creation. Then, a comparison with previous methods is discussed.

We ran the CIAO task `wavdetect` on the merged X-ray images of each galaxy to generate an initial source list which deliberately contained many more sources than we anticipated being statistically significant. We used a variety of binning (1, 2, 3, and 4 pixels) and energy ranges (0.35-8, 0.35-1, 1-2, and 2-8 keV), and `wavdetect` was run on each bin and energy combination with the following parameters: the source significance (*sigthresh*) was set to 10^{-4} (to catch all real sources and many false ones), the cleansing threshold (*bkgsigthresh*) was set to 10^{-2} [134], a maximum number of cleansing iterations (*maxiter*) of 5 was used, and we used *scale* sizes ranging from 1 to 16 in a power-of-two sequence. All other `wavdetect` parameters were left at their default values. The resulting candidate lists were merged and culled of duplicate sources.

Once the initial X-ray source lists were generated, we applied an iterative procedure to remove sources with increasing significance thresholds, until only a small number of false

sources remained in the final source list. Each time the source list was filtered, the output was visually examined for potentially lost (real) sources. Low rates of false detections using the `AE` *pns* threshold criteria result from values below $\sim 10^{-6}$ [290, 146, 407]. However, due to the high number of source candidates in our initial list, source crowding posed a serious issue and made defining background regions problematic. To address this issue, the output from our first `AE` iteration was filtered with $pns = 10^{-2}$. The filtered source list contained revised source properties and improved background estimates. All sources failing to meet this initial *pns* threshold were visually examined, and any obviously missed sources were added back to the candidate source list. We then ran `AE` again on the filtered source list, this time raising the *pns* threshold to 10^{-3}. Source crowding was again reduced and spurious sources were filtered out. Again, sources failing to meet our new *pns* criteria were visually examined and returned to the source list if necessary.

`AE` was run a final time on the resulting source list, and the *pns* value was computed in each of the following nine energy bands (in keV): 0.5-8, 0.5-2, 2-8, 0.5-1, 1-2, 2-4, 4-8, 0.35-1, and 0.35-8. To be included in the final source catalog, sources were required to have a *pns* value less than 4×10^{-6} (which results in ~ 0.5 false detections per megapixel) in *any* of the nine energy bands; if only the 0.35-8 keV band were considered, ∼4-8% of significant sources would have been lost. The final CLVS source catalogs contain a total of 629 sources[6]. The number of X-ray sources detected at each iteration, for each galaxy, is listed in Table 2.5.

The remainder of this work utilizes these highly-significant sources. However, it is possible that some marginally-detected sources (i.e., those sources that failed to meet our final *pns* requirement) are in fact genuine X-ray sources, and other observers may wish to use different source selection criteria than we employed here. For that reason, we additionally release an expanded version of each X-ray source catalog, where X-ray sources are required only to meet a *pns* threshold of 10^{-3}.

The positions and properties, such as detection significance (*pns* value), net counts, and photon fluxes in the 0.35-8 keV band for the expanded X-ray point source catalogs for all

[6]Source catalogs are available at: `http://www.astro.washington.edu/users/bbinder/CLVS/`

Table 2.5: Number of X-ray sources at each `AE` iteration

Galaxy	Initial	First pass	Second pass	Final
(1)	(2)	(3)	(4)	(5)
NGC 55	906	370	220	**154**
NGC 300	799	224	126	**95**
NGC 404	762	129	104	**74**
NGC 2403	1308	648	298	**190**
NGC 4214	1177	474	211	**116**
Total	4952	1845	959	**629**

five CLVS galaxies are listed in Table 2.6. Figure 2.1 the soft, 0.5-1 keV X-ray contours, the highly significant X-ray point sources, and the locations of the *HST* fields superimposed on each galaxy.

Table 2.6: *Chandra* Local Volume X-ray Source List

Galaxy	Source No.	Source ID (CXOLV J+...)	R.A. (J2000)	Decl. (J2000)	Positional Error ($''$)	θ ($'$)	log(pns) (0.35-8 keV)	$f^a_{0.35-8} \times 10^{-15}$ (erg s^{-1} cm^{-2})
(1)	(2)	(3)	(4)	(5)	(6)	(7)	(8)	(9)
NGC 300								
1	005411.98-373951.8	13.5499370	-37.664408	0.70	8.2	$22.8^{+6.6}_{-5.5}$	-9.1	4.0
2	005412.31-373359.6	13.5513190	-37.566583	0.93	9.3	$18.2^{+6.6}_{-5.5}$	-4.8	3.4
3	005413.98-373710.5	13.5582680	-37.619588	0.36	7.9	$70.8^{+9.8}_{-8.8}$	$<$ -10	12.4
4	005415.57-373316.4	13.5649070	-37.554563	0.59	9.2	$45.1^{+8.5}_{-7.4}$	$<$ -10	11.8
5	005419.92-373744.5	13.5830010	-37.629032	0.61	6.6	$12.1^{+5.0}_{-3.8}$	-6.0	2.0
6	005421.10-374241.2	13.5879360	-37.711458	0.51	7.5	$31.1^{+7.1}_{-6.0}$	$<$ -10	6.4
7	005422.16-374024.6	13.5923720	-37.673501	0.67	6.3	$9.4^{+4.7}_{-3.6}$	-3.8	1.5
8	005422.52-374312.1	13.5938400	-37.720045	0.59	7.5	$22.5^{+6.4}_{-5.3}$	$<$ -10	3.9
9	005422.52-373850.6	13.5938410	-37.647406	0.45	6.0	$16.1^{+5.5}_{-4.3}$	-9.0	2.7
10	005425.06-374358.2	13.6044550	-37.732836	0.53	7.6	$29.4^{+7.1}_{-6.0}$	$<$ -10	5.4
11	005425.22-374441.3	13.6051190	-37.744816	0.41	8.1	$65.0^{+9.6}_{-8.6}$	$<$ -10	11.1
12	005425.40-373247.0	13.6058710	-37.546400	0.47	8.1	$48.3^{+8.5}_{-7.4}$	$<$ -10	8.7
13	005425.56-373759.3	13.6065210	-37.633147	0.46	5.5	$10.5^{+4.6}_{-3.4}$	-7.0	1.9
14	005428.34-373735.8	13.6181210	-37.626632	0.50	5.0	$6.7^{+4.0}_{-2.8}$	-4.2	1.1

Continued on next page

Table 2.6 – continued from previous page

Galaxy	Source No.	Source ID (CXOLV J+...)	R.A. (J2000)	Decl. (J2000)	Positional Error ($''$)	θ ($'$)	log(pns) (0.35-8 keV)	$f^a_{0.35-8} \times 10^{-15}$ (erg s^{-1} cm^{-2})
(1)	(2)	(3)	(4)	(5)	(6)	(7)	(8)	(9)
15	005428.62-374129.7	13.6192570	-37.691584	0.58	5.6	$8.4^{+4.3}_{-3.1}$	-5.0	1.6
16	005429.51-373628.6	13.6229950	-37.607947	0.43	5.2	$9.7^{+4.4}_{-3.3}$	-6.7	1.9
17	005429.97-374030.8	13.6248990	-37.675247	0.38	4.9	$12.9^{+4.8}_{-3.7}$	< -10	2.1
18	005430.58-374315.7	13.6274510	-37.721040	0.30	6.4	$44.8^{+8.0}_{-6.9}$	< -10	7.4
19	005430.67-374004.3	13.6277970	-37.667867	0.17	4.6	$52.0^{+8.3}_{-7.3}$	< -10	8.4
20	005431.42-374526.3	13.6309440	-37.757318	0.70	8.0	$18.5^{+6.1}_{-5.0}$	-6.9	3.2
21	005431.63-373827.6	13.6317930	-37.641022	0.16	4.2	$36.3^{+7.1}_{-6.1}$	< -10	5.8
22	005432.05-373742.7	13.6335630	-37.628547	0.34	4.3	$8.3^{+4.1}_{-2.9}$	-7.2	1.6
23	005433.82-374426.4	13.6409260	-37.740691	0.26	6.9	$82.1^{+10.3}_{-9.3}$	< -10	15.7
24	005433.92-374746.9	13.6413660	-37.796388	0.55	9.8	$68.7^{+10.1}_{-9.1}$	< -10	13.4
25	005433.93-374443.1	13.6413760	-37.745315	0.31	7.1	$62.5^{+9.2}_{-8.2}$	< -10	11.9
26	005435.60-374059.4	13.6483500	-37.683193	0.36	4.1	$8.4^{+4.1}_{-2.9}$	-7.7	1.4
27	005435.94-373434.1	13.6497590	-37.576156	0.25	5.3	$35.5^{+7.1}_{-6.1}$	< -10	6.0
28	005437.61-374249.4	13.6567290	-37.713750	0.17	5.1	$65.6^{+9.2}_{-8.2}$	< -10	10.8
29	005437.72-373232.2	13.6571950	-37.542294	0.40	6.9	$37.8^{+7.6}_{-6.5}$	< -10	6.8
30	005437.74-373643.6	13.6572760	-37.612131	0.29	3.6	$7.6^{+4.0}_{-2.8}$	-7.9	1.2
31	005438.99-374207.1	13.6624950	-37.702000	0.44	4.4	$6.2^{+3.8}_{-2.6}$	-4.7	1.2
32	005440.52-374043.1	13.6688500	-37.678651	0.18	3.2	$16.7^{+5.2}_{-4.1}$	< -10	2.5
33	005440.63-373204.0	13.6693150	-37.534468	0.39	7.1	$51.3^{+8.4}_{-7.3}$	< -10	23.0
34	005440.98-374052.0	13.6707900	-37.681137	0.16	3.2	$22.7^{+5.9}_{-4.8}$	< -10	3.8
35	005441.16-373350.4	13.6715250	-37.564018	0.14	5.4	$126.1^{+12.3}_{-11.3}$	< -10	21.5
36	005442.23-373126.7	13.6759710	-37.524102	0.61	7.6	$22.5^{+6.5}_{-5.4}$	-9.3	4.2
37	005442.27-374327.9	13.6761520	-37.724439	0.38	5.2	$14.0^{+5.1}_{-4.0}$	-8.8	2.2
38	005442.56-373732.7	13.6773650	-37.625759	0.09	2.4	$33.8^{+6.9}_{-5.8}$	< -10	5.2
39	005442.56-374342.7	13.6773750	-37.728547	0.19	5.4	$64.1^{+9.2}_{-8.1}$	< -10	10.9
40	005443.63-374620.7	13.6818040	-37.772424	0.68	7.9	$18.7^{+6.0}_{-4.9}$	-8.0	3.7
41	005444.40-374115.2	13.6850010	-37.687556	0.14	3.1	$22.7^{+5.9}_{-4.8}$	< -10	3.5
42	005445.03-373742.3	13.6876490	-37.628418	0.11	1.9	$18.8^{+5.4}_{-4.3}$	< -10	3.0
43	005445.23-374146.2	13.6884870	-37.696173	0.09	3.4	$82.5^{+10.2}_{-9.1}$	< -10	13.4
44	005445.48-373233.8	13.6895200	-37.542735	0.28	6.3	$57.8^{+8.9}_{-7.8}$	< -10	10.0
45	005446.02-374520.7	13.6917640	-37.755777	0.34	6.8	$43.2^{+7.9}_{-6.8}$	< -10	7.1
46	005446.33-373129.8	13.6930780	-37.524964	0.68	7.3	$15.6^{+5.7}_{-4.6}$	-6.1	3.1
47	005446.90-373324.3	13.6954340	-37.556762	0.60	5.4	$7.1^{+4.1}_{-2.9}$	-3.7	1.2
48	005447.53-374827.2	13.6980830	-37.807556	1.30	9.8	$7.0^{+5.8}_{-4.6}$	-1.3	1.5
49	005447.84-373258.3	13.6993670	-37.549547	0.46	5.8	$14.6^{+5.2}_{-4.1}$	-8.7	2.6
50	005448.12-374539.0	13.7005400	-37.760861	0.23	7.0	$106.9^{+11.6}_{-10.5}$	< -10	17.9
51	005448.76-374658.3	13.7032040	-37.782883	0.72	8.3	$20.1^{+6.6}_{-5.5}$	-6.0	3.5

Continued on next page

Table 2.6 – continued from previous page

Galaxy	Source No.	Source ID (CXOLV J+...)	R.A. (J2000)	Decl. (J2000)	Positional Error ($''$)	θ ($'$)	log(pns) (0.35-8 keV)	$f^a_{0.35-8} \times 10^{-15}$ (erg s^{-1} cm^{-2})
(1)	(2)	(3)	(4)	(5)	(6)	(7)	(8)	(9)
52	005449.78-373057.0	13.7074570	-37.515847	0.42	7.8	$50.1^{+8.7}_{-7.6}$	< -10	9.3
53	005450.56-374600.5	13.7107080	-37.766825	0.35	7.3	$58.2^{+9.0}_{-7.9}$	< -10	11.8
54	005450.58-374128.0	13.7107710	-37.691124	0.12	2.8	$29.7^{+6.5}_{-5.4}$	< -10	4.9
55	005451.67-373535.1	13.7153290	-37.593103	0.21	3.1	$10.7^{+4.4}_{-3.3}$	< -10	1.9
56	005451.81-373646.0	13.7159110	-37.612798	0.22	1.9	$4.8^{+3.4}_{-2.2}$	-5.8	0.7
57	005451.92-374706.6	13.7163330	-37.785168	1.13	8.4	$6.3^{+5.0}_{-3.9}$	-1.4	1.0
58	005453.29-374309.9	13.7220830	-37.719444	0.61	4.5	$3.3^{+3.2}_{-1.9}$	-2.1	0.7
59	005453.34-374437.1	13.7222880	-37.743666	0.45	5.9	$15.5^{+5.3}_{-4.2}$	-9.3	2.7
60	005453.70-374657.8	13.7237500	-37.782722	1.83	8.3	$-2.2^{+3.9}_{-2.7}$	-0.1	-0.4
61	005454.15-373526.3	13.7256400	-37.590658	0.33	3.3	$4.7^{+3.4}_{-2.2}$	-4.6	0.8
62	005456.49-374724.4	13.7353750	-37.790138	0.87	8.7	$16.0^{+6.2}_{-5.1}$	-4.3	2.7
63	005456.82-374337.7	13.7367760	-37.727160	0.45	5.0	$9.7^{+4.4}_{-3.3}$	-6.6	1.6
64	005457.24-374311.3	13.7385080	-37.719819	0.17	4.6	$49.8^{+8.2}_{-7.1}$	< -10	8.0
65	005457.36-374537.0	13.7390400	-37.760297	0.68	7.0	$12.5^{+5.2}_{-4.1}$	-5.0	2.3
66	005459.09-374747.7	13.7462480	-37.796603	0.87	9.2	$19.0^{+6.4}_{-5.3}$	-5.9	4.5
67	005459.85-373330.5	13.7494120	-37.558477	0.48	5.4	$9.1^{+4.4}_{-3.3}$	-5.0	1.5
68	005500.93-373948.1	13.7539120	-37.663366	0.11	1.9	$20.8^{+5.7}_{-4.5}$	< -10	3.6
69	005500.94-373440.6	13.7539400	-37.577962	0.20	4.3	$26.2^{+6.3}_{-5.2}$	< -10	4.3
70	005502.87-374537.2	13.7619850	-37.760342	0.69	7.2	$14.8^{+5.5}_{-4.3}$	-6.8	2.7
71	005503.53-373739.9	13.7647330	-37.627752	0.07	2.3	$64.8^{+9.1}_{-8.0}$	< -10	10.1
72	005504.29-374234.7	13.7678990	-37.709659	0.39	4.5	$9.0^{+4.3}_{-3.1}$	-6.7	1.5
73	005504.84-374143.6	13.7702010	-37.695464	0.11	3.8	$69.4^{+9.4}_{-8.3}$	< -10	11.1
74	005505.81-374126.8	13.7742240	-37.690779	0.31	3.7	$8.3^{+4.1}_{-2.9}$	-7.3	1.3
75	005506.24-373754.1	13.7760370	-37.631704	0.19	2.7	$10.7^{+4.4}_{-3.3}$	< -10	1.7
76	005507.18-373017.7	13.7799250	-37.504917	0.67	8.9	$30.3^{+7.6}_{-6.5}$	-9.7	5.7
77	005507.54-374513.2	13.7814400	-37.753684	0.70	7.1	$13.9^{+5.3}_{-4.2}$	-6.3	2.5
78	005507.59-374419.6	13.7816510	-37.738799	0.29	6.3	$52.5^{+8.5}_{-7.5}$	< -10	8.9
79	005508.43-374357.6	13.7851420	-37.732691	0.56	6.1	$11.9^{+5.0}_{-3.8}$	-5.8	2.0
80	005510.00-374212.2	13.7916850	-37.703403	0.03	4.8	$1962.7^{+45.3}_{-44.3}$	< -10	343.8
81	005511.09-373925.5	13.7962310	-37.657096	0.24	3.6	$12.5^{+4.7}_{-3.6}$	< -10	2.0
82	005511.36-374637.5	13.7973750	-37.777084	1.35	8.7	$3.3^{+5.0}_{-3.8}$	-0.7	0.7
83	005511.56-374042.4	13.7981900	-37.678463	0.31	4.2	$11.2^{+4.6}_{-3.4}$	-9.9	1.8
84	005512.24-373823.6	13.8010110	-37.639907	0.16	3.8	$34.4^{+7.0}_{-5.9}$	< -10	5.5
85	005515.44-374439.6	13.8143630	-37.744350	0.44	7.4	$38.0^{+7.7}_{-6.6}$	< -10	7.0
86	005517.61-374454.5	13.8233810	-37.748482	0.34	7.9	$82.8^{+10.6}_{-9.6}$	< -10	14.5
87	005518.10-373314.2	13.8254460	-37.553972	0.35	7.4	$58.0^{+9.1}_{-8.0}$	< -10	10.3
88	005519.51-373502.3	13.8312960	-37.583986	0.46	6.4	$18.9^{+5.8}_{-4.7}$	< -10	3.5

Continued on next page

Table 2.6 – continued from previous page

Galaxy	Source No.	Source ID (CXOLV J+...)	R.A. (J2000)	Decl. (J2000)	Positional Error ($''$)	θ ($'$)	log(pns) (0.35-8 keV)	$f^a_{0.35-8} \times 10^{-15}$ (erg s^{-1} cm^{-2})
(1)	(2)	(3)	(4)	(5)	(6)	(7)	(8)	(9)
89	005521.07-372919.8	13.8378050	-37.488834	0.60	10.9	$81.4^{+10.8}_{-9.7}$	< -10	37.1
90	005526.75-373810.1	13.8614630	-37.636154	0.43	6.7	$29.9^{+6.9}_{-5.8}$	< -10	5.1
91	005527.06-373612.8	13.8627620	-37.603576	0.49	7.2	$29.5^{+7.0}_{-5.9}$	< -10	5.1
92	005527.45-373651.3	13.8643900	-37.614266	0.44	7.1	$36.2^{+7.2}_{-6.1}$	< -10	17.1
93	005527.56-374517.6	13.8648750	-37.754890	1.03	9.5	$14.6^{+6.0}_{-4.9}$	-4.1	3.6
94	005531.00-373754.9	13.8791830	-37.631941	0.46	7.6	$38.9^{+7.7}_{-6.6}$	< -10	7.0
95	005531.39-374001.5	13.8808330	-37.667084	0.89	7.7	$8.9^{+4.9}_{-3.7}$	-3.0	1.6
			NGC 404					
1	010838.25+354027.3	17.1593960	35.674264	0.23	10.0	$655.3^{+27.2}_{-26.1}$	< -10	95.3
2	010841.45+354056.8	17.1727100	35.682458	0.47	9.3	$116.5^{+13.1}_{-12.0}$	< -10	13.2
3	010842.38+354300.8	17.1765910	35.716903	0.55	8.9	$67.4^{+10.6}_{-9.5}$	< -10	7.8
4	010847.72+353948.3	17.1988680	35.663419	0.69	8.4	$33.2^{+8.3}_{-7.2}$	-9.5	3.7
5	010848.00+354437.4	17.2000240	35.743725	0.37	7.9	$34.2^{+7.1}_{-6.0}$	< -10	12.3
6	010848.45+354433.4	17.2018810	35.742616	0.37	7.8	$37.5^{+7.4}_{-6.3}$	< -10	10.1
7	010848.48+353906.9	17.2020350	35.651937	0.22	8.5	$454.3^{+22.8}_{-21.8}$	< -10	51.6
8	010850.31+353843.8	17.2096470	35.645503	0.60	8.3	$46.0^{+9.1}_{-8.0}$	< -10	5.1
9	010853.61+354501.9	17.2234150	35.750537	0.58	6.9	$26.2^{+6.8}_{-5.7}$	< -10	4.2
10	010854.69+354239.7	17.2279010	35.711041	0.41	6.4	$40.0^{+7.9}_{-6.8}$	< -10	4.2
11	010855.37+353927.3	17.2307350	35.657594	0.43	7.1	$54.6^{+9.1}_{-8.0}$	< -10	6.2
12	010858.32+354246.2	17.2430060	35.712858	0.60	5.6	$11.9^{+5.1}_{-4.0}$	-5.2	1.3
13	010858.97+353845.9	17.2457420	35.646107	0.32	6.8	$91.7^{+11.0}_{-10.0}$	< -10	10.3
14	010900.59+354150.6	17.2524900	35.697399	0.52	5.3	$12.9^{+5.1}_{-4.0}$	-6.7	1.5
15	010901.28+353821.3	17.2553430	35.639272	0.53	6.7	$11.8^{+4.7}_{-3.6}$	-9.1	3.0
16	010905.23+354541.8	17.2717970	35.761628	0.47	5.1	$14.1^{+5.2}_{-4.1}$	-7.7	1.5
17	010906.01+354245.9	17.2750700	35.712770	0.09	4.1	$190.6^{+14.9}_{-13.8}$	< -10	20.2
18	010906.58+354204.0	17.2774210	35.701136	0.20	4.0	$38.6^{+7.4}_{-6.3}$	< -10	3.8
19	010909.70+353838.4	17.2904550	35.644014	0.43	5.4	$21.4^{+6.1}_{-5.0}$	< -10	2.2
20	010909.77+354410.6	17.2907370	35.736294	0.12	3.6	$84.9^{+10.3}_{-9.3}$	< -10	8.1
21	010910.01+354348.8	17.2917400	35.730231	0.11	3.4	$83.2^{+10.2}_{-9.1}$	< -10	8.1
22	010910.49+353913.1	17.2937390	35.653640	0.58	4.8	$7.5^{+4.3}_{-3.1}$	-3.5	0.8
23	010911.22+354215.4	17.2967700	35.704305	0.17	3.1	$25.2^{+6.2}_{-5.1}$	< -10	2.4
24	010913.30+354000.7	17.3054370	35.666870	0.21	3.8	$30.7^{+6.7}_{-5.6}$	< -10	3.0
25	010913.91+354112.5	17.3079870	35.686816	0.15	3.0	$30.2^{+6.6}_{-5.5}$	< -10	2.9
26	010916.04+354454.6	17.3168550	35.748510	0.17	2.9	$20.9^{+5.8}_{-4.7}$	< -10	1.8
27	010916.82+354555.8	17.3201160	35.765524	0.26	3.6	$16.1^{+5.3}_{-4.2}$	< -10	1.4
28	010917.93+354644.0	17.3247100	35.778909	0.21	4.2	$41.0^{+7.6}_{-6.5}$	< -10	6.1
29	010918.46+354121.3	17.3269320	35.689264	0.27	2.1	$4.6^{+3.4}_{-2.2}$	-4.2	0.4

Continued on next page

Table 2.6 – continued from previous page

Galaxy	Source No.	Source ID (CXOLV J+...)	R.A. (J2000)	Decl. (J2000)	Positional Error ($''$)	θ ($'$)	log(pns) (0.35-8 keV)	$f^a_{0.35-8} \times 10^{-15}$ (erg s^{-1} cm^{-2})
(1)	(2)	(3)	(4)	(5)	(6)	(7)	(8)	(9)
30	010918.54+354107.3	17.3272680	35.685377	0.12	2.3	$25.5^{+6.2}_{-5.1}$	< -10	2.5
31	010920.03+354048.5	17.3334950	35.680148	0.15	2.4	$18.6^{+5.4}_{-4.3}$	< -10	2.2
32	010920.04+353952.1	17.3335070	35.664475	0.08	3.2	$128.9^{+12.4}_{-11.4}$	< -10	12.5
33	010920.87+354654.2	17.3369730	35.781748	0.19	4.2	$48.5^{+8.2}_{-7.1}$	< -10	6.2
34	010921.33+354232.4	17.3389020	35.709002	0.16	1.0	$6.6^{+3.8}_{-2.6}$	-6.4	0.6
35	010921.35+354618.8	17.3389930	35.771906	0.10	3.6	$124.0^{+12.3}_{-11.2}$	< -10	10.7
36	010921.87+354336.7	17.3411660	35.726863	0.12	1.1	$12.4^{+4.7}_{-3.6}$	< -10	1.0
37	010923.73+354339.6	17.3488930	35.727682	0.15	0.9	$7.5^{+4.0}_{-2.8}$	-6.9	0.6
38	010924.21+354300.4	17.3509080	35.716783	0.16	0.4	$5.6^{+3.6}_{-2.4}$	-5.1	0.5
39	010924.77+354601.0	17.3532100	35.766963	0.09	3.2	$102.6^{+11.2}_{-10.2}$	< -10	8.8
40	010926.32+354523.7	17.3596890	35.756608	0.21	2.6	$10.0^{+4.4}_{-3.3}$	-8.0	0.8
41	010926.99+354305.2	17.3624790	35.718134	0.02	0.3	$254.7^{+17.0}_{-16.0}$	< -10	20.7
42	010927.53+354617.4	17.3647430	35.771509	0.24	3.5	$16.9^{+5.4}_{-4.3}$	< -10	1.4
43	010927.79+354316.3	17.3658330	35.721211	0.12	0.6	$9.5^{+4.3}_{-3.1}$	-9.5	0.8
44	010929.56+354522.8	17.3731800	35.756348	0.14	2.6	$24.1^{+6.1}_{-5.0}$	< -10	2.0
45	010929.83+354022.6	17.3742920	35.672957	0.09	2.6	$58.1^{+8.7}_{-7.7}$	< -10	4.9
46	010930.21+353928.7	17.3758770	35.657995	0.08	3.5	$171.7^{+14.2}_{-13.2}$	< -10	14.9
47	010930.54+354158.4	17.3772750	35.699562	0.20	1.3	$4.5^{+3.4}_{-2.2}$	-3.8	0.4
48	010931.93+354352.4	17.3830810	35.731245	0.18	1.6	$6.4^{+3.8}_{-2.6}$	-5.5	0.5
49	010932.16+354318.9	17.3840140	35.721927	0.13	1.3	$11.6^{+4.6}_{-3.4}$	< -10	0.9
50	010932.96+354518.8	17.3873470	35.755246	0.12	2.8	$43.0^{+7.7}_{-6.6}$	< -10	3.6
51	010935.14+354558.1	17.3964210	35.766149	0.27	3.6	$15.1^{+5.2}_{-4.1}$	< -10	1.4
52	010935.73+354648.3	17.3988960	35.780098	0.16	4.4	$86.0^{+10.5}_{-9.5}$	< -10	7.6
53	010935.77+354238.1	17.3990660	35.710592	0.09	2.0	$38.4^{+7.3}_{-6.2}$	< -10	3.2
54	010936.35+354400.6	17.4014690	35.733506	0.09	2.4	$45.3^{+7.8}_{-6.8}$	< -10	3.9
55	010936.71+354612.9	17.4029930	35.770274	0.14	4.0	$81.1^{+10.2}_{-9.1}$	< -10	7.0
56	010939.06+354113.6	17.4127760	35.687132	0.09	3.1	$92.8^{+10.7}_{-9.7}$	< -10	7.8
57	010940.22+354041.8	17.4176010	35.678298	0.30	3.6	$12.2^{+4.8}_{-3.7}$	-8.0	1.1
58	010941.77+354620.3	17.4240540	35.772330	0.19	4.7	$73.6^{+9.9}_{-8.9}$	< -10	6.4
59	010944.92+354445.6	17.4371730	35.746017	0.37	4.3	$12.7^{+5.2}_{-4.1}$	-5.5	1.1
60	010949.49+354543.7	17.4562240	35.762140	0.33	5.6	$39.4^{+8.1}_{-7.0}$	< -10	3.5
61	010950.20+354042.6	17.4591750	35.678503	0.30	5.3	$46.8^{+8.5}_{-7.4}$	< -10	4.2
62	010951.93+354458.7	17.4663880	35.749652	0.43	5.7	$22.4^{+6.8}_{-5.7}$	-7.5	2.0
63	010958.02+354102.0	17.4917590	35.683895	0.55	6.7	$23.2^{+7.4}_{-6.3}$	-5.9	2.2
64	010959.17+354140.5	17.4965780	35.694603	0.37	6.8	$65.4^{+10.2}_{-9.1}$	< -10	6.0
65	010959.34+354206.3	17.4972650	35.701760	0.12	6.8	$713.0^{+28.1}_{-27.0}$	< -10	65.0
66	011001.75+354653.2	17.5073120	35.781461	0.75	8.3	$25.2^{+7.8}_{-6.8}$	-5.8	2.7

Continued on next page

Table 2.6 – continued from previous page

Galaxy	Source No.	Source ID (CXOLV J+...)	R.A. (J2000)	Decl. (J2000)	Positional Error ($''$)	θ ($'$)	log(pns) (0.35-8 keV)	$f^a_{0.35-8} \times 10^{-15}$ (erg s^{-1} cm^{-2})
(1)	(2)	(3)	(4)	(5)	(6)	(7)	(8)	(9)
67	011005.67+354702.8	17.5236440	35.784136	0.64	9.1	$53.8^{+9.9}_{-8.9}$	< -10	6.3
68	011006.04+354855.3	17.5251750	35.815367	0.65	10.1	$77.7^{+11.9}_{-10.9}$	< -10	9.0
69	011006.99+354145.9	17.5291450	35.696107	1.07	8.4	$4.5^{+6.4}_{-5.3}$	-0.7	0.5
70	011008.83+354244.8	17.5367990	35.712472	0.54	8.7	$71.9^{+10.7}_{-9.7}$	< -10	8.0
71	011013.46+354417.4	17.5560970	35.738183	0.76	9.7	$45.5^{+9.8}_{-8.8}$	< -10	5.2
72	011014.73+354624.4	17.5613770	35.773465	0.65	10.5	$91.4^{+12.7}_{-11.7}$	< -10	10.5
73	011018.61+354325.9	17.5775470	35.723865	0.55	10.7	$153.4^{+15.1}_{-14.1}$	< -10	17.7
74	011032.59+354321.8	17.6357980	35.722741	0.95	13.5	$72.6^{+13.5}_{-12.5}$	< -10	9.5
			NGC 55					
1	001503.50-391533.8	3.7645870	-39.259401	0.19	2.7	$9.8^{+4.3}_{-3.1}$	< -10	1.6
2	001502.09-391646.1	3.7587260	-39.279490	0.25	3.9	$11.6^{+4.6}_{-3.4}$	< -10	2.1
3	001458.59-392211.3	3.7441560	-39.369828	0.45	9.2	$81.1^{+10.7}_{-9.6}$	< -10	15.0
4	001459.11-391901.6	3.7463080	-39.317128	0.47	6.4	$18.7^{+5.7}_{-4.6}$	< -10	2.8
5	001459.34-391723.1	3.7472760	-39.289762	0.23	4.8	$30.0^{+6.6}_{-5.5}$	< -10	4.3
6	001502.18-391425.2	3.7591020	-39.240335	0.17	1.9	$7.9^{+4.0}_{-2.8}$	< -10	2.9
7	001451.70-392417.8	3.7154570	-39.404951	0.62	11.6	$103.3^{+12.2}_{-11.1}$	< -10	20.7
8	001448.96-392229.9	3.7040110	-39.374988	0.38	10.1	$168.6^{+14.5}_{-13.5}$	< -10	33.0
9	001457.84-391555.7	3.7410040	-39.265498	0.20	3.7	$17.4^{+5.3}_{-4.2}$	< -10	2.6
10	001500.62-391414.2	3.7525970	-39.237285	0.18	2.2	$3.0^{+2.9}_{-1.6}$	-5.2	1.1
11	001456.08-391618.6	3.7336880	-39.271835	0.11	4.2	$79.2^{+10.0}_{-8.9}$	< -10	11.0
12	001442.68-392047.1	3.6778680	-39.346439	0.94	9.2	$17.6^{+6.1}_{-4.9}$	-6.0	3.5
13	001454.67-391517.5	3.7278040	-39.254888	0.24	3.6	$12.7^{+4.7}_{-3.6}$	< -10	3.2
14	001451.82-391604.0	3.7159330	-39.267798	0.65	4.5	$4.9^{+3.4}_{-2.2}$	-6.2	5.4
15	001448.83-391615.5	3.7034710	-39.270996	0.19	5.1	$54.4^{+8.5}_{-7.5}$	< -10	8.2
16	001442.73-391723.4	3.6780680	-39.289853	0.50	6.7	$4.8^{+3.4}_{-2.2}$	-5.4	2.0
17	001447.26-391602.7	3.6969260	-39.267417	0.48	5.2	$9.9^{+4.4}_{-3.3}$	-7.2	2.1
18	001437.70-391701.6	3.6570920	-39.283790	0.70	7.2	$14.5^{+5.4}_{-4.2}$	-6.6	2.2
19	001446.51-391518.0	3.6938020	-39.255000	0.39	5.0	$12.8^{+4.8}_{-3.7}$	-9.9	2.1
20	001425.96-391748.5	3.6082010	-39.296819	1.29	8.3	$6.9^{+4.0}_{-2.8}$	-4.5	8.1
21	001437.12-391616.7	3.6546790	-39.271323	0.38	7.1	$48.7^{+8.2}_{-7.1}$	< -10	8.5
22	001434.57-391559.2	3.6440740	-39.266452	0.72	7.2	$12.4^{+5.3}_{-4.1}$	-4.6	1.9
23	001445.72-391435.6	3.6905350	-39.243239	0.02	4.7	$2692.3^{+52.9}_{-51.9}$	< -10	379.6
24	001438.30-391518.7	3.6596240	-39.255215	0.17	6.3	$35.8^{+7.1}_{-6.0}$	< -10	12.7
25	001438.31-391518.7	3.6596470	-39.255204	0.17	6.3	$34.8^{+7.0}_{-5.9}$	< -10	12.5
26	001454.59-391337.1	3.7274920	-39.226997	0.21	3.0	$5.9^{+3.6}_{-2.4}$	-8.0	1.2
27	001454.29-391332.1	3.7262280	-39.225607	0.24	2.9	$6.6^{+3.8}_{-2.6}$	-6.8	0.9
28	001449.81-391352.3	3.7075740	-39.231207	0.29	3.8	$9.4^{+4.3}_{-3.1}$	-9.0	1.3

Continued on next page

Table 2.6 – continued from previous page

Galaxy	Source No.	Source ID (CXOLV J+...)	R.A. (J2000)	Decl. (J2000)	Positional Error ($''$)	θ ($'$)	log(pns) (0.35-8 keV)	$f^a_{0.35-8} \times 10^{-15}$ (erg s^{-1} cm^{-2})
(1)	(2)	(3)	(4)	(5)	(6)	(7)	(8)	(9)
29	001456.77-391317.3	3.7365630	-39.221482	0.09	2.5	$36.8^{+7.1}_{-6.1}$	< -10	5.1
30	001452.57-391334.0	3.7190530	-39.226115	0.20	3.2	$11.5^{+4.6}_{-3.4}$	< -10	1.6
31	001446.83-391358.9	3.6951490	-39.233042	0.17	4.3	$35.2^{+7.1}_{-6.0}$	< -10	5.0
32	001452.12-391334.3	3.7171900	-39.226208	0.23	3.5	$11.6^{+4.6}_{-3.4}$	< -10	1.9
33	001445.44-391341.8	3.6893350	-39.228282	0.36	4.8	$4.9^{+3.4}_{-2.2}$	-7.2	2.1
34	001416.04-391347.8	3.5668490	-39.229954	0.72	7.7	$19.1^{+5.6}_{-4.4}$	< -10	26.8
35	001459.94-391249.1	3.7497580	-39.213659	0.13	2.0	$13.6^{+4.8}_{-3.7}$	< -10	2.0
36	001447.34-391302.5	3.6972530	-39.217382	0.44	4.4	$5.4^{+3.6}_{-2.4}$	-4.2	0.9
37	001430.40-391257.8	3.6266840	-39.216057	0.25	7.3	$123.0^{+12.4}_{-11.3}$	< -10	18.7
38	001454.41-391244.8	3.7267110	-39.212464	0.30	3.0	$5.7^{+3.6}_{-2.4}$	-5.9	1.0
39	001438.51-391242.2	3.6605000	-39.211724	0.25	5.7	$47.3^{+8.1}_{-7.0}$	< -10	7.1
40	001443.61-391240.0	3.6817090	-39.211124	0.22	4.7	$35.1^{+7.1}_{-6.0}$	< -10	5.6
41	001501.51-391243.1	3.7562970	-39.211989	0.17	1.7	$7.6^{+4.0}_{-2.8}$	-7.8	1.0
42	001452.59-391224.3	3.7191620	-39.206751	0.12	3.1	$36.6^{+7.1}_{-6.1}$	< -10	5.1
43	001448.62-391215.9	3.7025930	-39.204430	0.32	3.8	$7.4^{+4.0}_{-2.8}$	-6.3	1.2
44	001419.35-391113.5	3.5806500	-39.187089	0.15	6.8	$205.5^{+15.4}_{-14.3}$	< -10	255.0
45	001425.10-391116.7	3.6046240	-39.187981	0.71	8.4	$25.3^{+6.9}_{-5.8}$	-9.7	4.1
46	001448.34-391205.8	3.7014280	-39.201628	0.40	3.9	$7.4^{+4.0}_{-2.8}$	-6.3	1.2
47	001457.16-391227.7	3.7381950	-39.207715	0.22	2.6	$7.7^{+4.0}_{-2.8}$	-8.2	1.3
48	001438.07-391134.6	3.6586410	-39.192952	0.48	5.9	$15.4^{+5.4}_{-4.2}$	-7.9	2.7
49	001412.40-391017.8	3.5516680	-39.171618	1.26	8.2	$7.1^{+4.0}_{-2.8}$	-5.0	9.0
50	001447.97-391156.9	3.6998880	-39.199153	0.30	4.4	$4.9^{+3.4}_{-2.2}$	-7.3	2.1
51	001436.86-391119.8	3.6536090	-39.188858	0.67	6.7	$10.1^{+4.7}_{-3.6}$	-4.6	1.8
52	001419.22-391014.6	3.5801140	-39.170739	0.55	9.8	$65.5^{+9.8}_{-8.7}$	< -10	11.0
53	001452.34-391206.0	3.7181000	-39.201669	0.17	3.2	$20.6^{+5.7}_{-4.5}$	< -10	2.9
54	001444.61-391135.9	3.6859140	-39.193307	0.06	4.7	$439.3^{+22.0}_{-21.0}$	< -10	69.5
55	001443.81-391127.4	3.6825680	-39.190949	0.32	4.8	$19.5^{+5.7}_{-4.5}$	< -10	3.3
56	001450.90-391154.5	3.7121100	-39.198492	0.34	3.9	$6.6^{+3.8}_{-2.6}$	-6.1	1.2
57	001453.98-391204.8	3.7249530	-39.201341	0.30	3.3	$6.6^{+3.8}_{-2.6}$	-6.2	1.1
58	001445.01-391053.7	3.6875520	-39.181608	0.46	5.4	$9.7^{+4.4}_{-3.3}$	-6.6	1.8
59	001440.81-390937.8	3.6700630	-39.160525	0.24	6.2	$70.0^{+9.6}_{-8.5}$	< -10	10.7
60	001429.24-390752.4	3.6218390	-39.131244	0.70	6.1	$7.6^{+4.0}_{-2.8}$	-8.0	9.4
61	001500.68-391218.0	3.7528690	-39.205002	0.07	1.9	$44.6^{+7.8}_{-6.7}$	< -10	6.4
62	001457.00-391139.1	3.7375220	-39.194219	0.01	2.8	$1786.4^{+43.3}_{-42.3}$	< -10	269.1
63	001452.00-391045.2	3.7166680	-39.179227	0.02	3.7	$2986.9^{+55.7}_{-54.7}$	< -10	496.6
64	001447.43-390944.1	3.6976250	-39.162257	0.41	5.1	$13.5^{+5.0}_{-3.8}$	-9.8	2.0
65	001501.75-391217.4	3.7573180	-39.204846	0.20	1.8	$5.8^{+3.6}_{-2.4}$	-6.5	0.9

Continued on next page

Table 2.6 – continued from previous page

Galaxy	Source No.	Source ID (CXOLV J+...)	R.A. (J2000)	Decl. (J2000)	Positional Error ($''$)	θ ($'$)	log(pns) (0.35-8 keV)	$f^a_{0.35-8} \times 10^{-15}$ (erg s^{-1} cm^{-2})
(1)	(2)	(3)	(4)	(5)	(6)	(7)	(8)	(9)
66	001503.43-391239.5	3.7642970	-39.210987	0.24	2.1	$4.0^{+3.2}_{-1.9}$	-6.9	4.8
67	001450.55-390901.0	3.7106390	-39.150296	0.13	5.2	$139.3^{+12.9}_{-11.9}$	< -10	20.8
68	001442.91-390630.5	3.6787950	-39.108490	0.50	5.5	$10.8^{+4.4}_{-3.3}$	< -10	16.2
69	001455.47-390946.1	3.7311340	-39.162811	0.38	4.4	$8.3^{+4.1}_{-2.9}$	-6.7	1.4
70	001453.14-390656.1	3.7214200	-39.115610	0.74	6.7	$10.7^{+5.0}_{-3.8}$	-4.3	1.8
71	001502.05-391145.5	3.7585710	-39.195986	0.19	2.1	$7.8^{+4.0}_{-2.8}$	< -10	1.2
72	001457.52-390901.8	3.7396740	-39.150524	0.29	4.6	$20.8^{+5.8}_{-4.7}$	< -10	3.2
73	001454.51-390405.6	3.7271670	-39.068243	0.70	7.4	$16.3^{+5.2}_{-4.1}$	< -10	18.6
74	001500.14-390909.5	3.7506030	-39.152656	0.22	4.2	$27.2^{+6.4}_{-5.3}$	< -10	4.0
75	001502.74-391028.8	3.7614460	-39.174667	0.14	2.9	$6.0^{+3.8}_{-2.6}$	-3.5	2.1
76	001502.04-390618.2	3.7585200	-39.105073	0.59	7.1	$19.3^{+5.9}_{-4.8}$	-9.6	4.0
77	001503.67-391018.3	3.7653000	-39.171759	0.30	3.0	$6.7^{+3.8}_{-2.6}$	-7.3	1.1
78	001503.79-391241.4	3.7658110	-39.211500	0.18	1.4	$5.8^{+3.6}_{-2.4}$	-6.7	0.8
79	001504.03-391153.7	3.7668170	-39.198273	0.04	1.8	$127.8^{+12.3}_{-11.3}$	< -10	18.0
80	001504.56-391043.9	3.7690410	-39.178863	0.08	2.7	$54.8^{+8.5}_{-7.4}$	< -10	10.4
81	001504.68-391050.5	3.7695030	-39.180707	0.12	2.5	$23.8^{+6.0}_{-4.9}$	< -10	4.1
82	001508.68-390225.8	3.7862000	-39.040505	1.15	9.5	$15.1^{+5.2}_{-4.1}$	-9.9	20.6
83	001533.63-390306.2	3.8901660	-39.051731	0.71	11.1	$66.8^{+10.4}_{-9.3}$	< -10	16.1
84	001528.06-390509.0	3.8669440	-39.085839	0.73	8.8	$23.7^{+6.9}_{-5.8}$	-7.3	4.7
85	001512.52-391002.3	3.8021690	-39.167310	0.19	3.3	$6.8^{+3.8}_{-2.6}$	-8.7	2.5
86	001510.58-391045.5	3.7940900	-39.179317	0.27	2.5	$5.8^{+3.6}_{-2.4}$	-7.8	1.0
87	001521.96-390725.3	3.8415250	-39.123714	0.62	6.2	$9.0^{+4.5}_{-3.3}$	-4.3	2.0
88	001508.81-391118.0	3.7867310	-39.188337	0.19	1.9	$6.8^{+3.8}_{-2.6}$	-9.0	1.1
89	001523.87-390800.1	3.8494840	-39.133383	0.37	5.9	$20.9^{+5.8}_{-4.7}$	< -10	4.2
90	001519.40-390918.2	3.8308640	-39.155081	0.18	4.5	$43.1^{+7.7}_{-6.6}$	< -10	6.2
91	001530.35-390715.1	3.8764660	-39.120886	0.18	7.3	$200.0^{+15.4}_{-14.3}$	< -10	35.7
92	001511.92-391110.7	3.7996780	-39.186326	0.24	2.3	$5.7^{+3.6}_{-2.4}$	-6.4	0.8
93	001519.61-390945.9	3.8317450	-39.162774	0.27	3.9	$4.9^{+3.4}_{-2.2}$	-8.2	2.1
94	001504.25-391239.9	3.7677360	-39.211090	0.13	1.4	$10.8^{+4.4}_{-3.3}$	< -10	1.5
95	001523.78-390946.8	3.8490850	-39.163011	0.12	4.5	$104.1^{+11.3}_{-10.2}$	< -10	15.8
96	001513.65-391141.7	3.8068990	-39.194924	0.35	3.8	$5.0^{+3.4}_{-2.2}$	-8.9	5.7
97	001539.27-390857.6	3.9136310	-39.149341	0.54	7.1	$23.0^{+6.2}_{-5.1}$	< -10	4.6
98	001537.36-390945.6	3.9056880	-39.162678	0.62	6.6	$16.9^{+5.8}_{-4.7}$	-6.6	2.8
99	001514.84-391151.9	3.8118730	-39.197766	0.23	1.6	$3.9^{+3.2}_{-1.9}$	-5.1	0.7
100	001511.54-391208.1	3.7980930	-39.202258	0.20	1.4	$5.8^{+3.6}_{-2.4}$	-7.6	0.9
101	001520.02-391137.0	3.8334440	-39.193637	0.34	2.9	$7.6^{+4.0}_{-2.8}$	-7.9	1.2
102	001530.66-391059.2	3.8777660	-39.183112	0.51	4.9	$16.1^{+5.3}_{-4.2}$	< -10	2.3

Continued on next page

Table 2.6 – continued from previous page

Galaxy	Source No.	Source ID (CXOLV J+...)	R.A. (J2000)	Decl. (J2000)	Positional Error ($''$)	θ ($'$)	log(pns) (0.35-8 keV)	$f^a_{0.35-8} \times 10^{-15}$ (erg s^{-1} cm^{-2})
(1)	(2)	(3)	(4)	(5)	(6)	(7)	(8)	(9)
103	001522.25-391136.4	3.8427150	-39.193445	0.12	3.2	$47.5^{+8.0}_{-6.9}$	< -10	7.6
104	001545.89-391022.7	3.9412350	-39.172987	0.48	7.5	$38.5^{+7.6}_{-6.6}$	< -10	7.4
105	001529.75-391118.1	3.8739720	-39.188377	0.33	4.3	$11.4^{+4.6}_{-3.4}$	-9.1	1.9
106	001528.17-391151.2	3.8673980	-39.197567	0.28	3.8	$11.5^{+4.6}_{-3.4}$	< -10	2.0
107	001552.75-391059.9	3.9698150	-39.183327	0.57	8.6	$43.6^{+8.2}_{-7.1}$	< -10	9.3
108	001539.40-391147.3	3.9141830	-39.196496	0.48	5.9	$14.8^{+5.2}_{-4.1}$	-8.6	2.9
109	001520.60-391219.5	3.8358390	-39.205430	0.28	2.6	$8.6^{+4.1}_{-2.9}$	-9.1	1.2
110	001544.31-391208.9	3.9346400	-39.202489	0.18	6.9	$177.5^{+14.6}_{-13.5}$	< -10	29.9
111	001538.00-391232.8	3.9083420	-39.209137	0.19	5.9	$119.1^{+12.1}_{-11.0}$	< -10	17.5
112	001544.33-391232.2	3.9347150	-39.208962	0.67	6.9	$14.2^{+5.4}_{-4.3}$	-5.5	2.4
113	001552.14-391230.6	3.9672770	-39.208512	0.60	8.2	$29.7^{+7.1}_{-6.0}$	< -10	5.7
114	001533.91-391239.2	3.8912930	-39.210913	0.49	4.7	$6.5^{+3.8}_{-2.6}$	-4.9	1.2
115	001552.47-391250.3	3.9686600	-39.213988	0.73	8.2	$20.8^{+6.3}_{-5.2}$	-8.0	3.8
116	001506.45-391246.0	3.7768930	-39.212800	0.18	1.1	$5.8^{+3.6}_{-2.4}$	-7.5	0.8
117	001526.03-391256.3	3.8584760	-39.215652	0.31	3.1	$5.7^{+3.6}_{-2.4}$	-6.0	1.1
118	001556.81-391339.7	3.9867360	-39.227706	0.57	9.1	$49.3^{+8.6}_{-7.5}$	< -10	11.6
119	001528.89-391318.7	3.8703940	-39.221888	0.01	4.1	$11523.4^{+108.4}_{-107.4}$	< -10	1653.6
120	001523.36-391337.9	3.8473430	-39.227216	0.24	2.6	$6.8^{+3.8}_{-2.6}$	-7.1	1.3
121	001542.19-391431.9	3.9258010	-39.242203	0.71	6.8	$17.3^{+5.7}_{-4.6}$	-7.3	2.8
122	001534.29-391424.9	3.8928950	-39.240257	0.03	5.3	$1516.6^{+40.0}_{-39.0}$	< -10	222.9
123	001514.22-391320.6	3.8092730	-39.222397	0.14	0.8	$8.9^{+4.1}_{-2.9}$	< -10	3.0
124	001525.96-391406.5	3.8582070	-39.235155	0.15	3.7	$42.8^{+7.7}_{-6.6}$	< -10	6.1
125	001541.29-391507.3	3.9220430	-39.252051	0.42	6.4	$23.0^{+6.2}_{-5.1}$	< -10	4.3
126	001601.75-391624.9	4.0073230	-39.273587	0.56	10.5	$88.9^{+11.6}_{-10.5}$	< -10	19.8
127	001557.36-391611.8	3.9890270	-39.269966	1.06	9.7	$14.2^{+6.2}_{-5.1}$	-3.3	3.1
128	001608.27-391738.5	4.0344980	-39.294032	0.85	12.1	$60.5^{+10.5}_{-9.4}$	< -10	13.2
129	001548.20-391613.9	3.9508410	-39.270534	0.48	8.0	$39.2^{+7.8}_{-6.8}$	< -10	7.1
130	001533.98-391511.7	3.8915890	-39.253277	0.16	5.5	$110.3^{+11.7}_{-10.6}$	< -10	17.3
131	001543.52-391640.9	3.9313470	-39.278031	0.70	7.4	$12.7^{+5.3}_{-4.1}$	-4.8	2.3
132	001535.69-391558.7	3.8987420	-39.266325	0.37	5.7	$5.8^{+3.6}_{-2.4}$	-7.3	2.5
133	001522.78-391452.7	3.8449330	-39.247980	0.31	3.0	$4.7^{+3.4}_{-2.2}$	-4.6	0.8
134	001528.32-391546.8	3.8680400	-39.263019	0.34	4.4	$10.4^{+4.4}_{-3.3}$	-9.3	1.8
135	001548.25-391839.4	3.9510770	-39.310965	0.26	9.2	$246.9^{+17.1}_{-16.0}$	< -10	47.0
136	001528.49-391636.2	3.8687450	-39.276735	0.44	4.9	$9.0^{+4.3}_{-3.1}$	-6.5	1.6
137	001533.11-391736.4	3.8879900	-39.293449	0.24	6.7	$84.7^{+10.5}_{-9.4}$	< -10	13.0
138	001507.62-391323.5	3.7817760	-39.223207	0.11	0.9	$14.8^{+5.0}_{-3.8}$	< -10	2.0
139	001521.60-391613.2	3.8400400	-39.270345	0.17	3.8	$28.4^{+6.5}_{-5.4}$	< -10	5.1

Continued on next page

Table 2.6 – continued from previous page

Galaxy	Source No.	Source ID (CXOLV J+...)	R.A. (J2000)	Decl. (J2000)	Positional Error ($''$)	θ ($'$)	log(pns) (0.35-8 keV)	$f^a_{0.35-8} \times 10^{-15}$ (erg s^{-1} cm^{-2})
(1)	(2)	(3)	(4)	(5)	(6)	(7)	(8)	(9)
140	001515.88-391508.7	3.8161950	-39.252432	0.51	3.2	$5.7^{+3.6}_{-2.4}$	-6.2	1.9
141	001517.69-391616.6	3.8237220	-39.271290	0.38	3.4	$4.8^{+3.4}_{-2.2}$	-5.2	1.2
142	001530.10-392012.3	3.8754530	-39.336767	0.79	8.0	$20.6^{+6.3}_{-5.2}$	-7.5	3.7
143	001505.38-391313.7	3.7724200	-39.220479	0.07	1.1	$33.9^{+6.9}_{-5.8}$	< -10	4.7
144	001525.87-391941.8	3.8578300	-39.328279	0.59	7.2	$21.1^{+6.1}_{-5.0}$	< -10	5.3
145	001521.89-391842.9	3.8412480	-39.311921	0.18	6.0	$119.7^{+12.1}_{-11.0}$	< -10	20.4
146	001522.26-391956.3	3.8427820	-39.332314	0.60	7.1	$18.6^{+5.9}_{-4.8}$	-8.2	3.2
147	001519.92-391907.4	3.8330330	-39.318749	0.24	6.2	$71.1^{+9.6}_{-8.5}$	< -10	13.8
148	001513.70-391707.7	3.8070950	-39.285479	0.41	4.0	$6.5^{+3.8}_{-2.6}$	-6.0	1.3
149	001510.66-391631.3	3.7944170	-39.275387	0.27	3.7	$18.4^{+5.4}_{-4.3}$	< -10	2.7
150	001508.02-391527.3	3.7834380	-39.257586	0.18	2.3	$8.8^{+4.1}_{-2.9}$	< -10	1.4
151	001516.43-392059.1	3.8184900	-39.349751	0.32	7.9	$95.3^{+11.1}_{-10.1}$	< -10	16.9
152	001508.89-391648.6	3.7870620	-39.280181	0.13	3.9	$66.4^{+9.2}_{-8.2}$	< -10	11.3
153	001507.70-391657.9	3.7820970	-39.282777	0.15	4.1	$40.4^{+7.5}_{-6.4}$	< -10	7.2
154	001505.16-391519.4	3.7715040	-39.255414	0.15	2.3	$11.9^{+4.6}_{-3.4}$	< -10	2.1
			NGC 2403					
1	073706.49+652736.5	114.2770800	65.460154	0.72	8.2	$30.0^{+8.3}_{-7.2}$	-6.7	3.8
2	073707.39+653455.8	114.2808300	65.582175	0.02	1.9	$904.7^{+31.1}_{-30.1}$	< -10	31.4
3	073705.08+653146.7	114.2711900	65.529650	0.21	4.5	$54.9^{+8.9}_{-7.8}$	< -10	3.5
4	073701.86+652751.6	114.2577900	65.464334	0.82	8.0	$22.2^{+7.3}_{-6.2}$	-5.2	3.1
5	073707.11+653515.8	114.2796600	65.587735	0.16	1.6	$8.7^{+4.3}_{-3.1}$	-5.7	0.5
6	073703.99+653241.6	114.2666600	65.544909	0.37	3.6	$10.8^{+4.6}_{-3.4}$	-6.9	1.4
7	073706.42+653451.8	114.2767500	65.581057	0.08	1.9	$41.5^{+7.7}_{-6.6}$	< -10	1.4
8	073701.68+653236.3	114.2570200	65.543435	0.27	3.8	$20.3^{+6.2}_{-5.1}$	-8.0	0.9
9	073656.80+653029.4	114.2366800	65.508181	0.29	5.8	$82.2^{+11.2}_{-10.1}$	< -10	5.6
10	073659.27+653149.7	114.2469800	65.530482	0.29	4.5	$36.4^{+7.9}_{-6.8}$	< -10	2.3
11	073639.35+652339.2	114.1639900	65.394231	0.49	12.4	$274.9^{+22.2}_{-21.2}$	< -10	38.1
12	073650.18+652824.3	114.2091000	65.473438	0.45	7.9	$90.0^{+12.2}_{-11.1}$	< -10	7.0
13	073654.75+653043.0	114.2281300	65.511972	0.39	5.7	$33.1^{+8.2}_{-7.1}$	-8.8	2.2
14	073649.61+652844.0	114.2067500	65.478912	0.66	7.6	$30.8^{+9.0}_{-7.9}$	-5.7	2.7
15	073634.73+652546.8	114.1447200	65.429694	0.85	10.8	$38.7^{+11.8}_{-10.8}$	-4.5	3.6
16	073701.74+653411.5	114.2572600	65.569869	0.21	2.8	$11.2^{+4.9}_{-3.7}$	-5.1	0.6
17	073654.23+653207.9	114.2260000	65.535551	0.24	4.0	$39.7^{+7.6}_{-6.6}$	< -10	4.0
18	073702.94+653438.4	114.2622800	65.577342	0.16	2.2	$14.3^{+5.1}_{-4.0}$	-9.6	0.9
19	073636.47+652838.7	114.1519900	65.477436	0.44	8.2	$115.2^{+13.5}_{-12.4}$	< -10	9.2
20	073700.77+653417.7	114.2532500	65.571609	0.04	2.5	$363.6^{+20.2}_{-19.2}$	< -10	13.8
21	073646.23+653128.6	114.1926400	65.524629	0.55	5.3	$18.3^{+6.5}_{-5.4}$	-4.9	1.2

Continued on next page

Table 2.6 – continued from previous page

Galaxy	Source No.	Source ID (CXOLV J+...)	R.A. (J2000)	Decl. (J2000)	Positional Error ($''$)	θ ($'$)	log(pns) (0.35-8 keV)	$f^a_{0.35-8} \times 10^{-15}$ (erg s^{-1} cm^{-2})
(1)	(2)	(3)	(4)	(5)	(6)	(7)	(8)	(9)
22	073702.23+653445.9	114.2593200	65.579426	0.14	2.1	$18.2^{+5.7}_{-4.6}$	< -10	0.7
23	073617.36+652639.1	114.0723700	65.444207	0.81	10.8	$57.2^{+12.7}_{-11.7}$	-8.1	6.1
24	073631.53+652939.7	114.1313800	65.494388	0.84	7.1	$20.2^{+6.9}_{-5.8}$	-5.2	2.6
25	073653.83+653331.7	114.2243000	65.558810	0.16	3.3	$45.9^{+8.1}_{-7.1}$	< -10	2.0
26	073632.22+653031.4	114.1342600	65.508730	0.22	4.6	$51.1^{+8.3}_{-7.2}$	< -10	13.6
27	073648.65+653311.3	114.2027300	65.553162	0.41	3.7	$13.1^{+5.4}_{-4.3}$	-4.7	0.8
28	073650.05+653352.5	114.2085800	65.564588	0.30	3.9	$14.2^{+5.6}_{-4.5}$	-4.9	0.6
29	073632.12+653201.9	114.1338500	65.533866	0.20	5.6	$161.1^{+14.3}_{-13.3}$	< -10	12.5
30	073624.62+653138.4	114.1025900	65.527346	0.34	6.0	$73.0^{+10.0}_{-8.9}$	< -10	9.0
31	073542.57+652735.4	113.9273900	65.459842	0.81	13.5	$148.6^{+18.6}_{-17.0}$	< -10	37.4
32	073559.69+652932.0	113.9987200	65.492224	1.21	10.9	$29.5^{+8.5}_{-7.4}$	-5.9	7.7
33	073535.35+652748.3	113.8973200	65.463427	1.05	13.9	$101.3^{+13.7}_{-12.6}$	< -10	25.9
34	073612.98+653140.4	114.0540900	65.527889	0.80	6.9	$21.0^{+7.0}_{-5.9}$	-5.2	2.6
35	073559.86+653147.8	113.9994300	65.529949	1.03	9.6	$25.1^{+7.7}_{-6.6}$	-5.5	5.6
36	073542.68+653107.5	113.9278700	65.518766	1.15	11.5	$36.0^{+9.8}_{-8.7}$	-5.8	13.3
37	073552.75+653249.7	113.9698200	65.547140	1.14	9.8	$21.7^{+6.8}_{-5.6}$	-6.5	5.4
38	073632.54+653452.6	114.1356100	65.581293	0.28	3.9	$34.2^{+7.4}_{-6.3}$	< -10	2.1
39	073632.93+653457.9	114.1372500	65.582755	0.08	4.0	$62.5^{+9.1}_{-8.0}$	< -10	4.3
40	073653.95+653535.3	114.2248000	65.593149	0.13	2.6	$30.1^{+6.9}_{-5.8}$	< -10	1.7
41	073655.60+653540.8	114.2316700	65.594675	0.01	2.1	$10033.4^{+101.2}_{-100.2}$	< -10	431.5
42	073625.55+653539.9	114.1065000	65.594420	0.01	4.6	$16600.8^{+133.0}_{-131.7}$	< -10	1079.3
43	073604.27+653548.9	114.0178000	65.596939	0.43	7.1	$58.8^{+8.9}_{-7.9}$	< -10	14.5
44	073645.75+653549.6	114.1906600	65.597128	0.27	2.9	$13.3^{+5.1}_{-4.0}$	-7.0	0.8
45	073645.22+653557.4	114.1884400	65.599281	0.12	3.0	$74.4^{+9.9}_{-8.8}$	< -10	3.4
46	073646.80+653557.4	114.1950300	65.599289	0.26	2.8	$13.8^{+5.2}_{-4.1}$	-6.7	0.6
47	073640.06+653605.6	114.1669300	65.601568	0.34	3.4	$13.7^{+5.5}_{-4.4}$	-4.8	0.6
48	073635.63+653608.4	114.1484700	65.602361	0.12	3.7	$92.5^{+11.0}_{-9.9}$	< -10	5.4
49	073653.39+653559.4	114.2224600	65.599844	0.22	2.3	$9.5^{+4.6}_{-3.4}$	-4.7	0.4
50	073626.78+653620.7	114.1116200	65.605762	0.31	3.9	$13.9^{+5.3}_{-4.1}$	-6.2	1.4
51	073650.08+653603.8	114.2087000	65.601059	0.03	2.6	$658.2^{+26.7}_{-25.7}$	< -10	34.6
52	073538.27+653719.7	113.9095000	65.622155	0.72	9.8	$61.5^{+9.8}_{-8.7}$	< -10	20.1
53	073646.12+653613.7	114.1922000	65.603829	0.07	2.9	$109.7^{+11.7}_{-10.7}$	< -10	5.0
54	073657.22+653603.5	114.2384300	65.600991	0.09	2.0	$45.3^{+7.9}_{-6.8}$	< -10	1.9
55	073647.55+653619.1	114.1981500	65.605310	0.09	2.8	$111.6^{+11.8}_{-10.7}$	< -10	5.2
56	073655.36+653608.3	114.2307000	65.602327	0.10	2.2	$44.9^{+7.9}_{-6.8}$	< -10	1.9
57	073647.66+653623.0	114.1986100	65.606392	0.08	2.8	$105.0^{+11.4}_{-10.4}$	< -10	5.0
58	073527.44+653835.8	113.8643500	65.643287	0.91	11.1	$54.1^{+10.6}_{-9.5}$	< -10	11.4

Continued on next page

Table 2.6 – continued from previous page

Galaxy	Source No.	Source ID (CXOLV J+...)	R.A. (J2000)	Decl. (J2000)	Positional Error ($''$)	θ ($'$)	log(pns) (0.35-8 keV)	$f^a_{0.35-8} \times 10^{-15}$ (erg s^{-1} cm^{-2})
(1)	(2)	(3)	(4)	(5)	(6)	(7)	(8)	(9)
59	073624.55+653713.5	114.1023300	65.620425	0.52	3.6	$14.5^{+5.1}_{-4.0}$	< -10	3.8
60	073702.34+653601.5	114.2597600	65.600425	0.12	1.7	$17.4^{+5.4}_{-4.3}$	< -10	0.7
61	073645.83+653640.6	114.1909700	65.611302	0.20	3.3	$26.9^{+6.7}_{-5.6}$	< -10	1.6
62	073509.22+654024.5	113.7884400	65.673497	0.15	13.4	$5433.2^{+77.8}_{-76.5}$	< -10	1216.6
63	073700.66+653606.2	114.2527900	65.601725	0.10	1.8	$25.4^{+6.3}_{-5.2}$	< -10	1.1
64	073642.01+653651.9	114.1750500	65.614418	0.04	3.4	$771.8^{+28.9}_{-27.9}$	< -10	35.5
65	073624.49+653735.4	114.1020600	65.626522	0.29	4.6	$32.9^{+7.2}_{-6.1}$	< -10	3.3
66	073618.71+653800.7	114.0779600	65.633531	0.47	5.3	$18.6^{+6.1}_{-5.0}$	-6.7	1.9
67	073654.07+653630.8	114.2253300	65.608582	0.21	2.4	$9.1^{+4.4}_{-3.3}$	-5.0	0.5
68	073625.82+653757.1	114.1076000	65.632555	0.43	5.1	$17.8^{+5.6}_{-4.4}$	< -10	3.3
69	073642.94+653709.6	114.1789400	65.619355	0.26	3.3	$15.2^{+5.5}_{-4.4}$	-6.6	1.0
70	073652.02+653640.9	114.2167600	65.611379	0.13	2.5	$33.2^{+7.2}_{-6.1}$	< -10	1.5
71	073637.95+653737.4	114.1581500	65.627075	0.26	3.1	$11.0^{+4.6}_{-3.4}$	-8.4	2.4
72	073625.29+653841.0	114.1053800	65.644733	0.23	5.1	$53.0^{+8.8}_{-7.8}$	< -10	6.4
73	073632.59+653820.0	114.1358300	65.638893	0.61	4.3	$12.3^{+5.1}_{-4.0}$	-5.1	1.3
74	073620.95+653913.8	114.0873000	65.653854	0.43	5.8	$26.8^{+7.1}_{-6.0}$	-9.8	2.8
75	073702.56+653613.6	114.2606800	65.603798	0.17	1.7	$9.5^{+4.4}_{-3.3}$	-6.1	0.4
76	073624.86+653915.6	114.1036000	65.654344	0.36	5.5	$30.9^{+7.5}_{-6.4}$	< -10	3.1
77	073637.76+653815.9	114.1573600	65.637755	0.34	3.9	$12.6^{+5.0}_{-3.8}$	-7.0	1.2
78	073634.17+653854.9	114.1423800	65.648586	0.07	4.6	$541.2^{+24.5}_{-23.4}$	< -10	57.7
79	073630.13+653933.4	114.1255500	65.659302	0.36	5.3	$28.0^{+7.0}_{-5.9}$	< -10	3.1
80	073558.88+654410.6	113.9953600	65.736292	0.84	10.9	$42.4^{+11.6}_{-10.6}$	-5.5	9.4
81	073656.10+653715.6	114.2337500	65.621027	0.10	2.5	$52.1^{+8.4}_{-7.3}$	< -10	2.5
82	073614.52+654230.2	114.0605400	65.708396	0.67	8.6	$37.9^{+9.0}_{-7.9}$	-8.9	5.6
83	073624.58+654229.6	114.1024500	65.708223	0.56	8.0	$45.7^{+9.7}_{-8.7}$	< -10	5.6
84	073707.12+653556.6	114.2796800	65.599066	0.06	1.4	$58.1^{+8.8}_{-7.7}$	< -10	2.4
85	073702.62+653710.7	114.2609300	65.619666	0.10	2.0	$38.0^{+7.4}_{-6.3}$	< -10	1.6
86	073648.45+654108.1	114.2018900	65.685585	0.26	5.8	$83.3^{+10.8}_{-9.7}$	< -10	7.9
87	073654.42+654016.0	114.2267800	65.671127	0.34	4.5	$18.5^{+5.6}_{-4.5}$	< -10	1.8
88	073659.66+653936.7	114.2485900	65.660205	0.22	3.6	$25.0^{+6.2}_{-5.1}$	< -10	2.3
89	073700.47+653951.8	114.2520000	65.664415	0.23	3.9	$28.5^{+6.8}_{-5.7}$	< -10	2.0
90	073701.19+653939.7	114.2549600	65.661046	0.23	4.0	$40.4^{+8.3}_{-7.2}$	< -10	1.9
91	073707.01+653613.8	114.2792200	65.603851	0.10	1.4	$26.2^{+6.4}_{-5.3}$	< -10	1.1
92	073702.32+653934.9	114.2596800	65.659715	0.02	3.9	$5375.4^{+74.5}_{-73.5}$	< -10	254.8
93	073706.93+653621.6	114.2789100	65.606002	0.12	1.1	$12.0^{+4.7}_{-3.6}$	-9.7	0.6
94	073704.05+654311.9	114.2669100	65.719992	0.49	7.6	$61.8^{+10.0}_{-8.9}$	< -10	7.7
95	073706.99+653837.7	114.2791400	65.643813	0.39	3.2	$8.2^{+4.4}_{-3.3}$	-3.5	0.6

Continued on next page

Table 2.6 – continued from previous page

Galaxy	Source No.	Source ID (CXOLV J+...)	R.A. (J2000)	Decl. (J2000)	Positional Error ($''$)	θ ($'$)	log(pns) (0.35-8 keV)	$f^a_{0.35-8} \times 10^{-15}$ (erg s^{-1} cm^{-2})
(1)	(2)	(3)	(4)	(5)	(6)	(7)	(8)	(9)
96	073707.58+653919.9	114.2815900	65.655529	0.14	3.5	$87.0^{+10.7}_{-9.7}$	< -10	4.2
97	073707.98+654645.4	114.2832600	65.779298	0.70	11.1	$118.7^{+14.6}_{-13.6}$	< -10	17.3
98	073708.57+654214.1	114.2857100	65.703917	0.64	5.8	$12.6^{+5.2}_{-4.0}$	-4.8	2.8
99	073716.48+654624.6	114.3186800	65.773505	1.15	9.9	$23.1^{+7.3}_{-6.3}$	-5.7	5.5
100	073716.56+654455.0	114.3190200	65.748631	0.97	8.4	$18.2^{+6.3}_{-5.1}$	-5.8	4.4
101	073708.69+653649.5	114.2862100	65.613761	0.20	1.5	$10.0^{+4.6}_{-3.4}$	-5.4	0.6
102	073718.59+654520.7	114.3274600	65.755753	1.00	9.7	$28.0^{+9.5}_{-8.5}$	-4.1	3.8
103	073714.07+654014.1	114.3086300	65.670588	0.40	3.8	$8.3^{+4.1}_{-2.9}$	-5.6	1.1
104	073711.34+653813.8	114.2972800	65.637172	0.13	2.0	$17.2^{+5.3}_{-4.2}$	< -10	0.9
105	073721.74+654335.0	114.3406100	65.726400	0.69	8.1	$39.1^{+9.3}_{-8.2}$	-8.5	5.1
106	073725.67+654302.1	114.3569700	65.717268	0.26	7.7	$314.7^{+19.4}_{-18.4}$	< -10	38.6
107	073721.98+654028.3	114.3416200	65.674541	0.40	4.1	$10.7^{+4.6}_{-3.4}$	-6.2	1.1
108	073724.97+654015.0	114.3540600	65.670846	0.32	4.0	$14.9^{+5.4}_{-4.2}$	-6.6	0.9
109	073726.20+653922.0	114.3591900	65.656114	0.23	3.7	$81.0^{+10.6}_{-9.5}$	< -10	3.8
110	073812.36+654706.7	114.5515000	65.785218	0.68	12.0	$59.1^{+16.6}_{-15.6}$	-5.0	8.3
111	073742.28+654134.8	114.4261900	65.693014	0.46	5.6	$22.2^{+6.2}_{-5.1}$	< -10	2.5
112	073717.84+653726.5	114.3243700	65.624031	0.22	1.7	$15.6^{+5.3}_{-4.2}$	-9.3	0.7
113	073818.97+654552.0	114.5790700	65.764454	0.84	11.2	$55.7^{+11.9}_{-10.9}$	-9.2	14.2
114	073757.84+654251.9	114.4910200	65.714439	0.39	7.5	$85.3^{+11.1}_{-10.0}$	< -10	10.8
115	073731.12+653902.9	114.3796800	65.650821	0.14	2.9	$30.6^{+7.4}_{-5.7}$	-6.5	2.9
116	073743.60+654042.8	114.4316800	65.678573	0.32	4.9	$28.3^{+6.6}_{-5.5}$	< -10	3.0
117	073724.49+653759.0	114.3520500	65.633073	0.11	2.4	$61.4^{+9.1}_{-8.1}$	< -10	2.7
118	073838.98+654556.2	114.6624200	65.765624	0.92	12.5	$54.2^{+14.7}_{-13.6}$	-5.2	13.3
119	073747.68+654016.9	114.4486700	65.671369	0.17	4.8	$90.4^{+10.7}_{-9.6}$	< -10	9.8
120	073848.16+654644.3	114.7006900	65.778986	0.86	13.7	$83.7^{+17.1}_{-16.1}$	-8.4	20.5
121	073819.16+654328.8	114.5798600	65.724686	0.80	9.3	$33.1^{+11.2}_{-9.5}$	-3.3	4.8
122	073755.44+654021.7	114.4810200	65.672705	0.18	5.4	$133.5^{+12.7}_{-11.7}$	< -10	16.4
123	073737.79+653822.0	114.4074700	65.639458	0.24	2.9	$12.1^{+4.8}_{-3.7}$	-7.2	0.7
124	073751.19+653914.9	114.4633300	65.654143	0.18	4.3	$59.5^{+8.9}_{-7.8}$	< -10	6.1
125	073743.97+653839.8	114.4332300	65.644393	0.20	3.6	$29.5^{+6.7}_{-5.6}$	< -10	1.8
126	073725.13+653708.8	114.3547500	65.619130	0.07	1.1	$40.9^{+7.5}_{-6.5}$	< -10	2.2
127	073758.71+653928.5	114.4946500	65.657926	0.43	5.0	$15.9^{+5.5}_{-4.3}$	-8.4	1.6
128	073726.06+653656.3	114.3586100	65.615640	0.07	1.6	$141.2^{+13.0}_{-12.0}$	< -10	5.4
129	073717.53+653623.2	114.3230800	65.606460	0.11	0.9	$26.1^{+6.4}_{-5.3}$	< -10	1.0
130	073847.56+654112.7	114.6982000	65.686869	0.44	10.1	$202.6^{+16.7}_{-15.6}$	< -10	51.9
131	073825.00+653917.9	114.6041900	65.654992	0.49	7.2	$45.2^{+8.2}_{-7.1}$	< -10	12.6
132	073713.10+653558.1	114.3046100	65.599477	0.06	1.1	$61.1^{+9.0}_{-7.9}$	< -10	2.1

Continued on next page

Table 2.6 – continued from previous page

Galaxy	Source No.	Source ID (CXOLV J+...)	R.A. (J2000)	Decl. (J2000)	Positional Error ($''$)	θ ($'$)	log(pns) (0.35-8 keV)	$f^a_{0.35-8} \times 10^{-15}$ (erg s^{-1} cm^{-2})
(1)	(2)	(3)	(4)	(5)	(6)	(7)	(8)	(9)
133	073738.38+653629.8	114.4099500	65.608303	0.10	2.1	$108.9^{+11.5}_{-10.5}$	< -10	5.9
134	073747.02+653630.2	114.4459500	65.608402	0.27	3.0	$10.6^{+4.6}_{-3.4}$	-7.2	0.6
135	073717.05+653557.8	114.3210700	65.599390	0.01	1.0	$1257.8^{+36.5}_{-35.5}$	< -10	44.7
136	073823.75+653638.6	114.5989900	65.610730	0.30	7.1	$125.1^{+12.9}_{-11.8}$	< -10	16.3
137	073759.38+653610.0	114.4974300	65.602786	0.22	4.3	$43.1^{+8.1}_{-7.0}$	< -10	2.7
138	073735.27+653550.0	114.3969800	65.597228	0.09	1.9	$36.1^{+7.1}_{-6.1}$	< -10	2.0
139	073744.85+653547.5	114.4368900	65.596552	0.23	2.8	$11.4^{+4.7}_{-3.6}$	-7.2	0.6
140	073740.49+653521.6	114.4187400	65.589342	0.05	2.6	$248.5^{+16.8}_{-15.8}$	< -10	13.5
141	073709.86+653546.8	114.2911100	65.596336	0.06	1.3	$57.0^{+8.7}_{-7.7}$	< -10	2.0
142	073845.24+653327.1	114.6885300	65.557553	0.75	10.0	$55.2^{+10.5}_{-9.5}$	< -10	11.7
143	073750.21+653431.8	114.4592200	65.575524	0.23	3.8	$28.5^{+6.8}_{-5.7}$	< -10	1.6
144	073859.75+653217.9	114.7490000	65.538311	1.03	11.8	$39.1^{+10.8}_{-9.8}$	-5.6	8.8
145	073844.71+653217.0	114.6863300	65.538079	0.70	10.3	$81.6^{+11.7}_{-10.6}$	< -10	17.2
146	073752.93+653407.4	114.4705600	65.568734	0.23	4.5	$43.9^{+8.0}_{-6.9}$	< -10	3.8
147	073726.14+653504.9	114.3589400	65.584698	0.16	1.6	$9.1^{+4.3}_{-3.1}$	-6.9	0.5
148	073757.82+653347.0	114.4909300	65.563062	0.50	5.3	$14.4^{+5.5}_{-4.4}$	-5.6	2.3
149	073900.55+653110.4	114.7523200	65.519563	1.02	12.3	$52.7^{+11.8}_{-10.8}$	-8.3	12.0
150	073749.23+653402.6	114.4551400	65.567399	0.31	4.0	$15.7^{+5.6}_{-4.5}$	-6.7	0.9
151	073859.94+653027.0	114.7497700	65.507509	0.95	12.6	$78.3^{+12.8}_{-11.7}$	< -10	17.9
152	073826.57+653135.8	114.6107200	65.526635	0.59	9.0	$72.0^{+10.4}_{-9.3}$	< -10	15.2
153	073743.64+653345.6	114.4318400	65.562668	0.19	3.7	$35.8^{+7.4}_{-6.3}$	< -10	2.0
154	073804.38+653229.7	114.5182800	65.541599	0.65	6.6	$16.1^{+6.1}_{-5.0}$	-4.7	2.7
155	073709.14+653544.1	114.2881200	65.595596	0.01	1.4	$1318.4^{+37.4}_{-36.3}$	< -10	45.4
156	073717.99+653509.4	114.3249900	65.585957	0.08	1.3	$27.9^{+6.5}_{-5.4}$	< -10	1.4
157	073800.35+653208.5	114.5014800	65.535696	0.18	6.5	$269.6^{+17.8}_{-16.8}$	< -10	45.2
158	073739.51+653322.4	114.4146600	65.556226	0.38	3.6	$15.1^{+5.2}_{-4.1}$	-9.8	1.4
159	073725.25+653415.3	114.3552300	65.570918	0.18	2.3	$10.6^{+4.6}_{-3.4}$	-6.9	0.6
160	073753.06+653128.5	114.4710900	65.524611	0.58	6.4	$19.8^{+6.5}_{-5.4}$	-6.1	3.3
161	073736.55+653251.2	114.4023200	65.547583	0.21	4.0	$37.5^{+7.6}_{-6.5}$	< -10	2.1
162	073733.39+653307.5	114.3891400	65.552094	0.04	3.6	$956.7^{+32.0}_{-31.0}$	< -10	52.7
163	073801.78+652949.0	114.5074200	65.496955	0.87	8.3	$22.1^{+7.0}_{-5.9}$	-5.9	5.0
164	073740.48+653139.7	114.4186800	65.527706	0.25	5.4	$67.3^{+9.8}_{-8.7}$	< -10	5.7
165	073736.98+653200.8	114.4041100	65.533579	0.13	4.8	$170.5^{+14.5}_{-13.5}$	< -10	11.0
166	073758.80+652906.7	114.4950300	65.485214	0.93	8.7	$27.8^{+7.1}_{-6.0}$	< -10	6.3
167	073726.96+653312.2	114.3623600	65.553394	0.22	3.5	$23.7^{+6.4}_{-5.3}$	< -10	1.1
168	073731.80+653158.4	114.3825100	65.532914	0.34	4.7	$21.8^{+6.7}_{-5.5}$	-6.9	1.3
169	073721.83+653317.3	114.3409600	65.554821	0.05	3.2	$344.9^{+19.7}_{-18.7}$	< -10	15.2

Continued on next page

Table 2.6 – continued from previous page

Galaxy	Source No.	Source ID (CXOLV J+...)	R.A. (J2000)	Decl. (J2000)	Positional Error ($''$)	θ ($'$)	log(pns) (0.35-8 keV)	$f^a_{0.35-8} \times 10^{-15}$ (erg s^{-1} cm^{-2})
(1)	(2)	(3)	(4)	(5)	(6)	(7)	(8)	(9)
170	073714.88+653428.9	114.3120200	65.574716	0.02	2.1	$599.3^{+25.5}_{-24.5}$	< -10	25.4
171	073725.62+653216.1	114.3567700	65.537811	0.17	4.3	$68.9^{+9.7}_{-8.6}$	< -10	3.2
172	073726.35+653206.7	114.3598000	65.535209	0.30	4.4	$21.8^{+6.3}_{-5.2}$	-9.2	1.3
173	073732.18+653044.7	114.3841100	65.512429	0.29	5.9	$66.7^{+10.1}_{-9.0}$	< -10	6.0
174	073727.30+653102.2	114.3637800	65.517294	0.10	5.4	$464.0^{+23.3}_{-22.2}$	< -10	24.4
175	073716.02+653328.8	114.3167600	65.558010	0.14	2.9	$35.3^{+7.2}_{-6.1}$	< -10	1.6
176	073714.66+653345.4	114.3111100	65.562621	0.27	2.7	$6.7^{+4.0}_{-2.8}$	-4.0	0.4
177	073719.16+653053.0	114.3298600	65.514739	0.30	5.3	$45.9^{+9.1}_{-7.4}$	-8.5	4.9
178	073709.35+653500.9	114.2889700	65.583604	0.14	1.7	$13.9^{+5.0}_{-3.8}$	< -10	0.8
179	073711.60+653345.8	114.2983500	65.562723	0.02	2.7	$1352.6^{+37.8}_{-36.8}$	< -10	62.1
180	073727.96+652513.7	114.3665000	65.420477	1.10	11.3	$30.3^{+10.1}_{-9.0}$	-3.9	9.3
181	073714.81+653204.3	114.3117400	65.534548	0.30	4.2	$18.4^{+6.9}_{-5.8}$	-4.1	0.8
182	073717.82+652954.5	114.3242500	65.498481	0.25	6.2	$104.3^{+11.9}_{-10.8}$	< -10	9.7
183	073708.23+653525.5	114.2843200	65.590428	0.13	1.5	$13.0^{+4.8}_{-3.7}$	< -10	0.5
184	073714.08+653128.1	114.3087000	65.524474	0.37	4.8	$17.2^{+6.2}_{-5.1}$	-5.0	1.1
185	073712.81+653139.7	114.3033800	65.527707	0.22	4.6	$48.3^{+8.7}_{-7.6}$	< -10	2.4
186	073710.20+653311.0	114.2925100	65.553058	0.10	3.2	$75.9^{+9.9}_{-8.9}$	< -10	3.3
187	073709.58+653305.4	114.2899200	65.551521	0.13	3.3	$118.8^{+12.1}_{-11.0}$	< -10	5.2
188	073714.00+652450.5	114.3083400	65.414029	0.71	11.0	$95.6^{+13.7}_{-12.6}$	< -10	13.6
189	073713.30+652531.4	114.3054300	65.425399	1.25	11.0	$28.6^{+9.0}_{-8.0}$	-4.9	7.9
190	073711.18+652828.3	114.2966100	65.474547	0.54	6.7	$30.3^{+7.1}_{-6.0}$	< -10	8.4
			NGC 4214					
1	121537.80+361613.2	183.9075100	36.270343	0.41	3.7	$7.0^{+4.0}_{-2.8}$	-4.7	2.0
2	121531.56+360947.4	183.8815200	36.163172	0.92	9.2	$28.3^{+7.6}_{-6.4}$	-8.1	5.5
3	121533.96+361428.5	183.8915300	36.241258	0.36	3.1	$5.8^{+3.6}_{-2.4}$	-7.1	1.8
4	121530.29+361203.6	183.8762200	36.201004	0.39	5.6	$32.7^{+6.9}_{-5.8}$	< -10	10.6
5	121533.02+361531.2	183.8876100	36.258681	0.37	4.2	$19.8^{+6.0}_{-4.9}$	-9.3	2.5
6	121524.05+361252.1	183.8502100	36.214481	0.69	5.5	$8.7^{+4.3}_{-3.1}$	-5.7	3.4
7	121535.34+361752.0	183.8972800	36.297805	0.19	2.1	$11.1^{+4.6}_{-3.4}$	-9.1	1.0
8	121529.43+361545.4	183.8726600	36.262624	0.24	3.0	$16.1^{+5.2}_{-4.1}$	< -10	2.3
9	121528.30+361644.1	183.8679200	36.278920	0.26	3.3	$33.1^{+7.1}_{-6.0}$	< -10	3.1
10	121536.06+361847.3	183.9002900	36.313160	0.18	2.0	$10.3^{+4.4}_{-3.3}$	-9.3	0.9
11	121526.17+361646.9	183.8590600	36.279696	0.39	3.5	$18.6^{+5.8}_{-4.7}$	-10.0	1.8
12	121529.66+361738.8	183.8736000	36.294130	0.19	1.8	$7.5^{+4.0}_{-2.8}$	-6.4	1.0
13	121452.87+361057.5	183.7203100	36.182650	0.96	11.4	$46.4^{+8.8}_{-7.8}$	< -10	21.6
14	121511.02+361449.9	183.7959200	36.247199	0.58	7.2	$43.0^{+8.3}_{-7.2}$	< -10	8.3
15	121533.49+361838.8	183.8895700	36.310800	0.21	2.1	$11.0^{+4.6}_{-3.4}$	-8.7	1.0

Continued on next page

Table 2.6 – continued from previous page

Galaxy	Source No.	Source ID (CXOLV J+...)	R.A. (J2000)	Decl. (J2000)	Positional Error ($''$)	θ ($'$)	log(pns) (0.35-8 keV)	$f^a_{0.35-8} \times 10^{-15}$ (erg s^{-1} cm^{-2})
(1)	(2)	(3)	(4)	(5)	(6)	(7)	(8)	(9)
16	121538.24+361921.0	183.9093700	36.322521	0.01	2.0	$1827.6^{+43.8}_{-42.8}$	< -10	167.5
17	121502.05+361430.7	183.7585800	36.241884	0.27	8.5	$347.7^{+20.9}_{-19.8}$	< -10	47.2
18	121516.02+361644.9	183.8167500	36.279149	0.81	5.1	$11.0^{+4.9}_{-3.7}$	-5.2	2.0
19	121505.73+361555.0	183.7738900	36.265292	0.82	7.3	$35.8^{+7.8}_{-6.7}$	< -10	6.2
20	121539.18+361931.1	183.9132600	36.325326	0.11	2.3	$29.9^{+6.6}_{-5.5}$	< -10	9.5
21	121533.42+361859.8	183.8892900	36.316615	0.11	2.1	$40.2^{+7.5}_{-6.4}$	< -10	3.7
22	121427.34+361415.1	183.6139300	36.237536	0.68	14.0	$198.0^{+20.7}_{-19.7}$	< -10	41.0
23	121522.66+361819.8	183.8444400	36.305521	0.20	1.4	$4.9^{+3.4}_{-2.2}$	-5.5	1.4
24	121415.01+361330.1	183.5625600	36.225045	1.00	15.7	$77.9^{+19.7}_{-18.7}$	-5.6	33.2
25	121512.65+361800.0	183.8027200	36.300001	0.36	3.3	$6.7^{+3.8}_{-2.6}$	-6.7	2.2
26	121456.24+361707.6	183.7343600	36.285464	0.88	8.7	$30.5^{+8.4}_{-7.4}$	-6.6	4.1
27	121451.92+361729.4	183.7163400	36.291508	0.71	9.3	$58.0^{+10.4}_{-9.4}$	< -10	8.1
28	121458.44+361858.2	183.7435000	36.316170	0.53	8.0	$60.1^{+9.8}_{-8.7}$	< -10	7.3
29	121507.69+361920.3	183.7820800	36.322307	0.69	5.9	$27.3^{+6.8}_{-5.7}$	< -10	5.2
30	121445.68+361919.8	183.6903500	36.322170	0.71	10.5	$52.5^{+9.8}_{-8.7}$	< -10	9.0
31	121535.69+361936.9	183.8987100	36.326928	0.46	2.1	$5.1^{+3.6}_{-2.4}$	-3.5	0.5
32	121526.36+361944.2	183.8598400	36.328953	0.14	2.7	$61.9^{+9.1}_{-8.0}$	< -10	5.9
33	121440.51+362023.0	183.6688200	36.339734	0.69	10.9	$93.9^{+12.6}_{-11.5}$	< -10	18.5
34	121509.36+362005.8	183.7890200	36.334954	0.87	5.4	$13.5^{+5.4}_{-4.2}$	-5.2	2.8
35	121511.15+362006.1	183.7964700	36.335041	0.35	4.7	$72.4^{+9.8}_{-8.7}$	< -10	16.4
36	121524.20+361955.3	183.8508400	36.332039	0.15	1.0	$6.9^{+3.8}_{-2.6}$	-8.7	1.9
37	121513.93+362014.4	183.8080500	36.337348	0.16	4.8	$185.3^{+14.9}_{-13.8}$	< -10	29.1
38	121455.91+362047.1	183.7329900	36.346423	0.40	8.0	$89.3^{+11.1}_{-10.0}$	< -10	16.8
39	121523.19+362007.4	183.8466600	36.335412	0.37	3.4	$13.0^{+5.1}_{-4.0}$	-6.4	1.3
40	121507.08+362058.3	183.7795100	36.349541	0.54	6.1	$35.3^{+7.5}_{-6.4}$	< -10	7.2
41	121505.81+362125.0	183.7742300	36.356958	0.54	4.9	$9.9^{+4.4}_{-3.3}$	-7.2	3.3
42	121538.15+361944.8	183.9090000	36.329124	0.03	2.1	$380.0^{+20.6}_{-19.5}$	< -10	37.8
43	121512.76+362233.8	183.8031700	36.376065	0.59	4.5	$6.1^{+3.8}_{-2.6}$	-4.1	2.4
44	121520.92+362153.6	183.8371800	36.364896	0.35	4.8	$28.4^{+7.0}_{-5.9}$	< -10	2.8
45	121535.94+362006.6	183.8997500	36.335186	0.19	2.3	$12.0^{+4.7}_{-3.6}$	-9.8	1.1
46	121529.42+362107.6	183.8726200	36.352133	0.35	3.1	$10.8^{+4.6}_{-3.4}$	-7.8	1.5
47	121522.38+362237.7	183.8432700	36.377152	0.44	5.1	$30.4^{+7.1}_{-6.0}$	< -10	3.3
48	121529.02+362130.9	183.8709500	36.358611	0.28	3.0	$13.0^{+4.8}_{-3.7}$	< -10	1.8
49	121530.78+362204.5	183.8782900	36.367919	0.27	3.9	$25.2^{+6.4}_{-5.3}$	< -10	2.4
50	121532.25+362156.0	183.8843800	36.365568	0.42	3.7	$9.0^{+4.6}_{-3.4}$	-4.0	0.9
51	121537.26+362030.0	183.9052900	36.341678	0.33	2.6	$4.4^{+3.4}_{-2.2}$	-3.4	0.6
52	121517.62+362802.7	183.8234500	36.467437	0.73	10.2	$69.6^{+11.7}_{-10.6}$	< -10	17.5

Continued on next page

Table 2.6 – continued from previous page

Galaxy	Source No.	Source ID (CXOLV J+...)	R.A. (J2000)	Decl. (J2000)	Positional Error ($''$)	θ ($'$)	log(pns) (0.35-8 keV)	$f^a_{0.35-8} \times 10^{-15}$ (erg s^{-1} cm^{-2})
(1)	(2)	(3)	(4)	(5)	(6)	(7)	(8)	(9)
53	121534.38+362219.6	183.8932800	36.372129	0.10	3.9	$181.4^{+14.7}_{-13.6}$	< -10	17.2
54	121517.36+363123.2	183.8223700	36.523133	1.09	12.3	$49.3^{+10.3}_{-9.2}$	< -10	24.3
55	121538.14+362050.7	183.9089500	36.347436	0.10	1.8	$26.8^{+6.3}_{-5.2}$	< -10	7.4
56	121524.47+363010.9	183.8519700	36.503040	1.11	12.1	$44.0^{+10.9}_{-9.9}$	-7.0	9.4
57	121537.25+362219.3	183.9052500	36.372049	0.13	3.2	$47.0^{+8.0}_{-6.9}$	< -10	6.9
58	121539.36+362055.3	183.9140300	36.348722	0.14	2.7	$31.5^{+6.8}_{-5.7}$	< -10	2.9
59	121539.99+361935.9	183.9166600	36.326657	0.11	2.1	$24.6^{+6.6}_{-5.5}$	< -10	2.5
60	121543.07+362725.8	183.9294600	36.457168	0.82	9.4	$42.0^{+8.8}_{-7.7}$	< -10	7.8
61	121543.01+362633.1	183.9292500	36.442533	0.46	9.2	$131.1^{+15.8}_{-13.7}$	< -10	50.3
62	121541.39+362114.3	183.9224800	36.353998	0.04	2.9	$432.4^{+21.9}_{-20.8}$	< -10	40.4
63	121553.15+362450.9	183.9714600	36.414155	0.46	4.7	$14.0^{+5.0}_{-3.8}$	-8.7	4.8
64	121548.96+362256.9	183.9540400	36.382498	0.42	4.3	$22.3^{+6.8}_{-5.7}$	-6.8	3.2
65	121545.87+362137.2	183.9411400	36.360352	0.14	1.3	$9.8^{+4.3}_{-3.1}$	< -10	2.8
66	121547.74+362156.6	183.9489400	36.365736	0.33	3.8	$19.9^{+6.1}_{-5.0}$	-8.4	1.9
67	121600.38+362534.9	184.0016200	36.426386	0.47	5.9	$26.8^{+6.4}_{-5.3}$	< -10	10.4
68	121547.43+362124.7	183.9476600	36.356873	0.19	3.3	$52.7^{+8.5}_{-7.5}$	< -10	5.0
69	121549.26+362145.5	183.9552900	36.362665	0.23	3.2	$38.0^{+8.0}_{-8.0}$	-7.1	5.3
70	121608.86+362611.8	184.0369300	36.436614	0.90	7.4	$14.5^{+5.2}_{-4.1}$	-8.3	5.4
71	121554.94+362251.6	183.9789200	36.381016	0.35	3.0	$6.8^{+3.8}_{-2.6}$	-7.1	2.2
72	121637.09+362854.2	184.1545600	36.481733	0.94	13.3	$84.9^{+14.0}_{-13.0}$	< -10	34.3
73	121620.59+362609.8	184.0858200	36.436072	1.24	9.0	$14.9^{+5.5}_{-4.4}$	-6.2	5.7
74	121615.95+362519.6	184.0664800	36.422122	0.95	9.4	$41.6^{+9.8}_{-8.8}$	-8.4	9.1
75	121543.56+362009.9	183.9315100	36.336089	0.18	1.8	$13.5^{+4.8}_{-3.7}$	< -10	1.8
76	121646.43+362936.2	184.1934900	36.493390	1.09	15.2	$81.4^{+21.3}_{-19.3}$	-4.4	38.4
77	121559.11+362228.9	183.9963300	36.374716	0.10	4.5	$390.9^{+20.9}_{-19.8}$	< -10	99.3
78	121659.11+363033.5	184.2463100	36.509309	1.03	17.8	$96.1^{+15.7}_{-14.7}$	< -10	64.0
79	121648.03+362855.8	184.2001600	36.482186	1.11	15.0	$64.7^{+14.7}_{-13.6}$	-7.3	31.4
80	121618.40+362422.5	184.0767000	36.406257	0.80	7.5	$20.8^{+5.9}_{-4.8}$	< -10	7.6
81	121606.20+362138.8	184.0258600	36.360781	0.42	4.1	$9.5^{+4.3}_{-3.1}$	-7.4	3.4
82	121540.86+361939.7	183.9202600	36.327702	0.07	2.1	$74.5^{+9.8}_{-8.8}$	< -10	7.2
83	121647.98+362337.8	184.1999400	36.393850	0.88	12.8	$94.3^{+14.7}_{-13.7}$	< -10	40.4
84	121633.23+362209.6	184.1384600	36.369337	0.96	9.5	$30.8^{+7.4}_{-6.3}$	< -10	12.0
85	121604.95+362032.8	184.0206600	36.342455	0.34	3.7	$10.4^{+4.4}_{-3.3}$	-7.5	3.4
86	121545.65+361942.9	183.9402500	36.328607	0.39	3.1	$6.9^{+4.0}_{-2.8}$	-4.5	1.0
87	121639.43+362025.1	184.1643300	36.340317	1.48	10.6	$15.7^{+5.6}_{-4.5}$	-6.3	19.1
88	121613.63+361953.6	184.0568000	36.331566	0.34	5.4	$35.3^{+7.1}_{-6.0}$	< -10	13.1
89	121604.96+361903.1	184.0206800	36.317529	0.60	3.9	$3.8^{+3.2}_{-1.9}$	-4.0	1.3

Continued on next page

Table 2.6 – continued from previous page

Galaxy	Source No.	Source ID (CXOLV J+...)	R.A. (J2000)	Decl. (J2000)	Positional Error ($''$)	θ ($'$)	log(pns) (0.35-8 keV)	$f^a_{0.35-8} \times 10^{-15}$ (erg s^{-1} cm^{-2})
(1)	(2)	(3)	(4)	(5)	(6)	(7)	(8)	(9)
90	121620.44+361754.4	184.0852000	36.298450	0.54	10.7	$48.6^{+8.9}_{-7.8}$	< -10	43.4
91	121549.70+361847.0	183.9571000	36.313059	0.38	2.8	$11.1^{+4.9}_{-3.7}$	-5.4	1.0
92	121540.83+361927.5	183.9201600	36.324330	0.21	1.5	$6.5^{+3.8}_{-2.6}$	-5.4	1.8
93	121544.74+361846.3	183.9364400	36.312877	0.09	2.3	$91.5^{+10.7}_{-9.6}$	< -10	8.3
94	121541.89+361915.3	183.9245700	36.320929	0.13	2.1	$24.9^{+6.2}_{-5.1}$	< -10	2.3
95	121557.77+361519.5	183.9907500	36.255438	0.39	4.2	$12.6^{+4.7}_{-3.6}$	< -10	4.0
96	121557.59+361510.0	183.9899900	36.252787	0.49	4.3	$8.6^{+4.1}_{-2.9}$	-8.6	2.7
97	121541.63+361909.4	183.9234600	36.319284	0.21	2.1	$7.7^{+4.1}_{-2.9}$	-4.8	0.7
98	121548.83+361702.7	183.9534800	36.284108	0.27	2.6	$8.4^{+4.1}_{-2.9}$	-7.1	1.2
99	121551.56+361610.8	183.9648700	36.269684	0.52	3.2	$6.5^{+3.8}_{-2.6}$	-5.0	1.2
100	121600.89+361309.9	184.0037100	36.219433	0.81	6.8	$10.0^{+4.7}_{-3.6}$	-4.5	1.9
101	121544.63+361810.3	183.9359600	36.302879	0.14	1.7	$11.7^{+4.6}_{-3.4}$	< -10	1.6
102	121547.61+361645.5	183.9484000	36.279330	0.22	2.6	$12.3^{+4.7}_{-3.6}$	< -10	1.7
103	121552.63+361347.8	183.9693100	36.229950	0.33	4.5	$22.6^{+5.9}_{-4.8}$	< -10	7.7
104	121602.97+360902.1	184.0123800	36.150609	0.97	9.6	$33.3^{+7.3}_{-6.2}$	< -10	13.4
105	121557.69+361057.4	183.9904100	36.182632	0.86	8.5	$22.9^{+6.6}_{-5.5}$	-8.2	4.7
106	121550.74+361412.5	183.9614200	36.236820	0.50	3.9	$5.6^{+3.6}_{-2.4}$	-5.4	1.8
107	121541.18+361857.9	183.9216100	36.316104	0.17	1.6	$7.9^{+4.0}_{-2.8}$	< -10	2.1
108	121557.58+360753.3	183.9899200	36.131494	0.98	11.3	$49.5^{+10.1}_{-9.0}$	< -10	11.0
109	121549.45+361212.1	183.9560500	36.203365	0.33	6.8	$60.3^{+9.1}_{-8.0}$	< -10	12.3
110	121604.28+360019.1	184.0178400	36.005308	1.31	17.8	$82.4^{+18.8}_{-17.7}$	-6.5	36.3
111	121547.89+361020.3	183.9495600	36.172327	0.79	8.5	$25.7^{+7.3}_{-6.2}$	-7.2	5.0
112	121556.18+360033.1	183.9841200	36.009199	1.23	17.2	$75.6^{+18.6}_{-17.5}$	-5.7	31.9
113	121551.87+360326.7	183.9661400	36.057432	1.14	14.2	$48.1^{+14.3}_{-13.2}$	-4.4	19.4
114	121545.29+361107.0	183.9387200	36.185291	0.56	6.4	$23.1^{+6.1}_{-5.0}$	< -10	7.7
115	121541.93+361354.6	183.9247200	36.231848	0.35	3.5	$8.7^{+4.1}_{-2.9}$	-10.0	2.7
116	121540.00+361840.7	183.9167000	36.311315	0.10	2.0	$32.2^{+6.8}_{-5.7}$	< -10	3.0

[a] Unabsorbed X-ray flux, assuming the power law with $\Gamma = 1.9$ absorbed by the appropriate Galactic column given in Table 2.1; [b] θ is the off-axis angle from the *Chandra* ACIS aim point.

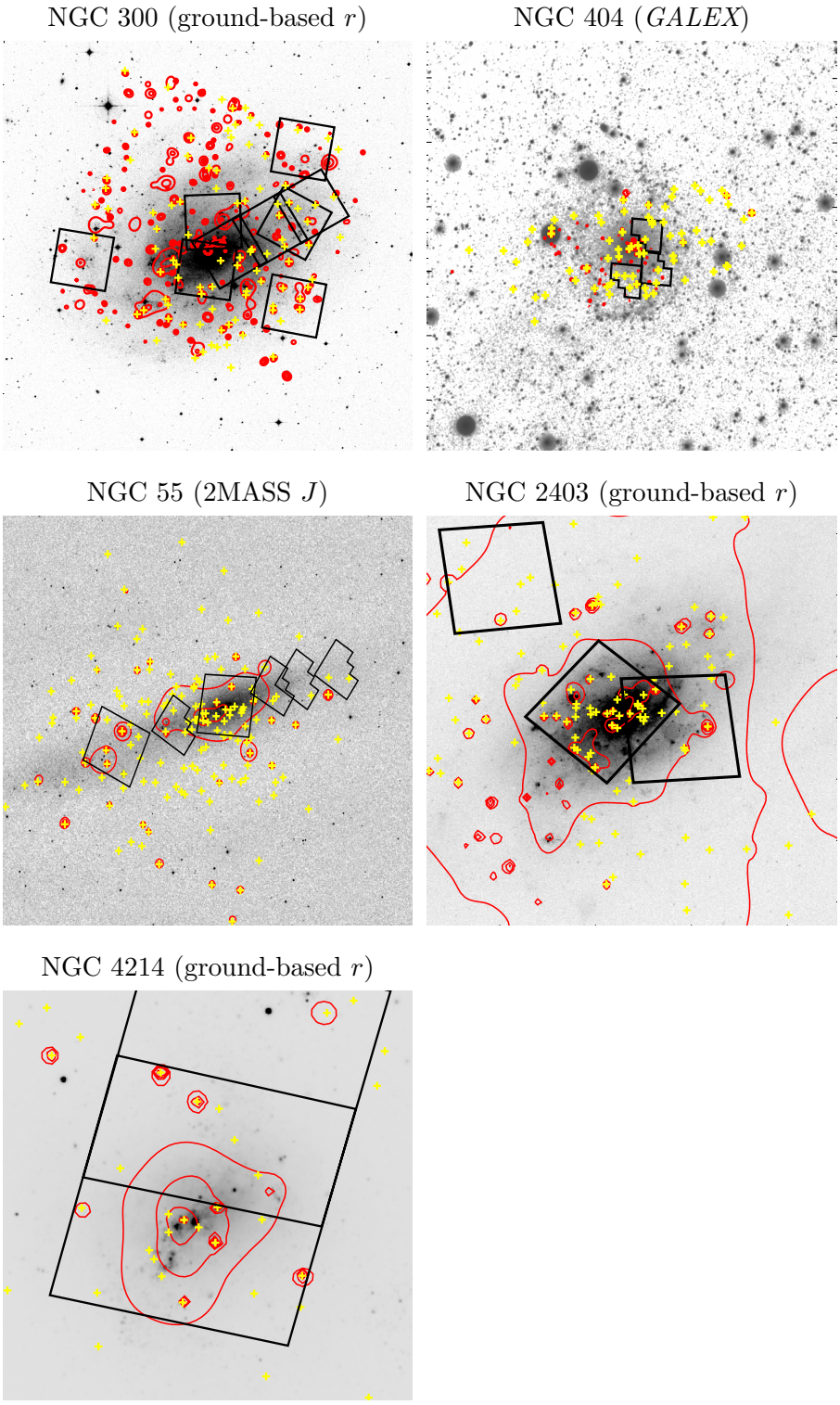

Figure 2.1: Observations of the CLVS galaxies. Soft (0.5-1 keV) X-ray contours superimposed in red and highly significant X-ray sources are shown as yellow crosses. Our *HST* fields are shown in black.

2.4.2 Comparison with Traditional Methods

The standard approach to X-ray source catalog generation is to use a pre-written source detection algorithm (such as `wavdetect`), with modifications applied to various parameters to change the threshold for classifying X-ray sources, signal-to-noise thresholds, etc. In this section, I examine how the traditional approach to detecting point sources differs from the more rigorous iterative source detection strategy employed to generate the CLVS source catalog.

The `wavdetect` algorithm, commonly used to detect *Chandra* X-ray sources, has a number of parameters which may be tuned. We investigated the effect of changing three of these parameters (*sigthresh*, *bkgsigthresh*, and *maxiter*) from their default values. Here, we briefly describe the three parameters; the reader is referred to the `wavdetect` help page[7] for additional information. The parameter *sigthresh* defines the threshold for identifying a pixel as belonging to an X-ray source whose default value is 10^{-6}; increasing the value of *sigthresh* will cause `wavdetect` to identify background flares as source detections. The significant threshold for cleansing data during iterations, *bkgsigthresh*, has a default value of 10^{-3}, and is the statistical criteria for rejecting the null hypothesis that the pixel in question has data solely sampled from the background. Increasing the value of *bkgsigthresh* will increase the number of sources assumed to be genuine (i.e., not background fluctuations). Finally, *maxiter* is the maximum number of cleansing iterations to perform – increasing the value of this parameter will increase the number of sources detected. To quantitatively evaluate the differences between the iterative source catalog creation approach and traditional source detection algorithm approach, we ran `wavdetect` on our merged 0.35-8 keV observations of each of the CLVS galaxies and compared the results to our final X-ray source catalogs.

The impact of bin size on the output source lists was first investigated by running `wavdetect` will all parameters left at their default settings for image bin sizes of 1, 2, 3, and 4 pixels. Using `wavdetect` on images with a bin size of 1 typically resulted in the lowest fraction of catalog sources recovered when all flux levels are considered (∼50-70%), but it performed best at recovering faint sources (up to 50% of of significant sources with

[7] `http://cxc.harvard.edu/ciao/ahelp/wavdetect.html`

a 0.35-8 keV flux below 10^{-15} erg s^{-1} cm^{-2} were recovered). Although a larger fraction of significant sources were detected when `wavdetect` was run on images with bin sizes of 2, 3, or 4 ($\sim$62-85%), these bin sizes recovered a significantly lower fraction of faint sources (typically less than 50%, and sometimes recovering zero faint sources). All bin sizes returned $\sim$10-20 sources returned by `wavdetect` but that were determined by `AE` to not be significant detections, hereafter referred to as "false positives." Thus, the assumption of bin size made when running `wavdetect` on the merged X-ray images of the CLVS galaxies significantly impacted the number of faint, but significant, X-ray sources we were able to recover.

We next combined the source lists for each bin size, so that a "total" source list was made which included all sources detected at any bin size. The overall fraction of recovered sources (at all flux levels) increased to $\sim$76-91%, while the fraction of faint X-ray sources increased by $\sim$15-20%. The total number of false positives also increased, with 20-40 false positives founds in each image.

Total source lists (including all sources found for bin sizes of 1, 2, 3, and 4) were generated using `wavdetect` for each of the following modifications: *sigthresh* = 10^5, *bkgsigthresh* = 10^{-2}, and *maxiter* = 5. All methods included a significant number of false positives – often yielding a more than 50% increase in the overall number of candidate X-ray sources. Changing the value of *sigthresh* resulted in a source list that frequently exhibited a 90% increase in the number of sources, with a majority of significant low-flux sources being recovered. However, this method returned the largest number of false positives. While changing *bkgsigthresh* and *maxiter* each returned equally high fractions of the total sources for each galaxy, these `wavdetect` runs failed to recover more than half of the faint sources.

Figure 2.2 shows the fraction of X-ray sources recovered for each of our `wavdetect` runs as a function of source flux. We found that increasing the values of *sigthresh*, *bkgsigthresh*, and *maxiter* from their default values all improved the number of faint sources recovered, albeit at the cost of including many more false positives in the final source lists. For sufficiently high-flux sources, above $\sim 10^{-14}$ erg s^{-1} cm^{-2}, nearly all of the methods we investigated converge to 100% recovery for every galaxy. The fraction of highly significiant sources recovered in each of these runs, and the number of false positives detected, are summarized in Table 2.7.

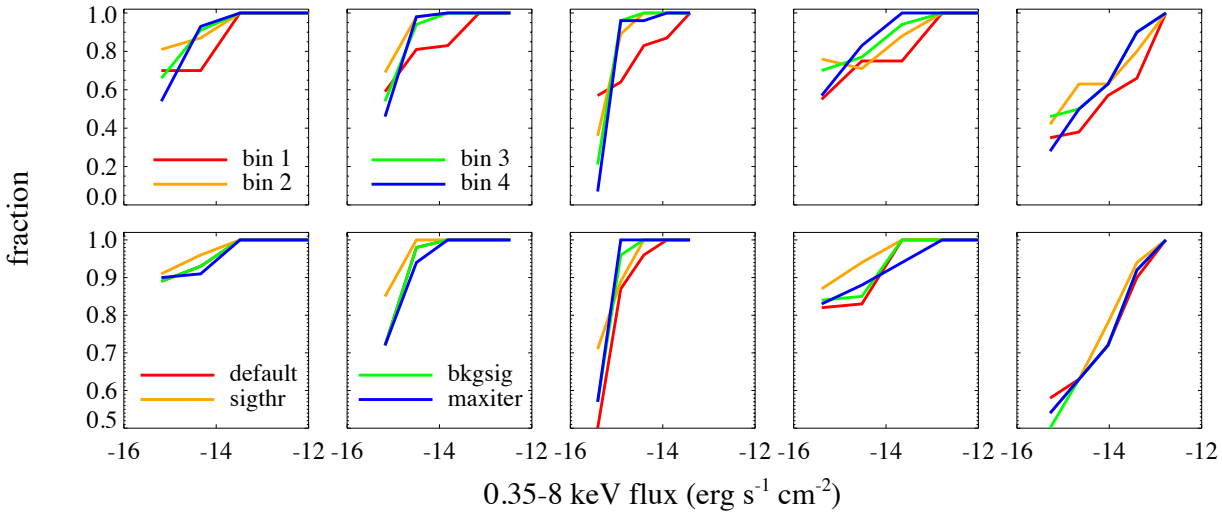

Figure 2.2: The fraction of highly significant sources in the CLVS X-ray source catalogs that were recovered by the `wavdetect` algorithm as a function of source flux. At sufficiently large fluxes, the iterative approach and the traditional `wavdetect` method converge. The top panel shows the fraction of sources recovered when `wavdetect` is run on images of different bin size with all default parameters. Red shows the results for bin sizes of 1, orange shows bin sizes of 2, green shows bin sizes of 3, and blue show bin sizes of 4. The bottom panel compares the output of `wavdetect` with all default parameters (shown in red) to the output when different parameters are changed: i.e., when $sigthesh = 10^{-5}$ (orange), $bkgsigthresh = 10^{-2}$ (green), and $maxiter = 5$ (blue.)

We conclude that an iterative source detection strategy is necessary to both capture many low-flux X-ray sources and remove false positives, which is beyond the capability of the `wavdetect` algorithm alone.

2.5 Sensitivity Maps

The remainder of the analyses in this work require sensitivity maps, which provide the energy flux level at which a source could be detected for each point in our survey area. We convert the `AE`-provided photon flux for each source (*flux2*, which is based on the net source

Table 2.7: Fraction of CLVS Sources Recovered by `wavdetect`

	all fluxes / $< 10^{-15}$ erg s^{-1} cm^{-2}/ # false positives				
`wavdetect` run	NGC 55	NGC 300	NGC 404	NGC 2403	NGC 4214
(1)	(2)	(3)	(4)	(5)	(6)
defaults, bin 1	72% / 40% / 34	72% / 25% / 10	73% / 45% / 11	67% / 69% / 23	53% / 50% / 10
defaults, bin 2	84% / 40% / 29	85% / 0% / 10	84% / 18% / 9	75% / 56% / 15	66% / 33% / 17
defaults, bin 3	77% / 0% / 22	77% / 0% / 9	84% / 9% / 13	76% / 49% / 10	67% / 33% / 16
defaults, bin 4	71% / 20% / 20	76% / 0% / 7	80% / 0% / 13	73% / 28% / 17	62% / 17% / 18
defaults, all bin sizes	91% / 50% / 48	86% / 25% / 18	84% / 45% / 20	85% / 69% / 43	76% / 50% / 27
sigthresh $= 10^{-5}$	94% / 70% / 108	93% / 75% / 39	91% / 64% / 53	92% / 88% / 117	78% / 67% / 82
bkgsigthresh $= 10^{-2}$	91% / 50% / 55	86% / 25% / 18	91% / 45% / 20	86% / 72% / 42	75% / 50% / 27
maxiter $= 5$	91% / 50% / 55	85% / 25% / 17	92% / 45% / 18	87% / 81% / 21	76% / 50% / 28

counts, exposure time, and the mean auxiliary response file (ARF) in the given energy band) into energy fluxes assuming a power law with Γ=1.9 that is absorbed by the appropriate Galactic column density for each galaxy. Since the majority of X-ray sources in each catalog are either XRBs or background AGN, we expect this model to be appropriate and not to systematically bias our subsequent analyses.

To create sensitivity maps, we calculated the number of source counts that would be required to meet our *pns* criteria ($< 4 \times 10^{-6}$) for each point in the survey area, following [146]. Sensitivity maps were constructed for the *Chandra* field of view in the 0.35-8 keV, 0.5-2 keV, and 2-8 keV energy bands. The limiting fluxes in the 0.35-8, 0.5-2, and 2-8 keV bands for each galaxy are summarized in Table 2.8.

Table 2.8: Limiting Fluxes (erg s^{-1} cm^{-2}) and Luminosities (erg s^{-1}) of Merged Observations

Galaxy	Energy band	70%		90%		95%	
	(keV)	f_X ($\times 10^{-15}$)	L_X ($\times 10^{37}$)	f_X ($\times 10^{-15}$)	L_X ($\times 10^{37}$)	f_X ($\times 10^{-15}$)	L_X ($\times 10^{37}$)
(1)	(2)	(3)	(4)	(5)	(6)	(7)	(8)
	0.35-8	16.2	0.8	31.5	1.5	94.4	4.5
NGC 300	0.5-2	9.4	0.4	18.5	0.9	56.7	2.7
	2-8	44.0	2.1	86.0	4.1	251.8	12.0
	0.35-8	62.0	6.9	198.0	22.0	500.0	55.5
NGC 404	0.5-2	3.0	0.3	13.0	1.4	44.0	4.9
	2-8	28.0	3.1	87.0	10.0	275.0	30.5
	0.35-8	24.9	1.3	33.0	1.7	35.9	1.9
NGC 55	0.5-2	0.8	0.04	0.60	0.03	0.7	0.04
	2-8	1.9	0.1	2.8	0.2	3.0	0.2
	0.35-8	6.7	0.9	9.8	1.3	10.9	1.4
NGC 2403	0.5-2	0.5	0.07	1.1	0.2	1.3	0.2
	2-8	0.3	0.04	1.4	0.2	21.3	2.8
	0.35-8	18.2	1.8	29.9	3.0	32.8	3.3
NGC 4214	0.5-2	0.3	0.03	0.6	0.06	0.7	0.07
	2-8	1.0	0.1	2.0	0.2	27.1	2.7

Chapter 3

X-RAY SOURCE CHARACTERISTICS

In this chapter, I present a summary of the X-ray source catalog characteristics for each of the five CLVS galaxies. The X-ray properties of individual sources, such as their spectral shape and temporal variability, can be used to constrain the physical origin of the X-ray emission (see Chapter 4). Bulk population properties, such as the radial distribution of sources, enable us to identify different X-ray populations in a statistical sense.

The X-ray point source populations of all five CLVS galaxies consist of HMXBs, LMXBs, SNRs, background AGN, and foreground stars. Other X-ray emitting objects – such as cataclysmic variables, active binaries, or flaring M-dwarfs – are too faint to be detectable at distances of a few Mpc, although our catalogs could contain a small number of such objects in the foreground. The source catalogs provide information on temporal variability of sources, hardness ratios (for faint sources) and spectral fitting (for bright sources), as well as the radial source distributions of X-ray sources.

3.1 Comparison Overall Catalog Properties

Figure 3.1 shows cumulative distributions of the net counts (in the 0.35-8 keV band), the 0.35-8 keV photon flux, *Chandra* error circle size, and off-axis angle for all five CLVS source catalogs. Of the 629 X-ray sources detected at high significance, ∼97% have fewer than 200 net counts. Nearly half of all X-ray sources have error circles smaller than $2''$ in radius, and 21% have error circles less than $1''$ in radius. Fifty-four percent of sources have off-axis angles less than $5'$, and 92% of sources are within $10'$ of the center of the host galaxy.

3.1.1 Hardness Ratios

The X-ray spectrum of a source can provide a key diagnostic for separating different populations. For example, XRBs and AGN are well-described by power laws with photon indices

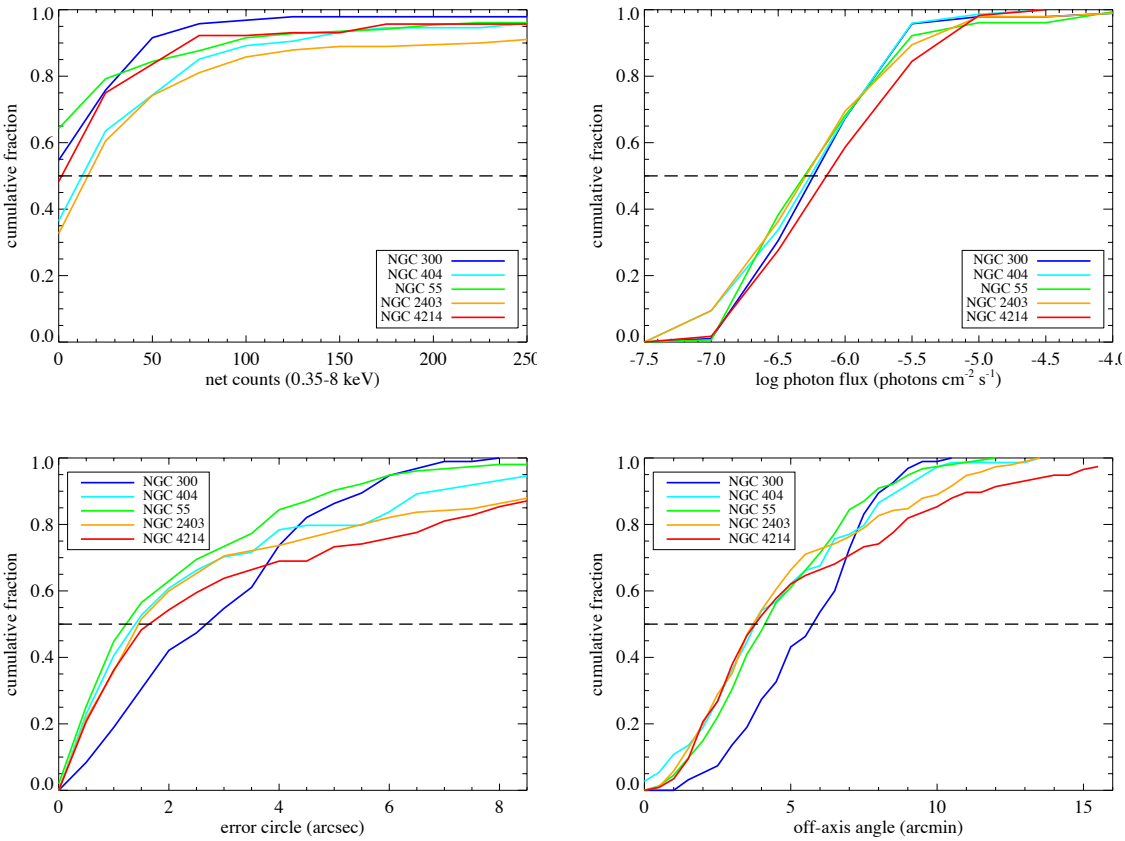

Figure 3.1: Cumulative distributions of various source catalog properties for all five CLVS galaxies. The top row shows the net counts in the 0.35-8 keV band (left) and the 0.35-8 keV photon flux (right), while the bottom row shows the *Chandra* error circle (left) and the off-axis angle (right.) On all plots, the 50% level is indicated by a horizontal dashed line.

ranging from $\Gamma \sim 1 - 2$, and may show high levels of intrinsic absorption (i.e., in the case of obscured AGN). Contaminating foreground stars will exhibit significantly softer, thermal X-ray emission with plasma temperatures of a few keV or less, similar to faint SNRs. However, when studying discrete X-ray sources at distances of a few Mpc, it is nearly impossible to constrain spectral parameters to any degree of accuracy for sources with < 50 counts. The majority of the CLVS X-ray sources fall within this low-count regime, as shown in Figure 3.1a.

Instead of directly measuring the X-ray spectral shape, we define hardness ratios (HRs; also called X-ray colors) to separate different populations. HRs measure the fraction of photons emitted by a source in three energy ranges: soft (S, 0.35-1.1 keV), medium (M, 1.1-2.6 keV), and hard (H, 2.6-8 keV). We evaluate two HRs for each source using the approach developed in [407] [see also 323]. Source and background counts were determined by `AE` in each band, and we define a "soft" color,

$$HR1 = \frac{M - S}{H + M + S}, \tag{3.1}$$

and a "hard" color,

$$HR2 = \frac{H - M}{H + M + S}. \tag{3.2}$$

The Bayesian Estimation of Hardness Ratios [*BEHR*, 308] code accounts for the fact that source and background counts are non-negative, however, it does not directly handle this form for the HRs. We adopt an approach described in [407]: for each source, the inputs are source counts, background counts, the `AE` "backscale" parameter (which accounts for the ratio of the source and background extraction areas and efficiencies), and a factor converting from counts to photon flux (i.e., the exposure time multiplied by the mean ARF over the extraction region). We additionally set the "softeff" and "hardeff" parameters to exposure time multiplied by the mean ARF values computed by `AE` for each observation in which the source was observed. Therefore, the hardness ratio calculations take into account the variations in effective area and exposure times between the different observations of a single source, especially important considering the differences in ACIS filter contamination

between the observations utilized in this work.

The *BEHR* code is then run twice (once for S and M, and again for S and H). For each energy band, we set the *BEHR* "burnin" parameter to 50,000 and the "total draws" parameter to 100,000. This provides 50,000 samples from the probability distribution for each energy band. Combining the results from the two *BEHR* runs, we obtain 50,000 samples from the probability distribution for the S, M, and H counts. Using these distributions, we compute 50,000 values for $HR1$ and $HR2$ for each source. The HR value is defined as the mean of the distribution, and the credible interval is evaluated based on the 68.2% equal-tail estimates (i.e., 0.682/2 of the samples have values below the lower limit, and 0.682/2 of the samples have values above the upper limit).

To aid in the interpretation of our HR calculations, we define six categories of X-ray sources: 'XRB' (which is likely contaminated with background AGN, given their X-ray similarities to LMXBs), 'BKG' for likely background sources with an indeterminate spectral shape, 'ABS' for heavily absorbed sources, 'SNR', and indeterminate 'HARD' and 'SOFT' sources [215, 34, 33]. The HR classification categories are listed in Table 3.1. The HRs and corresponding source classification is given in Table 3.2, and Figure 3.2 shows the HR values of all five CLVS galaxies with our X-ray color categories labeled.

Table 3.1: Hardness Ratio Source Classification Scheme

Classification	Definition
(1)	(2)
X-ray binary ('XRB')	$-0.4 < HR2 < 0.4$, $-0.4 < HR1 < 0.4$
Background source ('BKG')	$HR2 > -0.4$, $HR1 < -0.4$
Absorbed source ('ABS')	$HR1 > 0.4$
Supernova remnant ('SNR')	$HR2 < -0.4$, $HR1 < -0.4$
Indeterminate hard source ('HARD')	$HR2 > 0.4$, $-0.4 < HR1 < 0.4$
Indeterminate soft source ('SOFT')	$HR2 < -0.4$, $-0.4 < HR1 < 0.4$

Table 3.2: Hardness Ratios of the CLVS X-ray Sources

	NGC 300			NGC 404			NGC 55			NGC 2403			NGC 4214		
No.	HR1	HR2	ID	HR1	HR2	ID	HR1	HR2	ID	HR1	HR2	ID	HR1	HR2	ID
1	0.72 ± 0.25	-0.71 ± 0.32	ABS	0.42 ± 0.21	-0.69 ± 0.11	ABS	0.13 ± 0.50	-0.23 ± 0.41	XRB	0.27 ± 0.13	0.31 ± 0.24	XRB	-0.59 ± 0.28	0.06 ± 0.19	SNR
2	0.19 ± 0.41	-0.09 ± 0.51	XRB	0.08 ± 0.46	-0.08 ± 0.47	XRB	0.46 ± 0.32	-0.55 ± 0.26	ABS	-0.13 ± 0.03	-0.17 ± 0.02	XRB	0.36 ± 0.15	-0.25 ± 0.18	XRB
3	0.36 ± 0.13	-0.56 ± 0.12	SOFT	0.01 ± 0.48	-0.05 ± 0.43	XRB	0.35 ± 0.11	-0.39 ± 0.12	XRB	0.39 ± 0.13	-0.52 ± 0.13	SOFT	0.14 ± 0.39	-0.00 ± 0.51	XRB
4	0.50 ± 0.15	-0.47 ± 0.21	ABS	-0.01 ± 0.47	-0.03 ± 0.44	XRB	0.40 ± 0.13	0.07 ± 0.23	XRB	0.64 ± 0.25	-0.68 ± 0.20	ABS	0.08 ± 0.23	-0.23 ± 0.22	XRB
5	-0.07 ± 0.46	-0.15 ± 0.35	XRB	0.39 ± 0.48	-0.47 ± 0.35	SOFT	0.65 ± 0.18	-0.62 ± 0.21	ABS	0.15 ± 0.31	0.11 ± 0.46	XRB	-0.56 ± 0.21	-0.15 ± 0.12	SNR
6	0.31 ± 0.30	-0.18 ± 0.41	XRB	0.34 ± 0.48	-0.34 ± 0.48	XRB	0.42 ± 0.40	-0.38 ± 0.47	ABS	-0.54 ± 0.26	-0.03 ± 0.18	SNR	0.31 ± 0.38	-0.26 ± 0.44	XRB
7	-0.73 ± 0.23	-0.02 ± 0.12	SNR	0.28 ± 0.21	-0.62 ± 0.11	SOFT	0.36 ± 0.10	-0.45 ± 0.11	SOFT	0.52 ± 0.10	-0.14 ± 0.19	ABS	0.31 ± 0.33	-0.30 ± 0.35	XRB
8	-0.27 ± 0.38	-0.21 ± 0.22	XRB	0.01 ± 0.45	-0.01 ± 0.43	XRB	0.43 ± 0.06	-0.26 ± 0.07	ABS	0.48 ± 0.22	-0.30 ± 0.33	ABS	-0.18 ± 0.23	-0.25 ± 0.16	XRB
9	0.37 ± 0.42	-0.43 ± 0.37	SOFT	0.02 ± 0.44	-0.00 ± 0.46	XRB	-0.26 ± 0.35	-0.24 ± 0.21	XRB	0.15 ± 0.11	-0.33 ± 0.12	XRB	0.45 ± 0.13	-0.17 ± 0.19	ABS
10	0.16 ± 0.20	0.33 ± 0.34	XRB	0.17 ± 0.48	-0.17 ± 0.49	XRB	-0.37 ± 0.45	0.00 ± 0.28	XRB	0.30 ± 0.19	-0.33 ± 0.20	XRB	-0.05 ± 0.20	0.57 ± 0.33	HARD
11	0.22 ± 0.14	-0.27 ± 0.16	XRB	0.21 ± 0.48	-0.19 ± 0.51	XRB	0.08 ± 0.11	-0.33 ± 0.10	XRB	-0.51 ± 0.17	-0.21 ± 0.09	SNR	0.54 ± 0.19	-0.32 ± 0.31	ABS
12	0.36 ± 0.17	-0.55 ± 0.14	SOFT	0.06 ± 0.48	-0.09 ± 0.46	XRB	0.09 ± 0.30	-0.24 ± 0.27	XRB	0.40 ± 0.09	-0.03 ± 0.12	ABS	0.10 ± 0.35	-0.06 ± 0.38	XRB
13	0.07 ± 0.50	-0.20 ± 0.39	XRB	0.21 ± 0.55	-0.28 ± 0.45	XRB	0.36 ± 0.47	-0.35 ± 0.48	XRB	0.29 ± 0.22	-0.47 ± 0.19	SOFT	-0.03 ± 0.17	-0.10 ± 0.18	XRB
14	0.04 ± 0.34	0.20 ± 0.51	XRB	0.05 ± 0.49	-0.09 ± 0.44	XRB	-0.43 ± 0.34	-0.10 ± 0.21	SNR	0.26 ± 0.35	-0.38 ± 0.28	XRB	0.35 ± 0.12	-0.37 ± 0.13	XRB
15	-0.65 ± 0.31	-0.03 ± 0.16	SNR	0.08 ± 0.39	0.06 ± 0.51	XRB	0.37 ± 0.16	-0.57 ± 0.12	SOFT	0.07 ± 0.38	0.08 ± 0.50	XRB	0.66 ± 0.24	-0.66 ± 0.25	ABS
16	-0.22 ± 0.43	0.02 ± 0.34	XRB	0.16 ± 0.50	-0.19 ± 0.47	XRB	-0.00 ± 0.48	-0.06 ± 0.42	XRB	-0.45 ± 0.31	-0.13 ± 0.18	SNR	0.13 ± 0.02	-0.30 ± 0.02	XRB
17	0.33 ± 0.43	-0.46 ± 0.31	SOFT	0.24 ± 0.09	-0.51 ± 0.08	SOFT	0.37 ± 0.33	-0.21 ± 0.50	XRB	0.46 ± 0.15	-0.34 ± 0.18	ABS	0.18 ± 0.05	-0.28 ± 0.04	XRB
18	0.41 ± 0.18	-0.61 ± 0.13	ABS	0.57 ± 0.32	-0.62 ± 0.26	ABS	0.18 ± 0.32	-0.10 ± 0.40	XRB	-0.60 ± 0.28	-0.08 ± 0.15	SNR	0.41 ± 0.24	-0.31 ± 0.30	ABS
19	0.31 ± 0.11	0.27 ± 0.20	XRB	0.05 ± 0.43	0.01 ± 0.47	XRB	0.62 ± 0.26	-0.58 ± 0.32	ABS	0.14 ± 0.09	-0.33 ± 0.08	XRB	0.00 ± 0.15	-0.21 ± 0.13	XRB
20	0.47 ± 0.34	-0.52 ± 0.30	ABS	0.36 ± 0.15	-0.58 ± 0.12	SOFT	0.13 ± 0.48	-0.23 ± 0.40	XRB	-0.30 ± 0.05	-0.20 ± 0.03	XRB	0.57 ± 0.14	-0.36 ± 0.19	ABS
21	0.55 ± 0.21	-0.48 ± 0.28	ABS	0.41 ± 0.13	-0.47 ± 0.15	ABS	0.28 ± 0.12	-0.24 ± 0.13	XRB	-0.54 ± 0.25	-0.08 ± 0.16	SNR	-0.87 ± 0.10	-0.03 ± 0.05	SNR
22	0.12 ± 0.38	0.05 ± 0.52	XRB	0.02 ± 0.49	-0.08 ± 0.43	XRB	0.07 ± 0.17	0.57 ± 0.33	HARD	0.50 ± 0.23	-0.30 ± 0.37	ABS	0.19 ± 0.10	-0.56 ± 0.06	SOFT
23	0.69 ± 0.10	-0.63 ± 0.14	ABS	0.55 ± 0.31	-0.59 ± 0.28	ABS	-0.27 ± 0.02	-0.32 ± 0.01	XRB	0.32 ± 0.42	-0.38 ± 0.36	XRB	0.58 ± 0.26	-0.53 ± 0.32	ABS
24	0.42 ± 0.15	-0.59 ± 0.13	ABS	0.48 ± 0.38	-0.60 ± 0.24	ABS	0.36 ± 0.39	-0.53 ± 0.25	SOFT	0.52 ± 0.25	-0.43 ± 0.35	ABS	-0.73 ± 0.17	0.02 ± 0.11	SNR
25	0.37 ± 0.15	-0.61 ± 0.11	SOFT	0.64 ± 0.23	-0.65 ± 0.24	ABS	0.43 ± 0.38	-0.56 ± 0.25	ABS	0.66 ± 0.10	-0.43 ± 0.17	ABS	-0.16 ± 0.31	-0.10 ± 0.27	XRB
26	0.21 ± 0.48	-0.21 ± 0.48	XRB	0.01 ± 0.55	-0.26 ± 0.35	XRB	-0.03 ± 0.50	-0.11 ± 0.39	XRB	0.50 ± 0.09	-0.31 ± 0.12	ABS	0.48 ± 0.18	-0.33 ± 0.23	ABS
27	0.48 ± 0.19	-0.65 ± 0.14	ABS	0.17 ± 0.46	-0.14 ± 0.50	XRB	0.03 ± 0.37	0.13 ± 0.48	XRB	-0.70 ± 0.24	-0.05 ± 0.12	SNR	0.33 ± 0.10	-0.13 ± 0.12	XRB
28	0.54 ± 0.14	-0.63 ± 0.14	ABS	0.51 ± 0.43	-0.53 ± 0.39	ABS	0.07 ± 0.29	0.30 ± 0.52	XRB	0.29 ± 0.23	0.02 ± 0.34	XRB	0.40 ± 0.09	-0.25 ± 0.11	XRB
29	0.52 ± 0.22	-0.57 ± 0.23	ABS	-0.63 ± 0.31	0.00 ± 0.17	SNR	0.76 ± 0.18	-0.75 ± 0.25	ABS	0.34 ± 0.04	0.29 ± 0.08	XRB	0.23 ± 0.14	-0.13 ± 0.16	XRB
30	-0.02 ± 0.39	0.09 ± 0.45	XRB	0.26 ± 0.29	-0.47 ± 0.21	SOFT	0.40 ± 0.39	-0.39 ± 0.40	XRB	0.41 ± 0.12	-0.49 ± 0.14	ABS	0.33 ± 0.19	-0.43 ± 0.20	SOFT
31	-0.02 ± 0.42	0.03 ± 0.44	XRB	0.42 ± 0.27	-0.56 ± 0.20	ABS	0.33 ± 0.23	-0.57 ± 0.15	SOFT	0.37 ± 0.05	0.01 ± 0.07	XRB	-0.54 ± 0.41	0.00 ± 0.21	SNR
32	-0.80 ± 0.19	-0.02 ± 0.09	SNR	-0.34 ± 0.11	-0.31 ± 0.06	XRB	0.28 ± 0.37	-0.23 ± 0.41	XRB	0.11 ± 0.19	-0.11 ± 0.21	XRB	-0.07 ± 0.11	-0.13 ± 0.10	XRB
33	0.43 ± 0.26	-0.62 ± 0.17	ABS	0.58 ± 0.41	-0.61 ± 0.33	ABS	-0.46 ± 0.41	-0.04 ± 0.23	SNR	-0.36 ± 0.14	-0.19 ± 0.10	XRB	0.07 ± 0.09	-0.20 ± 0.10	XRB
34	-0.73 ± 0.27	-0.04 ± 0.12	SNR	-0.05 ± 0.32	0.27 ± 0.45	XRB	0.46 ± 0.31	-0.48 ± 0.31	ABS	-0.37 ± 0.27	0.18 ± 0.25	XRB	-0.16 ± 0.23	-0.22 ± 0.18	XRB
35	0.47 ± 0.06	-0.05 ± 0.10	ABS	0.58 ± 0.10	-0.23 ± 0.20	ABS	0.23 ± 0.28	0.15 ± 0.50	XRB	0.36 ± 0.16	-0.10 ± 0.23	XRB	0.05 ± 0.11	-0.27 ± 0.09	XRB

Continued on next page

Table 3.2 – continued from previous page

	NGC 300			NGC 404			NGC 55			NGC 2403			NGC 4214		
No.	HR1	HR2	ID	HR1	HR2	ID	HR1	HR2	ID	HR1	HR2	ID	HR1	HR2	ID
36	0.57 ± 0.30	-0.51 ± 0.43	ABS	0.03 ± 0.25	0.45 ± 0.50	HARD	0.03 ± 0.27	0.37 ± 0.48	XRB	0.05 ± 0.15	0.01 ± 0.15	XRB	0.12 ± 0.30	-0.14 ± 0.30	XRB
37	0.33 ± 0.38	-0.23 ± 0.50	XRB	0.06 ± 0.33	0.20 ± 0.51	XRB	0.26 ± 0.09	-0.49 ± 0.09	SOFT	0.31 ± 0.26	-0.45 ± 0.22	SOFT	0.51 ± 0.06	-0.18 ± 0.09	ABS
38	0.24 ± 0.32	-0.43 ± 0.24	SOFT	0.02 ± 0.51	-0.18 ± 0.38	XRB	-0.36 ± 0.47	-0.06 ± 0.27	XRB	0.03 ± 0.21	-0.40 ± 0.14	SOFT	0.18 ± 0.09	-0.37 ± 0.08	XRB
39	0.35 ± 0.17	-0.54 ± 0.14	SOFT	0.43 ± 0.13	-0.66 ± 0.09	ABS	0.30 ± 0.44	-0.40 ± 0.35	SOFT	-0.14 ± 0.19	-0.38 ± 0.10	XRB	0.49 ± 0.42	-0.56 ± 0.31	ABS
40	0.58 ± 0.31	-0.54 ± 0.40	ABS	0.19 ± 0.47	-0.18 ± 0.47	XRB	0.63 ± 0.18	-0.68 ± 0.16	ABS	0.41 ± 0.11	0.09 ± 0.20	ABS	0.38 ± 0.12	-0.13 ± 0.16	XRB
41	-0.53 ± 0.31	-0.15 ± 0.16	SNR	-0.10 ± 0.07	-0.31 ± 0.05	XRB	0.36 ± 0.49	-0.40 ± 0.43	XRB	0.28 ± 0.01	-0.34 ± 0.01	XRB	0.16 ± 0.44	-0.22 ± 0.41	XRB
42	0.63 ± 0.33	-0.64 ± 0.30	ABS	-0.06 ± 0.51	-0.11 ± 0.38	XRB	0.72 ± 0.13	-0.59 ± 0.21	ABS	0.36 ± 0.01	-0.39 ± 0.01	XRB	0.30 ± 0.05	-0.41 ± 0.04	SOFT
43	-0.68 ± 0.10	-0.14 ± 0.05	SNR	-0.71 ± 0.29	0.00 ± 0.14	SNR	0.34 ± 0.42	-0.27 ± 0.51	XRB	0.67 ± 0.13	-0.77 ± 0.10	ABS	0.71 ± 0.26	-0.71 ± 0.26	ABS
44	0.75 ± 0.13	-0.74 ± 0.16	ABS	0.55 ± 0.35	-0.61 ± 0.27	ABS	0.43 ± 0.06	-0.34 ± 0.07	ABS	0.35 ± 0.38	-0.28 ± 0.46	XRB	0.25 ± 0.24	-0.50 ± 0.17	SOFT
45	-0.01 ± 0.05	0.89 ± 0.09	HARD	0.27 ± 0.18	-0.56 ± 0.11	SOFT	0.69 ± 0.20	-0.67 ± 0.24	ABS	0.73 ± 0.13	-0.68 ± 0.16	ABS	-0.25 ± 0.44	-0.03 ± 0.31	XRB
46	-0.46 ± 0.30	0.08 ± 0.24	SNR	0.43 ± 0.12	-0.64 ± 0.09	ABS	-0.51 ± 0.35	0.01 ± 0.22	SNR	-0.02 ± 0.53	-0.19 ± 0.36	XRB	0.36 ± 0.44	-0.34 ± 0.47	XRB
47	0.04 ± 0.34	0.21 ± 0.51	XRB	0.15 ± 0.48	-0.18 ± 0.45	XRB	0.53 ± 0.39	-0.56 ± 0.32	ABS	-0.71 ± 0.25	-0.04 ± 0.12	SNR	0.13 ± 0.25	-0.39 ± 0.20	XRB
48	0.17 ± 0.41	-0.07 ± 0.51	XRB	0.16 ± 0.42	-0.07 ± 0.51	XRB	0.19 ± 0.24	0.05 ± 0.31	XRB	0.21 ± 0.12	-0.43 ± 0.11	SOFT	0.07 ± 0.25	-0.03 ± 0.26	XRB
49	0.34 ± 0.35	-0.53 ± 0.23	SOFT	0.09 ± 0.45	-0.25 ± 0.36	XRB	0.34 ± 0.44	-0.35 ± 0.44	XRB	-0.51 ± 0.48	-0.02 ± 0.22	SNR	0.50 ± 0.37	-0.54 ± 0.31	ABS
50	0.32 ± 0.10	-0.36 ± 0.11	XRB	0.80 ± 0.16	-0.83 ± 0.11	ABS	-0.42 ± 0.46	-0.00 ± 0.26	SNR	-0.40 ± 0.30	-0.10 ± 0.20	XRB	-0.74 ± 0.24	-0.02 ± 0.12	SNR
51	0.61 ± 0.23	-0.56 ± 0.32	ABS	-0.06 ± 0.50	-0.08 ± 0.39	XRB	-0.47 ± 0.37	-0.06 ± 0.21	SNR	0.20 ± 0.04	-0.44 ± 0.03	SOFT	0.51 ± 0.41	-0.51 ± 0.41	ABS
52	0.71 ± 0.14	-0.69 ± 0.18	ABS	0.30 ± 0.39	-0.14 ± 0.59	XRB	0.34 ± 0.10	-0.13 ± 0.13	XRB	0.50 ± 0.11	-0.34 ± 0.14	ABS	0.29 ± 0.09	-0.23 ± 0.09	XRB
53	0.32 ± 0.15	-0.60 ± 0.10	SOFT	0.31 ± 0.22	-0.56 ± 0.14	SOFT	0.49 ± 0.26	-0.40 ± 0.35	ABS	0.49 ± 0.07	-0.30 ± 0.09	ABS	0.36 ± 0.07	-0.43 ± 0.07	SOFT
54	-0.73 ± 0.24	-0.06 ± 0.11	SNR	0.52 ± 0.18	-0.30 ± 0.29	ABS	0.34 ± 0.04	-0.20 ± 0.04	XRB	-0.61 ± 0.15	-0.16 ± 0.08	SNR	0.32 ± 0.16	-0.33 ± 0.22	XRB
55	0.20 ± 0.48	-0.30 ± 0.38	XRB	0.73 ± 0.22	-0.74 ± 0.21	ABS	0.07 ± 0.48	-0.12 ± 0.44	XRB	-0.24 ± 0.10	-0.29 ± 0.07	XRB	0.35 ± 0.18	-0.51 ± 0.14	SOFT
56	-0.06 ± 0.41	0.09 ± 0.44	XRB	0.29 ± 0.09	0.35 ± 0.17	XRB	0.17 ± 0.33	0.11 ± 0.51	XRB	-0.39 ± 0.17	-0.24 ± 0.10	XRB	0.00 ± 0.47	-0.35 ± 0.27	XRB
57	0.06 ± 0.46	-0.13 ± 0.42	XRB	-0.03 ± 0.50	-0.10 ± 0.40	XRB	-0.43 ± 0.42	0.05 ± 0.26	SNR	0.27 ± 0.10	-0.30 ± 0.09	XRB	-0.57 ± 0.12	-0.16 ± 0.07	SNR
58	0.11 ± 0.45	-0.07 ± 0.48	XRB	0.28 ± 0.60	-0.39 ± 0.42	XRB	-0.13 ± 0.50	-0.07 ± 0.36	XRB	-0.06 ± 0.14	0.66 ± 0.20	HARD	-0.80 ± 0.16	-0.05 ± 0.08	SNR
59	-0.00 ± 0.30	0.28 ± 0.45	XRB	0.03 ± 0.46	-0.04 ± 0.45	XRB	0.74 ± 0.26	-0.76 ± 0.19	ABS	-0.87 ± 0.13	0.00 ± 0.06	SNR	-0.80 ± 0.19	-0.03 ± 0.09	SNR
60	-0.09 ± 0.44	0.03 ± 0.41	XRB	0.08 ± 0.48	-0.10 ± 0.46	XRB	-0.07 ± 0.52	-0.17 ± 0.35	XRB	-0.82 ± 0.16	-0.00 ± 0.08	SNR	0.06 ± 0.17	-0.29 ± 0.17	XRB
61	0.04 ± 0.41	0.04 ± 0.48	XRB	0.06 ± 0.44	-0.02 ± 0.47	XRB	0.52 ± 0.16	-0.34 ± 0.22	ABS	-0.70 ± 0.16	-0.10 ± 0.09	SNR	0.27 ± 0.07	-0.27 ± 0.07	XRB
62	0.40 ± 0.32	-0.34 ± 0.40	ABS	0.04 ± 0.48	-0.07 ± 0.45	XRB	0.40 ± 0.02	-0.22 ± 0.02	ABS	-0.47 ± 0.01	-0.21 ± 0.01	SNR	0.12 ± 0.05	-0.26 ± 0.04	XRB
63	0.19 ± 0.50	-0.31 ± 0.39	XRB	0.00 ± 0.46	-0.02 ± 0.43	XRB	0.33 ± 0.02	-0.48 ± 0.01	SOFT	0.51 ± 0.24	-0.53 ± 0.23	ABS	0.35 ± 0.22	-0.36 ± 0.22	XRB
64	0.41 ± 0.16	-0.64 ± 0.11	ABS	0.00 ± 0.49	-0.07 ± 0.43	XRB	0.15 ± 0.48	-0.17 ± 0.47	XRB	-0.59 ± 0.03	-0.20 ± 0.01	SNR	-0.63 ± 0.31	-0.09 ± 0.15	SNR
65	-0.11 ± 0.38	0.08 ± 0.39	XRB	-0.99 ± 0.05	-0.01 ± 0.01	SNR	0.12 ± 0.50	-0.27 ± 0.37	XRB	0.63 ± 0.15	-0.40 ± 0.27	ABS	0.67 ± 0.18	-0.57 ± 0.26	ABS
66	0.51 ± 0.29	-0.39 ± 0.46	ABS	0.03 ± 0.46	-0.04 ± 0.45	XRB	0.26 ± 0.48	-0.31 ± 0.42	XRB	0.19 ± 0.37	-0.28 ± 0.33	XRB	0.45 ± 0.29	-0.47 ± 0.30	ABS
67	0.32 ± 0.47	-0.35 ± 0.43	XRB	0.03 ± 0.46	-0.04 ± 0.46	XRB	0.61 ± 0.11	-0.76 ± 0.07	ABS	-0.02 ± 0.44	-0.04 ± 0.40	XRB	0.37 ± 0.16	0.09 ± 0.28	XRB
68	0.50 ± 0.37	-0.53 ± 0.33	ABS	0.04 ± 0.46	-0.04 ± 0.44	XRB	0.11 ± 0.43	-0.04 ± 0.49	XRB	0.28 ± 0.24	-0.37 ± 0.24	XRB	0.02 ± 0.22	-0.42 ± 0.13	SOFT
69	-0.13 ± 0.31	-0.32 ± 0.19	XRB	-0.01 ± 0.46	-0.02 ± 0.43	XRB	0.15 ± 0.32	0.16 ± 0.52	XRB	0.24 ± 0.25	0.09 ± 0.39	XRB	0.20 ± 0.09	0.41 ± 0.14	HARD
70	0.20 ± 0.49	-0.28 ± 0.40	XRB	0.02 ± 0.48	-0.06 ± 0.44	XRB	0.02 ± 0.49	-0.08 ± 0.43	XRB	-0.75 ± 0.18	-0.04 ± 0.09	SNR	0.18 ± 0.41	-0.26 ± 0.37	XRB
71	0.30 ± 0.17	-0.57 ± 0.12	SOFT	0.00 ± 0.46	-0.02 ± 0.44	XRB	-0.16 ± 0.47	0.01 ± 0.36	XRB	0.49 ± 0.25	-0.36 ± 0.36	ABS	0.06 ± 0.35	-0.19 ± 0.28	XRB
72	0.19 ± 0.42	-0.10 ± 0.51	XRB	0.00 ± 0.47	-0.03 ± 0.44	XRB	0.16 ± 0.31	-0.37 ± 0.24	XRB	0.02 ± 0.15	-0.18 ± 0.14	XRB	0.07 ± 0.18	-0.47 ± 0.11	SOFT

Continued on next page

Table 3.2 – continued from previous page

	NGC 300			NGC 404			NGC 55			NGC 2403			NGC 4214		
No.	HR1	HR2	ID	HR1	HR2	ID	HR1	HR2	ID	HR1	HR2	ID	HR1	HR2	ID
73	0.34 ± 0.10	0.21 ± 0.19	XRB	0.07 ± 0.47	-0.08 ± 0.47	XRB	0.67 ± 0.25	-0.73 ± 0.17	ABS	-0.54 ± 0.31	-0.05 ± 0.18	SNR	0.03 ± 0.35	-0.20 ± 0.29	XRB
74	0.03 ± 0.35	0.18 ± 0.50	XRB	0.03 ± 0.46	-0.04 ± 0.45	XRB	0.50 ± 0.24	-0.63 ± 0.17	ABS	0.52 ± 0.22	-0.47 ± 0.25	ABS	0.18 ± 0.15	-0.22 ± 0.16	XRB
75	0.40 ± 0.44	-0.41 ± 0.44	ABS				0.42 ± 0.32	-0.56 ± 0.23	ABS	0.53 ± 0.33	-0.59 ± 0.26	ABS	-0.35 ± 0.34	-0.16 ± 0.21	XRB
76	-0.01 ± 0.07	0.83 ± 0.13	HARD				0.04 ± 0.16	0.58 ± 0.29	HARD	-0.74 ± 0.16	-0.06 ± 0.09	SNR	0.01 ± 0.06	0.15 ± 0.07	XRB
77	-0.41 ± 0.46	-0.04 ± 0.25	SNR				-0.65 ± 0.33	0.00 ± 0.17	SNR	-0.76 ± 0.19	0.01 ± 0.11	SNR	0.08 ± 0.05	-0.25 ± 0.04	XRB
78	0.80 ± 0.11	-0.74 ± 0.20	ABS				0.11 ± 0.45	-0.08 ± 0.48	XRB	-0.12 ± 0.04	-0.31 ± 0.03	XRB	0.23 ± 0.21	-0.54 ± 0.13	SOFT
79	-0.04 ± 0.45	-0.16 ± 0.34	XRB				0.50 ± 0.08	-0.19 ± 0.11	ABS	0.28 ± 0.13	0.30 ± 0.23	XRB	-0.76 ± 0.22	-0.03 ± 0.11	SNR
80	0.12 ± 0.02	-0.37 ± 0.02	XRB				0.41 ± 0.23	-0.59 ± 0.16	ABS	-0.05 ± 0.38	0.12 ± 0.44	XRB	0.33 ± 0.19	-0.42 ± 0.19	SOFT
81	-0.83 ± 0.16	0.00 ± 0.08	SNR				0.73 ± 0.27	-0.74 ± 0.22	ABS	0.68 ± 0.13	-0.57 ± 0.17	ABS	0.32 ± 0.18	0.12 ± 0.31	XRB
82	0.07 ± 0.37	0.07 ± 0.49	XRB				0.43 ± 0.37	-0.54 ± 0.27	ABS	0.60 ± 0.17	-0.55 ± 0.22	ABS	0.51 ± 0.12	-0.31 ± 0.12	ABS
83	0.51 ± 0.36	-0.48 ± 0.45	ABS				0.42 ± 0.10	-0.32 ± 0.12	ABS	0.38 ± 0.16	-0.55 ± 0.14	SOFT	0.01 ± 0.21	-0.45 ± 0.12	SOFT
84	0.44 ± 0.22	-0.62 ± 0.15	ABS				0.12 ± 0.26	-0.27 ± 0.23	XRB	0.40 ± 0.14	-0.39 ± 0.14	ABS	0.63 ± 0.16	-0.53 ± 0.21	ABS
85	-0.70 ± 0.16	-0.10 ± 0.09	SNR				-0.62 ± 0.28	-0.05 ± 0.15	SNR	-0.85 ± 0.10	-0.03 ± 0.05	SNR	0.56 ± 0.18	-0.33 ± 0.28	ABS
86	0.38 ± 0.12	-0.55 ± 0.12	SOFT				-0.45 ± 0.46	-0.00 ± 0.25	SNR	0.42 ± 0.07	0.03 ± 0.12	ABS	-0.52 ± 0.33	-0.09 ± 0.19	SNR
87	0.22 ± 0.17	-0.53 ± 0.11	SOFT				0.22 ± 0.33	-0.38 ± 0.25	XRB	0.65 ± 0.14	-0.51 ± 0.19	ABS	0.12 ± 0.24	0.18 ± 0.34	XRB
88	0.47 ± 0.33	-0.53 ± 0.29	ABS				-0.01 ± 0.50	-0.10 ± 0.40	XRB	0.47 ± 0.15	-0.35 ± 0.18	ABS	0.04 ± 0.16	-0.35 ± 0.12	XRB
89	0.42 ± 0.10	-0.52 ± 0.11	ABS				0.37 ± 0.18	-0.21 ± 0.21	XRB	0.45 ± 0.16	-0.40 ± 0.18	ABS	0.28 ± 0.40	-0.41 ± 0.32	SOFT
90	0.41 ± 0.24	-0.57 ± 0.19	ABS				0.15 ± 0.18	-0.40 ± 0.16	XRB	0.14 ± 0.14	-0.34 ± 0.13	XRB	0.14 ± 0.12	-0.15 ± 0.12	XRB
91	0.33 ± 0.25	-0.39 ± 0.26	XRB				0.41 ± 0.05	0.01 ± 0.07	ABS	0.18 ± 0.26	-0.46 ± 0.18	SOFT	0.37 ± 0.33	-0.41 ± 0.31	SOFT
92	0.35 ± 0.39	-0.51 ± 0.26	SOFT				-0.00 ± 0.39	0.11 ± 0.48	XRB	0.26 ± 0.01	-0.23 ± 0.01	XRB	-0.67 ± 0.30	-0.00 ± 0.15	SNR
93	0.28 ± 0.45	-0.26 ± 0.48	XRB				-0.03 ± 0.50	-0.11 ± 0.39	XRB	-0.76 ± 0.21	-0.02 ± 0.11	SNR	0.50 ± 0.08	-0.31 ± 0.10	ABS
94	0.59 ± 0.19	-0.59 ± 0.21	ABS				0.16 ± 0.53	-0.28 ± 0.40	XRB	0.42 ± 0.07	0.05 ± 0.12	ABS	-0.27 ± 0.24	-0.29 ± 0.14	XRB
95	-0.21 ± 0.48	-0.04 ± 0.33	XRB				0.40 ± 0.08	-0.29 ± 0.10	XRB	-0.17 ± 0.41	-0.26 ± 0.24	XRB	0.18 ± 0.33	0.06 ± 0.50	XRB
96							0.03 ± 0.46	-0.16 ± 0.38	XRB	-0.70 ± 0.08	-0.12 ± 0.05	SNR	0.09 ± 0.42	-0.08 ± 0.44	XRB
97							0.62 ± 0.17	-0.63 ± 0.16	ABS	-0.30 ± 0.10	-0.30 ± 0.06	XRB	0.14 ± 0.47	-0.25 ± 0.37	XRB
98							0.07 ± 0.29	-0.30 ± 0.23	XRB	0.07 ± 0.27	-0.38 ± 0.19	XRB	0.49 ± 0.25	-0.43 ± 0.29	ABS
99							-0.03 ± 0.50	-0.10 ± 0.40	XRB	0.43 ± 0.32	-0.56 ± 0.23	ABS	-0.68 ± 0.22	0.05 ± 0.15	SNR
100							-0.06 ± 0.49	-0.07 ± 0.39	XRB	0.56 ± 0.23	-0.53 ± 0.29	ABS	0.03 ± 0.23	0.46 ± 0.42	HARD
101							0.37 ± 0.44	-0.38 ± 0.43	XRB	-0.37 ± 0.31	0.25 ± 0.27	XRB	0.50 ± 0.19	-0.28 ± 0.28	ABS
102							0.62 ± 0.24	-0.67 ± 0.19	ABS	0.63 ± 0.26	-0.67 ± 0.20	ABS	0.35 ± 0.20	-0.05 ± 0.29	XRB
103							0.61 ± 0.22	-0.71 ± 0.15	ABS	0.36 ± 0.20	0.02 ± 0.32	XRB	-0.60 ± 0.25	-0.13 ± 0.13	SNR
104							0.36 ± 0.18	-0.55 ± 0.14	SOFT	0.43 ± 0.23	-0.55 ± 0.19	ABS	0.19 ± 0.15	-0.04 ± 0.18	XRB
105							0.33 ± 0.26	-0.45 ± 0.22	SOFT	0.06 ± 0.15	-0.33 ± 0.14	XRB	0.35 ± 0.18	-0.33 ± 0.21	XRB
106							0.08 ± 0.15	0.61 ± 0.27	HARD	0.31 ± 0.05	-0.34 ± 0.05	XRB	0.20 ± 0.50	-0.30 ± 0.39	XRB
107							0.46 ± 0.16	-0.44 ± 0.18	ABS	0.40 ± 0.22	-0.21 ± 0.31	XRB	0.20 ± 0.25	0.09 ± 0.34	XRB
108							0.19 ± 0.25	0.14 ± 0.38	XRB	0.35 ± 0.20	-0.05 ± 0.31	XRB	0.04 ± 0.15	-0.32 ± 0.14	XRB
109							-0.13 ± 0.47	-0.00 ± 0.01	XRB	0.31 ± 0.09	-0.25 ± 0.10	XRB	0.21 ± 0.12	-0.27 ± 0.12	XRB

Continued on next page

Table 3.2 – continued from previous page

	NGC 300			NGC 404			NGC 55			NGC 2403			NGC 4214		
No.	HR1	HR2	ID	HR1	HR2	ID	HR1	HR2	ID	HR1	HR2	ID	HR1	HR2	ID
110							0.16 ± 0.07	-0.33 ± 0.06	XRB	0.31 ± 0.51	-0.31 ± 0.50	XRB	-0.03 ± 0.09	0.14 ± 0.13	XRB
111							0.32 ± 0.08	-0.46 ± 0.07	SOFT	0.36 ± 0.24	-0.39 ± 0.27	XRB	-0.09 ± 0.12	0.59 ± 0.15	HARD
112							0.32 ± 0.17	0.09 ± 0.27	XRB	-0.62 ± 0.24	-0.07 ± 0.14	SNR	-0.06 ± 0.17	0.48 ± 0.23	HARD
113							0.46 ± 0.20	-0.30 ± 0.28	ABS	-0.21 ± 0.44	0.00 ± 0.34	XRB	0.31 ± 0.27	-0.56 ± 0.16	SOFT
114							0.24 ± 0.31	-0.38 ± 0.26	XRB	0.42 ± 0.09	-0.27 ± 0.12	ABS	0.49 ± 0.17	-0.53 ± 0.18	ABS
115							-0.19 ± 0.30	-0.12 ± 0.25	XRB	0.27 ± 0.12	-0.03 ± 0.16	XRB	0.22 ± 0.47	-0.27 ± 0.42	XRB
116							0.14 ± 0.46	-0.13 ± 0.47	XRB	0.29 ± 0.28	-0.44 ± 0.23	SOFT	-0.89 ± 0.10	-0.02 ± 0.05	SNR
117							-0.06 ± 0.41	-0.19 ± 0.30	XRB	0.47 ± 0.08	-0.09 ± 0.14	ABS			
118							0.69 ± 0.09	-0.45 ± 0.18	ABS	-0.62 ± 0.28	-0.08 ± 0.15	SNR			
119							0.19 ± 0.01	-0.48 ± 0.01	SOFT	0.46 ± 0.10	-0.38 ± 0.12	ABS			
120							0.30 ± 0.22	0.09 ± 0.34	XRB	0.07 ± 0.24	-0.45 ± 0.15	SOFT			
121							0.19 ± 0.12	0.41 ± 0.21	HARD	-0.20 ± 0.12	-0.11 ± 0.10	XRB			
122							0.32 ± 0.02	-0.21 ± 0.02	XRB	0.34 ± 0.07	-0.19 ± 0.09	XRB			
123							0.05 ± 0.24	0.43 ± 0.47	HARD	0.14 ± 0.47	-0.26 ± 0.38	XRB			
124							0.57 ± 0.10	-0.24 ± 0.18	ABS	0.41 ± 0.09	0.07 ± 0.16	ABS			
125							-0.73 ± 0.16	0.02 ± 0.11	SNR	0.68 ± 0.20	-0.70 ± 0.19	ABS			
126							0.06 ± 0.04	0.80 ± 0.07	HARD	0.62 ± 0.10	-0.33 ± 0.17	ABS			
127							-0.61 ± 0.24	-0.03 ± 0.15	SNR	0.40 ± 0.35	-0.45 ± 0.31	SOFT			
128							0.35 ± 0.13	-0.19 ± 0.16	XRB	0.41 ± 0.08	-0.47 ± 0.07	ABS			
129							0.65 ± 0.11	-0.47 ± 0.16	ABS	-0.50 ± 0.21	-0.19 ± 0.12	SNR			
130							-0.48 ± 0.09	-0.24 ± 0.05	SNR	0.30 ± 0.06	-0.31 ± 0.06	XRB			
131							-0.61 ± 0.24	-0.08 ± 0.14	SNR	0.55 ± 0.15	-0.59 ± 0.15	ABS			
132							-0.21 ± 0.50	-0.04 ± 0.33	XRB	-0.83 ± 0.09	-0.06 ± 0.05	SNR			
133							-0.33 ± 0.43	-0.03 ± 0.28	XRB	-0.98 ± 0.02	0.00 ± 0.01	SNR			
134							0.26 ± 0.37	-0.44 ± 0.26	SOFT	0.36 ± 0.42	-0.33 ± 0.47	XRB			
135							0.24 ± 0.06	-0.49 ± 0.05	SOFT	0.03 ± 0.03	-0.31 ± 0.02	XRB			
136							0.24 ± 0.29	0.10 ± 0.49	XRB	0.01 ± 0.09	-0.24 ± 0.08	XRB			
137							0.48 ± 0.09	-0.51 ± 0.10	ABS	0.53 ± 0.14	-0.19 ± 0.25	ABS			
138							0.46 ± 0.36	-0.44 ± 0.41	ABS	0.20 ± 0.21	-0.47 ± 0.15	SOFT			
139							0.40 ± 0.13	0.03 ± 0.23	ABS	-0.56 ± 0.36	-0.05 ± 0.19	SNR			
140							0.25 ± 0.46	-0.38 ± 0.34	XRB	0.40 ± 0.05	-0.32 ± 0.06	XRB			
141							-0.06 ± 0.42	-0.18 ± 0.32	XRB	0.27 ± 0.08	0.37 ± 0.14	XRB			
142							-0.27 ± 0.24	0.12 ± 0.24	XRB	0.38 ± 0.12	0.06 ± 0.20	XRB			
143							0.32 ± 0.18	0.15 ± 0.32	XRB	0.44 ± 0.20	-0.15 ± 0.36	ABS			
144							-0.13 ± 0.26	-0.30 ± 0.17	XRB	-0.56 ± 0.33	-0.00 ± 0.19	SNR			
145							0.37 ± 0.07	-0.18 ± 0.09	XRB	0.43 ± 0.13	-0.42 ± 0.13	ABS			
146							0.07 ± 0.29	-0.09 ± 0.32	XRB	-0.35 ± 0.15	-0.24 ± 0.10	XRB			

Continued on next page

Table 3.2 – continued from previous page

	NGC 300			NGC 404			NGC 55			NGC 2403			NGC 4214		
No.	HR1	HR2	ID	HR1	HR2	ID	HR1	HR2	ID	HR1	HR2	ID	HR1	HR2	ID
147							0.12 ± 0.11	-0.28 ± 0.09	XRB	0.35 ± 0.29	-0.07 ± 0.46	XRB			
148							-0.44 ± 0.34	0.10 ± 0.26	SNR	0.07 ± 0.14	0.66 ± 0.29	HARD			
149							0.29 ± 0.34	-0.29 ± 0.37	XRB	0.33 ± 0.38	-0.55 ± 0.22	SOFT			
150							0.33 ± 0.38	-0.38 ± 0.34	XRB	0.38 ± 0.34	-0.39 ± 0.35	XRB			
151							0.33 ± 0.09	-0.31 ± 0.11	XRB	0.28 ± 0.16	-0.45 ± 0.17	SOFT			
152							0.52 ± 0.11	-0.31 ± 0.15	ABS	0.45 ± 0.10	-0.18 ± 0.13	ABS			
153							0.56 ± 0.14	-0.31 ± 0.22	ABS	-0.22 ± 0.20	-0.30 ± 0.12	XRB			
154							0.24 ± 0.40	-0.14 ± 0.50	XRB	0.29 ± 0.22	0.09 ± 0.37	XRB			
155										0.35 ± 0.02	-0.07 ± 0.03	XRB			
156										0.40 ± 0.21	-0.56 ± 0.17	SOFT			
157										0.16 ± 0.06	-0.41 ± 0.05	SOFT			
158										-0.88 ± 0.11	0.00 ± 0.06	SNR			
159										0.16 ± 0.25	0.34 ± 0.45	XRB			
160										0.47 ± 0.23	-0.40 ± 0.29	ABS			
161										0.10 ± 0.18	-0.22 ± 0.19	XRB			
162										0.03 ± 0.03	-0.30 ± 0.02	XRB			
163										0.32 ± 0.19	0.01 ± 0.27	XRB			
164										0.09 ± 0.12	-0.12 ± 0.12	XRB			
165										0.05 ± 0.08	-0.34 ± 0.06	XRB			
166										-0.57 ± 0.18	0.18 ± 0.17	SNR			
167										0.34 ± 0.23	-0.50 ± 0.18	SOFT			
168										-0.49 ± 0.24	-0.14 ± 0.14	SNR			
169										-0.99 ± 0.01	-0.00 ± 0.00	SNR			
170										0.31 ± 0.03	-0.32 ± 0.03	XRB			
171										0.40 ± 0.07	0.15 ± 0.13	ABS			
172										0.57 ± 0.19	-0.47 ± 0.26	ABS			
173										0.24 ± 0.13	-0.43 ± 0.12	SOFT			
174										0.27 ± 0.04	-0.33 ± 0.04	XRB			
175										-0.65 ± 0.16	-0.12 ± 0.09	SNR			
176										-0.02 ± 0.23	0.51 ± 0.40	HARD			
177										0.51 ± 0.10	-0.35 ± 0.12	ABS			
178										0.02 ± 0.23	0.34 ± 0.30	XRB			
179										0.45 ± 0.02	-0.34 ± 0.02	ABS			
180										-0.05 ± 0.18	-0.08 ± 0.18	XRB			
181										-0.69 ± 0.21	-0.03 ± 0.12	SNR			
182										0.35 ± 0.09	-0.51 ± 0.09	SOFT			
183										0.61 ± 0.26	-0.64 ± 0.22	ABS			

Continued on next page

Table 3.2 – continued from previous page

	NGC 300			NGC 404			NGC 55			NGC 2403			NGC 4214		
No.	HR1	HR2	ID	HR1	HR2	ID	HR1	HR2	ID	HR1	HR2	ID	HR1	HR2	ID
184										-0.07 ± 0.26	-0.02 ± 0.26	XRB			
185										0.63 ± 0.11	-0.44 ± 0.16	ABS			
186										0.06 ± 0.14	-0.47 ± 0.09	SOFT			
187										-0.98 ± 0.02	-0.00 ± 0.01	SNR			
188										0.28 ± 0.15	-0.47 ± 0.15	SOFT			
189										-0.31 ± 0.48	-0.02 ± 0.29	XRB			
190										0.08 ± 0.18	-0.35 ± 0.15	XRB			

Figure 3.2 hints at some differences in the X-ray source populations of the five CLVS galaxies. For example, NGC 404 (cyan dots) shows significantly fewer sources in the 'SNR'-like category than the disk galaxies. This is not surprising, as one would not expect to find true SNRs in the older stellar populations and earlier morphology of NGC 404. The three 'SNR'-like sources in NGC 404 are likely foreground stars, whose soft thermal emission is easily confused with that of a true SNR in hardness ratio analysis.

To compare the X-ray source populations of the five CLVS galaxies in a quantitative manner, we calculate the fraction of each HR class found for each galaxy and for the total 629 X-ray sources, given in Table 3.3. We find that most of the X-ray sources fall within the 'XRB' category ($\sim 40-60\%$), with an additional $\sim 20-30\%$ of sources showing evidence for additional absorption beyond the Galactic column. These two categories comprise roughly three quarters of all the X-ray point sources and are likely contain the majority of XRBs associated with their host galaxies with some contamination from background AGN (whose X-ray properties are similar to many XRBs). We note that NGC 404 contains a higher fraction of sources classified as 'XRBs' than the disk galaxies, deviating from the sample average 'XRB' percentage at about the $\sim 1.6\sigma$ level.

The softer HR categories (i.e., 'SNR' and 'SOFT') likely contain contamination by foreground stars. This is especially true for the $\sim$4% X-ray sources in NGC 404 designated as 'SNR'-like by their hardness ratios. The fraction of 'SNR'-type sources in NGC 404 is below the sample average by more than 3σ, as would be expected when comparing an S0-type galaxy with very little recent star formation with the later-type spirals and irregulars. 'SOFT' sources are observed in comparable fractions to 'SNR'-like sources, and may consist of very soft XRBs, background sources with unusual absorption properties, or foreground objects. Only a small fraction of X-ray sources, $\sim 1-4\%$, are classified as 'HARD.' These sources are likely background AGN that have experienced a high degree of absorption.

The information in Table 3.3 is represented graphically in Figure 3.3. The relatively high fraction of 'XRB'-type sources and deficit of 'SNR'-like sources in NGC 404 is easily observable in this figure.

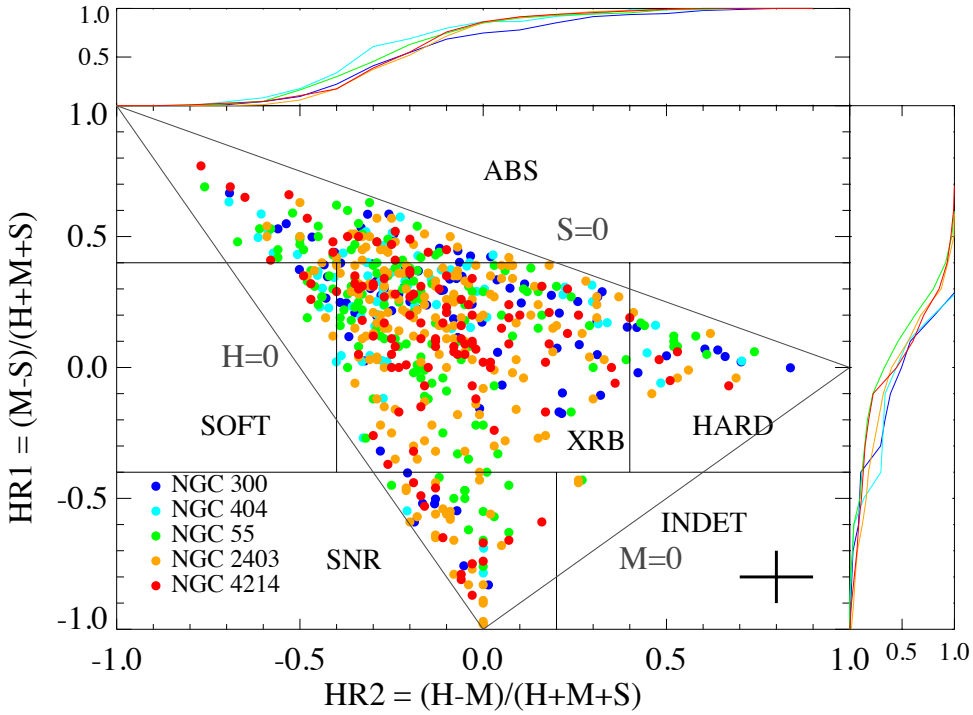

Figure 3.2: X-ray color-color diagram of all X-ray sources detected in the five CLVS galaxies. The thick cross in the lower-right corner shows the typical size of the errors. The diagram has been broken into preliminary source identification regions. The regions are labeled as: 'ABS' for absorbed sources, 'XRB' for X-ray binaries, 'SNR' for supernova remnants, 'SOFT' for indeterminate soft sources, 'HARD' for indeterminate hard sources, and 'INDET' for sources with an indeterminate spectral shape (although we do not observe any sources in this category). The gray lines indicate the zero-count limits in the hard ('H'), medium ('M'), and soft ('S') bands. The top and right panels show the cumulative fraction of sources at each HR for each of the five galaxies.

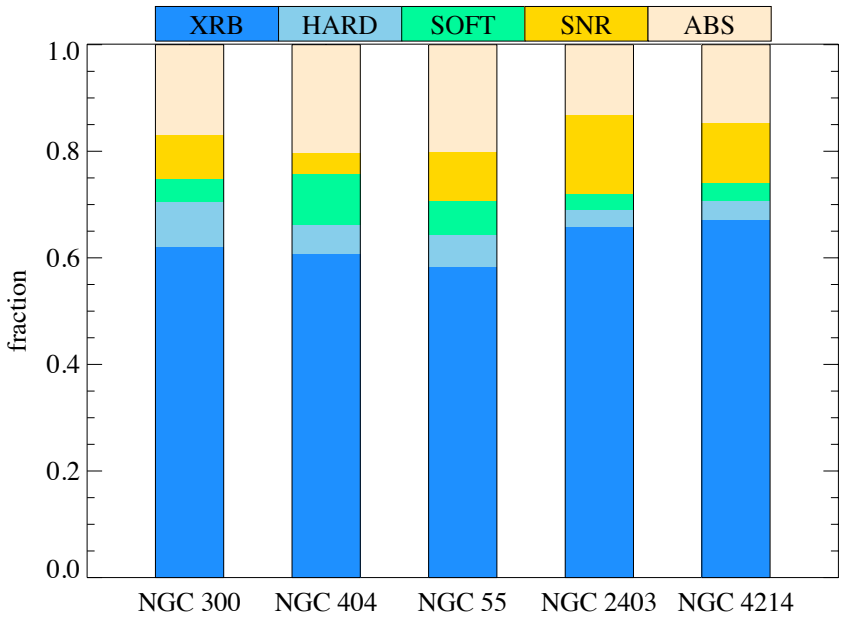

Figure 3.3: The percentage of preliminary X-ray source classifications based on hardness ratios (Table 3.3) for each galaxy.

Table 3.3: Percentage (%) of Preliminary Classifications Based on Hardness Ratio Analysis

Galaxy	XRB	HARD	SOFT	SNR	ABS
(1)	(2)	(3)	(4)	(5)	(6)
NGC 55	49.4±3.4	3.9±0.3	9.7±0.8	9.1±0.7	27.9±2.3
NGC 300	41.1±4.2	2.1±0.2	13.7±1.4	11.6±1.2	31.6±3.2
NGC 404	63.5±7.4	1.4±0.2	9.5±1.1	4.1±0.5	21.6±2.5
NGC 2403	40.5±2.9	1.6±0.1	11.1±0.8	18.9±1.4	28.9±2.1
NGC 4214	50.9±4.7	4.3±0.4	12.1±1.1	13.8±1.3	19.0±1.8
Total	47.5±9.8	2.7±0.6	11.0±2.3	12.6±2.7	26.2±5.5

3.1.2 Radial Source Distributions

We assign an inclination-corrected galactocentric distance to each X-ray sources assuming the RA, Dec, inclination angle, and position angle for each galaxy. The X-ray sources are then divided into radial bins based on their inclination-corrected distance from the center of each galaxy, with bins spaced ∼0.5-1 kpc apart. We use the cumulative log$N$-log$S$ distribution of [56] to estimate the expected contamination by background AGN, which should be nearly flat with galactocentric radius. The radial X-ray source distributions are shown in Figure 3.4, and clearly shows that the number of X-ray sources per square kiloparsec decreases with galactocentric radius for all five galaxies.

The late-type galaxies in the sample (NGC 300, NGC 55, NGC 2403, and NGC 4214) do not possess substantial bulges, allowing the background-subtracted radial X-ray source distributions to be modeled with a simple exponential profile, given by

$$\mathcal{N}_X(r) = \mathcal{N}_0 e^{-r/r_x} + C, \tag{3.3}$$

where $\mathcal{N}_X(r)$ is the number of X-ray sources per kpc^2 expected at a given galactocentric radius r (in kpc), $\mathcal{N}_0$ is the "core" X-ray source surface density, and r_x is the X-ray scale length of the sources. For the S0 galaxy NGC 404, we assumed a de Vaucoulers profile,

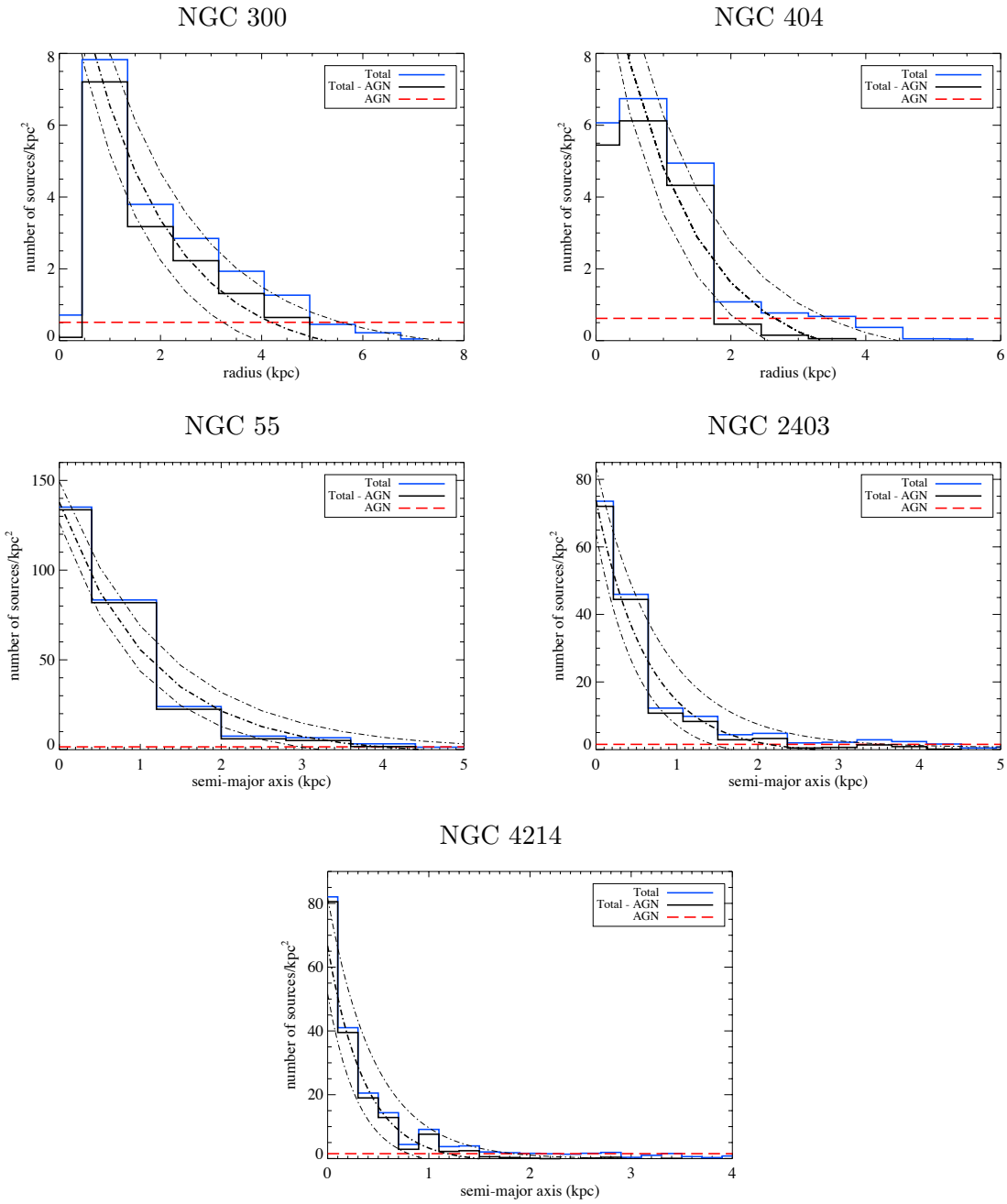

Figure 3.4: Radial source distributions. The total distributions (e.g., for all X-ray sources) is shown in blue. Red shows the expected contribution from background AGN, and blue shows the radial source distribution corrected for AGN contamination. The thick dot-dashed lines show the best fit radial source density profile and the 1σ errors. Top row: NGC 300 and NGC 404. Middle row: NGC 55 and NGC 2403. Bottom: NGC 4214.

Table 3.4: X-ray Radial Source Distribution Scale Lengths

Galaxy	X-ray scale length (kpc)	r_{90} (kpc)	Optical scale length (kpc)	Reference
(1)	(2)	(3)	(4)	(5)
NGC 55	0.9±0.1	2.2	0.96	[364]
NGC 300	1.7±0.2	4.0	1.3	[153], [286]
NGC 404	0.9±0.3	1.8	0.9	[11]
NGC 2403	1.6±0.3	3.9	1.7	[13]
NGC 4214	0.9±0.2	1.4	0.6	[446]

$$\mathcal{N}_{dV}(r) = \mathcal{N}_e e^{-7.669\left[\left(\frac{r}{r_e}\right)^{1/4}-1\right]} + D, \tag{3.4}$$

where now $\mathcal{N}_{dV}(r)$ is the number of X-ray sources per kpc^2, $\mathcal{N}_e$ is the effective X-ray source surface density, and r_e is the effective radius.

The X-ray scale lengths (or, in the case of NGC 404, the effect radius; summarized in Table 3.4) are remarkably consistent with the optical scale lengths found for each galaxy. [364] found an optical scale length of 0.96 kpc for NGC 55, while NGC 2403 has a scale length of 1.7 kpc [13]. NGC 4214 was found to have a scale length of 0.6 kpc by [446], and [11] reported an effective bulge radius of NGC 404 of 0.9 kpc. The optical scale length of NGC 300 is 1.3±0.1 kpc scale length found by [153], in agreement with estimates derived from the K-band surface brightness [284].

The X-ray point source populations of the CLVS galaxies (corrected for contamination by background AGN) appears to follow the underlying stellar population of each galaxy. In Figure 3.5, we plot our X-ray scale length against the optical scale lengths found in the literature. The best-fit line through the data yields a slope of 0.99±0.08, and a Spearman-Rank test yields only a 3.7% probability of the X-ray and optical scale lengths being drawn from different distributions.

Using the optical scale lengths from the literature and assuming an exponential disk,

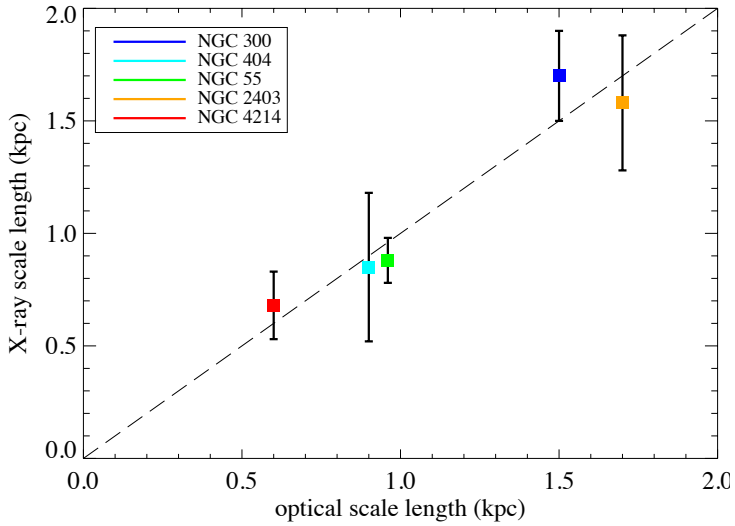

Figure 3.5: Our derived X-ray scale lengths, derived from the radial source distribution for each galaxy, plotted against the optical scale lengths from the literature. The dashed line shows a one-to-one correlation.

we define for each galaxy a radius r_{90} at which we expect to enclose 90% of the stars. At galactocentric distances larger than r_{90}, we expect the X-ray source population to be dominated by background or foreground sources. Roughly $\sim 40-60\%$ of the discrete X-ray sources observed for each galaxy have $r > r_{90}$, consistent with the $\sim 45-50\%$ contamination by background AGN predicted by the [56] AGN log$N$-log$S$ distribution.

3.2 Individual Source Properties

We next examined the X-ray properties the CLVS sources on a more individual level. This included performing spectral fitting for the brightest sources and searching for X-ray source variability.

3.2.1 X-ray Spectral Analysis

For sufficiently bright sources (>50 counts), the X-ray spectrum of a source can constrain the physical origin of the X-ray emission. Both XRBs and AGN are typically described by

power laws, with photon indices ranging from $\Gamma \sim 1-2$. If the source is a likely XRB, the photon index can sometimes be used to constrain the nature of the compact object: NS primaries typically exhibit harder X-ray emission, with $\Gamma < 1.5$, while BHs produce $\Gamma \sim$2-2.5 or softer due to the lack of a solid surface [268]. Foreground stars and SNRs exhibit significantly softer X-ray emission with emission lines indicative of a thermal plasma.

Spectra were extracted for sources with >50 counts by `AE` using the CIAO tool `dmextract`, and response products were created using `mkacisrmf` and `mkarf`. Due to the low number of counts found for most of the sources in our catalogs, we fit spectral models to the unbinned spectra and use C-statistics in lieu of traditional χ^2 statistics [see e.g., 61, 192]. The ungrouped spectra of 104 sources (16 in NGC 300, 23 in NGC 404, 11 in NGC 55, 40 in NGC 2403, and 14 in NGC 4214) were automatically fit in `XSPEC` with one of four models: a power-law model or an `APEC` model [382] with only absorption due to the Galactic column, or a power-law or thermal model with additional absorption. The Galactic absorption was modeled with the `tbabs` model [450]. The best-fit model and parameters for sources with greater than 50 net counts are listed in Table 3.5. All errors represent the 90% uncertainties. The background emission was modeled simultaneously using the `AE` model `cplinear`, which is more appropriate when the C-statistic is used [49].

Because the C-statistic cannot be directly interpreted as a goodness-of-fit, we use a different approach to select the preferred spectral model for each source. We first rejected those models that predicted unreasonably high photon indices ($\Gamma > 4$) or plasma temperatures (kT >6 keV). We next used the `XSPEC` v12.6.0z `goodness` command to perform 5,000 Monte Carlo simulations for each spectral model (power law and thermal models, both with Galactic absorption only and with additional absorption beyond the Galactic column). The `goodness` command simulates spectra based on the model parameters and finds the number of simulations with a fit statistic less than that found for the data. If the observed spectrum was produced by that model, the "goodness" should be ∼50%. For some sources, the choice of preferred spectral model was obvious: three of the spectral models yielded a goodness of less than ∼2%, while one model produced a goodness in the range of $\sim 40-60$%. Where no obviously preferred model was found, we chose the simple power law (absorbed only by the Galactic column) unless the spectrum showed indications for emission features (in which

case, the unabsorbed thermal model was selected).

Table 3.5: Best-Fit Spectral Models for X-ray Sources with More Than 50 Counts

Source No.	Best-fit[a] Model	$N_{\rm H}$ [b] (10^{21} cm^{-2})	Γ	kT (keV)	C/dof[c]	f_X^d (0.5-2 keV) (10^{-15} erg s^{-1} cm^{-2})	f_X^e (0.5-8 keV) (10^{-15} erg s^{-1} cm^{-2})	"goodness[f]" (%)
(1)	(2)	(3)	(4)	(5)	(6)	(7)	(8)	(9)
				NGC 300				
3	pow	...	1.7±0.3	...	576/1016	6.9±2.3	$17.8^{+6.9}_{-4.4}$	45
11	pow	...	1.5±0.4	...	626/1016	5.5±1.5	$16.8^{+4.6}_{-3.8}$	83
23	pow	$0.7^{+0.6}_{-0.4}$	$2.2^{+0.9}_{-0.7}$	...	464/1016	$5.7^{+2.3}_{-1.9}$	$21.6^{+8.8}_{-6.9}$	33
24	apec	...	...	$4.8^{+20.7}_{-2.7}$	751/1016	$7.1^{+1.9}_{-6.5}$	$16.6^{+3.8}_{-8.0}$	98
25	pow	<0.4	$2.3^{+1.4}_{-0.7}$	...	385/1016	$6.7^{+4.0}_{-2.1}$	$13.0^{+8.0}_{-4.0}$	55
28	pow	<0.4	1.4±0.2	...	439/1016	5.0±1.5	$17.2^{+5.7}_{-4.2}$	45
33	pow	$0.2^{+0.5}_{-0.2}$	$1.8^{+0.9}_{-0.7}$	...	680/1015	$15.5^{+5.5}_{-14.7}$	$35.0^{+6.9}_{-22.0}$	55
35	pow	$1.1^{+1.0}_{-0.5}$	$1.3^{+0.7}_{-0.4}$	...	707/1016	$15.5^{+2.1}_{-5.9}$	$57.7^{+12.8}_{-22.9}$	41
39	pow	...	1.5±0.4	...	590/1016	$5.2^{+1.5}_{-1.0}$	$16.1^{+5.2}_{-3.8}$	64
43	apec	...	...	0.4±0.1	456/1016	$14.3^{+2.5}_{-3.6}$	$14.2^{+2.5}_{-2.9}$	67
50	pow	...	1.6±0.3	...	631/1016	$9.2^{+1.7}_{-1.9}$	$25.8^{+6.3}_{-4.4}$	92
52	pow	$0.9^{+0.9}_{-0.6}$	$2.5^{+1.7}_{-1.1}$	...	391/1016	$3.4^{+2.3}_{-1.5}$	$12.0^{+8.2}_{-5.2}$	56
53	pow	<0.3	$2.1^{+1.0}_{-0.4}$	...	380/1016	$7.3^{+3.6}_{-1.5}$	$14.1^{+6.7}_{-2.7}$	53
87	apec	< 0.2	...	$2.6^{+1.5}_{-0.8}$	371/1016	$5.7^{+3.4}_{-1.7}$	$10.5^{+6.1}_{-3.1}$	73
89	pow	$0.3^{+0.4}_{-0.3}$	$2.4^{+0.6}_{-0.5}$	...	565/1015	$36.3^{+8.4}_{-25.2}$	$58.1^{+14.7}_{-26.6}$	71
95	apec	...	...	$0.6^{+0.8}_{-0.3}$	541/1016	$1.5^{+6.3}_{-1.3}$	$1.5^{+1.0}_{-1.3}$	99
				NGC 404				
1	pow	...	$1.65^{+0.12}_{-0.11}$	...	496/510	$41.1^{+1.5}_{-1.4}$	$73.4^{+5.2}_{-4.1}$	34
2	pow	...	0.6±0.3	...	943/1015	$3.8^{+0.7}_{-2.9}$	$31.1^{+6.2}_{-13.6}$	88
3	pow	...	1.5±0.4	...	819/1016	$1.6^{+0.5}_{-0.4}$	$4.8^{+1.9}_{-1.3}$	0.4
7	pow	...	1.8±0.1	...	414/510	$65.6^{+7.3}_{-8.3}$	$40.7^{+4.6}_{-4.0}$	58
11	pow	...	0.8±0.4	...	964/1016	$0.9^{+0.4}_{-0.3}$	$5.5^{+3.9}_{-1.7}$	12
13	pow	...	1.2±0.3	...	953/1016	1.8±0.4	$7.3^{+1.7}_{-1.8}$	25
17	pow	...	1.9±0.2	...	796/1016	$5.0^{+0.7}_{-0.6}$	$10.8^{+2.0}_{-1.5}$	60
20	pow	...	1.5±0.3	...	671/1016	$1.6^{+0.2}_{-0.4}$	$5.0^{+1.8}_{-1.0}$	2
32	apec	...	...	0.8±0.1	128/521	$8.6^{+0.3}_{-0.5}$	$9.0^{+0.2}_{-0.3}$	63
35	apec	$3.71^{+1.30}_{-1.10}$	...	$2.8^{+3.2}_{-1.0}$	830/1015	$12.2^{+2.2}_{-3.6}$	$19.4^{+2.6}_{-10.1}$	95
39	pow	...	1.4±0.3	...	718/1016	1.5±0.2	$4.8^{+1.4}_{-1.1}$	66
41	pow	...	2.1±0.2	...	657/1016	$4.3^{+0.6}_{-0.3}$	$8.0^{+1.1}_{-1.0}$	82
45	pow	...	1.6±0.4	...	543/1016	$0.9^{+0.3}_{-0.2}$	$2.4^{+0.9}_{-0.6}$	0.1
46	pow	...	1.4±0.2	...	823/1016	$2.7^{+0.4}_{-0.5}$	$8.7^{+1.8}_{-1.5}$	33
55	pow	...	0.9±0.3	...	846/1016	0.9±0.3	$5.5^{+1.5}_{-1.3}$	62

Continued on next page

Table 3.5 – continued from previous page

Source No.	Best-fit[a] Model	$N_{\rm H}$ [b] (10^{21} cm^{-2})	Γ	kT (keV)	C/dof[c]	f_X^d (0.5-2 keV) (10^{-15} erg s^{-1} cm^{-2})	f_X^e (0.5-8 keV) (10^{-15} erg s^{-1} cm^{-2})	"goodness[f]" (%)
(1)	(2)	(3)	(4)	(5)	(6)	(7)	(8)	(9)
58	pow	...	$1.5^{+0.4}_{-0.3}$	...	762/1016	1.1±0.3	$3.3^{+1.5}_{-0.8}$	29
64	pow	...	1.8±0.4	...	781/1016	$1.3^{+0.4}_{-0.2}$	$3.0^{+1.2}_{-0.7}$	55
65	apec	...	...	$0.57^{+0.03}_{-0.04}$	106/98	$40.5^{+2.3}_{-2.4}$	$41.2^{+1.5}_{-1.9}$	32
67	pow	...	1.2±0.5	...	924/1016	1.1±0.3	$4.7^{+2.0}_{-1.4}$	49
68	pow	...	1.2±0.4	...	992/1016	1.5±0.4	$6.4^{+3.2}_{-1.7}$	34
70	pow	...	1.8±0.5	...	899/1016	1.9±0.4	$4.3^{+1.4}_{-0.8}$	41
72	pow	...	1.7±0.4	...	1071/1016	$2.3^{+0.6}_{-0.5}$	$5.8^{+3.2}_{-1.2}$	54
73	pow	...	1.1±0.3	...	1109/1016	$3.0^{+0.7}_{-0.5}$	$13.1^{+3.3}_{-2.7}$	72
				NGC 55				
23	apec+apec	...	...	0.32±0.02, 1.27±0.03	455/519	270.4±18.1	330.6±22.1	99
44	pow	$1.1^{+1.7}_{-0.8}$	$1.52^{+0.36}_{-0.34}$	...	354/521	$134.2^{+11.1}_{-16.6}$	$418.7^{+42.1}_{-71.7}$	41
54	pow	1.4±1.0	$1.39^{+0.20}_{-0.25}$	...	428/520	$35.1^{+30.3}_{-25.7}$	$1202.2^{+180.8}_{-96.2}$	14
62	pow	3.0±0.5	1.56±0.11	...	525/520	$180.3^{+22.1}_{-94.1}$	$530.9^{+81.4}_{-370.1}$	44
63	brems	1.4±0.3	...	$2.0^{+0.2}_{-0.1}$	435/520	$360.7^{+36.2}_{-18.1}$	$641.2^{+58.3}_{-32.9}$	39
67	pow	...	1.6±0.2	...	793/1016	$9.1^{+1.9}_{-1.7}$	$24.8^{+4.4}_{-4.2}$	66
119	disk+pow	$1.8^{+1.4}_{-0.2}$	$2.72^{+0.72}_{-0.69}$	$0.36^{+0.02}_{-0.03}$	426/516	$1860.8^{+1787.9}_{-1165.2}$	$2571.2^{+5670.6}_{-3678.1}$	89
122	apec	1.3±0.5	...	1.4±0.1	500/520	$120.2^{+8.6}_{-6.9}$	$390.6^{+27.4}_{-23.6}$	34
128	apec	...	...	<8.9	614/1016	$4.8^{+1.3}_{-4.6}$	$13.7^{+2.5}_{-13.5}$	35
135	pow	2.3±1.3	2.8±0.4	...	294/520	55.1±32.1	100.2±58.4	37
151	pow	...	$1.3^{+0.3}_{-0.3}$	...	538/1016	$6.3^{+1.3}_{-1.0}$	$23.2^{+7.0}_{-4.6}$	36
				NGC 2403				
2	pow	...	1.70±0.09	...	540/521	9.6±0.5	24.4±1.9	99
11	apec	...	...	$2.73^{+1.9}_{-0.7}$	1063/1016	$5.2^{+0.8}_{-0.6}$	$9.6^{+1.9}_{-2.6}$	63
19	apec	...	...	$2.58^{+1.9}_{-0.8}$	591/1016	$1.9^{+0.4}_{-0.3}$	$3.4^{+0.7}_{-0.8}$	18
20	apec	...	...	$2.41^{+0.6}_{-0.5}$	622/1016	2.2±0.2	$3.8^{+0.3}_{-0.5}$	67
23	pow	<0.1	1.9±1.9	...	889/1015	$1.1^{+0.8}_{-1.1}$	$2.2^{+1.1}_{-2.2}$	30
31	apec	...	...	5.6±5.6	725/1016	$2.7^{+0.7}_{-2.5}$	$6.6^{+2.5}_{-6.4}$	29
41	pow	2.5±0.1	1.87±0.05	...	646/520	175.8±48.8	$488.8^{+19.3}_{-15.4}$	100
42	pow	4.0±0.2	2.26±0.05	...	882/520	871.1±154.2	$1472.4^{+38.5}_{-30.8}$	100
43	apec	4.3±0.2	...	$1.96^{+0.8}_{-0.5}$	509/1015	$5.0^{+1.7}_{-1.1}$	$7.9^{+2.5}_{-3.1}$	39
48	apec	$4.0^{+0.8}_{-1.8}$	...	$2.51^{+1.2}_{-0.7}$	524/1015	$1.6^{+0.3}_{-0.4}$	$2.9^{+0.5}_{-0.9}$	15
51	pow	3.1±0.6	$2.60^{+0.21}_{-0.26}$	...	340/520	$27.2^{+2.7}_{-2.1}$	$39.2^{+4.2}_{-2.2}$	39
62	apec+apec	...	...	1.22±0.03, 0.35±0.02	602/519	$393.9^{+16.2}_{-1.5}$	$434.0^{+13.9}_{-24.7}$	100
64	brems	4.1±0.7	...	0.23±0.03	211/520	$101.0^{+31.6}_{-30.0}$	$101.0^{+31.6}_{-30.0}$	100
72	pow	...	$1.4^{+0.6}_{-0.4}$	...	452/1016	$1.0^{+0.3}_{-0.2}$	$3.2^{+1.4}_{-0.8}$	46
78	pow	2.1±0.6	$2.86^{+0.34}_{-0.30}$	...	393/520	$41.3^{+2.1}_{-1.5}$	$54.1^{+3.6}_{-2.5}$	96
92	pow	1.5±0.2	1.54±0.07	...	577/520	104.1±46.3	$301.4^{+20.8}_{-17.0}$	66

Continued on next page

Table 3.5 – continued from previous page

Source No.	Best-fit[a] Model	$N_{\rm H}$ [b] (10^{21} cm^{-2})	Γ	kT (keV)	C/dof[c]	f_X^d (0.5-2 keV) (10^{-15} erg s^{-1} cm^{-2})	f_X^e (0.5-8 keV) (10^{-15} erg s^{-1} cm^{-2})	"goodness[f]" (%)
(1)	(2)	(3)	(4)	(5)	(6)	(7)	(8)	(9)
96	apec	...	...	$0.39^{+0.1}_{-0.1}$	341/1016	1.1±0.2	1.1±0.2	21
106	apec	...	...	$5.30^{+4.7}_{-1.4}$	593/1016	7.2±0.8	$17.6^{+2.2}_{-2.3}$	21
109	pow	...	0.96±0.31	...	523/1016	1.3±0.3	$6.9^{+2.1}_{-1.5}$	49
110	pow	...	$0.83^{+0.54}_{-0.52}$	...	1069/1016	$2.5^{+1.0}_{-0.9}$	$15.1^{+17.0}_{-5.7}$	89
113	pow	<200	$3.69^{+5.69}_{-3.24}$	...	850/1015	168.9±26.4	185.2±15.9	55
114	pow	<12.7	$1.61^{+0.76}_{-0.69}$	...	598/1015	$7.9^{+1.9}_{-3.3}$	$21.4^{+5.8}_{-10.7}$	51
117	apec	...	...	2.8±0.3	611/1016	0.4±0.1	0.8±0.2	50
118	apec	...	...	$0.7^{+10.6}_{-0.5}$	942/1016	1.1±0.4	$1.2^{+1.0}_{-0.9}$	56
120	pow	...	$1.53^{+0.53}_{-0.38}$	...	1063/1016	$7.4^{+2.1}_{-3.1}$	$21.4^{+14.2}_{-11.9}$	80
124	pow	...	0.44±0.35	...	494/1016	$1.6^{+0.6}_{-0.2}$	$15.4^{+12.5}_{-9.0}$	46
128	apec	...	...	$12.7^{+17.8}_{-6.0}$	615/1016	0.8±0.1	$2.5^{+0.2}_{-2.4}$	28
135	pow	2.4±0.4	$2.41^{+0.16}_{-0.14}$	...	475/520	$28.1^{+1.9}_{-1.6}$	$44.1^{+3.2}_{-2.6}$	77
136	pow	<0.1	< 3.4	...	608/1015	$2.6^{+0.2}_{-2.6}$	$6.5^{+1.2}_{-5.6}$	78
141	pow	...	0±0.3	...	511/1016	<0.2	$2.5^{+0.8}_{-1.1}$	48
145	pow	...	1.50±0.36		637/1016	$8.6^{+3.5}_{-2.5}$	$26.0^{+7.7}_{-6.2}$	15
151	apec	...	...	$3.7^{+1.3}_{-1.8}$	851/1016	$3.3^{+0.8}_{-0.9}$	$6.9^{+2.1}_{-6.6}$	48
155	pow	3.2±0.6	1.07±0.13	...	546/520	$16.4^{+3.1}_{-3.8}$	$76.0^{+12.6}_{-10.9}$	68
162	apec	...	...	$3.76^{+0.9}_{-0.5}$	673/1016	8.5±0.5	$18.0^{+1.2}_{-1.7}$	61
165	apec	...	...	$3.66^{+2.4}_{-1.1}$	545/1016	1.9±0.2	3.9±0.8	54
170	pow	3.3±0.7	$1.84^{+0.18}_{-0.22}$	...	445/520	$14.4^{+1.4}_{-1.7}$	$32.4^{+6.8}_{-4.0}$	55
173	pow	...	$1.6^{+0.3}_{-0.3}$	...	484/1016	1.0±0.2	$2.8^{+0.9}_{-0.8}$	31
179	pow	6.8±0.8	2.16±0.15	...	509/520	60.9±2.2	$109.5^{+1.2}_{-0.9}$	61
186	apec	...	...	$3.50^{+4.3}_{-1.6}$	507/1016	0.5±0.1	1.1±0.3	22
188	apec	...	...	$5.14^{+35.4}_{-2.9}$	856/1016	$2.4^{+0.4}_{-0.9}$	$5.7^{+1.5}_{-2.4}$	33
				NGC 4214				
16	pow	1.5±0.3	1.86±0.12	...	422/520	92.0±5.9	$203.4^{+192.2}_{-172.0}$	18
17	pow	...	$2.23^{+0.23}_{-0.21}$	...	354/521	$27.5^{+2.8}_{2.6}$	$27.6^{+6.8}_{-5.0}$	16
22	pow	...	1.71±0.24	...	497/521	$19.7^{+0.3}_{-0.2}$	$48.7^{+12.1}_{-8.6}$	28
24	apec	<0.1	...	< 3.8	1058/1015	$4.0^{+1.1}_{-4.0}$	$6.3^{+0.5}_{-6.3}$	35
27	pow	2.0±0.9	$1.36^{+1.16}_{-0.62}$	...	705/1015	$4.1^{1.40+}_{-2.67}$	$14.1^{+4.8}_{-7.4}$	78
28	pow	...	$1.28^{+0.36}_{-0.42}$	...	559/1016	$3.2^{+0.98}_{-0.96}$	$11.7^{+4.6}_{-3.2}$	43
30	pow	...	$1.28^{+0.56}_{-0.49}$	...	638/1016	$3.7^{+1.23}_{-1.42}$	$13.6^{+11.5}_{-4.0}$	47
33	apec	...	...	$4.8^{+16.1}_{-2.3}$	761/1016	$4.3^{+1.3}_{-3.7}$	$10.1^{+2.7}_{-9.7}$	33
42	pow	3.4±0.1	$2.24^{+0.26}_{-0.31}$	...	374/520	$33.4^{+0.1}_{-0.5}$	$57.7^{+12.8}_{-6.5}$	56
52	pow	...	$1.64^{+0.46}_{-0.44}$		571/1016	$9.2^{+2.60}_{-2.53}$	$24.3^{+9.1}_{-6.4}$	51
62	pow	...	1.36±0.12	...	405/521	14.8±0.2	$50.8^{+7.4}_{-6.0}$	27
68	apec	<0.1	...	< 11.8	496/1015	0.8±0.4	$2.1^{+0.3}_{-2.1}$	28

Continued on next page

Table 3.5 – continued from previous page

Source No.	Best-fit[a] Model	$N_{\rm H}$ [b] (10^{21} cm^{-2})	Γ	kT (keV)	C/dof[c]	f_X^d (0.5-2 keV) (10^{-15} erg s^{-1} cm^{-2})	f_X^e (0.5-8 keV) (10^{-15} erg s^{-1} cm^{-2})	"goodness[f]" (%)
(1)	(2)	(3)	(4)	(5)	(6)	(7)	(8)	(9)
76	apec	...	...	$3.0^{+-3.0}_{-1.5}$	674/1016	$5.0^{+2.2}_{-4.8}$	$9.7^{+5.8}_{-9.4}$	42
77	pow	...	1.89±0.14	...	367/521	$53.7^{+0.3}_{-0.1}$	$115.8^{+14.2}_{-11.5}$	28
78	pow	5.7±0.5	$4.38^{+3.11}_{-1.60}$	...	413/520	$192.0^{+60.6}_{-56.0}$	$198.6^{+55.4}_{-25.7}$	91
83	apec	...	...	$2.5^{+7.2}_{-0.9}$	950/1016	$6.6^{+1.5}_{-1.1}$	$11.7^{+5.8}_{-3.7}$	70
109	pow	...	$1.65^{+0.40}_{-0.41}$	...	462/1016	$6.0^{+1.46}_{-1.29}$	$16.0^{+3.5}_{-3.8}$	53
112	pow	<0.1	0±0.2	...	1128/1015	$1.4^{+0.3}_{-1.4}$	31.4±17.3	98

[a] The best-fit model is either a `powerlaw` or `vapec` model, depending on which one has the lower C/dof.

[b] Intrinsic source absorption, if beyond the Galactic column was required.

[c] Degrees of freedom.

[d,e] Unabsorbed X-ray fluxes.

[f] Results of the `XSPEC` "goodness" command, run using 5000 realizations.

These simple, single-component models sometimes provided a poor fit to the most luminous X-ray sources. Therefore, we also attempted to use multi-component spectral models to describe those sources with >200 net counts. The NGC 404 central engine is not included here, and is instead discussed in more detail in Chapter 6. In NGC 300, only one source was detected with >200 net counts (NGC 300 X-1). Both NGC 300 X-1 and the "supernova impostor" SN 2010da are omitted in this section and discussed in detail in Chapter 6

Bright Sources in NGC 404

Three sources in NGC 404 have more than two hundred net counts. The 0.35-8 keV spectra, with the best-fit spectral model superimposed, are shown in Figure 3.6 (spectra have been binned for display purposes only).

Background AGN

Source 1 has a total of 655 net counts in the combined spectrum of source 1 from ObsIDs 12239 and 870. We found the best-fit spectral model to be a power law with $\Gamma = 1.65^{+0.12}_{-0.11}$, yielding C/dof=496/510. We do not find evidence for additional absorption beyond the

Galactic column. The 0.35-8 keV flux predicted by our best-fit model is 1.18×10^{-13} erg s^{-1} cm^{-2}. We note that source 1 exhibits evidence for rapid variability during our 97 ks *Chandra* observation. With a galactocentric radius of $r = 4.8$ kpc and HRs consistent with being a background object, source 1 is likely an AGN. The value of Γ and variability on timescales of hours are consistent with the AGN interpretation, and a UV counterpart was detected by GALEX with a NUV magnitude of 22.07±0.22. To demonstrate the plausibility of the identification of this source as a background AGN, we note that a quasar with this X-ray flux and a luminosity of 10^{45} erg s^{-1} would be at a distance of 8.4 Gpc (or $z \sim 1.21$) and a Seyfert galaxy with this flux and a luminosity of 10^{43} erg s^{-1} would be at a distance of 84 Mpc (or $z \sim 0.02$).

Source 7 has a total of 454 net counts in the combined spectrum of source 7 from ObsIDs 12239 and 870. We found the best-fit spectral model to be a power law with Γ =1.81±0.13, yielding C/dof=414/510. We do not find evidence for additional absorption beyond the Galactic column. The 0.35-8 keV flux predicted by our best-fit model is 6.54×10^{-14} erg s^{-1} cm^{-2}. A UV counterpart was detected by GALEX, with a FUV magnitude of 22.86 ± 0.09 and a NUV magnitude 21.74 ± 0.04. Given its large galactocentric radius ($r = 4.1$ kpc), source 7 is unlikely to be associated with NGC 404. As for source 1, we again estimate the distance to illustrate the plausibility of a background AGN identification. A quasar with this flux and a luminosity of 10^{45} erg s^{-1} would be at a distance of 11.3 Gpc ($z \sim 1.54$), while a Seyfert galaxy with a luminosity of 10^{43} erg s^{-1} would be at a distance of 1.13 Gpc ($z \sim 0.26$).

Other X-ray Sources

Source 65 is the brightest X-ray source in our total NGC 404 X-ray point source catalog, excluding the NGC 404 central engine, detected with 708 net counts in the 0.35-8 keV band during Obs ID 12239. The X-ray source is very soft – 97% of the counts were detected at energies below 2 keV. Source 65 was detected in two of the observations considered here (Obs IDs 12239 and 384). The X-ray source was detected on the back-illuminated S3 chip in Obs ID 12239, while it was detected on the front-illuminated S4 detector in Obs ID 384. The differences in front and back-illuminated responses make merging the source 65 spectrum

problematic; we therefore only fit the spectrum extracted from the 97 ks Obs ID 12239 observation (which is much higher quality than the 1.8 ks snapshot taken in Obs ID 384). Source 65 has a large off-axis angle of $\sim$6′.8. The best fit model is a thermal plasma `APEC` model, with kT=$0.57^{+0.03}_{-0.04}$ keV (C/dof=106/98), predicting a 0.35-8 keV flux of 3.6×10^{-14} erg s^{-1} cm^{-2}.

Source 65 is spatially coincident within $\sim$0″.6 of a high proper motion F5 star [HD 6892, 183], with $M_V \sim 8.5$ (located at a distance of $d \sim 110$ pc). This optical magnitude implies an X-ray-to-optical flux ratio $log(f_X/f_V)$ of -2.9, typical of the X-ray-to-optical flux ratios reported for F stars [2]. A UV counterpart has also been detected by GALEX, with a FUV magnitude of 17.60 ± 0.07. Our observations support the classification of this object as a foreground star not previously detected in X-rays.

Bright Sources in NGC 55

Eight of the NGC 55 sources have more than two hundred net counts. The 0.35-8 keV spectra, with the best-fit spectral model superimposed, are shown in Figure 3.7 (spectra have been binned for display purposes only).

X-ray Binaries

Source 44 was best described by single power law. There were 205 net counts detected for this source. The best fit model has a photon index $\Gamma = 1.52^{+0.36}_{-0.34}$ with an absorbing column of $N_{\rm H} = (1.1^{+1.7}_{-0.8})\times10^{21}$ cm^{-2}, a C/dof = 354/520, and a goodness of 56%. The model yields an unabsorbed 0.5-2 keV flux of $(1.34^{+0.02}_{-0.10})\times10^{-13}$ erg s^{-1} cm^{-2} and an unabsorbed 0.35-8 keV flux of $(4.18^{+2.04}_{-0.90})\times10^{-13}$ erg s^{-1} cm^{-2}. The source is within the optical extent of NGC 55, with a semi-major axis distance of 0.7 kpc. Optical colors are consistent with a HMXB origin. At a distance of 2.1 Mpc, the unabsorbed 0.35-8 keV luminosity of this source is $\sim 2\times10^{38}$ erg s^{-1}, consistent with the Eddington limit of an accreting NS. Previous analysis of this source [391, their source 20] also found it to be consistent with an absorbed power law. Their best fit photon index $\Gamma = 1.67^{+0.09}_{-0.08}$ and $N_{\rm H} = (2.56^{+0.44}_{-0.39})\times10^{21}$ cm^{-2} are consistent with our best fit spectral model. We see no evidence for long-term variability of this source, with the 0.35-8 keV luminosity varying by $\sim$12% between the [391] work and

this work.

Source 54 has a total of 439 net counts. The best fit model was found to be a simple power law, with no additional spectral components necessary. The best fit photon index is $\Gamma = 1.39^{+0.20}_{-0.25}$, with an additional absorption component $N_{\rm H} = (1.4 \pm 0.1) \times 10^{21}$ cm^{-2} (C/dof=428/520). The unabsorbed fluxes in the 0.5-2 keV and 0.35-8 keV bands are 3.5×10^{-14} erg s^{-1} cm^{-2} and 1.2×10^{-13} erg s^{-1} cm^{-2}, respectively. The optical colors of the candidate optical counterparts are red. The location of the X-ray source is within the optical extent of NGC 55 (with a semi-major axis of 0.9 kpc) and the relatively hard photon index make it a likely LMXB candidate. The implied 0.35-8 keV luminosity at the distance of NGC 55 is $\sim 6 \times 10^{37}$ erg s^{-1}.

Source 62 has a total of 1783 net counts detected for source 62 in the archival *Chandra* observations. An absorbed power law yielded a C/dof=525/520 and a goodness of 41%, but the addition of a `diskbb` component improved the C/dof to 518/518 and the goodness to 53%. We find the best fit photon index to be $\Gamma = 3.46^{+1.99}_{-2.45}$ with a disk temperature $kT_{\rm in} = 2.04^{+0.66}_{-0.83}$ keV. There is an additional absorbing column with $N_{\rm H} = (4.2^{+3.2}_{-1.3}) \times 10^{21}$ cm^{-2}. The model yields 0.5-2 keV and 0.35-8 keV fluxes of 2.58×10^{-13} erg s^{-1} cm^{-2} and 7.00×10^{-13} flux, respectively. We find that 54% of the unabsorbed 0.35-8 keV X-ray flux originates in the multicolor disk component. Source 62 is located within the optical extent of NGC 55 (with a semi-major axis of 0.4 kpc), and with red optical colors is a likely a LMXB candidate.

An absorbed ($N_{\rm H} \sim 1.1 \times 10^{22}$ cm^{-2}) power law plus disk blackbody model was found to be the best spectral model for *XMM-Newton* observations of this source [391, their source 47] Those model parameters were quite different from those found by our archival *Chandra* analysis. The best fit *XMM-Newton* photon index was soft, $\Gamma_{\rm XMM} = 2.08^{+0.09}_{-0.13}$, but it was still harder than *Chandra* observed, and the disk blackbody temperature was significantly lower ($kT_{\rm in,XMM} = 0.11^{+0.02}_{-0.2}$ keV). These spectral parameters are consistent with a steep power law (SPL, also called "very high") state observed in BH XRBs, while the archival *Chandra* observations are consistent with a thermally-dominated state [268]. We additionally investigate whether the timing properties of the archival *Chandra* observations of source 62 are consistent with a thermally-dominated state. The power density spectra

(PDS) of BHs in the thermally-dominated state show that power scales roughly as ν^{-1} [characteristic of many physical processes, including turbulence; 24, 421]. Additionally, quasi-periodic oscillations (QPOs) – which are observed in intermediate or hard states of BHBs – are typically absent in the thermally-dominated state. We constructed a PDS of source 62 but did not find any evidence for QPOs. The spectral index of the PDS is found to be 1.09±0.08. Both the spectral index and lack of QPOs indicate that the timing properties of source 62 are consistent with a thermally-dominated state.

The presence of such state transitions between the *Chandra* and *XMM-Newton* observations of source 62, along with the soft photon index and PDS spectral index, provide evidence for a BH primary. The X-ray luminosity of source 62 ($\sim$3.7$\times10^{38}$ erg s^{-1}) is near the Eddington luminosity of a $\sim$3 $M_\odot$ compact object, also consistent with a low-mass BH-LMXB.

Source 63 contained 2962 counts. Although the *XMM-Newton* observations [391, their source 43] were best fit by an absorbed power law (Γ =0.82 ± 0.04) and disk blackbody ($kT_{\rm in} = 4.92^{+0.74}_{-0.78}$ keV) model, we were unable to obtain an acceptable fit using this model. We additionally were unable to find a single component power law model which adequately described the data. Instead, our best fit model to the archival *Chandra* data was absorbed bremsstrahlung emission, with $N_{\rm H}$ = (1.4±0.3)$\times10^{21}$ cm^{-2} and a temperature of $kT = 2.0^{+0.2}_{-0.1}$ keV. The C/dof of the model is 435/520, with unabsorbed model fluxes in the 0.5-2 keV and 0.35-8 keV bands of 3.6×10^{-13} erg s^{-1} cm^{-2} (1.9×10^{38} erg s^{-1}) and 6.4×10^{-13} erg s^{-1} cm^{-2} (3.4×10^{38} erg s^{-1}), respectively. The goodness of the model was 35%. The X-ray source has a semi-major axis of 0.1 kpc, within the optical extent of the galaxy, and red colors indicative of an AGN or LMXB origin – we *marginally* favor the LMXB interpretation due to source location.

Source 119 is the NGC 55 ULX designated XMMU J001528.9-391319 [390]. It was detected in the archival *Chandra* observations with 11,432 net counts. This source is a dipping BH binary, with a BH mass of >11 $M_\odot$. Previous spectral modeling with *XMM-Newton* [390] yielded a best fit model consisting of a power law (Γ =4.2) and a disk blackbody ($kT_{\rm in}$=0.86 keV) with additional absorption ($N_{\rm H}$ =4.2$\times10^{21}$ cm^{-2}). This model was applied to the observed counts during three epochs of the *XMM-Newton* observation, showing a

variation in luminosity throughout the observation from 8.9×10^{38} erg s^{-1} to 1.6×10^{39} erg s^{-1} in the 0.5-10 keV energy range.

Due to the large number of counts detected for this source, pile-up presented an issue in the archival *Chandra* observations. We included pile-up in our spectral model, and found a pile-up fraction of ∼32%. Our best fit model was an absorbed power law with a disk blackbody component (C/dof=426/516). The absorbing column was found to be $(1.8^{+1.4}_{-0.2})\times10^{21}$ cm^{-2} and the power law photon index was $\Gamma = 2.72^{+0.72}_{-0.69}$. The disk (with temperature $kT_{\rm in}$ $= 0.36^{+0.02}_{-0.03}$ keV) dominated the spectrum, with >95% of X-ray photons originating from the disk component. The unabsorbed, pile-up corrected fluxes were 1.86×10^{-12} erg s^{-1} cm^{-2} in the 0.5-2 keV band and 2.57×10^{-12} erg s^{-1} cm^{-2} in the 0.35-8 keV band, implying a 0.35-8 kev luminosity of 1.4×10^{39} erg s^{-1}. Taken at face value, this luminosity implies a BH with a mass of $\sim 11\ M_{\odot}$, consistent with the BH mass predicted by [390].

We note that the *Chandra* observations of source 119 yields a flatter power law photon index and cooler inner disk temperature than was observed with *XMM-Newton*, although the overall luminosity is comparable to the high-end values found in the *XMM-Newton* observations. Unlike Galactic BH-XRBs, ULXs lack obvious spectral state transitions [126, 453, 385]. Although the *Chandra* observations show a relatively cool disk temperature, the thermal component still dominates the spectrum. This result is contrary to the results in [390], who observed nearly ∼ 100% of the X-ray flux originating in the power law component at the beginning of the *XMM-Newton* observation and <27% of the flux from the power law component towards the end of their observation. The *Chandra* observations of a disk-dominated origin for the X-ray emission further suggests that Source 119, unlike other known BH-XRBs, exhibits spectral state transitions.

Source 122 has a total of 1510 net counts in the archival *Chandra* observations. We find the best fit model is an absorbed power law, with $N_{\rm H} = (1.3\pm0.5) \times 10^{21}$ cm^{-2} and a photon index of Γ =1.4±0.1 (C/dof=500/520, and a goodness of 22%). The red colors of the candidate optical counterparts and location of the source within the optical extent of the galaxy make it an LMXB candidate. The unabsorbed model fluxes in the 0.5-2 keV and 0.35-8 keV energy bands are 1.2×10^{-13} erg s^{-1} cm^{-2} and 3.9×10^{-13} erg s^{-1} cm^{-2}, respectively. This source shows some evidence for long-term variability, and the long-term

X-ray flux varied by a factor of ∼6. The implied 0.35-8 keV luminosity of the source is $\sim 2 \times 10^{38}$ erg s^{-1}, consistent with accretion by a ∼1.4 $M_{\odot}$ NS at the Eddington limit.

Source 135 has 246 net counts, which is spatially coincident with a globular cluster [299] with a metallicity [Fe/H] = -1.61. The 0.35-8 keV spectrum is best fit with an absorbed power law, with $N_{\rm H} = (2.3 \pm 1.3) \times 10^{21}$ cm^{-2} and $\Gamma = 2.8 \pm 0.4$ (C/dof=294/520). The best fit model yielded unabsorbed fluxes of 5.5×10^{-14} erg s^{-1} cm^{-2} in the 0.5-2 keV band and 1.0×10^{-13} erg s^{-1} cm^{-2} in the 0.35-8 keV band, implying a 0.35-8 keV luminosity of $\sim 5 \times 10^{37}$ erg s^{-1}. Although the luminosity of the source and the spatial coincidence with a globular cluster provide good evidence for a LMXB origin, the best fit value of Γ is unusually soft for a NS primary – such soft photon indices are typically only seen in BH-XRBs, making source 135 a good BH candidate.

Other X-ray Sources

Source 23 has a total of 2644 net counts. Although the spectrum was obviously dominated by thermal emission, a single-component `apec` model provided a poor fit (C/dof=755/521). The addition of a second `apec` component significantly improved the fit (C/dof=455/519). We find no evidence for additional absorption beyond the Galactic column, and best-fit temperatures from the spectral model are $kT_1 = 0.32 \pm 0.02$ keV and $kT_2 = 1.27 \pm 0.03$ keV. We additionally see evidence for rapid X-ray variability in our observations (see Section 3.6). This source was observed using *XMM-Newton* [391, their source 39], and a Galactic RS CVn origin was suggested to explain the X-ray emission. Our low value of the absorption column and consistent thermal plasma temperatures support this conclusion. Our spectral model yields of 0.5-2 keV flux of 2.7×10^{-13} erg s^{-1} cm^{-2}, and 0.35-8 keV flux of 3.3×10^{-13} erg s^{-1} cm^{-2}. The corresponding luminosities are 1.4×10^{38} erg s^{-1} in the 0.5-2 keV band and 1.7×10^{38} erg s^{-1} in the 2-8 keV band.

Bright Sources NGC 2403

The X-ray point source catalog of NGC 2403 contains numerous bright sources; below, we comment on those 23 X-ray sources with more than 200 net counts. The 0.35-8 keV spectra, with the best-fit spectral model superimposed, are shown in Figure 3.8 (spectra have been

binned for display purposes only).

X-ray Binaries

Source 2 has a total of 904 net counts in the 0.35-8 keV energy range. The best fit model was a simple power law with no additional spectral components or absorption beyond the Galactic column. The best fit photon index was $\Gamma = 1.70 \pm 0.09$ and $C/dof = 540/521$, although we were unable to obtain an acceptable goodness (>99%). The model yields 0.5-2 keV flux of $(9.6 \pm 0.4) \times 10^{-15}$ erg s^{-1} cm^{-2} and a 0.35-8 keV flux of $(2.4 \pm 1.1) \times 10^{-14}$ erg s^{-1} cm^{-2}. At the distance of NGC 2403, these fluxes correspond to luminosities of 1.2×10^{37} erg s^{-1} and 3.1×10^{37} erg s^{-1}, respectively. Source 2 additionally exhibits rapid variability. With a galactocentric radius of 1.4 kpc and red optical colors, this source is most likely an LMXB.

Source 20 has 364 net counts in the 0.35-8 keV energy range. The best fit model was a combined power law ($\Gamma = 2.25^{+0.19}_{-0.20}$) and thermal plasma ($kT = 0.80^{+0.23}_{-0.22}$ keV) with no evidence for absorption beyond the Galactic column ($C/dof = 309/519$, with a "goodness" of 72%). The best fit model yields fluxes of 5.6×10^{-15} erg s^{-1} cm^{-2} in the 0.5-2 keV energy range and 1.1×10^{-14} erg s^{-1} cm^{-2} in the full 0.35-8 keV energy range. At the distance of NGC 2403, these fluxes imply luminosities of 7.2×10^{36} erg s^{-1} and 1.4×10^{37} erg s^{-1}, respectively. The red colors and apparent location of the X-ray source within the disk of NGC 2403 make it an LMXB candidate.

Source 41 was designated source 20 in a previous analysis of Obs ID 2014 only [361]. The spectrum was found to be equally well-fit with bremsstrahlung emission with $kT \sim 3.5 - 4$ keV or a power law with $\Gamma \sim 1.9$. A total of 10,033 net counts were detected in the 0.35-8 keV energy range, and we find the spectrum is best described by a power law with $\Gamma = 1.87^{+0.04}_{-0.05}$ ($C/dof = 646/520$), consistent with [361]. An additional absorption component with $N_{\rm H} = (2.5 \pm 0.1) \times 10^{21}$ cm^{-2} was required in our model. The best-fit model yields unabsorbed fluxes in the 0.5-2 keV and 0.35-8 keV bands of 2.2×10^{-13} erg s^{-1} cm^{-2} (2.9×10^{38} erg s^{-1}) and 4.9×10^{-13} erg s^{-1} cm^{-2} (6.4×10^{38} erg s^{-1}), respectively. Between *Chandra* observations, the flux of Source 41 was observed to fluctuate by a factor of $\sim$11. With a galactocentric radius of 0.3 kpc and red optical colors, source 41 is most likely an

LMXB.

Source 42 is a ULX, originally discovered by the *Einstein* observatory [123], with a BH mass $M \sim 10 - 15\ M_{\odot}$ [201]. Later observations with *ASCA* revealed a multi-color disk spectrum, with an innermost disk temperature of $kT_{\rm in} \sim 1$ keV and an innermost disk radius of $R_{\rm in}$ ∼130 km [227]. Additional follow-up observations of this source with *Suzaku* and *Chandra* Obs ID 4628 are consistent with this model [201], although the *Chandra* observation Obs ID 4630 is consistent with a power law model ($\Gamma \sim 2.7$), bremsstrahlung (with kT ∼1.8 keV), or a multicolor disk model [$kT_{\rm in}$ ∼0.6 keV 361]. The luminosity of Source 42 is observed to vary by ∼20% over a several year time period.

The 16,601 net counts in the 0.35-8 keV band for this source were well described by a simple absorbed power law. The best-fit photon index $\Gamma = 2.26 \pm 0.05$, with an absorbing column $N_{\rm H} = (4.0 \pm 0.2) \times 10^{21}$ cm^{-2} (C/dof=634/520). The estimated 0.5-2 keV and 0.35-8 keV fluxes are $(8.7 \pm 0.5) \times 10^{-13}$ erg s^{-1} cm^{-2} and $(1.5 \pm 0.8) \times 10^{-12}$ erg s^{-1} cm^{-2}, respectively, corresponding to luminosities of $(1.1 \pm 0.1) \times 10^{39}$ erg s^{-1} and $(1.9 \pm 0.6) \times 10^{39}$ erg s^{-1} at the distance of NGC 2403.

Source 51 has 658 net counts in the 0.35-8 keV energy range. This source was previously classified as a transient source within the nuclear star cluster of NGC 2403 [461]. Although previous work has found the X-ray spectrum of this source to be consistent with a disk blackbody model [261, 260], we find the best fitting model to the 0.35-8 keV spectrum is a rather soft absorbed power law, with $\Gamma = 2.60^{+0.21}_{-0.26}$ and an absorbing column $N_{\rm H} = (3.1 \pm 0.6) \times 10^{21}$ cm^{-2} (C/dof=340/520). The model yields 0.5-2 keV and 0.35-8 keV fluxes of 2.7×10^{-14} erg s^{-1} cm^{-2} and 3.9×10^{-14} erg s^{-1} cm^{-2}, respectively, corresponding to luminosities at the distance of NGC 2403 of 3.5×10^{37} erg s^{-1} and 5.1×10^{37} erg s^{-1}. We find no evidence for rapid variability, although the transient nature of the source is discussed in [461]. The relativity soft X-ray emission from source 51, and its high X-ray luminosity in earlier observations (∼7×10^{38} erg s^{-1}, [461]), are suggestive of a BH with $M \sim 5\ M_{\odot}$ [461].

Source 64 has a total of 772 net counts in the 0.35-8 keV energy range. The spectrum was best described as thermal bremsstrahlung emission ($kT = 0.23 \pm 0.03$) with an absorbing column larger than the nominal Galactic value, $N_{\rm H} = (4.1 \pm 0.7) \times 10^{21}$ cm^{-2} ($C/dof = 211/520$). The best fit model yields fluxes in the 0.5-2 keV energy band of

1×10^{-13} erg s^{-1} cm^{-2}, implying a luminosity of 1.3×10^{38} erg s^{-1} at the distance of NGC 2403. The soft X-ray spectrum and association with UV emission within the optical extent of the disk make source 64 consistent with a young SNR or a very soft HMXB.

Source 92 has a total of 5,375 net counts. The best fit model was an absorbed power law, with Γ =1.54±0.07 and $N_{\rm H}$ =(1.5±0.2)$\times10^{21}$ cm^{-2} (C/dof=577/520). The unabsorbed fluxes in the 0.5-2 keV and 0.35-8 keV energy bands are 1×10^{-13} erg s^{-1} cm^{-2} and 3×10^{-13} erg s^{-1} cm^{-2}, respectively, implying luminosities at the distance of NGC 2403 of 1.4×10^{38} erg s^{-1} and 3.9×10^{38} erg s^{-1}. This source was previously designated source 1 in an earlier analysis [361], with a similar spectral shape. The photon index is quite hard, suggestive of a neutron star origin rather than a black hole, and the luminosity is near the Eddington limit for a $\sim3M_{\odot}$ neutron star. We support the interpretation of this source as a LMXB.

Source 140 contained 248 net counts. The spectrum was best described by an absorbed power law, with a photon index of $\Gamma=1.74^{+0.34}_{-0.33}$ and an absorbing column of $(4.3^{+1.5}_{-1.4})\times10^{21}$ cm^{-2} (C/dof = 380/520). The best fit model yielded fluxes in the 0.5-2 and 0.35-8 keV energy ranges of 1.1×10^{-14} erg s^{-1} cm^{-2} and 2.8×10^{-14} erg s^{-1} cm^{-2}, respectively. At the distance of NGC 2403, these fluxes correspond to a 0.5-2 keV luminosity of 1.4×10^{37} erg s^{-1} and a 0.35-8 keV luminosity of 3.7×10^{37} erg s^{-1}. Although no *HST* or multiwavelength observations are currently available for this source, the apparent association with the NGC 2403 disk and the shape of the X-ray spectrum are consistent with an XRB origin. We have therefore classified this source as an HMXB candidate, although additional multiwavelength observations are required to support this conclusion.

Source 155 has 1,318 net counts in the 0.35-8 keV energy range. The spectrum was best described by a power law with Γ =1.07±0.13 and an absorbing column with $N_{\rm H}$ =(3.2±0.6)$\times10^{21}$ cm^{-2} (C/dof=546/520). The model yielded unabsorbed fluxes in the 0.5-2 keV and 0.35-8 keV energy bands of 1.6×10^{-14} erg s^{-1} cm^{-2} and 7.6×10^{14} erg s^{-1} cm^{-2}, corresponding to luminosities of 2.1×10^{37} erg s^{-1} and 9.9×10^{37} erg s^{-1}, respectively. With a galactocentric radius of 1.2 kpc and apparent association with the spiral arms of NGC 2403, we classify this source as an HMXB candidate.

Source 162 is best described by a power law (Γ =1.82±0.09, with C/dof=673/1016) with no absorption beyond the Galactic column. This source contains 957 net counts. The

best fit model yielded unabsorbed fluxes of 1.8×10^{-14} erg s^{-1} cm^{-2} in the 0.5-2 keV band and 4.2×10^{-14} erg s^{-1} cm^{-2} in the 0.35-8 keV band, corresponding to luminosities of 2.4×10^{37} erg s^{-1} and 5.4×10^{37} erg s^{-1}, respectively. Source 162 appears to be coincident with the spiral arms of NGC 2403, so we tentatively classify this source a an HMXB, although more information is needed to for confirmation.

Source 170 has 599 net counts in the 0.35-8 keV energy band, which were best described by a power law with $\Gamma = 1.84^{+0.18}_{-0.22}$ and an absorbing column $N_{\rm H} = (3.3 \pm 0.7) \times 10^{21}$ cm^{-2}. The model yielded a C/dof=445/520 and fluxes in the 0.5-2 keV and 035-8 keV energy bands of 1.5×10^{-14} erg s^{-1} cm^{-2} and 3.2×10^{-14} erg s^{-1} cm^{-2}, respectively, which correspond to luminosities of 1.9×10^{37} erg s^{-1} and 4.2×10^{37} erg s^{-1} at the distance of NGC 2403. This source has a galactocentric radius of 1.0 kpc and shows evidence for long term X-ray variability. We therefore classify this source tentatively as an LMXB, although more information is needed to support this classification.

Source 174 contained 464 net counts in the 0.35-8 keV energy range. The best fit model was an absorbed power law, with $\Gamma = 2.15^{+0.37}_{-0.33}$ and an absorbing column of $N_{\rm H} = (2.2^{+1.1}_{-1.0}) \times 10^{21}$ cm^{-2} (C/dof=458/520). The best fit model implies 0.5-2 keV and 0.35-8 keV fluxes of 1.8×10^{-14} erg s^{-1} cm^{-2} and 3.7×10^{-14} erg s^{-1} cm^{-2}, respectively. At the distance of NGC 2403, these fluxes imply 0.5-2 keV and 0.35-8 keV luminosities of 2.3×10^{37} erg s^{-1} and 4.8×10^{37} erg s^{-1}, respectively. USNO-B1.0 optical observations reveal a red counterpart, and the apparent association of Source 174 with the disk of NGC 2403 make it a likely LMXB.

Source 179 has 1,353 net counts. The 0.35-8 keV spectrum is best described by an absorbed power law (C/dof=509/520), with $\Gamma = 2.16 \pm 0.15$ and an absorbing column with $N_{\rm H} = (6.8 \pm 0.8) \times 10^{21}$ cm^{-2}. The 0.5-2 keV flux is $(8.3 \pm 0.1) \times 10^{-14}$ erg s^{-1} cm^{-2} and the flux in the 0.35-8 keV band is $(1.7 \pm 0.2) \times 10^{-13}$ erg s^{-1} cm^{-2}, corresponding to unabsorbed luminosities of 1.1×10^{38} erg s^{-1} and 2.2×10^{38} erg s^{-1}, respectively. The spectrum of source 179 was previously found to be consistent with either a power law with a photon index of ~ 2 or bremsstrahlung emission with a temperature of $kT \sim 4$ keV [361, their source 28]. The apparent association with the spiral structure of NGC 2403, a galactocentric radius of 2.6 kpc and evidence for both rapid and long-term X-ray variability are consistent with an

HMXB origin, and the softness of the power law photon index is consistent with observations of BH-HMXBs.

Background AGN

Source 106 has 315 net counts. The best fit spectral model an absorbed power law, with $N_{\rm H} = (3.5^{+0.17}_{-0.14})\times10^{21}$ cm^{-2} and $\Gamma = 2.57^{+0.52}_{-0.43}$ (C/dof=356/520). The best fit model yields unabsorbed 0.5-2 and 0.35-8 keV fluxes of 4.6×10^{-14} erg s^{-1} cm^{-2} and 8.5×10^{-14} erg s^{-1} cm^{-2}, respectively. The softness of the power law makes classifying this source difficult; although it may be a foreground stellar object, we lack the optical *HST* coverage to determine whether the X-ray emission is coincident with a foreground star. The red USNO-B1.0 and 2MASS magnitudes are consistent with an AGN origin. Assuming a typical AGN luminosity of 10^{44} erg s^{-1} implies a redshift to Source 106 of $z \approx 0.7$. If we instead assume a Galactic origin of Source 106 of 2–8 kpc, we derive a luminosity range of 4×10^{31} erg s^{-1} to 6.5×10^{32} erg s^{-1}. These luminosities are typical of luminous CVs [357], which is also consistent with the relative softness of the power law photon index (we note that, with so few counts, a thermal model does not improve our fit by a statistically significant amount). We moderately favor the AGN interpretation, although additional observations of this source are needed to confirm the origin of the X-ray emission.

Source 130 has 202 net counts. The best fit spectral model is a simple power law, with $\Gamma = 2.17^{+0.30}_{-0.28}$ and no evidence for absorption beyond the Galactic column. The C/dof is 337/521, and the model yields unabsorbed fluxes of 2.8×10^{-14} erg s^{-1} cm^{-2} in the 0.5-2 keV band and 5.8×10^{-14} erg s^{-1} cm^{-2} in the full 0.35-8 keV band. At the distance of NGC 2403, these fluxes correspond to luminosities of 3.6×10^{37} erg s^{-1} and 7.5×10^{37} erg s^{-1}, respectively.

Source 157 has 270 net counts in the 0.35-8 keV band that are best described by a single power law. The best fit photon index with $\Gamma = 1.73\pm0.18$ with no evidence for absorption beyond the Galactic column (C/dof=341/502). The unabsorbed fluxes predicted by the best-fit model are 1.9×10^{-14} erg s^{-1} cm^{-2} in the 0.5-2 keV band and 5.1×10^{-14} erg s^{-1} cm^{-2} in the 0.35-8 keV band. At the distance of NGC 2403, these fluxes predict 2.5×10^{37} erg s^{-1} and 6.6×10^{37} erg s^{-1}, respectively. Assuming a typical AGN luminosity of 10^{44} erg

s^{-1}, we predict the redshift of Source 157 to be ∼0.9.

Other X-ray Sources

Source 11 contained 275 net counts in the 0.35-8 keV energy band. The spectrum was best described by a combined power law and thermal plasma, absorbed by the Galactic column ($C/dof = 511/519$). The best fit photon index $\Gamma = 1.49^{+0.57}_{-0.59}$ and plasma temperature $kT = 0.26^{+0.08}_{-0.04}$ keV. The best fit spectral model implies fluxes of 1.4×10^{-14} erg s^{-1} cm^{-2} in the 0.5-2 keV energy band, and 3.7×10^{-14} erg s^{-1} cm^{-2} in the full 0.35-8 keV band. At the distance of NGC 2403, these fluxes imply 0.5-2 keV and 0.35-8 keV luminosities of 1.9×10^{37} erg s^{-1} and 4.8×10^{37} erg s^{-1}, respectively. The source has a large galactocentric radius ($r \sim 9$ kpc), making it unlikely to be associated with the NGC 2403 disk. If the source were located within the Milky Way (at a distance of 2–8 kpc), we predict a 0.35-8 keV luminosity in the range of 1.8×10^{31} erg s^{-1} to 2.8×10^{32} erg s^{-1}, consistent with known luminous Galactic CVs [357]. We therefore tentatively classify this source as a foreground star and a possible CV candidate.

Source 62 required two thermal components to obtain a reasonable fit to the 5,433 detected counts, with $kT_1 = 1.22 \pm 0.03$ keV and $kT_2 = 0.35 \pm 0.02$ keV (C/dof=602/519). The best-fit model yields a 0.5-2 keV flux of 3.9×10^{-13} erg s^{-1} cm^{-2}. The X-ray source is coincident with a foreground star, with USNO-B1.0 apparent magnitudes of $m_B = 8.8$, m_R=8.1, and $m_I = 7.9$. This source was also detected in the 2MASS catalog, with $J = 7.5$, $H = 7.2$, and $K = 7.1$. With a $R - I$ color of ~ 0.2, the star is likely a mid-to-early F type. Assuming an F-star absolute magnitude of ∼3.5 implies a distance to the source of ∼100 pc. We therefore estimate the 0.5-2 keV flux of Source 62 is $\sim 5 \times 10^{29}$ erg s^{-1}. Both the implied luminosity of Source 62 and the two-temperature thermal plasma fit to the spectrum are typical of other nearby F stars in the Milky Way [274, 326, 86].

Source 78 has 541 net counts, best described by a single soft power law in the 0.35-8 keV energy range. The best fit model has a photon index $\Gamma = 2.86^{+0.34}_{-0.30}$ with an absorbing column $N_{\rm H} = (2.1\pm0.6)\times10^{21}$ cm^{-2} (C/dof=393/520). The model yields an unabsorbed 0.5-2 keV flux of 4.1×10^{-14} erg s^{-1} cm^{-2} and a 0.35-8 keV flux of 5.4×10^{-14} erg s^{-1} cm^{-2}. Source 78 additionally exhibits rapid variability, and with a galactocentric radius of 3 kpc is within

the optical confines of NGC 2403. However, this source was included in the USNO-B1.0 catalog with $m_R = 11.7$ and $m_I = 13.1$ and in the 2MASS catalog with $J = 13.4$, $H = 12.8$, and $K = 12.7$. The source has been identified as a K4III giant at a heliocentric distance of ∼16 kpc [312]. At this distance, the corresponding X-ray luminosities are $1.2{\times}10^{33}$ erg s^{-1} in the 0.5-2 keV band and $1.6{\times}10^{33}$ erg s^{-1} in the 0.35-8 keV band. Following [2], we find the X-ray-to-optical flux ratio $log(f_X/f_V)$ of source 78 is -1.7, broadly consistent with other X-ray emitting K-type stars. We therefore conclude that the X-ray emission is likely to originate from a foreground star.

Source 135 has 1258 net counts, best described by a single power law. The best fit photon index was $\Gamma = 2.41^{+0.16}_{-0.14}$, with an absorbing column $N_{\rm H} = (2.4{\pm}0.4){\times}10^{21}$ cm^{-2} (C/dof=457/520). The unabsorbed fluxes in the 0.5-2 keV and 0.35-8 keV energy bands are 2.8×10^{-14} erg s^{-1} cm^{-2} and 4.4×10^{-14} erg s^{-1} cm^{-2}, respectively, and correspond to luminosities of 3.6×10^{37} erg s^{-1} and 5.7×10^{37} erg s^{-1} at the distance of NGC 2403. The X-ray emission is spatially coincident with SN 2004dj, with an estimated progenitor mass of 14-15 $M_\odot$ [257, 433, 427]. SN 2004dj is additionally coincident with the compact cluster Sandage 96 [459], which is thought to host the progenitor star. With only ∼1200 counts, the relatively soft power law X-ray spectrum is consistent with a luminous young SNR (thermal features may not be detectable without a longer exposure) or a soft HMXB. We favor the SNR interpretation, giving source 135's spatial coincidence with SN 2004dj.

Source 169 contained 345 net counts in the 0.35-8 keV energy band. The spectrum was best described by a thermal bremsstrahlung model, with $kT = 0.10 \pm 0.02$ keV (C/dof = 83/41). An absorbing column of $(5.1^{+1.9}_{-0.4}){\times}10^{21}$ cm^{-2} was required to adequately fit the observed spectrum. The best fit model implies 0.5-2 keV and 0.35-8 keV fluxes of $1.8{\times}10^{-13}$ erg s^{-1} cm^{-2} and $9.6{\times}10^{-13}$ erg s^{-1} cm^{-2}, respectively. At the distance of NGC 2403, these fluxes imply luminosities of $2.4{\times}10^{38}$ erg s^{-1} (0.5-2 keV) and $1.2{\times}10^{39}$ erg s^{-1} (0.35-8 keV). Although tentatively classified as a SNR, the relatively high luminosity of this source make it unlikely to be a genuine SNR located in NGC 2403. If we assume that the X-ray emission is instead Galactic in origin (at a distance in the range of 2–8 kpc), we find an implied luminosity of $4.6{\times}10^{32}$ – $7.3{\times}10^{33}$ erg s^{-1}. Colliding wind binaries and massive Wolf-Rayet companions are both observed to emit X-rays in this luminosity range [380], and

bremsstrahlung emission from Wolf-Rayet stars has been predicted [319, 65]. We therefore favor the interpretation of this X-ray source as a Galactic, X-ray emitting Wolf-Rayet star, although further optical observations are required to support this conclusion.

Bright Sources in NGC 4214

The X-ray point source catalog of NGC 4214 contains 5 X-ray sources with more than 200 net counts. The 0.35-8 keV spectra, with the best-fit spectral model superimposed, are shown in Figure 3.9 (spectra have been binned for display purposes only).

X-ray Binaries

Source 16 was previously designated CXOU J121538.2+361921 [105, their source 11] and has been identified as an X-ray binary with a period of 3.62 hours and an X-ray luminosity of a few 10^{38} erg s^{-1}. It has been proposed that the system consists of a slightly evolved helium star with $M \sim 2-3\ M_{\odot}$ and either a NS or low mass BH primary [105, 147], although the favored interpretation is a NS-LMXB. This classification would make the system a direct progenitor of a double-NS binary. We detect 1827 counts in the 0.35-8 keV energy range for this source. The spectrum is best described as a power law (C/dof=422/520) with Γ=1.86±0.12 and an absorbing column $N_{\rm H} = (1.5\pm0.3)\times10^{21}$ cm^{-2}, consistent with the analysis presented in [105]. The best fit model yielded fluxes of 9.2×10^{-14} erg s^{-1} cm^{-2} in the 0.5-2 keV band and 2.0×10^{-13} erg s^{-1} cm^{-2} in the full 0.35-8 keV energy band, implying luminosities of 9×10^{37} erg s^{-1} and 2×10^{38} erg s^{-1}, respectively. We additionally find evidence of rapid X-ray variability. Our observations are consistent with previous detections of this source, and we support the interpretation as a helium star-NS LMXB.

Source 42 has 380 net counts in the 0.35-8 keV energy band consistent with an absorbed power law (C/dof=374/520). The best fit photon index is $\Gamma = 2.24^{+0.26}_{-0.31}$ with an absorbing column $N_{\rm H} = (1.36\pm0.12)\times10^{21}$ cm^{-2}. The model yields fluxes of 3.3×10^{-14} erg s^{-1} cm^{-2} in the 0.5-2 keV band and 5.8×10^{-14} erg s^{-1} cm^{-2} in the 0.35-8 keV band, corresponding to luminosities of 3.3×10^{37} erg s^{-1} and 5.8×10^{37} erg s^{-1} at the distance of NGC 4214. This model is broadly consistent with the absorbed power law and inferred luminosity found in

[171], who designated this source as 'Source 10.' This source is coincident with a young star cluster (∼3.5 Myr old) in NGC 4214, believed to be the dynamical center of the galaxy [171, 240, 255]; therefore, we favor an HMXB interpretation of source 42.

Source 62 has 432 net counts in the 0.35-8 keV band. The spectrum is best described with a power law (C/dof=405/521) with $\Gamma = 1.36 \pm 0.12$. No absorption beyond the Galactic column was required. We find the 0.5-2 keV and 0.35-8 keV fluxes from the best-fit model of 1.5×10^{-14} erg s^{-1} cm^{-2} and 5.1×10^{-14} erg s^{-1} cm^{-2}, respectively, corresponding to luminosities of 1.5×10^{37} erg s^{-1} and 5×10^{37} erg s^{-1} at the distance of NGC 4214. These results are consistent with those found by [147], who also found the spectrum best described by a power law with $\Gamma \sim 1.4$ and a corresponding 0.35-8 keV luminosity of 7×10^{37} erg s^{-1}. Source 62 is coincident with a known H II region associated with NGC 4214, and we therefore consider it an HMXB candidate.

Background AGN

Source 17 contains 348 net counts in the 0.35-8 keV energy band. The spectrum is best described by a power law with $\Gamma = 2.23^{+0.23}_{-0.21}$ (C/dof=354/521). No absorption beyond the Galactic column was required. The best fit model yielded 0.5-2 keV and 0.35-8 keV fluxes of 2.8×10^{-14} erg s^{-1} cm^{-2} and 4.7×10^{-14} erg s^{-1} cm^{-2}, which correspond to luminosities of 2.8×10^{37} erg s^{-1} and 4.7×10^{37} erg s^{-1} at the distance of NGC 4214. This source does not appear to be associated with NGC 4214, and the long-term variability and optical/UV colors are consistent with an AGN origin.

Source 77 contains 391 net counts. The best fit model to the 0.35-8 keV spectrum is a power law with $\Gamma = 1.89 \pm 0.14$ and no additional absorption beyond the Galactic column necessary (C/dof=367/521). The best fit model yielded fluxes of 5.4×10^{-14} erg s^{-1} cm^{-2} in the 0.5-2 keV energy range, and 1.2×10^{-13} erg s^{-1} cm^{-2} in the 0.35-8 keV energy band. The X-ray source does not appear to be within the optical extent of the galaxy, and its optical and UV colors are consistent with an AGN origin.

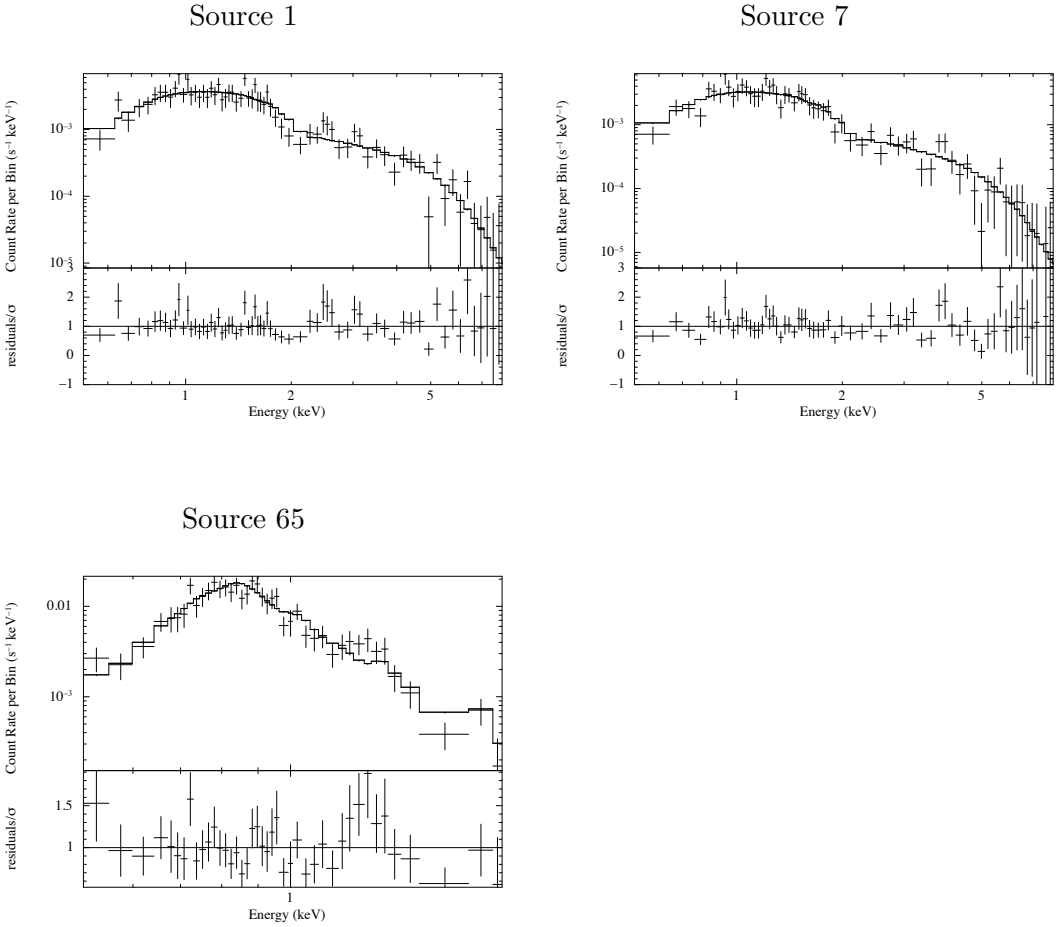

Figure 3.6: The 0.35-8 keV spectra (with best fit models superimposed) and residuals for the NGC 404 sources with more than 200 net counts. Spectra are binned for display purposes only.

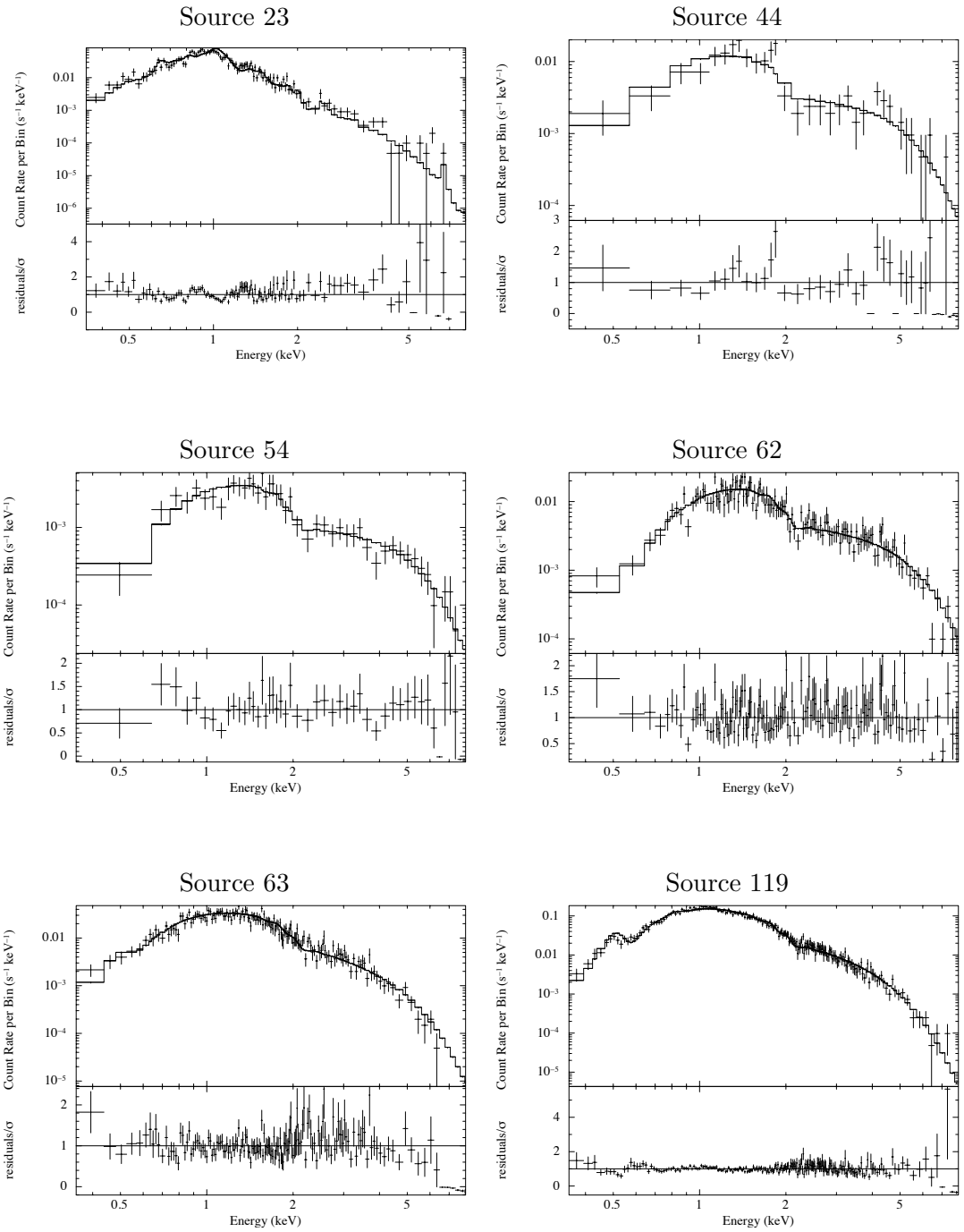

Figure 3.7: The 0.35-8 keV spectra (with best fit models superimposed) and residuals for the NGC 55 sources with more than 200 net counts. Spectra are binned for display purposes only.

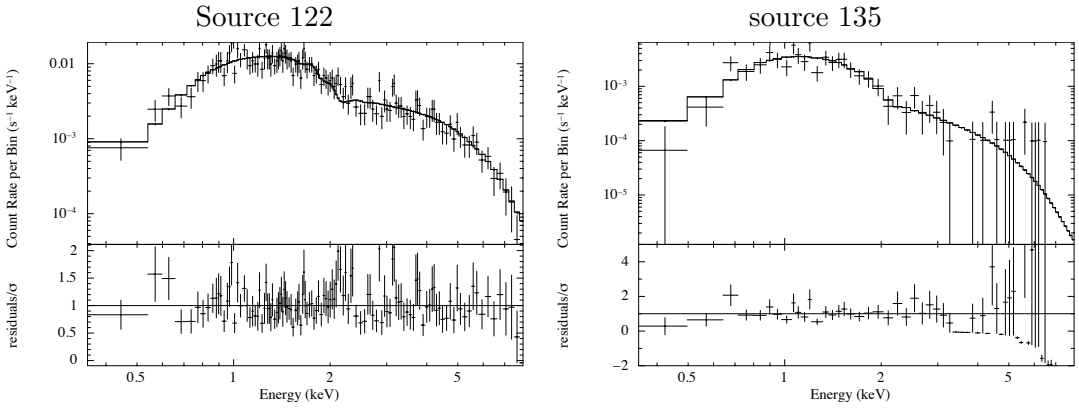

Figure 3.7: *continued*

3.2.2 Temporal Variability

Many XRBs and AGN exhibit long-term X-ray variability on timescales of months to years [424], while SNRs and some HMXBs will show persistent X-ray emission. A large fraction of HMXBs and LMXBs containing BH primaries are observed to experience "outbursting" behavior [47, 131, 309, 344], often on timescales of minutes to days. More detail about how X-ray variability is used to aid in source classification is given in the next chaper. To quantify the degree of variability in the detected X-ray sources, the five X-ray catalogs were systematically searched for sources showing both significant short-term (i.e., variability that occurs on timescales less than the observation exposure time) and long-term variability in the 0.35-8 keV band.

To quantify long-term variability, the catalogs were searched for sources that were detected in at least one exposure, but were not detected in another (despite the source's position being within the field of view). We use these non-detections to place an upper limit on the source flux at the time of the exposure; some of these sources are faint, and so may have been just below the detection limit of the shallower exposure without requiring a significant change in flux. Archival *XMM-Newton* observations were available for some of the galaxies in our sample; we used the Flux Limits from Images from *XMM-Newton*

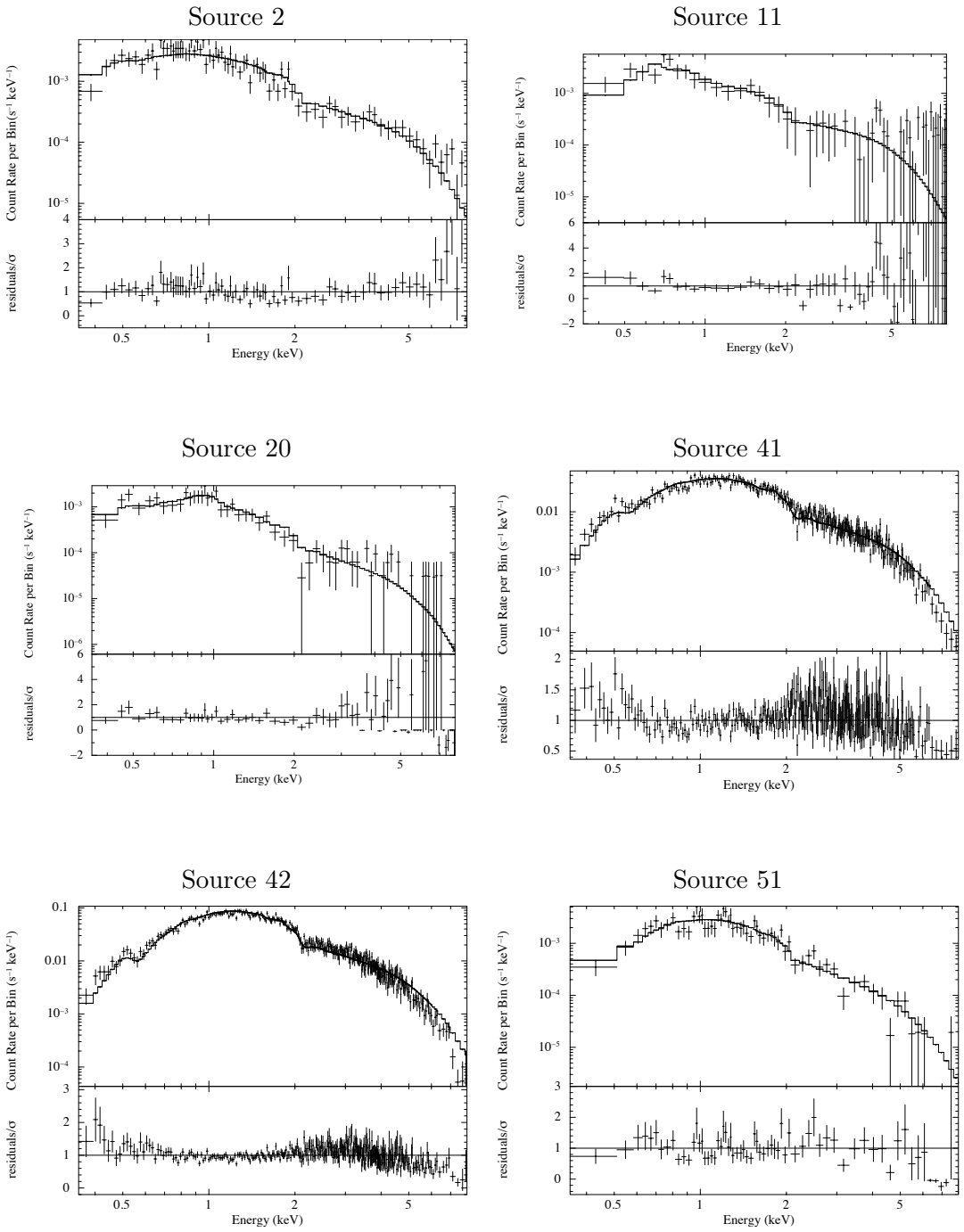

Figure 3.8: The 0.35-8 keV spectra (with best fit models superimposed) and residuals for the NGC 2403 sources with more than 200 net counts. Spectra are binned for display purposes only.

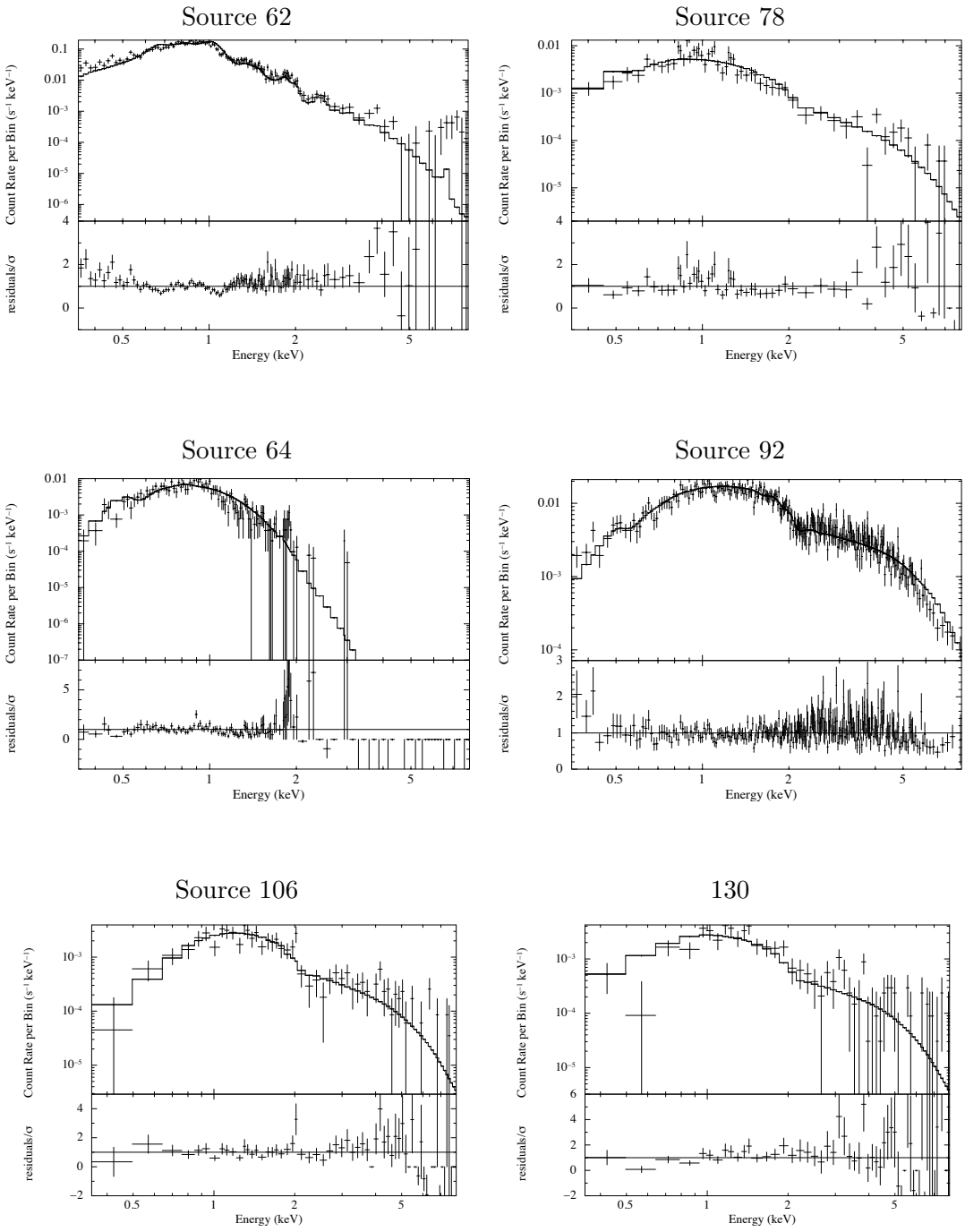

Figure 3.8: *continued*

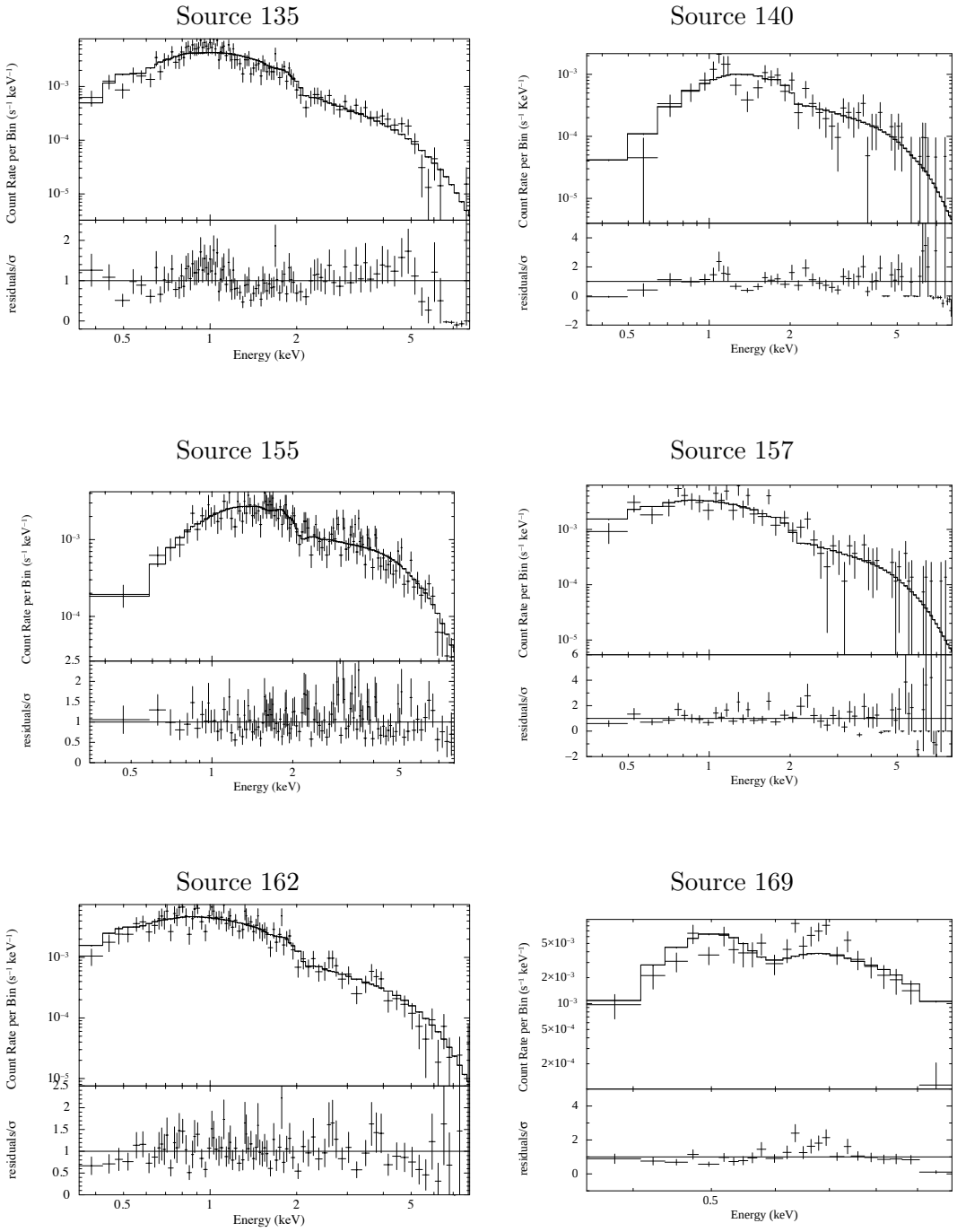

Figure 3.8: *continued*

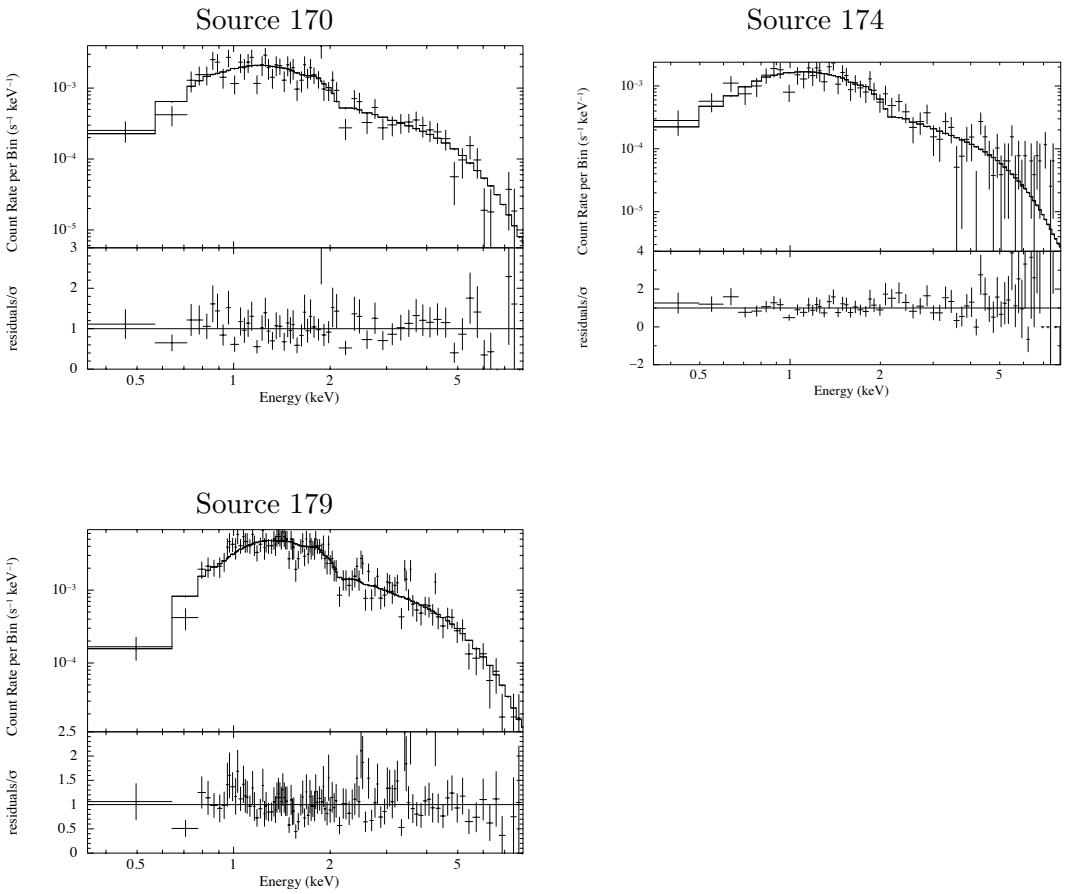

Figure 3.8: *continued*

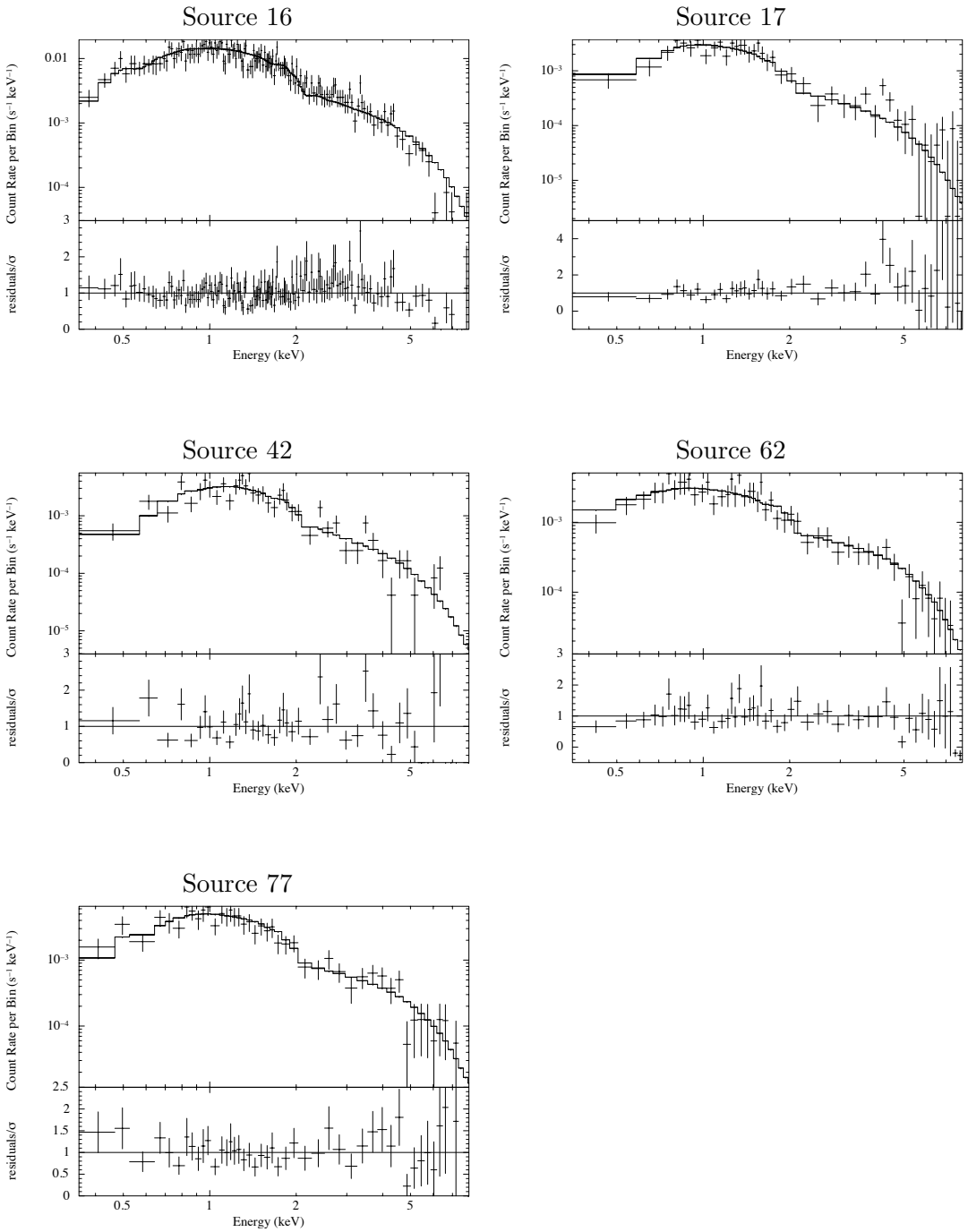

Figure 3.9: The 0.35-8 keV spectra (with best fit models superimposed) and residuals for the NGC 4214 sources with more than 200 net counts. Spectra are binned for display purposes only.

(FLIX[1]) to determine fluxes and upper limits at each source's position. The variability threshold η was used to determine the degree of long-term variability exhibited by each source [407], defined as $\eta = (\mathrm{flux_{max}} - \mathrm{flux_{min}})/\Delta\mathrm{flux}$, where $\mathrm{flux_{max}}$ and $\mathrm{flux_{min}}$ are the maximum and minimum observed fluxes of the source, respectively. The flux error Δflux is calculated using the Gehrels approximation [appropriate for low count data; 145],

$$\Delta\mathrm{flux} = \left(\frac{1+\sqrt{\mathrm{counts}+0.75}}{\mathrm{counts}}\right)\mathrm{flux} \tag{3.5}$$

We consider any sources with $\eta \geq 5$ potentially variable.

For rapid variability (i.e., variability occurring on timescales less than the exposure time), a Kolmogorov-Smirnov (K-S) test was used to compare the cumulative photon arrival time distribution for each X-ray source to a uniform count rate model in each observation. The K-S test returns the probability (denoted by ξ) that both distributions were drawn from the same parent distribution. Sources with variability exceeding the 3σ level (roughly ξ $<5\times10^{-3}$) are denoted as exhibiting potential rapid variability. Table 3.6 lists all the X-ray sources showing evidence for either rapid or long-term variability.

Table 3.6: Rapid and Long-Term Source X-ray Variability

	NGC 300			NGC 404			NGC 55			NGC 2403			NGC 4214		
No.	ξ^a	η^b	f_{max}/f^c_{min}	ξ	η	f_{max}/f_{min}	ξ	η	f_{max}/f_{min}	ξ	η	f_{max}/f_{min}	ξ	η	f_{max}/f_{min}
1				**0.0006**	0.1	2.6									
2							0.78	**6.4**	1.7	**0.00011**	2.6	1.3	0.30	**9.0**	3.6
3							0.76	**5.1**	1.9	0.85	**119**	**27.1**	0.53	**19.5**	2.7
4	0.56	**16.1**	**21.8**							0.99	**6.5**	2.4			
5															
6							0.74	**5.8**	1.6						
7										0.34	**5.2**	5.2			
8															
9															
10							0.81	**11.8**	2.3				0.54	**9.9**	3.3
11															
12	0.53	**11.5**	**15.8**				0.92	**22.5**	**36.5**	0.08	**20.1**	1.6	0.94	**12.4**	7.3
13							0.99	**38.5**	3.4	0.94	**8.6**	2.0			
14							0.81	**11.1**	2.7				0.62	**13.0**	1.5
15										0.34	**10.6**	5.3			
16				0.09	**5.2**	**25.3**	0.23	**11.7**	2.3	0.62	**6.6**	1.6	**0.00001**	4.0	3.1
17													0.44	**57.6**	4.5

Continued on next page

[1]See `http://www.ledas.ac.uk/flix/flix.html`.

Table 3.6 – continued from previous page

	NGC 300			NGC 404			NGC 55			NGC 2403			NGC 4214		
No.	ξ^a	η^b	f_{max}/f^c_{min}	ξ	η	f_{max}/f_{min}	ξ	η	f_{max}/f_{min}	ξ	η	f_{max}/f_{min}	ξ	η	f_{max}/f_{min}
18	**0.0036**	0.8	1.4	0.87	2.0	**14.7**	0.48	**39.2**	3.4	0.48	**7.6**	3.0	0.89	**16.5**	1.4
19													0.15	**7.4**	2.3
20	0.53	**5.8**	9.7				**0.00001**	**2255**	**141**	**0.00005**	**13.9**	3.1	0.73	**49.7**	6.1
21										0.48	**20.8**	9.2	0.55	**47.8**	**18.5**
22							0.75	**34.6**	2.7				0.74	**6.2**	2.5
23							**0.00506**	**1449**	**33.5**				0.56	**11.1**	1.2
24	0.52	**15.4**	**21.8**							0.25	**24.8**	2.9	**0.00001**	3.1	2.5
25							0.32	**30.0**	**10.6**	0.16	**8.4**	2.9			
26															
27				0.94	1.8	9.2	0.60	**19.8**	2.6	0.04	**23.5**	3.2	0.94	**9.6**	1.8
28										0.48	**5.7**	9.0	0.26	**11.7**	1.7
29	0.74	**9.9**	**12.5**										0.73	**11.3**	1.8
30							0.52	**8.3**	2.3				0.84	**20.5**	3.5
31							0.02	**37.7**	9.8	0.35	**26.0**	3.2	0.10	**16.1**	3.2
32															
33	0.65	**32.2**	**42.5**				0.81	**10.0**	2.6				0.66	**11.1**	4.6
34							**0.00001**	**92.0**	4.4						
35										0.68	**6.1**	2.3	0.17	**22.1**	5.5
36							0.24	**93.0**	**26.7**	**0.00018**	1.0	1.0	0.39	**32.2**	2.9
37				0.25	2.6	**10.1**	0.58	**29.2**	2.8				0.86	**7.0**	7.0
38													0.25	**10.4**	1.4
39							0.06	**6.4**	1.9	0.54	**6.2**	3.1	0.13	**9.0**	1.4
40				0.04	3.4	**14.7**	0.95	**15.0**	5.2	0.57	**55.5**	**28.4**			
41										0.54	3.9	**10.8**	0.25	**8.4**	1.6
42							0.28	**556**	**55.4**	0.34	**15.4**	1.2			
43							0.01	**1269**	**47.0**	0.14	**53.7**	1.4	0.73	**18.7**	2.1
44	0.92	**12.9**	**18.5**				0.20	**17.4**	5.2						
45	0.52	**10.5**	**27.6**												
46										0.40	**8.1**	3.1			
47							0.33	**5.7**	2.0	0.60	**6.8**	9.5			
48													0.72	**7.8**	4.0
49				0.29	2.1	9.5	**0.00001**	**29.4**	3.6	0.12	**9.1**	5.9			
50															
51							0.61	**13.8**	3.2						
52	0.69	**12.2**	**17.3**				0.35	**46.8**	1.1	0.82	**80.6**	**382**			
53				0.92	1.9	**13.8**	0.14	**5.7**	4.1				0.01	**24.5**	1.9
54				0.69	3.0	**23.5**	0.61	**6.6**	2.0	0.39	**20.0**	**125**			
55				0.79	4.2	**42.6**				0.79	**5.3**	3.4			
56										0.18	**52.2**	**25.7**	0.12	**28.6**	**26.4**
57				0.56	2.0	9.2	0.67	**10.8**	1.2	0.09	**7.9**	6.6	0.77	**10.9**	1.5
58							**0.00005**	**29.1**	2.8	0.28	**15.7**	5.6	0.52	**11.9**	2.9
59	0.65	**5.4**	**15.6**	0.49	**5.0**	**23.2**	0.20	**117**	1.1						
60							**0.00001**	**478**	1.4						
61				0.89	3.4	**26.6**							0.39	**7.9**	1.6
62										**0.00001**	**8.1**	6.8			
63													0.46	**26.6**	2.2
64				0.99	4.7	**42.5**	0.20	**9.3**	**51.2**						
65							0.01	**90.5**	8.0	0.04	**8.8**	1.4	0.85	**6.0**	2.4
66							0.81	**8.0**	1.8				0.11	**6.1**	3.2
67															
68							**0.00001**	1.2	1.5						
69	0.05	**7.8**	**20.3**							0.34	**6.5**	5.6	0.77	**6.3**	2.3
70							0.11	**5.9**	1.4						

Continued on next page

Table 3.6 – continued from previous page

	NGC 300			NGC 404			NGC 55			NGC 2403			NGC 4214		
No.	ξ^a	η^b	f_{max}/f^c_{min}	ξ	η	f_{max}/f_{min}	ξ	η	f_{max}/f_{min}	ξ	η	f_{max}/f_{min}	ξ	η	f_{max}/f_{min}
71				0.06	4.5	**34.8**	0.18	**8.1**	1.7						
72				**0.0009**	0.1	1.1	0.96	**9.9**	2.6	0.93	**7.1**	5.5			
73	0.84	**13.5**	**20.5**				**0.00001**	**18.6**	4.5	0.46	**9.9**	2.1			
74															
75							0.44	**96.2**	**28.5**				0.12	**31.2**	4.3
76	0.52	**8.3**	**10.6**				0.30	**7.4**	2.5						
77							0.14	**94.7**	4.1						
78							0.92	**31.2**	3.4	**0.00001**	0.7	1.2	0.50	**18.0**	1.2
79							0.67	**7.2**	1.6	0.69	**24.9**	2.3	**0.00731**	0.4	1.0
80							0.52	**14.5**	2.5						
81													0.63	**32.2**	3.3
82	0.92	**7.7**	5.3				**0.00001**	3.1	1.9						
83										0.67	**15.9**	2.5			
84							**0.00130**	0.0	1.0						
85							0.05	**82.5**	**22.0**	0.39	**5.6**	3.9	0.56	**18.4**	2.0
86							0.15	**20.3**	4.0				0.68	**5.5**	1.6
87	0.03	**12.9**	**18.8**				**0.00037**	**19.4**	2.2	0.89	**14.1**	**12.2**	0.04	**7.2**	7.4
88							**0.00088**	**231**	**35.7**				0.40	**9.9**	1.3
89	0.32	**41.3**	**68.6**				0.41	**126**	**26.1**	0.42	**5.4**	3.7			
90							0.94	**22.9**	5.1	0.68	**7.4**	4.0			
91							0.23	**18.9**	5.0	0.03	**7.7**	3.2			
92							0.10	**18.8**	2.5				0.07	**8.5**	5.4
93							0.81	**10.9**	6.2	0.03	**14.6**	1.2			
94							0.39	**23.4**	4.4				0.46	**14.5**	3.7
95															
96							0.81	**22.5**	**19.1**						
97							0.17	**20.7**	8.4	0.39	**6.7**	1.9			
98										0.23	**18.2**	1.8			
99															
100							**0.00004**	**17.7**	1.6	0.85	**13.7**	2.0	0.96	**6.3**	6.5
101										0.93	**5.3**	1.4			
102							0.23	**87.7**	**11.9**						
103							0.49	**59.0**	7.0	0.10	**27.1**	4.2			
104							0.84	**24.6**	8.1	0.07	**8.0**	6.3			
105															
106							0.54	**70.9**	6.5	0.38	**9.8**	1.9			
107							0.20	**7.9**	2.8	0.03	**45.9**	3.0			
108															
109							**0.00001**	**6.7**	3.4	0.47	**5.8**	3.7	0.18	**7.7**	1.3
110							0.36	**16576**	**3254**	0.85	**21.4**	6.2	0.70	**17.2**	2.4
111							0.56	**4439**	**502**						
112							0.09	**12.7**	5.8						
113															
114										0.84	**8.4**	1.7			
115													0.56	**11.5**	3.4
116										0.20	**7.0**	4.9			
117							**0.00140**	0.7	1.0						
118															
119															
120															
121							0.26	**71.5**	6.8						
122							0.22	**13.8**	6.4	0.49	**6.4**	1.4			
123															

Continued on next page

Table 3.6 – continued from previous page

	NGC 300			NGC 404			NGC 55			NGC 2403			NGC 4214		
No.	ξ^a	η^b	f_{max}/f_{min}^c	ξ	η	f_{max}/f_{min}	ξ	η	f_{max}/f_{min}	ξ	η	f_{max}/f_{min}	ξ	η	f_{max}/f_{min}
124							0.57	**5.2**	1.5	**0.00669**	1.5	1.7			
125							0.94	**44.3**	5.7						
126							0.17	**6.2**	2.0	**0.00105**	3.7	2.3			
127															
128															
129										0.80	**5.1**	1.8			
130															
131															
132							0.05	**8.1**	2.0						
133							0.33	**6.9**	1.8						
134							0.37	**51.2**	4.2	0.56	**5.1**	**14.8**			
135							0.99	**31.4**	2.9						
136										0.01	**67.8**	**427**			
137															
138							0.43	**13.2**	2.6						
139							0.70	**68.2**	**14.9**						
140							0.81	**30.5**	3.7						
141							**0.00541**	0.5	1.0	0.72	**6.5**	1.8			
142							0.49	**10.3**	2.3	**0.00278**	3.2	1.9			
143															
144							0.92	**205**	**13.7**						
145															
146															
147										0.83	**5.9**	4.8			
148															
149							0.16	**9.8**	2.4						
150							0.11	**11.2**	**16.8**						
151							0.29	**22.0**	2.0						
152															
153															
154															
155															
156										0.17	**286**	**189**			
157															
158															
159															
160															
161															
162															
163										0.84	**7.3**	1.3			
164															
165															
166										**0.00440**	3.7	1.3			
167															
168															
169															
170										0.94	**18.3**	**119**			
171										0.22	**11.2**	2.2			
172															
173															
174															
175										**0.00642**	**29.5**	2.9			
176															

Continued on next page

Table 3.6 – continued from previous page

	NGC 300			NGC 404			NGC 55			NGC 2403			NGC 4214		
No.	ξ[a]	η[b]	f_{max}/f_{min}[c]	ξ	η	f_{max}/f_{min}	ξ	η	f_{max}/f_{min}	ξ	η	f_{max}/f_{min}	ξ	η	f_{max}/f_{min}
177															
178															
179										**0.00008**	**5.5**	**11.4**			
180										0.11	**13.6**	1.8			
181															
182															
183										0.33	**7.7**	1.8			
182															
183															
184															
185										0.15	**9.5**	7.6			
186															
187															
188										0.87	**7.9**	3.5			
189										0.72	**8.6**	1.5			
190										0.69	**11.8**	2.6			

[a] The K-S probability of the source being constant. Sources with K-S probabilities of $\xi \leq 5 \times 10^{-3}$ are likely to show are likely to show short-term variability, and are shown in boldface.

[b] η is the long-term variability index [407]. Sources with $\eta \geq 5$ are likely to show long-term variability, and are shown in boldface.

[c] Sources whose fluxes changed by more than an order of magnitude are shown in boldface.

Chapter 4

MULTIWAVELENGTH OBSERVATIONS AND SOURCE CLASSIFICATION

In this Chapter, I present the matched *HST* observations available for each CLVS galaxy. These observations were searched for optical counterpart candidates for each X-ray source contained with the field of view of at least one *HST* pointing. Additionally, public multi-wavelength archives were searched for objects matching the X-ray source position.

With the available X-ray and multiwavelength information compiled for each of the 629 CLVS X-ray sources, a classification scheme was developed to place each X-ray source into the most likely category for the origin of the X-ray emission (e.g., HMXB, LMXB, SNR, background AGN, etc.).The ability to identify likely XRB candidates from contaminating sources is a key strength of the *Chandra* Local Volume Survey (and this dissertation) when compared to earlier studies, which were only able to characterize the XRB populations of galaxies in a strictly statistical sense.

4.1 Optical Counterparts from HST

I will first present the optical counterpart candidates found for each of the five CLVS galaxies. The typical *Chandra* error circle of sources contained within one or more *HST* fields was $\sim 0\farcs6$, and typical limiting magnitudes of the *HST* observations correspond to absolute magnitudes of $M_{F814} = -1.4$ and $M_{F606W} = -0.6$. The optical observations are therefore sensitive to late-B/early-A type main sequence stars. The X-ray source positions were matched to the stars in the *HST* good star catalogs that met the quality cuts (described in Chapter 3). For many X-ray sources, multiple optical counterpart candidates were found within the *Chandra* error circle. In these cases, the optical counterpart candidates are labeled 'a,' 'b,' 'c,' etc. in order of increasing distance away from the nominal X-ray source location.

Figures 4.1-4.5 show finding charts for X-ray sources with overlapping *HST* fields in

each of the five CLVS galaxies. The box size is given in the upper-left corner; sources without a size listed are $5'' \times 5''$. For NGC 300, three *HST* filters were available for all *HST* fields covered; we therefore rendered RGB-images of each finding chart. For the remaining galaxies, only two filters were available for optical counterpart identification, so finding charts were constructed using the $F606W$ or $F555W$ filter images only (whichever is available). The X-ray source position is shown by a cross, with a circle indicating the extent of the *Chandra* error circle. Lines are used to indicate the likely optical counterpart. In cases of multiple optical counterparts, the optical sources are labeled.

In severely crowded fields, dozens of optical sources fall within the *Chandra* error circle; in these cases no optical source candidate is indicated to avoid confusion. In a small number of cases, the X-ray source is coincident with a saturated foreground star or the disk of a background galaxy. Since both of these optical sources failed to meet the *HST* quality criteria of a stellar object in NGC 300, they were not included in the *HST* star catalogs. We used the IRAF task `imexamine` to estimate the magnitudes of these objects.

For each source with at least one optical counterpart candidate, we compute a logarithmic X-ray-to-optical flux ratio $\log(f_X/f_V)$, where f_X is the 2-10 keV X-ray flux and and the f_V is the optical flux measured in either $F555W$ or $F606W$, whichever is available. For sources with multiple optical counterpart candidates, $\log(f_X/f_V)$ is computed assuming the bluest counterpart candidate. For sources within the *HST* footprint but for which no optical counterpart was found, we assume an optical flux equal to the limiting magnitude in that filter. Although the $F606W$ has a slightly larger bandpass (by about 22%) than the $F555W$ filter, we estimate that for the majority of stars accessible in our *HST* exposures (earlier than A-type stars, with roughly flat spectra) the affect on $\log(f_X/f_V)$ will be ~ 0.1.

4.2 Multiwavelength Observations: Ultraviolet, Optical, Infrared, and Radio Counterparts

We have attempted to place additional constraints on the nature of the CLVS X-ray sources by examining archival multi-wavelength data. We searched for counterparts in the following point source catalogs: the *GALEX* GR6 data release (NUV, FUV), USNO-B1.0 ($B1$, $R1$), 2MASS All Sky (J, H, K), and NVSS (1.4 GHz).

UV emission can be a good tracer of young stars and background AGN; however, since the stellar populations of NGC 404 are primarily old, we expect the majority of UV-detect sources to be background AGNs. It is possible that some LMXBs will exhibit detectable levels of UV emission, although their optical colors are expected to be significantly redder than that of an AGN. The optical USNO-B1.0 catalog is sensitive to Milky Way stars, compact clusters, and AGN. The infrared data are also sensitive to Milky Way stars, red giants, associations of older stars located within the parent galaxy, and background galaxies, while radio emission is indicative of radio-loud background AGN.

Table 4.1 summarizes the multi-wavelength observations available for each of the X-ray sources with at lease one multi-wavelength detection. As discussed in §4.1, in many cases many optical counterpart candidates were found for a single X-ray source. Since the primary goal of this multiwavelength analysis is to search for strong HMXB candidates, we therefore provide the optical information for the bluest optical counterpart candidate for each X-ray source.

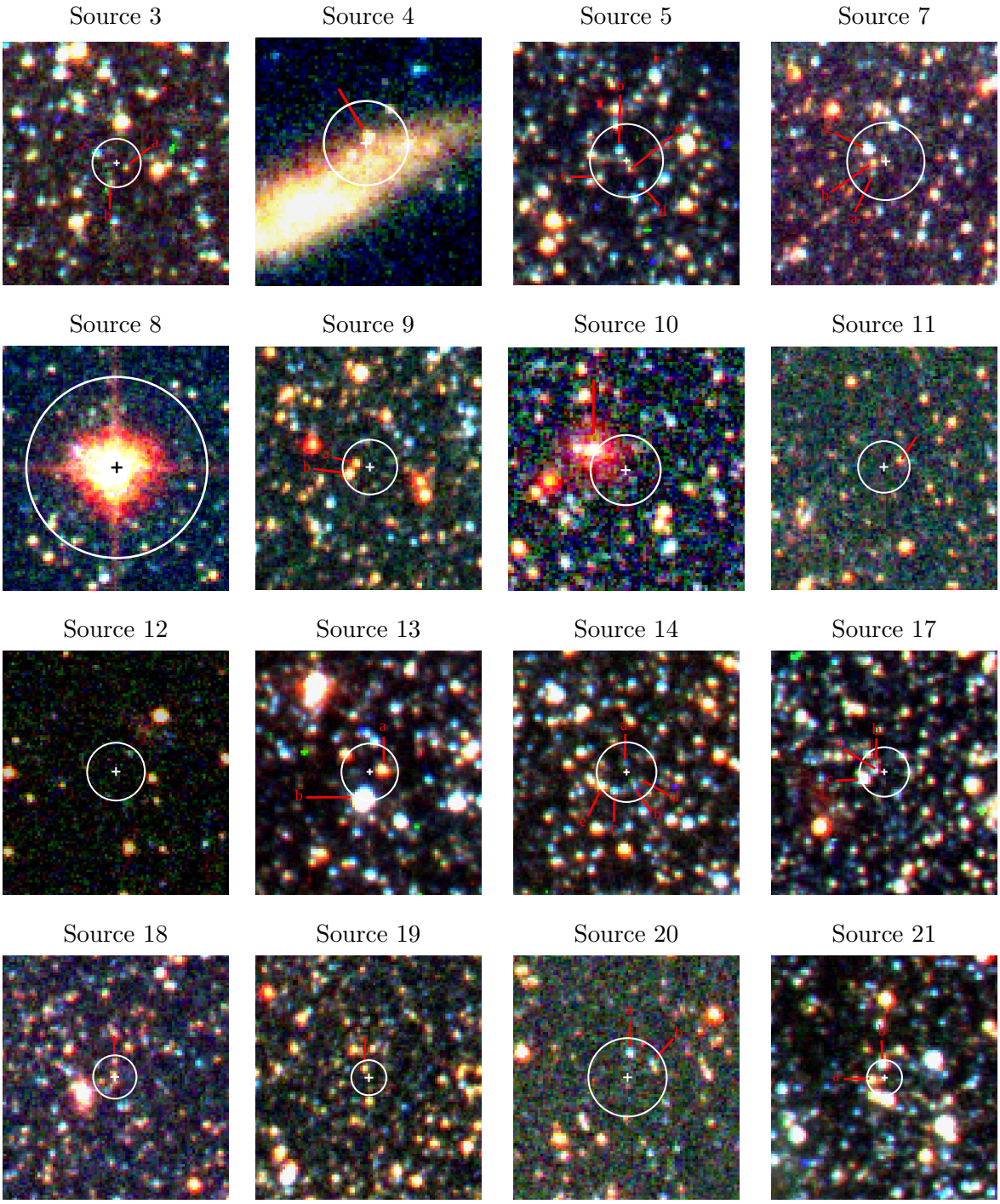

Figure 4.1: Optical RGB-rendered *HST* images for X-ray sources detected in NGC 300. Finding starts are $5'' \times 5''$ in size.

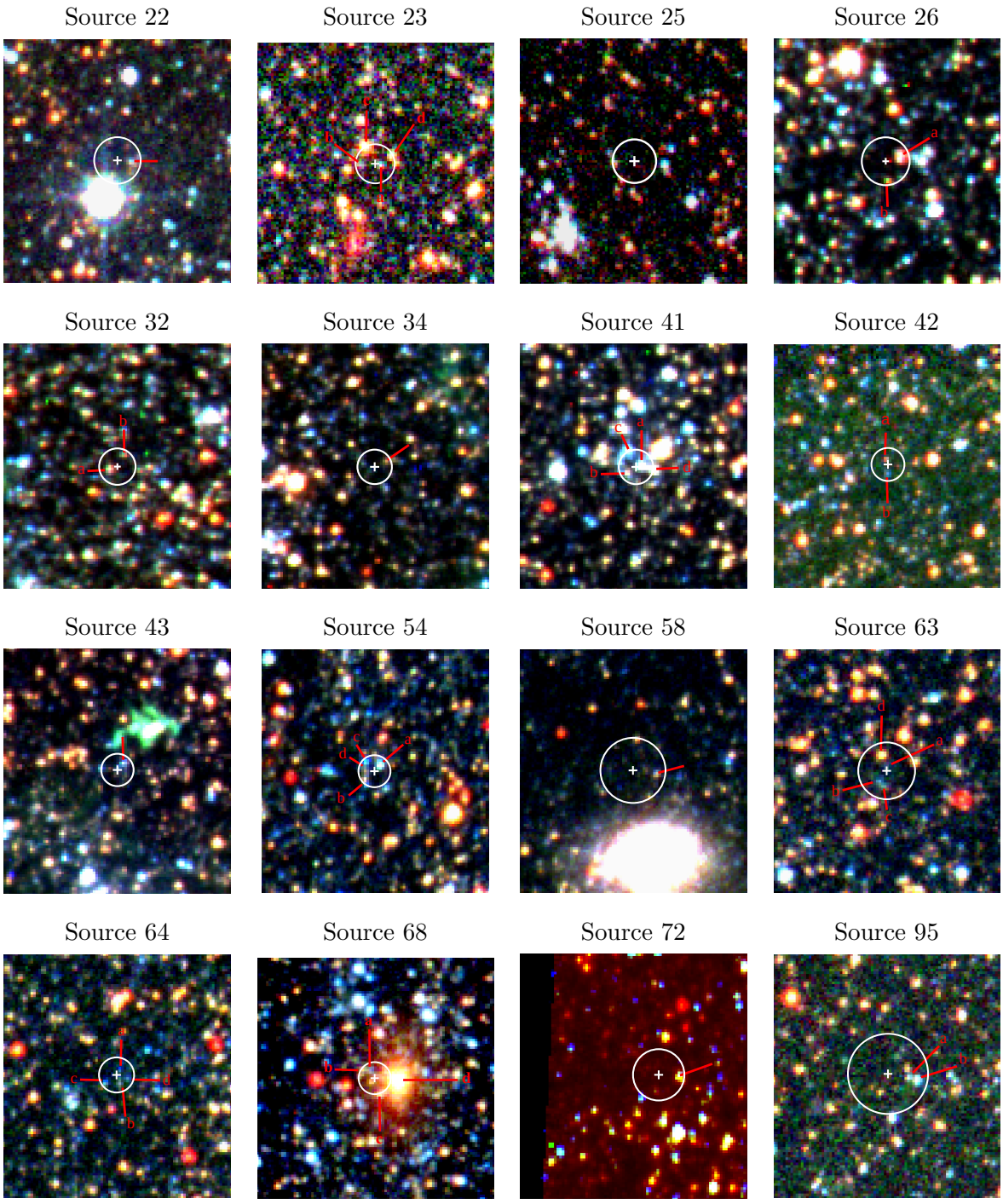

Figure 4.1: *Continued*

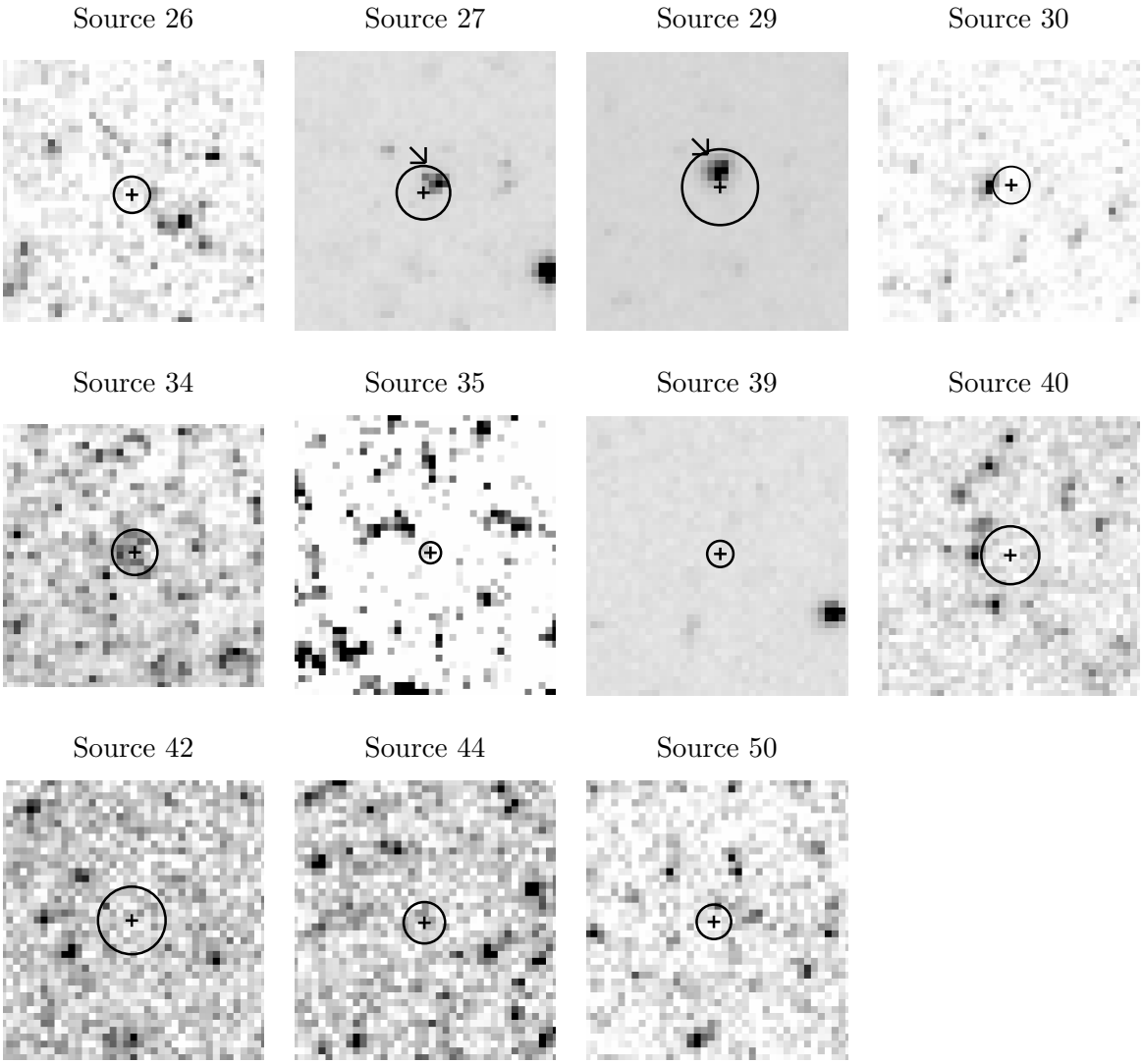

Figure 4.2: Optical *HST* images for X-ray sources detected in NGC 404. Finding charts are $5'' \times 5''$ in size.

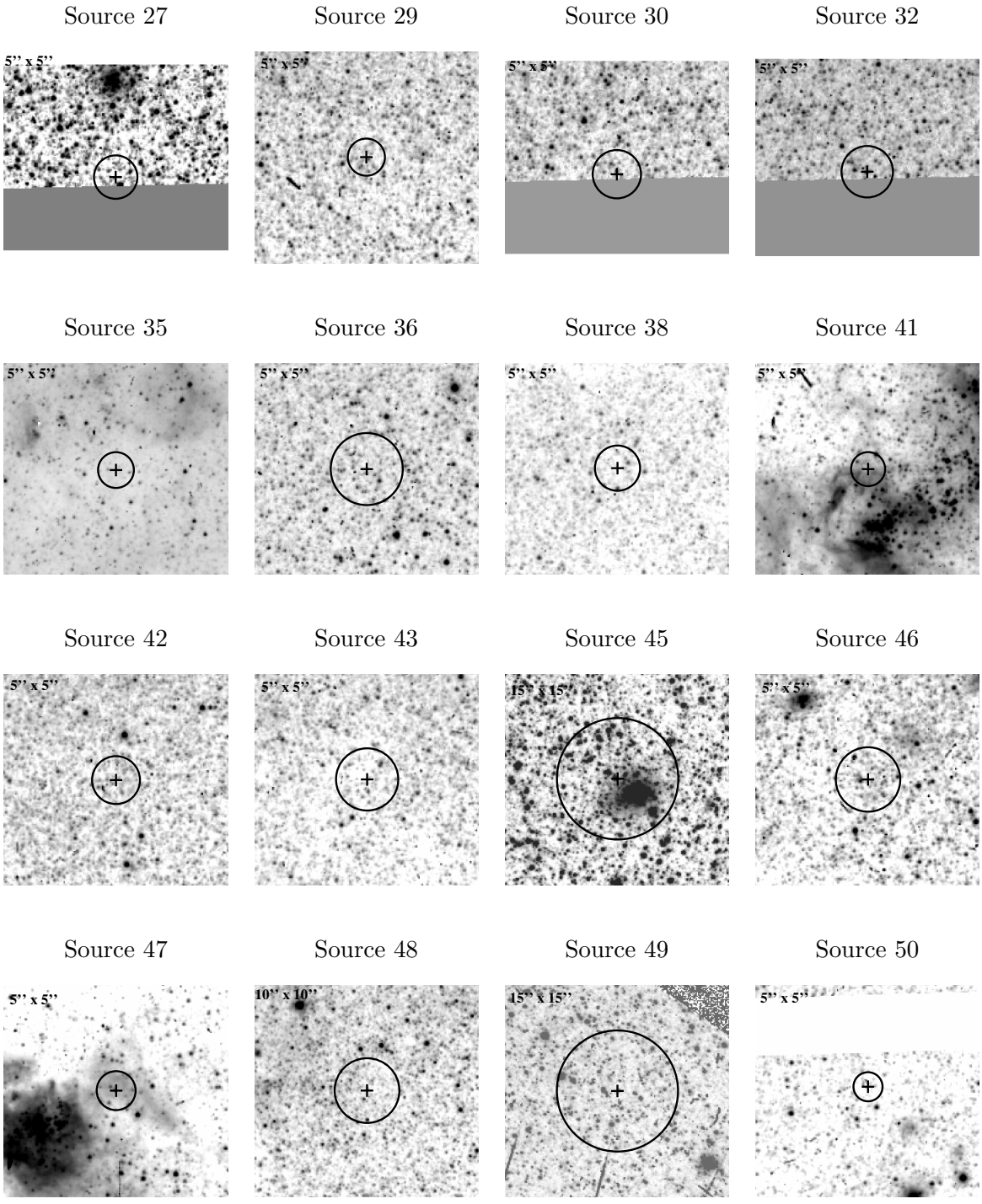

Figure 4.3: Optical *HST* images for X-ray sources detected in NGC 55.

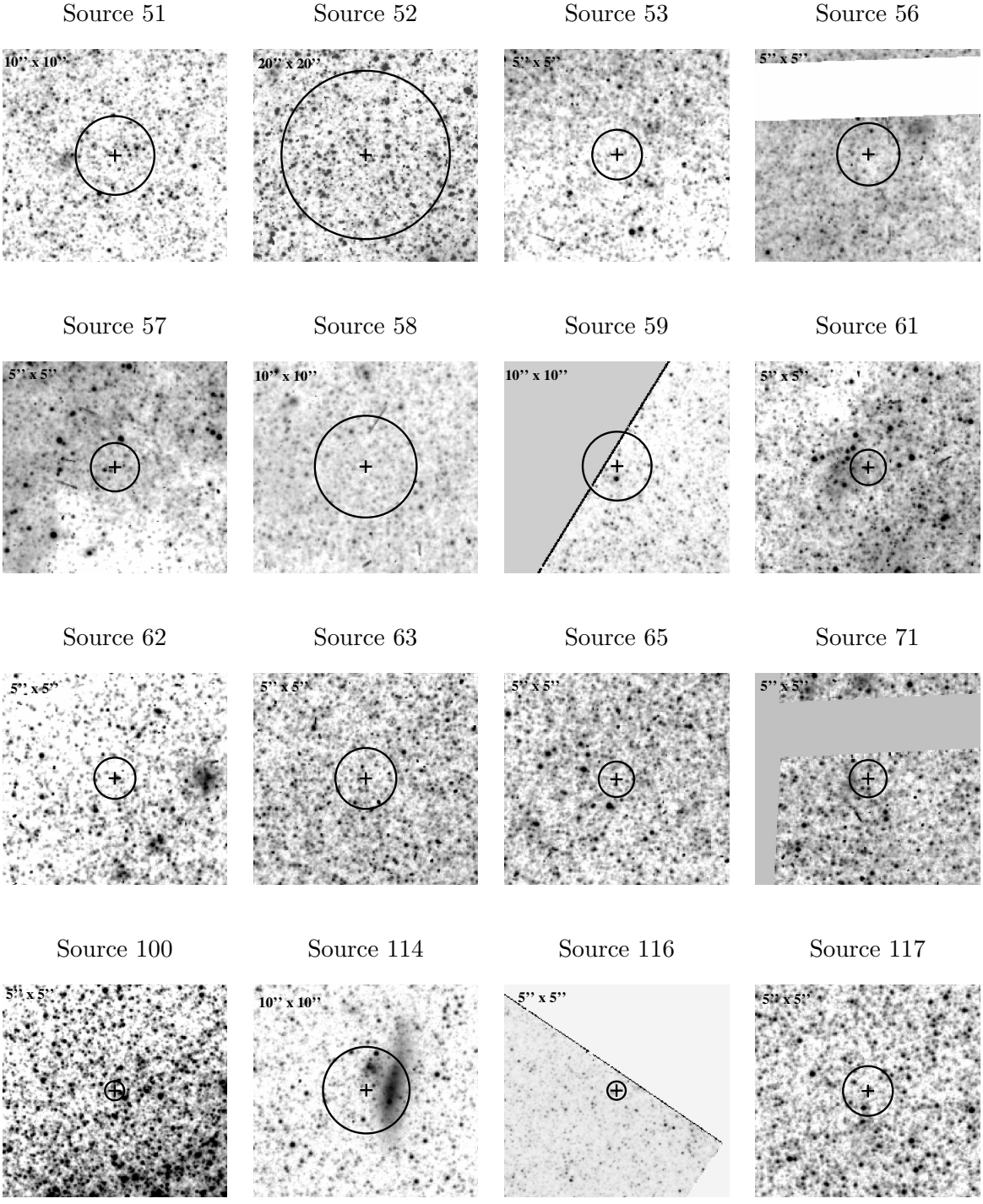

Figure 4.3: *Continued*

Source 119

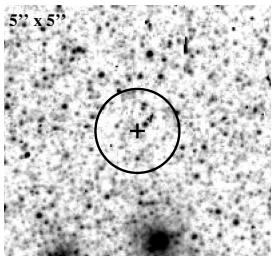

Source 120

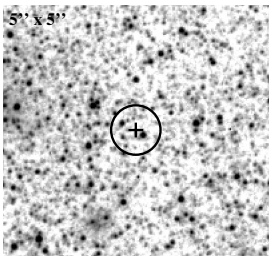

Source 122

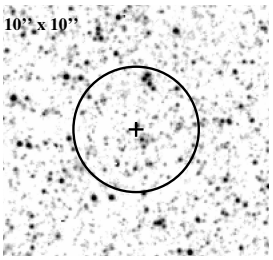

Source 123

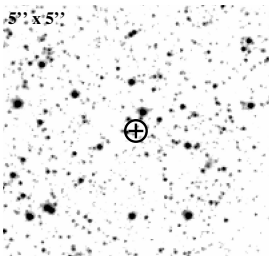

Source 124

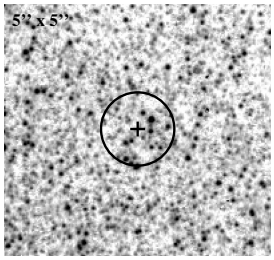

Source 130

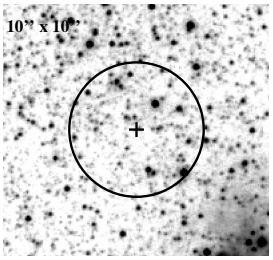

Source 133

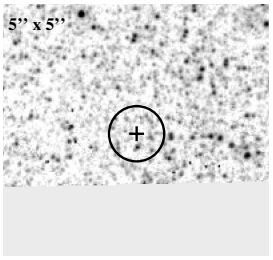

Source 134

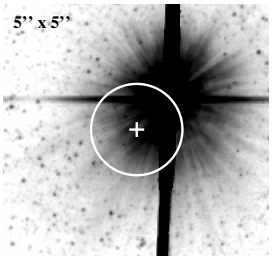

Source 138

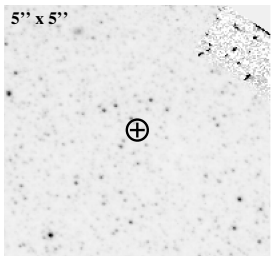

Figure 4.3: *Continued*

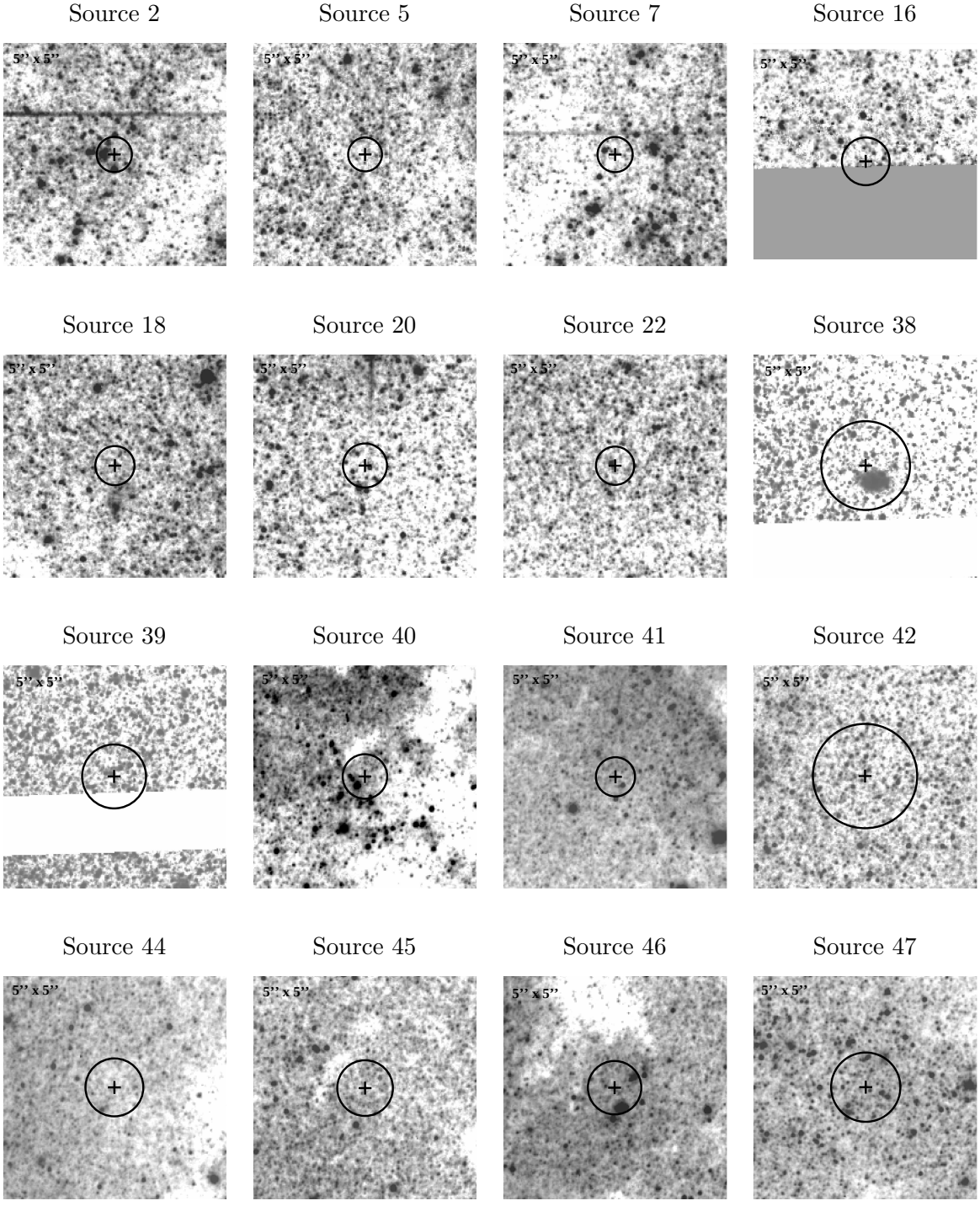

Figure 4.4: Optical *HST* images for X-ray sources detected in NGC 2403.

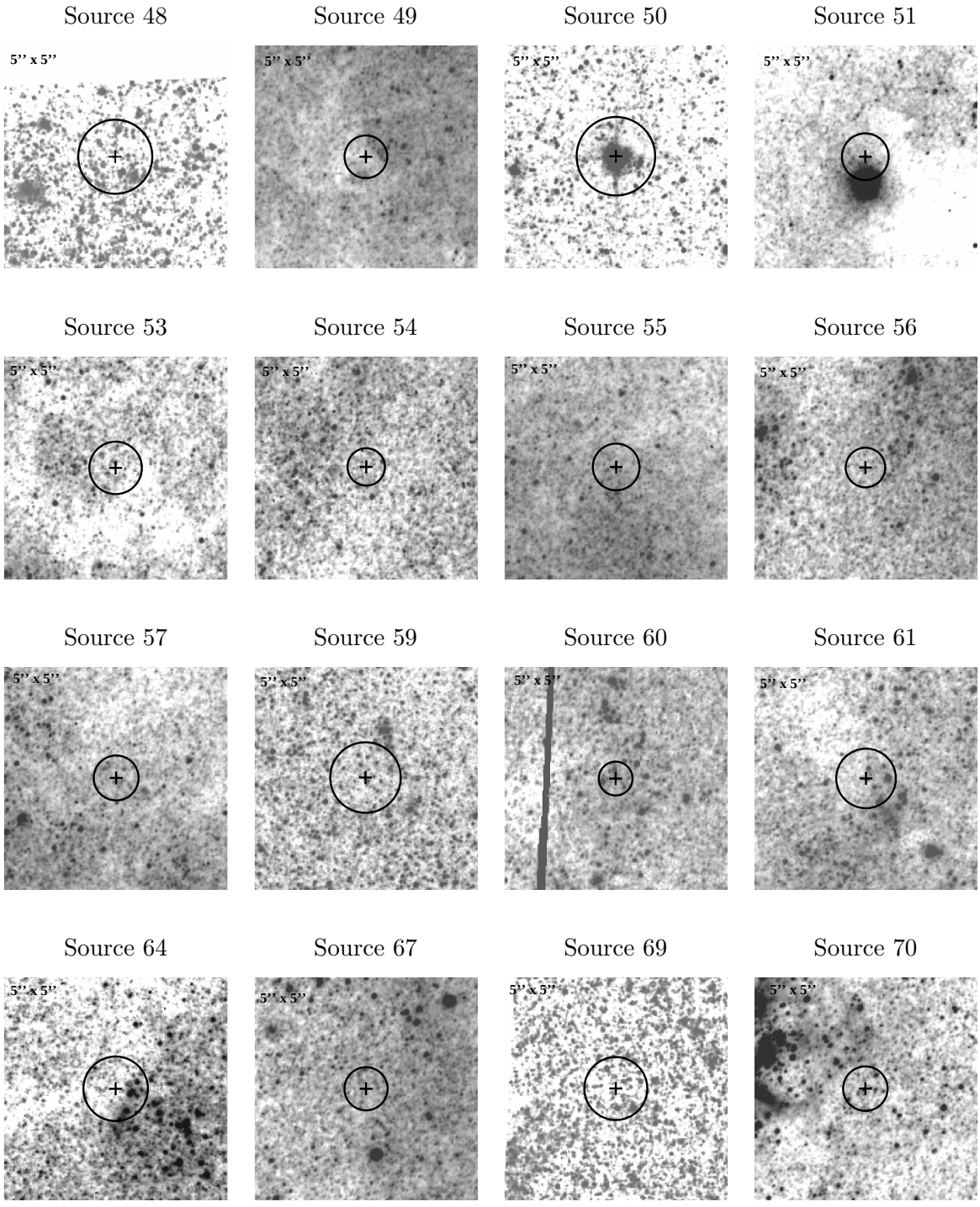

Figure 4.4: *Continued*

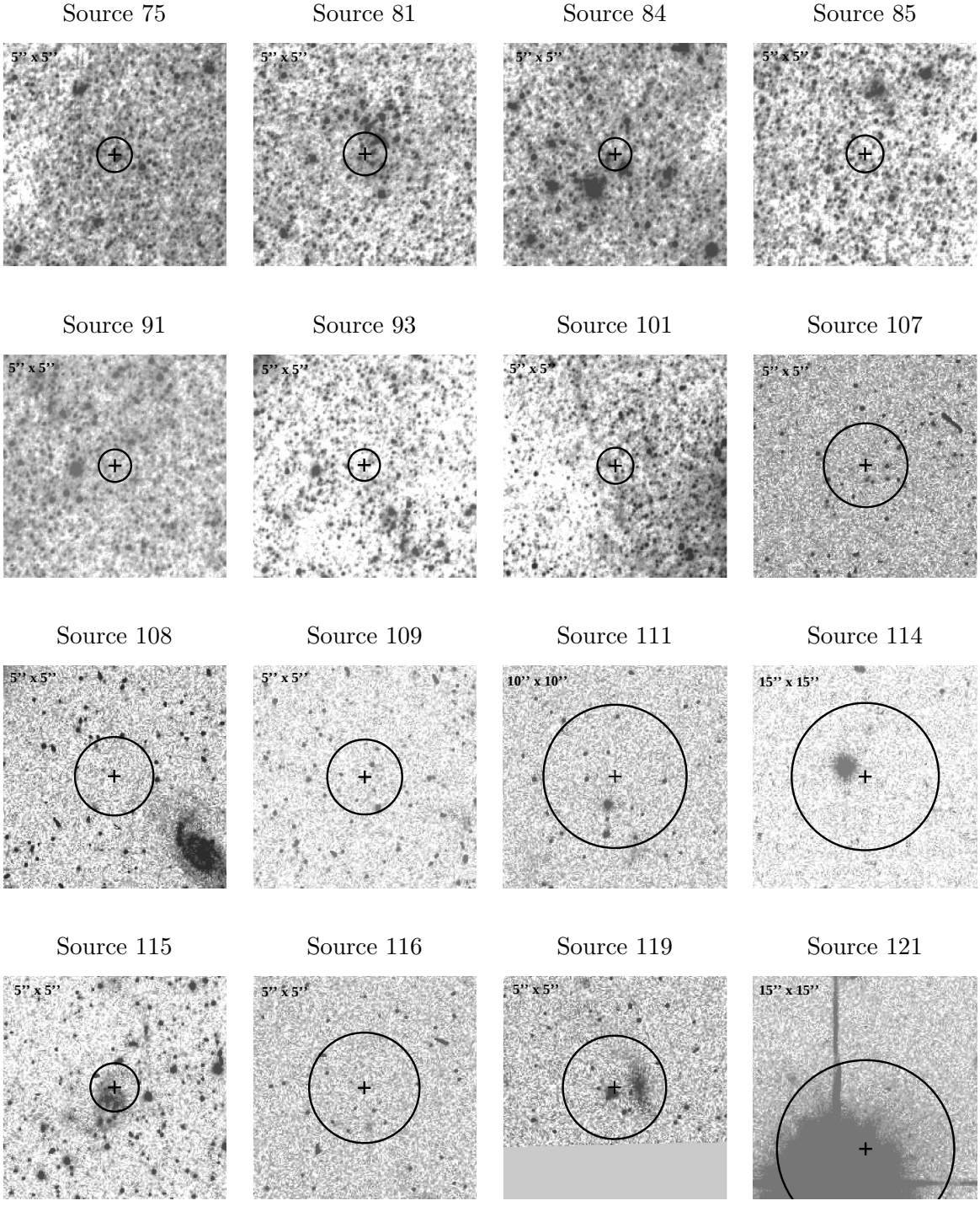

Figure 4.4: *Continued*

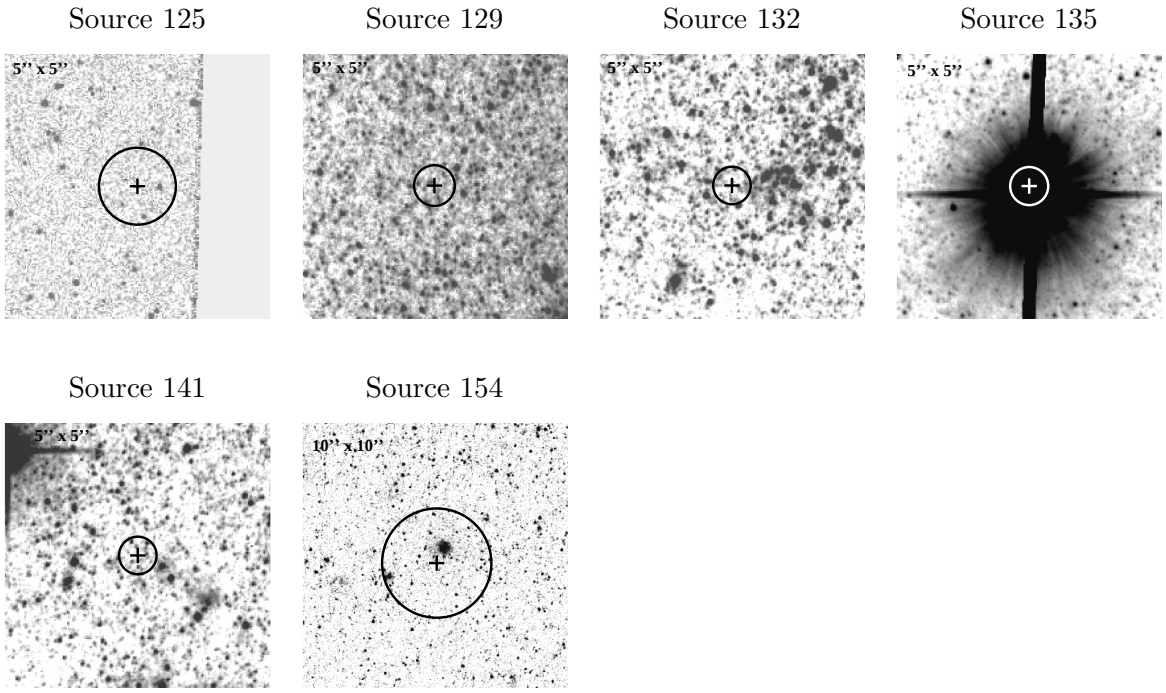

Figure 4.4: *Continued*

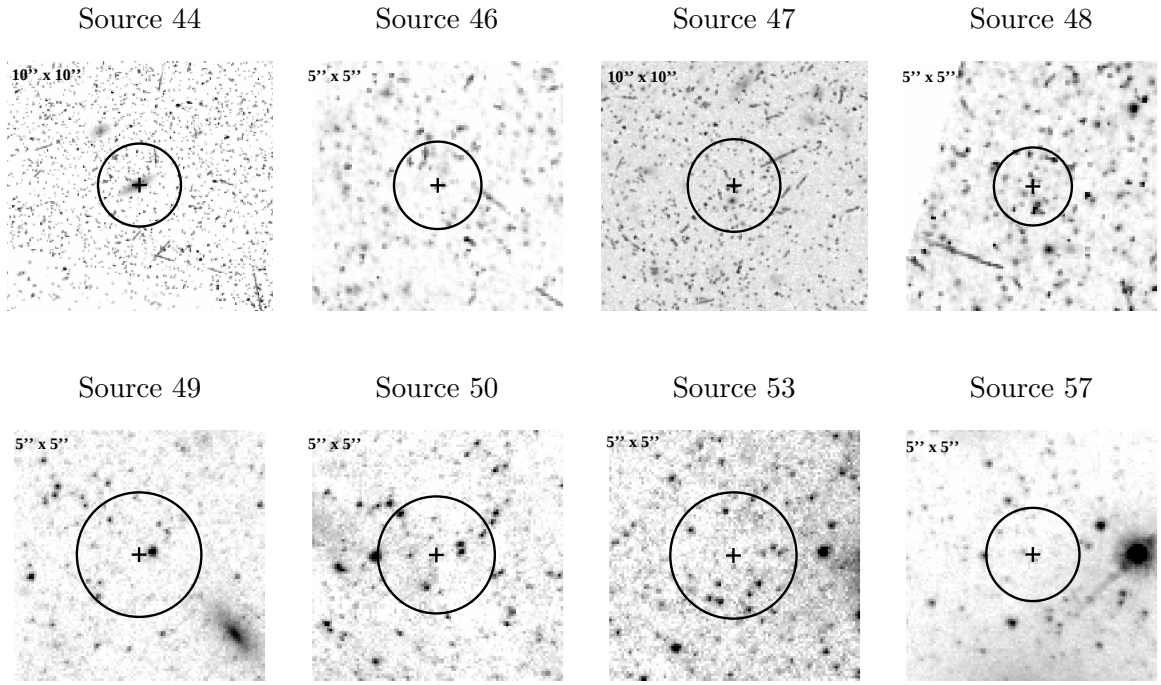

Figure 4.5: Optical *HST* images for X-ray sources detected in NGC 4214.

Table 4.1: Multiwavelength Observations of CLVS X-ray Sources

No.	*GALEX*		*HST*			USNO-B1.0		2MASS			NVSS
	NUV	FUV	$F435W$ or $F475W$	$F606W$ or $F555W$	$F814W$	B	R	J	H	K	$S_{1.4\mathrm{GHz}}$ (mJy)
(1)	(2)	(3)	(4)	(5)	(6)	(7)	(8)	(9)	(10)	(11)	(12)
NGC 300											
1		17.65±0.07									
3	19.18±0.01	18.95±0.01				20.37	19.44				
4			24.7±0.6	23.8±0.6	23.7±0.6						
5			25.51±0.03	25.60±0.03	25.86±0.08						
7	16.97±0.01	16.93±0.01	24.04±0.02	24.13±0.06	24.25±0.03		17.68				
8			19.7±0.5	18.5±0.5	16.6±0.4	19.97	17.84	15.67±0.07	15.08±0.10	14.68±0.10	
9	18.55±0.01	18.69±0.01	25.43±0.03	24.40±0.01	23.53±0.02						
10			26.00±0.07	25.49±0.06	23.72±0.02						
11			27.35±0.20	26.36±0.10	25.46±0.06						
12	23.81±0.16	23.33±0.11									
13			22.10±0.01	22.13±0.01	22.10±0.01		18.21				
14		17.44±0.01	26.69±0.12	26.96±0.17	26.86±0.19						
15	15.57±0.01	15.67±0.01					18.34				
16	19.58±0.02	19.91±0.02									
17			24.59±0.02	24.06±0.01	23.56±0.02						
18			27.35±0.21	26.52±0.12	25.49±0.06						
19			26.34±0.06	25.42±0.03	24.69±0.03						
20			26.61±0.11	26.51±0.11	26.42±0.12						
21			26.00±0.05	25.11±0.03	24.08±0.02						
22	16.33±0.01	16.05±0.01	24.66±0.04	25.63±0.04	25.66±0.07						
23		20.32±0.23	26.80±0.13	26.52±0.12	25.85±0.08						

Continued on next page

Table 4.1 – continued from previous page

No.	*GALEX*		*HST*			USNO-B1.0		2MASS			NVSS
	NUV	FUV	$F435W$ or $F475W$	$F606W$ or $F555W$	$F814W$	B	R	J	H	K	$S_{1.4\mathrm{GHz}}$ (mJy)
(1)	(2)	(3)	(4)	(5)	(6)	(7)	(8)	(9)	(10)	(11)	(12)
25		19.32±0.18				20.41	19.63				
26		17.82±0.01	26.02±0.06	24.83±0.03	22.46±0.01						
31						19.87	19.70				
32			26.74±0.10	25.57±0.04	24.80±0.04						
33	21.43±0.27										
34			27.12±0.13	25.93±0.05	24.82±0.04						
37	22.69±0.37										
40								14.83±0.06	14.16±0.08	13.73±0.07	
41			25.66±0.05	25.83±0.05	26.07±0.12	16.05	14.63				
42			26.60±0.11	26.91±0.16	26.72±0.17						
43			25.22±0.03	25.30±0.03	25.12±0.05			14.83±0.06	14.16±0.08	13.73±0.07	
44							17.11				
45	23.59±0.13	23.46±0.12									
46							19.61				
49		22.64±0.08									
51							19.59				
53	24.50±0.21					20.17	19.71				
54			24.80±0.04	25.03±0.05	24.95±0.07		19.07				
58			26.87±0.16	25.74±0.07	24.49±0.04			16.15±0.10	15.33±0.11	14.84±0.14	
59	17.56±0.01	17.93±0.01				19.80	19.52				
63			27.03±0.16	27.03±0.19	27.09±0.25						
64			26.81±0.14	27.19±0.22	26.98±0.22						
66	23.66±0.13					20.31	19.71				
67		19.73±0.16									

Continued on next page

Table 4.1 – continued from previous page

No.	*GALEX*		*HST*			USNO-B1.0		2MASS			NVSS
	NUV	FUV	*F*435*W* or *F*475*W*	*F*606*W* or *F*555*W*	*F*814*W*	*B*	*R*	*J*	*H*	*K*	$S_{1.4\mathrm{GHz}}$ (mJy)
(1)	(2)	(3)	(4)	(5)	(6)	(7)	(8)	(9)	(10)	(11)	(12)
68			26.52±0.11	26.36±0.12	25.52±0.08						
69	23.36±0.11	23.71±0.16				17.72	15.34	12.59±0.03	12.00±0.03	11.71±0.03	
72			25.90±0.08	24.59±0.04	22.91±0.02						
74	16.72±0.01	16.85±0.01									
76	20.59±0.02	21.79±0.04				17.30	15.22				
84						20.36	17.53				
85	21.18±0.08	19.56±0.02				20.24	19.43				
86	21.71±0.04	22.22±0.06				20.11	18.95				
87		19.64±0.19									
88	21.65±0.25	22.65±0.45				20.42	18.44				
92						20.34	23.53				
95			25.21±0.04	25.39±0.05	25.64±0.07						
					NGC 404						
1	22.07 ± 0.22					20.22	18.57				
3	22.96 ± 0.15										
4						19.22	17.21	16.32 ± 0.12	15.89 ± 0.18	15.47 ± 0.23	
5						19.45	18.73				
7	21.74 ± 0.04	22.86 ± 0.09				19.05	20.77				
8											53.7 ± 2.0
15	22.74 ± 0.08	23.38 ± 0.12									
17	22.11 ± 0.10					18.83					
19	22.06 ± 0.07	22.20 ± 0.09									
20		22.57 ± 0.30									
21		24.05 ± 0.26									

Continued on next page

Table 4.1 – continued from previous page

No.	*GALEX*		*HST*			USNO-B1.0		2MASS			NVSS
	NUV	FUV	*F*435*W* or *F*475*W*	*F*606*W* or *F*555*W*	*F*814*W*	*B*	*R*	*J*	*H*	*K*	$S_{1.4\mathrm{GHz}}$ (mJy)
(1)	(2)	(3)	(4)	(5)	(6)	(7)	(8)	(9)	(10)	(11)	(12)
27	24.30 ± 0.21			25.33 ± 0.02	24.25 ± 0.01	20.36	19.11				
28	23.87 ± 0.27										
29				21.68 ± 0.01	19.21 ± 0.01						
32	21.69 ± 0.41										
39	22.14 ± 0.11										
41	15.12 ± 0.01	17.07 ± 0.01						11.46 ± 0.04	10.56 ± 0.03	10.55 ± 0.04	3.4 ± 0.4
44	20.73 ± 0.36										
50	21.94 ± 0.38										
51	20.18 ± 0.17	20.45 ± 0.31				18.39	16.59	16.35 ± 0.13	15.61 ± 0.13	14.98 ± 0.14	
52	23.03 ± 0.12	23.83 ± 0.23				20.75					
53	19.98 ± 0.04										
59	21.72 ± 0.09										
65		17.60 ± 0.07				9.02	8.32	7.66 ± 0.02	7.52 ± 0.02	7.47 ± 0.02	
66	22.71 ± 0.11	23.39 ± 0.22									
67	22.50 ± 0.10	24.07 ± 0.19				20.65	18.88				
68						20.64					
69								16.25 ± 0.09	15.55 ± 0.11	14.97 ± 0.13	
70	22.75 ± 0.13										
72	24.41 ± 0.52										
74	22.37 ± 0.06										
				NGC 55							
1		19.40±0.15									
2	21.28±0.20	22.24±0.22				19.88	17.83				
3	23.41±0.09	24.18±0.14									

Continued on next page

Table 4.1 – continued from previous page

No.	*GALEX*		*HST*			USNO-B1.0		2MASS			NVSS
	NUV	FUV	*F*435*W* or *F*475*W*	*F*606*W* or *F*555*W*	*F*814*W*	*B*	*R*	*J*	*H*	*K*	$S_{1.4\mathrm{GHz}}$ (mJy)
(1)	(2)	(3)	(4)	(5)	(6)	(7)	(8)	(9)	(10)	(11)	(12)
5	22.66±0.45										
7	20.25±0.01	23.29±0.07				19.93	20.45				
8	22.31±0.05					20.17	20.22				
10		16.47±0.02									
11		21.67±0.16									
12	22.82±0.08	23.44±0.08									
13	22.66±0.07	21.88±0.03									
14		21.65±0.40									
15	24.72±0.21										
17	22.74±0.27										
18	24.18±0.17	24.16±0.12									
19	24.60±0.18										
20	23.95±0.15										
21		22.86±0.34									
22	23.01±0.09	24.96±0.21									
23	17.74±0.01	18.53±0.01				13.11	11.45	9.96±0.02	9.48±0.02	9.35±0.02	
24	22.07±0.24	21.78±0.16				21.27	24.15				
29				22.68±0.01	22.01±0.01						
35				21.52±0.01	21.66±0.01						
36	16.55±0.01			23.12±0.02	21.77±0.01						
37		23.28±0.06				18.81	23.64				
38				24.16±0.03	22.81±0.02						
41	12.22±0.01	12.86±0.01									
42				23.09±0.02	21.84±0.01						

Continued on next page

Table 4.1 – continued from previous page

No.	*GALEX*		*HST*			USNO-B1.0		2MASS			NVSS
	NUV	FUV	$F435W$ or $F475W$	$F606W$ or $F555W$	$F814W$	B	R	J	H	K	$S_{1.4\mathrm{GHz}}$ (mJy)
(1)	(2)	(3)	(4)	(5)	(6)	(7)	(8)	(9)	(10)	(11)	(12)
43				22.02±0.01	20.89±0.01						
45							18.09	16.86±0.16	15.85±0.16	15.65±0.16	
46				23.77±0.03	21.68±0.01						
47	13.76±0.01	13.75±0.01									
48	16.01±0.01	16.15±0.01									
50		10.84±0.01		23.72±0.03	23.08±0.02						
52	16.58±0.01	16.81±0.01		20.82±0.01	20.68±0.01						
53				23.11±0.02	21.91±0.01						
54	15.62±0.01			23.12±0.02	21.87±0.02						
55		13.90±0.01									
56	15.16±0.01	15.12±0.01		21.61±0.01	20.47±0.01						
57	15.53±0.01	15.50±0.01		22.37±0.01	20.71±0.01						
58				21.66±0.01	20.41±0.01						
60	22.65±0.28										
61				22.78±0.01	21.66±0.01						
62				23.80±0.03	23.75±0.04						
63				23.48±0.02	22.76±0.02						
65				22.55±0.01	21.30±0.01						
66	16.21±0.01										
67	21.50±0.41										
68	23.87±0.13										
69	24.41±0.14	24.09±0.10									
71	15.80±0.01	16.05±0.01		24.44±0.04	22.92±0.02						
73	22.44±0.04					19.92	20.56				

Continued on next page

Table 4.1 – continued from previous page

No.	*GALEX*		*HST*			USNO-B1.0		2MASS			NVSS
	NUV	FUV	*F*435*W* or *F*475*W*	*F*606*W* or *F*555*W*	*F*814*W*	*B*	*R*	*J*	*H*	*K*	$S_{1.4\mathrm{GHz}}$ (mJy)
(1)	(2)	(3)	(4)	(5)	(6)	(7)	(8)	(9)	(10)	(11)	(12)
74	23.81±0.11	23.40±0.09									
75		20.43±0.12									
76	23.68±0.12										
77		24.01±0.09									
78	16.21±0.01										
82	22.00±0.03	22.94±0.07				19.83	21.12				
83	24.79±0.36										
84						19.79	21.29	15.73±0.07	15.09±0.08	14.95±0.12	
90						21.29	20.86				
91	20.92±0.02	22.62±0.08				12.47	12.42	14.07±0.07	13.28±0.09	12.71±0.06	
94	16.21±0.01										
98	19.39±0.01	20.25±0.01				13.39	13.24	14.81±0.09	13.99±0.12	13.40±0.09	4.2±0.5
100	15.49±0.01	15.31±0.01									
103		19.25±0.15									
104	22.35±0.06	22.64±0.05									
106		23.77±0.08					19.23				
107	21.47±0.11					21.01	20.59				
110	23.49±0.08					19.86	20.49				
111		20.98±0.34									
112	24.76±0.18										
113	22.66±0.05	23.19±0.07				21.04	23.14				
114		20.10±0.02		22.45±0.01	22.42±0.1	17.35	19.11				
115	20.46±0.23					15.63	16.09	15.42±0.08	14.83±0.09	14.14±0.08	
117				22.98±0.01	22.79±0.02						

Continued on next page

Table 4.1 – continued from previous page

No.	*GALEX*		*HST*			USNO-B1.0		2MASS			NVSS
	NUV	FUV	$F435W$ or $F475W$	$F606W$ or $F555W$	$F814W$	B	R	J	H	K	$S_{1.4\mathrm{GHz}}$ (mJy)
(1)	(2)	(3)	(4)	(5)	(6)	(7)	(8)	(9)	(10)	(11)	(12)
119				23.29±0.02	23.13±0.03		19.06				
120		18.63±0.01		22.19±0.01	22.80±0.02						
122		16.95±0.01		23.19±0.01	22.80±0.02						
123		15.17±0.01									
124				22.34±0.01	21.26±0.01						
125	14.46±0.01	14.49±0.01						16.04±0.11	15.47±0.12	14.72±0.13	
126							17.20	16.29±0.12	15.55±0.14	14.90±0.13	
127		15.07±0.01					12.09				
128						20.26	19.54				
129	17.69±0.01	17.90±0.01									
130	15.56±0.01	15.54±0.01		21.02±0.01	19.86±0.01						
133				23.86±0.03	22.18±0.02						
134	18.49±0.01							10.18±0.02	9.66±0.02	9.52±0.02	
135	21.72±0.03	24.22±0.16					16.87	16.21±0.11	15.66±0.15	15.52±0.14	
139		23.85±0.09									
142	23.70±0.16										
145	21.07±0.08										
146	24.22±0.18										
149	21.20±0.44										
151	23.36±0.11										
152	21.63±0.36										
					NGC 2403						
1	21.02±0.04	21.03±0.04									
2			25.86±0.06	24.27±0.03	22.76±0.02						

Continued on next page

Table 4.1 – continued from previous page

No.	*GALEX*		*HST*			USNO-B1.0		2MASS			NVSS
	NUV	FUV	$F435W$ or $F475W$	$F606W$ or $F555W$	$F814W$	B	R	J	H	K	$S_{1.4\mathrm{GHz}}$ (mJy)
(1)	(2)	(3)	(4)	(5)	(6)	(7)	(8)	(9)	(10)	(11)	(12)
3	17.32±0.01	17.47±0.01									
5			27.26±0.18	25.57±0.07	24.28±0.05						
7	15.80±0.01	16.01±0.01	24.08±0.02	22.43±0.01	20.75±0.01						
9	19.01±0.09	20.92±0.19									
11	22.37±0.07	23.46±0.17									
12						20.85	20.06				
14	22.83±0.10	23.48±0.17				20.99					
15							20.56				
16			25.24±0.05	24.91±0.06	24.33±0.07						
17	20.31±0.02	20.08±0.02									
18	15.12±0.01	15.46±0.01	27.35±0.20	25.83±0.08	23.97±0.04						
20			24.79±0.03	23.38±0.02	21.42±0.01						
21	18.78±0.01	18.61±0.01					18.67	15.72±0.06	15.20±0.07	14.89±0.11	
22			24.23±0.02	22.68±0.01	21.25±0.01						
24		20.05±0.14									
25						18.57	17.68				
31	19.82±0.02	20.12±0.04				19.75	19.11				
33	23.61±0.17					17.66	15.40	12.79±0.02	12.15±0.02	11.99±0.02	
34	19.23±0.01					14.13	12.33	11.52±0.02	11.08±0.02	11.02±0.02	
35		21.72±0.09									
36	23.98±0.44										
37	22.57±0.10	23.24±0.16									
38				25.39±0.08	25.30±0.05						
39				26.42±0.16	24.35±0.03						

Continued on next page

Table 4.1 – continued from previous page

No.	*GALEX*		*HST*			USNO-B1.0		2MASS			NVSS
	NUV	FUV	$F435W$ or $F475W$	$F606W$ or $F555W$	$F814W$	B	R	J	H	K	$S_{1.4\mathrm{GHz}}$ (mJy)
(1)	(2)	(3)	(4)	(5)	(6)	(7)	(8)	(9)	(10)	(11)	(12)
40	17.25±0.01	16.84±0.01	25.50±0.06	25.20±0.06	24.93±0.10						
41	15.95±0.01	16.53±0.01	21.95±0.01	21.82±0.01	21.69±0.01						
42				24.98±0.08	25.05±0.04						
43	23.65±0.14					20.47	19.66				
44			27.05±0.19	25.53±0.08	23.74±0.04						
45			27.42±0.27	25.42±0.07	22.84±0.02						
46	15.83±0.01	16.33±0.01	23.84±0.02	23.66±0.02	23.26±0.03						
47		17.02±0.01	23.54±0.01	23.49±0.02	23.36±0.03						
48				26.85±0.18	25.32±0.06						
49	10.45±0.01		25.64±0.07	25.31±0.08	25.03±0.14						
50				26.10±0.18	25.01±0.04		17.06	15.31±0.04	14.66±0.05	14.43±0.07	
51	17.97±0.01	18.39±0.01									
53	10.50±0.01		25.98±0.08	24.46±0.04	22.83±0.02						
54			25.93±0.11	24.93±0.07	23.83±0.06						
55	10.50±0.01		24.24±0.02	24.02±0.03	23.87±0.05						
56	16.59±0.01	17.66±0.01	26.50±0.13	25.05±0.06	24.05±0.05						
57	10.50±0.01		25.49±0.06	23.88±0.03	22.49±0.02						
58	22.11±0.10	21.69±0.08									
59				27.11±0.21	25.38±0.06						
60	17.03±0.01	17.60±0.01	24.86±0.03	23.64±0.02	22.52±0.02						
61			22.89±0.01	22.89±0.01	23.00±0.02						
62	12.92±0.01	18.30±0.01				8.84	8.10	7.40±0.02	7.20±0.02	7.14±0.02	
63	17.03±0.01	17.60±0.01	26.19±0.09	24.72±0.04	23.56±0.03						
64	17.79±0.01	17.90±0.01	23.04±0.01	22.91±0.01	22.80±0.02						

Continued on next page

Table 4.1 – continued from previous page

No.	*GALEX*		*HST*			USNO-B1.0		2MASS			NVSS
	NUV	FUV	*F*435*W* or *F*475*W*	*F*606*W* or *F*555*W*	*F*814*W*	*B*	*R*	*J*	*H*	*K*	$S_{1.4\mathrm{GHz}}$ (mJy)
(1)	(2)	(3)	(4)	(5)	(6)	(7)	(8)	(9)	(10)	(11)	(12)
66		18.26±0.01				17.51					
67			25.63±0.06	24.26±0.03	23.15±0.03						
68	15.69±0.01	16.27±0.01									
69				26.16±0.18	25.39±0.05						
70	15.13±0.01	15.44±0.01	23.23±0.01	23.18±0.02	23.28±0.03						
75		17.64±0.01	25.82±0.07	24.73±0.04	23.50±0.03						
77	17.64±0.01	17.52±0.01									
78	15.82±0.01	15.80±0.01					11.73	13.41±0.03	12.77±0.02	12.66±0.02	
81			24.14±0.02	24.10±0.02	24.03±0.04						
82	19.42±0.01	19.56±0.02				20.59					
83		23.85±0.18									
84		17.82±0.01	22.23±0.01	22.12±0.01	22.05±0.01						
85			25.66±0.05	24.69±0.04	23.76±0.03						
86	18.07±0.01	18.07±0.01									
87						18.91	16.43	15.60±0.05	15.16±0.06	14.99±0.11	
89						19.27	19.32				
91			26.45±0.10	25.46±0.06	24.50±0.06						
92	21.48±0.03	21.29±0.03									
93			26.52±0.11	25.56±0.07	24.52±0.06						
94	23.03±0.41										
95	22.52±0.04										
97						18.76	15.54	13.08±0.02	12.48±0.02	12.24±0.02	
98	23.35±0.13	22.19±0.06				20.36	18.06	16.81±0.16	15.82±0.15	15.40±0.17	
100	24.51±0.51										

Continued on next page

Table 4.1 – continued from previous page

No.	*GALEX*		*HST*			USNO-B1.0		2MASS			NVSS
	NUV	FUV	$F435W$ or $F475W$	$F606W$ or $F555W$	$F814W$	B	R	J	H	K	$S_{1.4\mathrm{GHz}}$ (mJy)
(1)	(2)	(3)	(4)	(5)	(6)	(7)	(8)	(9)	(10)	(11)	(12)
101			26.08±0.07	24.72±0.03	23.89±0.04						
102	23.38±0.35					21.07	20.98				
103	20.38±0.16										
104		23.62±0.13									
106	22.22±0.10	23.19±0.13				20.60	19.47	16.88±0.15	16.22±0.18	15.52±0.19	
107				25.03±0.04	24.30±0.04						
108	21.75±0.06	21.62±0.05		26.76±0.13	26.56±0.20						
109	22.84±0.16	22.60±0.11		24.71±0.03	24.68±0.05						
110		22.04±0.58									
111	24.77±0.47			27.33±0.22	26.81±0.23						
112	23.25±0.10	22.31±0.07									
113							20.14				
114	21.80±0.05	23.14±0.11		20.46±0.01	20.20±0.01	20.89	20.02				
116	22.03±0.27			26.60±0.11	25.31±0.07						
118	22.30±0.16					21.06	19.82				
119				22.55±0.01	21.89±0.01						
120						20.97	20.13	15.57±0.06	14.94±0.07	14.57±0.09	
121	18.21±0.01	23.72±0.23		25.14±0.04	24.12±0.03	14.50	13.42	12.92±0.02	12.68±0.02	12.59±0.02	
122							19.58				
124	24.45±0.21										
125				25.48±0.05	24.38±0.04						
126	18.26±0.01	18.17±0.01									
127	22.41±0.33										
129			27.14±0.15	25.48±0.05	23.36±0.02						

Continued on next page

Table 4.1 – continued from previous page

No.	*GALEX*		*HST*			USNO-B1.0		2MASS			NVSS
	NUV	FUV	$F435W$ or $F475W$	$F606W$ or $F555W$	$F814W$	B	R	J	H	K	$S_{1.4\mathrm{GHz}}$ (mJy)
(1)	(2)	(3)	(4)	(5)	(6)	(7)	(8)	(9)	(10)	(11)	(12)
130	23.68±0.18										
131	22.42±0.42	22.62±0.40									
132	23.12±0.01	17.58±0.01	25.81±0.06	25.74±0.07	26.09±0.19						
135	17.30±0.01	17.57±0.01					17.56	16.19±0.08	15.54±0.11	15.42±0.19	
136						20.10	19.82				
139	23.07±0.01					14.36	13.33				
141	17.69±0.01	17.89±0.01	26.27±0.09	25.33±0.05	23.95±0.04						
144	14.46±0.01	19.39±0.01				11.14	10.55	9.95±0.02	9.77±0.02	9.72±0.02	
145	23.07±0.47										
146						19.12	17.91				
148		21.80±0.05									
149	23.84±1.03					20.84	18.65	16.69±0.13	15.81±0.13	15.85±0.26	
150		20.58±0.02									
151						2057	18.78	16.62±0.12	16.30±0.21	15.65±0.21	
152	22.07±0.49										
153	18.97±0.01	20.30±0.02									
154	21.01±0.24	21.16±0.24		25.25±0.04	24.10±0.03						
155	17.69±0.01	17.89±0.01									
157	18.74±0.01	20.06±0.02				20.91	20.10				
158		19.35±0.02				19.77	18.98				
163		19.81±0.03									
165		23.01±0.11									
166						18.72	15.90	14.46±0.03	13.76±0.03	13.64±0.04	
167		22.82±0.08									

Continued on next page

Table 4.1 – continued from previous page

No.	*GALEX*		*HST*			USNO-B1.0		2MASS			NVSS
	NUV	FUV	$F435W$ or $F475W$	$F606W$ or $F555W$	$F814W$	B	R	J	H	K	$S_{1.4\mathrm{GHz}}$ (mJy)
(1)	(2)	(3)	(4)	(5)	(6)	(7)	(8)	(9)	(10)	(11)	(12)
168	22.60±0.07	22.59±0.08					19.25				
170	16.83±0.01	16.81±0.01									
171	20.18±0.02	19.91±0.02									
173		20.51±0.03									
174	18.75±0.01	18.65±0.01				20.66	19.92				
175	17.51±0.01	17.72±0.01									
179	15.15±0.01										
181	14.60±0.01	14.74±0.01				12.47	16.81				
182						20.64	20.13				
184							19.59	16.68±0.14	16.15±0.16	15.96±0.16	
186	17.77±0.01	18.32±0.01				18.43	16.91				
188	22.48±0.08							15.87±0.06	15.49±0.10	15.28±0.15	
190	23.48±0.17										
NGC 4214											
1						18.25	19.79				
3	22.64±0.57										
4	24.34±0.65										
5		20.15±0.20				19.47	20.59	15.83±0.07	15.12±0.09	14.60±0.09	
6	23.53±0.52										
8	21.32±0.36										
10							19.91				
13	21.79±0.04	22.65±0.09				20.25	20.25				
14	21.99±0.14										
17	21.26±0.08	22.10±0.14									

Continued on next page

Table 4.1 – continued from previous page

No.	*GALEX*		*HST*			USNO-B1.0		2MASS			NVSS
	NUV	FUV	*F*435*W* or *F*475*W*	*F*606*W* or *F*555*W*	*F*814*W*	*B*	*R*	*J*	*H*	*K*	$S_{1.4\mathrm{GHz}}$ (mJy)
(1)	(2)	(3)	(4)	(5)	(6)	(7)	(8)	(9)	(10)	(11)	(12)
18	23.29±0.49										
20	11.52±0.01										
22	24.85±0.33										
23		20.27±0.22									
24	23.56±0.14					16.65	14.88	13.29±0.02	12.64±0.03	12.43±0.02	
25	21.91±0.24							16.70±0.16	15.95±0.10	14.91±0.12	
27	20.42±0.05										
29	23.01±0.36										
30	22.86±0.38										
33	21.48±0.08	22.44±0.17				20.54	20.47				
34	21.92±0.39										
37						21.16	19.88				
38	20.67±0.12	21.35±0.34				18.96	19.82				
40	23.11±0.37										
42	11.55±0.01							14.59±0.08	14.15±0.08	13.72±0.07	
43	23.10±0.30	22.85±0.27									
44		20.63±0.25				20.99	20.40				
46				26.17±0.04	26.19±0.07						
48				27.13±0.09	26.24±0.08						
53				25.27±0.03	24.30±0.03						
54	23.47±0.39					20.62	21.22				
56	22.83±0.25					20.56	20.30	15.46±0.08	14.87±0.10	14.23±0.09	6.3±0.4
57				25.31±0.03	24.27±0.02	16.85	16.19	14.39±0.04	13.88±0.04	13.58±0.04	
59	11.52±0.01										

Continued on next page

Table 4.1 – continued from previous page

No.	*GALEX*		*HST*			USNO-B1.0		2MASS			NVSS
	NUV	FUV	$F435W$ or $F475W$	$F606W$ or $F555W$	$F814W$	B	R	J	H	K	$S_{1.4\mathrm{GHz}}$ (mJy)
(1)	(2)	(3)	(4)	(5)	(6)	(7)	(8)	(9)	(10)	(11)	(12)
60	20.43±0.11	21.49±0.36				18.68	17.40				
61	22.33±0.34						20.54				
62						19.33	18.77				
63	21.43±0.20	21.68±0.39									
64		19.25±0.10				19.16	16.97				
67	23.50±0.37										
72	22.84±0.28										
75								16.26±0.09	15.98±0.20	15.71±0.23	
76	23.27±0.61					20.46	20.28				
77		20.96±0.17				19.76	20.10				
78							19.68	13.74±0.02	13.34±0.03	13.23±0.04	
79	23.11±0.24					20.65	19.98				
83	22.79±0.37					20.00					
90	22.11±0.15					20.54	20.63				
95	21.24±0.20	20.49±0.15				18.15	19.86				
96	20.81±0.19	20.76±0.26									
98							18.10				
99		20.12±0.21									
100	23.90±0.43										
103	23.40±0.40					18.62	16.82	15.07±0.05	14.45±0.05	14.28±0.07	
104	21.98±0.42										
106						20.96	19.40	15.90±0.07	15.20±0.09	14.98±0.12	
108	21.62±0.24										
109	22.23±0.49					19.41	20.19				

Continued on next page

Table 4.1 – continued from previous page

No.	*GALEX*		*HST*			USNO-B1.0		2MASS			NVSS
	NUV	FUV	*F*435*W* or *F*475*W*	*F*606*W* or *F*555*W*	*F*814*W*	*B*	*R*	*J*	*H*	*K*	$S_{1.4\mathrm{GHz}}$ (mJy)
(1)	(2)	(3)	(4)	(5)	(6)	(7)	(8)	(9)	(10)	(11)	(12)
110	21.76±0.36							14.41±0.03	13.71±0.04	13.65±0.04	
111	21.61±0.26	21.68±0.41				18.60	17.57	16.74±0.14	16.04±0.20	15.20±0.14	
112							20.79				
113	23.05±0.29	23.23±0.37				20.86	19.40	15.97±0.08	15.36±0.12	15.05±0.13	
114	23.36±0.36										
115	23.31±0.46										

4.3 Source Classification

We used the detection of optical counterpart candidates, along with any available multi-wavelength observations, to assign a source classification to each X-ray source. Many X-ray sources are faint or do not have optical coverage, making their physical nature more ambiguous — we therefore attempt to combine other statistical quantities (i.e., using the radial source distribution, location in spiral arms, inter-arm regions, or background regions, etc.) with individual source properties (variability, X-ray spectral shape, and optical colors) to determine the most likely source classification.

We first consider the statistical properties of each X-ray source. For example, an X-ray source with a galactocentric radius within the optical extent of the host galaxy that is coincident with a spiral arm is very likely to be associated with that galaxy, while an X-ray source at a large galactocentric radius is likely to be a background object. The "optical extent" of each galaxy is estimated as $\sim 3\times$ the optical scale length. We visually examined ground-based, optical R-band and Hα images of each galaxy to identify spiral arms and inter-arm regions (with the exception of NGC 404, which does not possess spiral arms, and NGC 55, which is nearly edge-on), and define background regions not obviously associated with the galaxy.

We next consider the individual X-ray properties of each source. Long-term X-ray variability is observed for both AGN and XRBs. However, SNRs and some HMXB systems do not show significant X-ray variability. We therefore do not discount the possibility of an XRB nature for non-variable sources. The data on galactocentric radius, location relative to the host galaxy structure, and X-ray variability is then combined with the preliminary source classifications defined using our hardness ratio analysis. For sources without overlapping *HST* exposures, we then assign a likely source classification based on our X-ray observations. For example: a source with $r \sim 0.5$ kpc, located within a spiral arm, no significant long-term X-ray variability, and a soft X-ray spectral shape is classified as a likely SNR. Figure 4.6 shows a flowchart of the logic of our classification scheme when no overlapping *HST* images are present.

To determine a likely source classification for X-ray sources *with* overlapping *HST* fields,

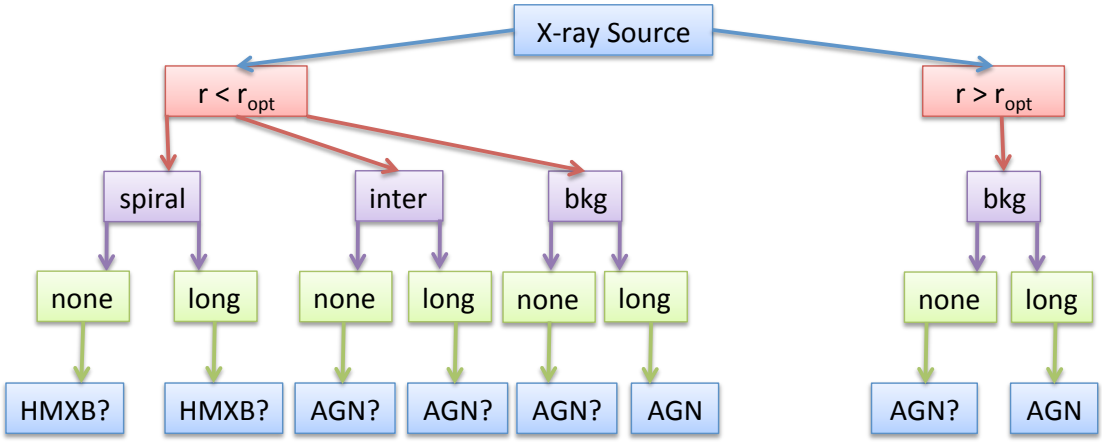

Figure 4.6: Source classification flowchart, when no overlapping *HST* fields are available.

we generated color-magnitude diagrams (CMDs) of each *HST* field and candidate optical counterparts were classified as falling either on the main sequence (MS) or red giant branch (RGB). Additionally, we constructed X-ray color-magnitude diagrams (XCMDs), where the optical color was plotted as a function of $\log(f_X/f_V)$. Many authors have utilized optical and X-ray colors in discriminating between XRBs and background AGN [189, 374]; pulsars and HMXBs located in the Small Magellanic Cloud occupy a region of the XCMD bounded by $B-V<0$ and $\log(f_X/f_V)<1$ [270].

Optical counterpart candidates were then compared to the XCMD generated for each *HST* field. Sources with blue optical colors ($F435W-F555W$ or $F475W-F606W<0.2$) and $\log(f_X/f_V)<1$ are likely to match a young massive main sequence star and are therefore designated as HMXB candidates. Sources falling in the other region of the XCMD are associated with either RGB stars or background galaxies, and are therefore classified as either AGNs or LMXBs. For illustration, Figure 4.7 presents a sample CMD and XCMD for the field 'NGC300-5' (top panel) as well as a CMD and XCMD of our X-ray/optical source candidates. The sample CMD was generated using the *HST* $F435W$ and $F814W$ catalog magnitudes for all optical sources in the 'NGC300-5' field. For illustrative purposes, we have created a sample XCMD using the mean X-ray flux of sources in the NGC 300

catalog ($\sim 5 \times 10^{-15}$ erg s^{-1} cm^{-2}, corresponding to $\sim 2 \times 10^{36}$ erg s^{-1} at the distance of NGC 300). Using this X-ray flux, we calculate a $\log(f_X/f_V)$ for every optical source in the *HST* 'NGC300-5' field. The bottom panels show the magnitudes, colors, and X-ray/optical flux ratios for the candidate optical counterparts only. Regions corresponding to likely MS and RGB stars are labeled on the CMD, and the regions defining likely HMXBs and AGNs are labeled on the XCMD.

Figure 4.8 shows a flowchart of the logic of our classification scheme when no overlapping *HST* images are present.

To expedite the process of classifying each X-ray source based on the plethora of data available, an IDL routine called `xclass.pro` was constructed to automatically process each X-ray source. The routine reads in an input source file containing all X-ray and, if available, optical information, and returns a preliminary source classification. The routine additionally tracks which classification channels were utilized by the input sources. The `xclass.pro` routine has been made publicly available[1].

The source classification reported by the `xclass` routine was then compared to the classification determined by our hardness ratio analysis. In some cases, the multiwavelength and hardness ratio classifications disagreed. This was most commonly seen with sources classified as XRBs by our hardness ratio analysis but with multiwavelength properties consistent with a background AGN. In these cases, we favor the AGN classification. Sources that are initially classified as AGN but which exhibit a soft X-ray spectrum (i.e., classified as 'SOFT' in our HR analysis) may be potential LMXBs. A summary of all X-ray and optical data and our final source classification for all 629 X-ray sources in the CLVS catalog is presented in Table 4.2.

We use the [56] AGN log$N$-log$S$ distribution to estimate the expected number of AGN in our X-ray source catalogs to determine if, statistically, `xclass` is providing reasonable classifications. The similarities in both the X-ray and optical properties of AGN and LMXBs (especially at the distance of a few Mpc) is likely to cause confusion in separating these two populations. However, our X-ray/optically-classified sources differ from the predictions by,

[1]See `http://www.astro.washington.edu/users/bbinder/xclass/`

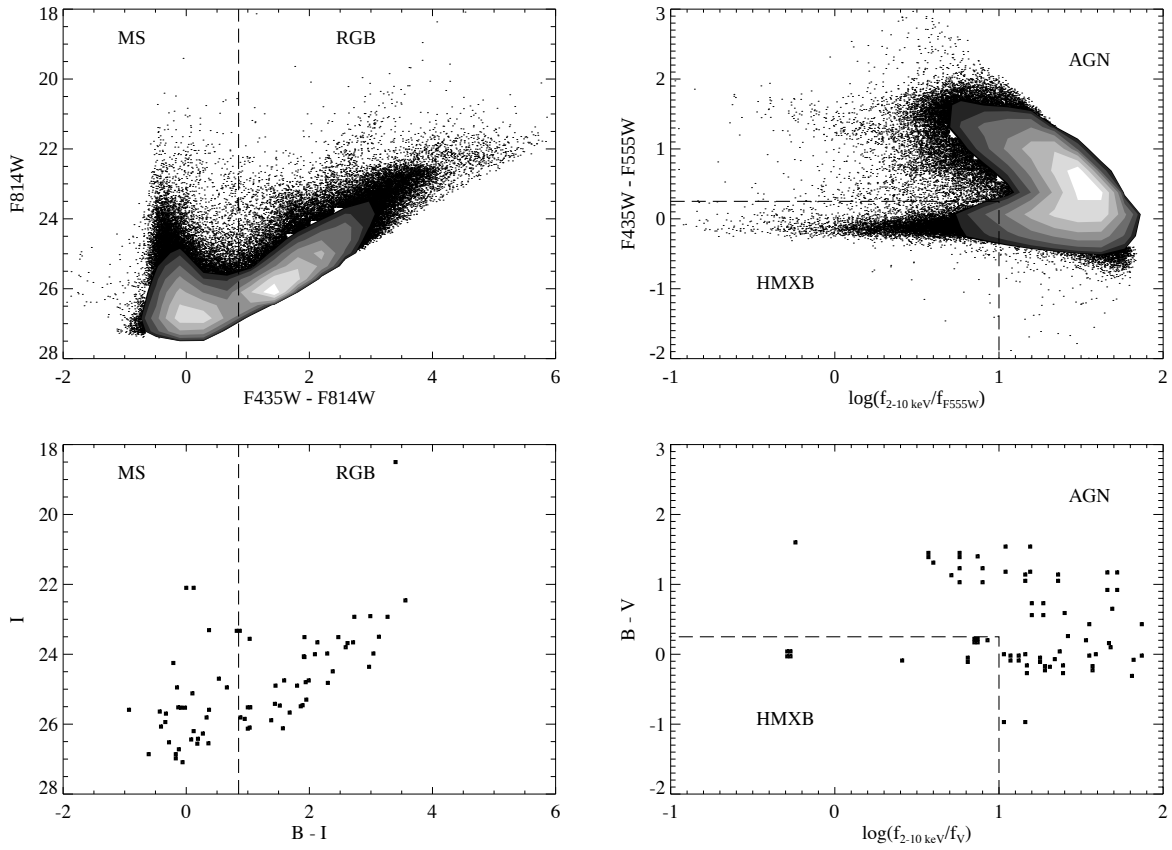

Figure 4.7: Top row: a sample color-magnitude diagram (CMD; *left*) and X-ray color-magnitude diagram (XCMD; *right*). The MS and RGB regions are marked on the CMD, and the HMXB and AGN regions are marked on the XCMD. Bottom row: the locations of our candidate optical counterparts as either MS or RGB stars on a CMD (*left*), and an XCMD (*right*) showing the actual values of the X-ray/optical flux ratio for our candidate optical counterparts to each X-ray source.

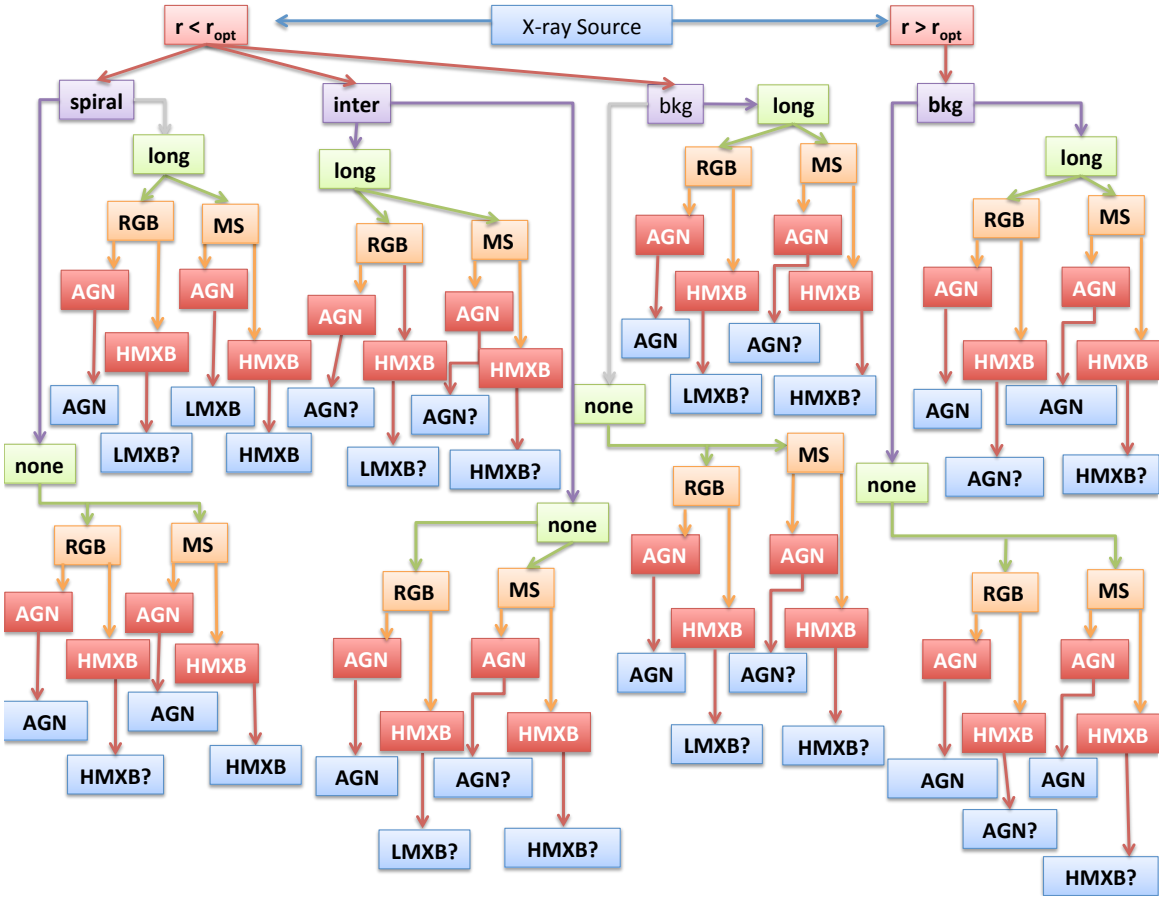

Figure 4.8: Source classification flowchart, when overlapping *HST* fields are available.

at most, ∼10–15% for each galaxy, and our source classification scheme correctly classifies several known HMXBs, ULXs, and SNRs. We are therefore confident that our source classification scheme provides the most reliable indicator of the physical nature of the CLVS X-ray sources possible with the available data.

Figure 4.9 shows the fraction of X-ray sources in each galaxy belonging to each of the following categories: HMXBs, LMXBs, background AGN, foreground stars (FSs), and SNRs.

Table 4.2: X-ray Point Source Classifications

Source No. (1)	r^a (kpc) (2)	Assoc. with galaxy? (3)	Variability^b (4)	In *HST* footprint? (5)	# Optical Counterparts (6)	Location on CMD (7)	Location on XCMD (8)	ID. from HRs (9)	Final ID (10)
				NGC 300					
1	5.2	no	none	no				ABS	AGN
2	6.7	no	long	no				XRB	AGN
3	5.5	no	none	yes	2	RGB	AGN	SOFT	LMXB?
4	6.7	no	long	yes	1			ABS	Galaxy/FS?
5	4.6	no	none	yes	10	MS	HMXB	XRB	HMXB
6	4.1	no	none	no				XRB	AGN
7	3.9	yes	none	yes	3	MS	HMXB	SNR	SNR
8	4.0	no	none	yes	3	RGB	AGN	XRB	FS
9	4.1	yes	none	yes	4	RGB	AGN	SOFT	LMXB?
10	3.9	yes	none	yes	1	RGB	AGN	XRB	AGN
11	4.2	yes	none	yes	1	RGB	AGN	XRB	AGN
12	6.2	no	long	yes	2	MS	AGN	SOFT	LMXB?
13	3.9	yes	none	yes	7	MS	HMXB	XRB	HMXB
14	3.8	yes	none	yes	10	MS	HMXB	XRB	HMXB
15	3.1	yes	none	no				SNR	SNR
16	4.1	no	none	no				XRB	AGN
17	2.9	yes	none	yes	6	RGB	AGN	SOFT	LMXB?
18	3.1	yes	rapid	yes	1	RGB	AGN	ABS	LMXB
19	2.9	yes	none	yes	2	RGB	AGN	XRB	AGN
20	3.9	no	long	yes	2	MS	AGN	ABS	AGN
21	3.1	yes	none	yes	5	MS	AGN	ABS	AGN
22	3.4	yes	none	yes	3	MS	HMXB	XRB	HMXB
23	3.2	yes	none	yes	4	RGB	AGN	ABS	AGN
24	4.8	no	long	no				ABS	AGN
25	3.3	yes	none	yes	0			SOFT	HMXB

Continued on next page

Table 4.2 – continued from previous page

Source No.	r^a (kpc)	Assoc. with galaxy?	Variability^b	In *HST* footprint?	# Optical Counterparts	Location on CMD	Location on XCMD	ID. from HRs	Final ID
(1)	(2)	(3)	(4)	(5)	(6)	(7)	(8)	(9)	(10)
26	2.2	yes	none	yes	4	RGB	AGN	XRB	AGN
27	4.6	no	none	no				ABS	AGN
28	2.2	yes	none	no				ABS	HMXB?
29	5.7	no	long	no				ABS	AGN
30	3.3	yes	none	no				XRB	HMXB
31	1.9	yes	none	no				XRB	HMXB
32	1.6	yes	none	yes	5	MS	AGN	SNR	SNR
33	5.8	no	long	no				ABS	AGN
34	1.5	yes	long	yes	0			SNR	SNR
35	4.8	no	none	no				ABS	AGN
36	6.2	no	long	no				ABS	AGN
37	2.0	yes	none	no				XRB	HMXB
38	2.3	yes	none	no				SOFT	LMXB
39	2.1	yes	none	no				SOFT	HMXB
40	3.5	no	long	no				ABS	AGN
41	1.1	yes	none	yes	7	MS	HMXB	SNR	SNR
42	2.3	yes	none	yes	2	MS	AGN	ABS	AGN
43	1.1	yes	none	yes	3	MS	AGN	SNR	SNR
44	5.4	no	long	no				ABS	AGN
45	2.8	yes	long	no				HARD	HMXB?
46	6.0	no	long	no				SNR	AGN?
47	4.8	no	none	no				XRB	AGN
48	4.7	no	none	no				XRB	AGN
49	5.1	no	none	no				SOFT	LMXB?
50	2.9	yes	none	no				XRB	HMXB
51	3.7	no	long	no				ABS	AGN
52	6.3	no	long	no				ABS	AGN
53	3.1	no	none	no				SOFT	LMXB?
54	0.4	yes	none	yes	6	MS	HMXB	SNR	SNR
55	3.4	yes	none	no				XRB	HMXB
56	2.7	yes	none	no				XRB	HMXB
57	3.8	no	none	no				XRB	AGN
58	1.3	yes	none	yes	4	RGB	AGN	XRB	AGN
59	2.2	yes	long	no				XRB	AGN
60	3.7	no	none	no				XRB	AGN
61	3.5	yes	none	no				XRB	HMXB
62	4.0	no	none	no				ABS	AGN

Continued on next page

Table 4.2 – continued from previous page

Source No.	r^a (kpc)	Assoc. with galaxy?	Variability^b	In *HST* footprint?	# Optical Counterparts	Location on CMD	Location on XCMD	ID. from HRs	Final ID
(1)	(2)	(3)	(4)	(5)	(6)	(7)	(8)	(9)	(10)
63	1.7	yes	none	yes	4	RGB	AGN	XRB	AGN
64	1.4	yes	none	yes	4	MS	AGN	ABS	LMXB?
65	2.9	yes	none	no				XRB	HMXB
66	4.3	no	none	no				ABS	AGN
67	4.8	no	none	no				XRB	AGN
68	1.2	yes	long	yes	4	RGB	AGN	ABS	AGN
69	4.1	no	long	no				XRB	AGN
70	3.1	yes	none	no				XRB	HMXB
71	2.5	yes	none	no				SOFT	HMXB
72	1.6	yes	none	yes	3	RGB	AGN	XRB	AGN
73	1.5	yes	long	no				XRB	HMXB?
74	1.5	yes	none	no				XRB	HMXB
75	2.5	yes	none	no				ABS	HMXB
76	6.9	no	long	no				HARD	AGN
77	3.1	yes	none	no				SNR	SNR
78	2.7	yes	none	no				ABS	AGN
79	2.6	yes	none	no				XRB	AGN
80	2.2	yes	none	no				XRB	HMXB
81	2.4	yes	none	no				SNR	SNR
82	4.1	no	long	no				XRB	AGN
83	2.2	yes	none	no				ABS	HMXB?
84	2.9	yes	none	no				ABS	HMXB?
85	3.5	yes	none	no				SNR	SNR
86	3.8	yes	none	no				SOFT	HMXB
87	5.7	no	long	no				SOFT	LMXB?
88	4.9	no	long	no				ABS	AGN
89	8.1	no	long	no				ABS	AGN
90	4.5	no	none	no				ABS	AGN?
91	5.1	no	none	no				XRB	AGN
92	4.9	no	none	no				SOFT	LMXB?
93	4.9	no	long	no				XRB	AGN
94	5.0	no	none	no				ABS	AGN
95	4.7	no	none	yes	2	MS	HMXB	XRB	HMXB
				NGC 404					
1	4.8	no	rapid	no				ABS	AGN
2	4.5	no	none	no				XRB	AGN
3	4.3	no	none	no				XRB	AGN

Continued on next page

Table 4.2 – continued from previous page

Source No. (1)	r^a (kpc) (2)	Assoc. with galaxy? (3)	Variability^b (4)	In *HST* footprint? (5)	# Optical Counterparts (6)	Location on CMD (7)	Location on XCMD (8)	ID. from HRs (9)	Final ID (10)
4	4.1	no	none	no				XRB	AGN
5	3.8	no	none	no				SOFT	FS
6	3.8	no	none	no				XRB	AGN
7	4.1	no	none	no				SOFT	AGN
8	4.1	no	none	no				XRB	AGN
9	3.3	no	none	no				XRB	AGN
10	3.1	yes	none	no				XRB	AGN
11	3.5	no	none	no				XRB	AGN
12	2.7	yes	none	no				XRB	AGN
13	3.4	no	none	no				XRB	AGN
14	2.6	yes	none	no				XRB	AGN
15	3.3	no	none	no				XRB	AGN
16	2.4	yes	long	no				XRB	XRB
17	2.0	yes	none	no				SOFT	AGN
18	2.0	yes	long	no				ABS	AGN
19	2.7	yes	none	no				XRB	AGN
20	1.7	yes	none	no				HARD	AGN?
21	1.7	yes	none	no				ABS	AGN?
22	2.4	yes	none	no				XRB	XRB
23	1.6	yes	none	no				ABS	AGN
24	2.0	yes	none	no				ABS	AGN
25	1.5	yes	none	no				ABS	AGN
26	1.4	yes	none	yes	0			XRB	XRB
27	1.7	yes	long	yes	1	RGB	AGN	BKG	AGN?
28	1.9	yes	none	no				ABS	AGN?
29	1.2	yes	none	yes	1	RGB	HMXB	SNR	SSS?
30	1.2	yes	none	yes	0			HARD	AGN
31	1.3	yes	none	no				ABS	AGN
32	1.7	yes	none	no				XRB	SSS?
33	1.9	yes	none	no				ABS	AGN
34	0.6	yes	none	yes	0			XRB	XRB
35	1.6	yes	none	yes	0			ABS	SSS?
36	0.6	yes	none	no				HARD	AGN
37	0.4	yes	long	no				XRB	XRB
38	0.3	yes	none	no				XRB	XRB
39	1.4	yes	none	yes	0			ABS	AGN?
40	1.1	yes	long	yes	0			XRB	XRB

Continued on next page

Table 4.2 – continued from previous page

Source No.	r^a (kpc)	Assoc. with galaxy?	Variability[b]	In *HST* footprint?	# Optical Counterparts	Location on CMD	Location on XCMD	ID. from HRs	Final ID
(1)	(2)	(3)	(4)	(5)	(6)	(7)	(8)	(9)	(10)
41	0.0	yes	none	no				XRB	NUCLEUS
42	1.5	yes	none	yes	0			XRB	XRB
43	0.1	yes	none	no				SNR	SSS?
44	1.1	yes	none	yes	0			ABS	AGN
45	1.3	yes	none	no				SOFT	AGN
46	1.7	yes	none	no				ABS	AGN
47	0.6	yes	none	no				XRB	XRB
48	0.6	yes	none	no				XRB	XRB
49	0.5	yes	long	yes	0			XRB	XRB
50	1.2	yes	none	no				ABS	AGN?
51	1.6	yes	none	no				XRB	XRB
52	1.9	yes	none	no				XRB	XRB
53	0.9	yes	long	no				HARD	XRB?
54	1.0	yes	long	no				ABS	AGN
55	1.7	yes	long	no				ABS	XRB?
56	1.5	yes	none	no				XRB	XRB
57	1.7	yes	long?	no				XRB	XRB
58	2.1	yes	none	no				XRB	XRB
59	1.9	yes	none	no				XRB	XRB
60	2.5	yes	none	no				XRB	XRB
61	2.5	yes	long	no				XRB	XRB
62	2.6	yes	none	no				XRB	XRB
63	3.1	yes	none	no				XRB	AGN
64	3.2	no	long	no				XRB	AGN
65	3.1	yes	none	no				SNR	FS
66	3.8	no	none	no				XRB	AGN
67	4.2	no	none	no				XRB	AGN
68	4.6	no	none	no				XRB	AGN
69	3.9	no	none	no				XRB	AGN
70	4.0	no	none	no				XRB	AGN
71	4.8	no	long	no				XRB	AGN
72	4.8	no	none	no				XRB	AGN
73	4.9	no	rapid	no				XRB	AGN
74	6.3	no	none	no				XRB	AGN
				NGC 55					
1	2.3	no	none	no				XRB	AGN
2	3.0	no	long	no				ABS	AGN

Continued on next page

Table 4.2 – continued from previous page

Source No.	r^a (kpc)	Assoc. with galaxy?	Variability[b]	In *HST* footprint?	# Optical Counterparts	Location on CMD	Location on XCMD	ID. from HRs	Final ID
(1)	(2)	(3)	(4)	(5)	(6)	(7)	(8)	(9)	(10)
3	6.3	no	long	no				XRB	AGN
4	4.4	no	none	no				XRB	AGN
5	3.2	no	none	no				ABS	AGN
6	0.6	yes	long	no				ABS	HMXB
7	7.6	no	none	no				SOFT	AGN
8	6.4	no	none	no				ABS	AGN
9	2.3	no	none	no				XRB	AGN
10	0.2	yes	long	no				XRB	LMXB?
11	2.1	no	none	no				XRB	AGN
12	2.0	no	long	no				XRB	AGN
13	0.9	no	long	no				XRB	AGN
14	3.9	no	long	no				SNR	AGN
15	2.5	no	none	no				SOFT	AGN
16	3.6	no	long	no				XRB	AGN
17	0.5	no	none	no				XRB	AGN
18	3.5	no	long	no				XRB	AGN
19	1.7	no	none	no				ABS	AGN
20	3.1	no	rapid	no				XRB	AGN
21	2.1	no	none	no				XRB	AGN
22	1.0	no	long	no				HARD	AGN
23	0.2	yes	rapid, long	no				XRB	FS
24	2.3	no	none	no				SOFT	AGN
25	2.3	no	long	no				ABS	AGN
26	0.9	yes	none	no				XRB	HMXB
27	0.6	yes	long	yes	0		AGN	XRB	LMXB
28	0.5	yes	long	no				XRB	HMXB
29	0.2	yes	none	yes	20	MS	HMXB	ABS	HMXB
30	0.1	yes	long	yes	0		AGN	XRB	LMXB
31	0.9	yes	long	no				SOFT	HMXB
32	0.5	yes	none	yes	0		AGN	XRB	LMXB
33	1.4	yes	long	no				SNR	SNR?
34	3.4	no	rapid, long	no				ABS	AGN?
35	0.6	yes	none	yes	23	MS	HMXB	XRB	HMXB
36	0.1	yes	long	yes	60	MS	HMXB	XRB	HMXB
37	0.5	yes	long	no				SOFT	LMXB
38	0.4	yes	none	yes	26	MS	AGN	XRB	HMXB
39	0.8	yes	long	no				SOFT	LMXB?

Continued on next page

Table 4.2 – continued from previous page

Source No. (1)	r^a (kpc) (2)	Assoc. with galaxy? (3)	Variability^b (4)	In *HST* footprint? (5)	# Optical Counterparts (6)	Location on CMD (7)	Location on XCMD (8)	ID. from HRs (9)	Final ID (10)
40	0.4	yes	long	no				ABS	HMXB
41	1.1	yes	none	yes	0		AGN	XRB	LMXB
42	0.4	yes	long	yes	33	MS	HMXB	ABS	HMXB
43	0.6	yes	long	yes	59	MS	HMXB	XRB	HMXB
44	0.7	yes	long	no				ABS	HMXB
45	2.6	yes	none	yes	0		AGN	ABS	AGN
46	0.6	yes	none	yes	51	MS	HMXB	SRN	SNR
47	0.6	yes	long	yes	0		AGN	ABS	LMXB
48	0.6	yes	none	yes	0		AGN	XRB	FS
49	0.5	yes	rapid, long	yes	0		AGN	XRB	LMXB
50	0.3	yes	none	yes	14	MS	AGN	SNR	SNR?
51	1.4	yes	long	yes	0		AGN	SNR	SNR?
52	2.6	yes	long	yes	255	MS	HMXB	XRB	HMXB
53	0.2	yes	long	yes	39	MS	HMXB	ABS	HMXB
54	0.9	yes	none	no	13	MS	AGN	XRB	LMXB
55	0.6	yes	none	no				XRB	LMXB?
56	0.1	yes	none	yes	41	MS	HMXB	XRB	HMXB
57	0.2	yes	long	yes	20	RGB	HMXB	SNR	SNR?
58	1.1	yes	rapid, long	yes	137	MS	HMXB	XRB	HMXB
59	1.7	yes	long	yes	0		AGN	ABS	LMXB
60	1.6	yes	rapid, long	no				XRB	AGN
61	0.2	yes	none	yes	15	MS	HMXB	ABS	HMXB
62	0.4	yes	none	yes	24	MS	AGN	ABS	LMXB
63	0.1	yes	none	yes	54	MS	AGN	SOFT	LMXB
64	1.1	yes	long	no				XRB	HMXB
65	0.2	yes	long	yes	13	RGB	AGN	XRB	LMXB
66	1.9	yes	long	no				XRB	HMXB
67	1.7	no	none	no				ABS	AGN
68	1.3	no	rapid	no				XRB	AGN
69	0.4	yes	none	no				XRB	HMXB?
70	1.0	no	long	no				XRB	AGN
71	0.4	yes	long	yes	19	MS	HMXB	XRB	HMXB
72	0.8	no	long	no				XRB	AGN
73	1.2	no	rapid	no				ABS	AGN
74	0.5	no	none	no				ABS	AGN
75	0.4	yes	long	no				ABS	HMXB?
76	2.3	no	long	no				HARD	AGN

Continued on next page

Table 4.2 – continued from previous page

Source No.	r^a (kpc)	Assoc. with galaxy?	Variability^b	In *HST* footprint?	# Optical Counterparts	Location on CMD	Location on XCMD	ID. from HRs	Final ID
(1)	(2)	(3)	(4)	(5)	(6)	(7)	(8)	(9)	(10)
77	1.2	yes	long	no				SNR	SNR?
78	1.1	yes	long	no				XRB	HMXB?
79	1.2	yes	long	no				ABS	HMXB?
80	0.4	yes	long	no				ABS	HMXB?
81	0.3	yes	none	no				ABS	HMXB?
82	0.0	no	rapid	no				ABS	AGN
83	5.0	no	none	no				ABS	AGN
84	4.5	no	rapid	no				XRB	AGN
85	2.4	no	long	no				SNR	AGN
86	0.1	yes	long	no				SNR	SNR?
87	3.6	no	rapid, long	no				XRB	AGN
88	1.8	yes	rapid, long	no				XRB	LMXB
89	1.6	no	long	no				XRB	AGN
90	1.5	no	long	no				XRB	AGN
91	3.4	no	long	no				ABS	AGN
92	2.2	yes	long	no				XRB	HMXB?
93	3.1	no	long	no				XRB	AGN
94	0.7	yes	long	no				XRB	HMXB?
95	3.8	no	none	no				XRB	AGN
96	3.9	yes	long	no				XRB	HMXB?
97	1.1	no	long	no				ABS	AGN
98	4.2	no	none	no				XRB	AGN
99	0.9	yes	none	no				XRB	HMXB?
100	1.8	no	rapid, long	yes	0		AGN	XRB	AGN
101	0.6	yes	none	no				XRB	HMXB?
102	4.4	no	long	no				ABS	AGN
103	0.5	yes	long	no				ABS	HMXB?
104	1.0	no	long	no				SOFT	AGN
105	3.5	no	none	no				SOFT	AGN
106	3.0	yes	long	no				HARD	LMXB
107	6.0	no	long	no				ABS	AGN
108	5.3	no	none	no				XRB	AGN
109	3.1	yes	rapid, long	no				XRB	LMXB
110	4.1	yes	long	no				XRB	HMXB
111	2.8	yes	long	no				SOFT	HMXB
112	0.4	no	long	no				XRB	AGN
113	5.0	no	none	no				ABS	AGN

Continued on next page

Table 4.2 – continued from previous page

Source No. (1)	r^a (kpc) (2)	Assoc. with galaxy? (3)	Variability^b (4)	In *HST* footprint? (5)	# Optical Counterparts (6)	Location on CMD (7)	Location on XCMD (8)	ID. from HRs (9)	Final ID (10)
114	4.7	yes	none	yes	28	MS	HMXB	XRB	AGN
115	4.7	no	none	no				XRB	AGN
116	1.4	yes	none	yes	0		AGN	XRB	LMXB
117	1.6	yes	rapid	yes	29	MS	HMXB	XRB	HMXB
118	6.7	yes	none	no				ABS	HMXB?
119	4.2	yes	none	yes	54	RGB	AGN	SOFT	ULX
120	2.2	yes	none	yes	23	MS	HMXB	XRB	HMXB
121	4.0	yes	long	no				HARD	HMXB?
122	4.9	yes	long	yes	135	MS	AGN	XRB	LMXB
123	2.1	yes	none	yes	0		AGN	HARD	LMXB
124	0.3	yes	long	yes	45	MS	AGN	ABS	LMXB
125	1.8	yes	long	no				SNR	SNR?
126	6.1	yes	long	no				HARD	FS
127	3.9	yes	none	no				SNR	SNR?
128	8.8	yes	none	no				XRB	FS
129	3.4	yes	none	no				ABS	HMXB?
130	1.0	yes	none	yes	140	MS	HMXB	SNR	HMXB
131	2.9	yes	none	no				SNR	SNR?
132	3.6	yes	none	no				XRB	SNR?
133	3.3	yes	none	yes	26	MS	HMXB	XRB	HMXB
134	4.2	yes	none	yes	0		AGN	SOFT	FS
135	1.9	no	none	no				SOFT	BH-LMXB?
136	2.2	no	none	no				XRB	AGN
137	5.7	no	none	no				ABS	AGN
138	1.4	yes	long	yes	0		AGN	ABS	LMXB
139	0.8	no	long	no				ABS	AGN
140	3.1	yes	long	no				XRB	HMXB?
141	3.9	no	rapid	no				XRB	AGN
142	6.7	no	long	no				XRB	AGN
143	1.0	yes	none	no				XRB	HMXB?
144	0.8	no	long	no				XRB	AGN
145	0.3	no	none	no				XRB	AGN
146	5.2	no	none	no				XRB	AGN
147	2.4	no	none	no				XRB	AGN
148	3.1	no	none	no				SNR	FS?
149	1.1	no	long	no				SNR	FS?
150	2.3	no	long	no				SNR	FS?

Continued on next page

Table 4.2 – continued from previous page

Source No. (1)	r^a (kpc) (2)	Assoc. with galaxy? (3)	Variability^b (4)	In *HST* footprint? (5)	# Optical Counterparts (6)	Location on CMD (7)	Location on XCMD (8)	ID. from HRs (9)	Final ID (10)
151	1.0	no	long	no				SNR	FS?
152	3.5	no	none	no				ABS	AGN
153	3.2	no	none	no				ABS	AGN
154	0.7		none	no				SNR	FS?
				NGC 2403					
1	0.5	no	none	no				XRB	AGN
2	1.4	yes	rapid	yes	2	RGB	AGN	XRB	LMXB
3	3.1	yes	long	no				SOFT	LMXB?
4	1.7	no	long	no				ABS	AGN
5	1.0	yes	none	yes	3	RGB	AGN	XRB	LMXB
6	2.8	yes	none	no				SNR	HMXB
7	1.3	yes	long	yes	11	MS	AGN	ABS	LMXB
8	3.5	yes	none	no				ABS	HMXB
9	4.9	no	none	no				XRB	AGN
10	0.8	yes	none	no				XRB	HMXB
11	9.0	no	none	no				SNR	FS
12	0.4	no	long	no				ABS	AGN
13	5.0	no	long	no				SOFT	AGN
14	4.5	no	none	no				XRB	AGN
15	9.9	no	long	no				XRB	AGN
16	1.8	yes	long	yes	3	RGB	HMXB	SNR	SNR
17	3.5	yes	none	no				ABS	HMXB
18	1.6	yes	long	yes	13	MS	AGN	SNR	SNR
19	6.5	no	none	no				XRB	AGN
20	0.0	yes	rapid, long	yes	12	MS	AGN	XRB	LMXB
21	1.3	yes	long	no				SNR	SNR
22	1.6	yes	none	yes	7	MS	HMXB	ABS	HMXB
23	9.9	no	none	no				XRB	AGN
24	6.5	no	long	no				ABS	AGN
25	0.8	yes	long	no				ABS	LMXB
26	2.3	no	none	no				ABS	AGN
27	2.5	yes	long	no				SNR	SNR?
28	2.1	yes	long	no				XRB	HMXB?
29	3.5	no	none	no				XRB	AGN
30	2.4	no	none	no				ABS	AGN
31	9.5	no	long	no				XRB	AGN
32	8.5	no	none	no				XRB	AGN

Continued on next page

Table 4.2 – continued from previous page

Source No. (1)	r^a (kpc) (2)	Assoc. with galaxy? (3)	Variability^b (4)	In *HST* footprint? (5)	# Optical Counterparts (6)	Location on CMD (7)	Location on XCMD (8)	ID. from HRs (9)	Final ID (10)
33	11.2	no	none	no				XRB	AGN
34	4.1	no	none	no				XRB	AGN
35	4.1	no	long	no				XRB	AGN
36	2.0	no	rapid	no				XRB	AGN
37	3.9	no	none	no				SOFT	AGN
38	1.7	yes	none	yes	18	MS	HMXB	SOFT	AGN
39	4.6	yes	long	yes	12	MS	HMXB	XRB	HMXB
40	0.3	yes	long	yes	8	RGB	AGN	ABS	LMXB
41	0.3	yes	long	yes	12	RGB	AGN	XRB	LMXB
42	0.2	yes	long	yes	33	MS	HMXB	XRB	ULX
43	0.9	no	long	no				ABS	AGN
44	0.0	yes	none	yes	15	MS	HMXB	XRB	HMXB
45	1.5	yes	none	yes	25	MS	AGN	ABS	LMXB
46	1.3	yes	long	yes	3	RGB	AGN	XRB	LMXB
47	0.9	yes	long	yes	15	RGB	AGN	SNR	FS?
48	2.4	yes	none	yes	8	MS	AGN	SOFT	SNR?
49	0.6	yes	long	yes	1	RGB	AGN	SNR	SNR
50	2.3	yes	none	yes	12	RGB	AGN	XRB	FS
51	0.3	yes	none	yes	0		AGN	SOFT	BH-LMXB?
52	1.3	no	long	no				ABS	AGN
53	0.3	yes	none	yes	19	RGB	AGN	ABS	LMXB
54	0.2	yes	long	yes	5	RGB	AGN	SNR	LMXB
55	0.9	yes	long	yes	21	MS	HMXB	XRB	HMXB
56	0.3	yes	long	yes	7	RGB	AGN	XRB	LMXB
57	0.1	yes	long	yes	13	MS	HMXB	XRB	HMXB
58	6.5	no	long	no				HARD	AGN
59	1.8	yes	none	yes	8	RGB	AGN	SNR	FS?
60	0.7	yes	none	yes	8	RGB	HMXB	SNR	SNR
61	0.7	yes	none	yes	14	MS	AGN	SNR	SNR
62	7.2	no	rapid, long	no				SNR	FS
63	0.1	yes	none	no				ABS	HMXB
64	0.8	yes	none	yes	20	MS	HMXB	SNR	SNR
65	1.0	yes	long	no				ABS	HMXB
66	3.6	yes	none	no				XRB	HMXB
67	0.4	yes	none	yes	8	RGB	AGN	XRB	LMXB
68	0.8	yes	none	no				XRB	HMXB
69	0.3	yes	long	yes	5	MS	HMXB	XRB	HMXB

Continued on next page

Table 4.2 – continued from previous page

Source No.	r^a (kpc)	Assoc. with galaxy?	Variability[b]	In *HST* footprint?	# Optical Counterparts	Location on CMD	Location on XCMD	ID. from HRs	Final ID
(1)	(2)	(3)	(4)	(5)	(6)	(7)	(8)	(9)	(10)
70	0.2	yes	none	yes	10	MS	HMXB	SNR	HMXB
71	0.1	yes	none	no				ABS	HMXB
72	0.7	yes	long	no				XRB	HMXB
73	2.6	yes	long	no				SNR	HMXB
74	3.8	yes	none	no				ABS	HMXB
75	0.3	yes	none	yes	6	MS	AGN	ABS	LMXB
76	3.5	yes	none	no				SNR	HMXB
77	1.0	yes	none	no				SNR	FS?
78	3.0	yes	rapid	no				XRB	FS?
79	3.7	yes	long	no				XRB	HMXB
80	0.0	no	none	no				XRB	AGN
81	0.9	yes	none	yes	5	MS	HMXB	ABS	HMXB
82	0.2	no	none	no				ABS	AGN
83	5.6	no	long	no				SOFT	AGN
84	1.6	yes	none	yes	4	MS	HMXB	ABS	HMXB
85	0.4	yes	long	yes	8	MS	HMXB	SNR	HMXB
86	3.7	yes	none	no				ABS	HMXB
87	1.6	yes	long	no				ABS	LMXB
88	1.3	yes	none	no				ABS	HMXB
89	0.2	yes	long	no				ABS	HMXB
90	3.3	yes	long	no				XRB	HMXB
91	1.1	yes	long	yes	5	MS	AGN	SOFT	LMXB?
92	2.7	yes	none	no				XRB	LMXB
93	0.9	yes	long	yes	3	RGB	AGN	SNR	FS?
94	3.3	no	none	no				ABS	AGN
95	2.2	yes	none	no				XRB	HMXB
96	2.7	yes	none	no				SNR	SNR
97	7.4	no	long	no				XRB	AGN
98	3.0	no	long	no				XRB	AGN
99	4.2	no	none	no				ABS	AGN
100	8.4	no	long	no				ABS	AGN
101	1.8	yes	long	yes	5	RGB	HMXB	XRB	HMXB
102	8.4	no	none	no				ABS	AGN
103	3.1	no	long	no				XRB	AGN
104	2.2	yes	long	no				ABS	HMXB?
105	6.8	no	none	no				XRB	AGN
106	4.3	no	long	no				XRB	FS?

Continued on next page

Table 4.2 – continued from previous page

Source No. (1)	r^a (kpc) (2)	Assoc. with galaxy? (3)	Variability^b (4)	In *HST* footprint? (5)	# Optical Counterparts (6)	Location on CMD (7)	Location on XCMD (8)	ID. from HRs (9)	Final ID (10)
107	1.7	no	long	yes	3	RGB	AGN	XRB	AGN
108	4.2	no	none	yes	2	RGB	HMXB	XRB	AGN
109	2.5	no	long	yes	2	RGB	HMXB	XRB	HMXB
110	10.6	no	long	no				XRB	AGN
111	5.4	no	none	yes	3	RGB	AGN	XRB	AGN
112	0.9	yes	none	no				SNR	SNR?
113	12.2	no	none	no				XRB	AGN
114	8.4	no	long	yes	3	RGB	AGN	ABS	FS
115	4.2	no	none	yes	0		AGN	XRB	AGN
116	6.2	no	long	yes	6	RGB	AGN	SOFT	AGN
117	1.7	yes	none	no				ABS	HMXB?
118	2.8	no	none	no				SNR	FS
119	4.0	no	none	yes	1	RGB	AGN	ABS	AGN
120	6.8	no	none	no				SOFT	AGN
121	9.6	no	none	yes	20	RGB	AGN	XRB	FS
122	3.1	no	long	no				XRB	AGN
123	3.0	no	none	no				XRB	AGN
124	4.5	no	rapid	no				ABS	HMXB?
125	3.6	no	none	yes	3	RGB	AGN	ABS	AGN
126	0.4	yes	rapid	no				ABS	LMXB?
127	3.6	no	none	no				SOFT	AGN
128	1.8	yes	none	no				ABS	HMXB?
129	2.6	yes	long	yes	4	RGB	AGN	SNR	FS?
130	6.7	no	none	no				XRB	AGN
131	7.3	no	none	no				ABS	AGN
132	2.0	yes	none	yes	4	RGB	HMXB	SNR	FS?
133	2.3	yes	none	no				SNR	SNR?
134	0.2	no	long	no				XRB	HMXB
135	1.6	yes	none	yes	0		AGN	XRB	SNR
136	4.7	no	long	no				XRB	AGN
137	1.4	no	none	no				ABS	AGN
138	4.2	yes	none	no				SOFT	LMXB?
139	4.0	yes	none	no				SNR	FS
140	0.9	yes	none	no				XRB	HMXB
141	1.7	yes	long	yes	3	RGB	AGN	XRB	LMXB
142	7.1	no	rapid	no				XRB	AGN
143	2.5	yes	none	no				ABS	HMXB

Continued on next page

Table 4.2 – continued from previous page

Source No. (1)	r^a (kpc) (2)	Assoc. with galaxy? (3)	Variability^b (4)	In *HST* footprint? (5)	# Optical Counterparts (6)	Location on CMD (7)	Location on XCMD (8)	ID. from HRs (9)	Final ID (10)
144	8.8	no	none	no				SNR	FS
145	4.2	no	none	no				ABS	AGN
146	4.6	yes	none	no				XRB	LMXB
147	3.4	yes	none	no				XRB	HMXB
148	3.4	no	none	no				HARD	AGN
149	13.6	no	none	no				SOFT	AGN
150	5.1	yes	none	no				XRB	HMXB?
151	13.0	no	none	no				SOFT	AGN
152	0.3	no	none	no				ABS	AGN
153	4.3	no	none	no				XRB	AGN
154	7.1	no	long	yes	28	1.15	AGN	XRB	AGN
155	1.2	yes	none	no				XRB	HMXB
156	2.8	yes	long	no				SOFT	LMXB?
157	7.8	no	none	no				SOFT	AGN
158	0.7	yes	none	no				SNR	SNR?
159	2.0	yes	none	no				XRB	HMXB
160	6.6	no	none	no				ABS	AGN
161	4.9	yes	none	no				XRB	HMXB
162	3.4	yes	none	no				XRB	HMXB?
163	4.7	no	long	no				XRB	AGN
164	5.7	no	none	no				XRB	AGN
165	4.4	no	none	no				XRB	AGN
166	9.5	no	rapid	no				SNR	FS?
167	4.5	yes	none	no				SOFT	LMXB?
168	5.7	no	none	no				SNR	AGN
169	3.9	yes	none	no				SNR	SNR
170	1.0	yes	long	no				XRB	LMXB?
171	4.0	no	long	no				ABS	AGN
172	5.2	yes	none	no				ABS	HMXB
173	5.3	no	none	no				SOFT	AGN
174	5.3	yes	none	no				XRB	LMXB
175	0.9	yes	rapid, long	no				SNR	FS?
176	0.4	yes	none	no				HARD	HMXB
177	3.7	yes	none	no				ABS	HMXB
178	1.1	yes	none	no				XRB	HMXB
179	2.6	yes	rapid, long	no				ABS	HMXB
180	5.4	no	long	no				XRB	AGN

Continued on next page

Table 4.2 – continued from previous page

Source No.	r^a (kpc)	Assoc. with galaxy?	Variability[b]	In *HST* footprint?	# Optical Counterparts	Location on CMD	Location on XCMD	ID. from HRs	Final ID
(1)	(2)	(3)	(4)	(5)	(6)	(7)	(8)	(9)	(10)
181	0.1	yes	none	no				SNR	SNR?
182	2.5	no	none	no				SOFT	AGN
183	1.4	yes	long	no				ABS	HMXB
184	4.3	yes	none	no				XRB	LMXB
185	4.3	no	long	no				ABS	AGN
186	2.1	yes	none	no				SOFT	LMXB
187	2.3	yes	none	no				SNR	SNR?
188	5.6	no	long	no				SOFT	AGN
189	3.2	no	long	no				XRB	AGN
190	6.9	no	long	no				XRB	AGN
				NGC 4214					
1	0.8	no	none	no				SNR	FS?
2	1.5	no	long	no				XRB	AGN
3	1.8	no	long	no				XRB	AGN
4	0.0	no	none	no				XRB	AGN
5	0.6	no	none	no				SNR	FS?
6	0.6	no	none	no				XRB	AGN
7	1.2	yes	none	no				XRB	HMXB
8	0.8	no	none	no				XRB	AGN
9	0.6	no	none	no				ABS	AGN
10	1.5	yes	long	no				HARD	LMXB
11	0.0	no	none	no				ABS	AGN
12	0.1	no	long	no				XRB	AGN
13	5.2	no	none	no				XRB	AGN
14	0.6	no	long	no				XRB	AGN
15	1.3	yes	none	no				ABS	HMXB
16	0.7	yes	rapid	no				XRB	LMXB
17	1.7	no	long	no				XRB	AGN
18	1.6	no	long	no				ABS	AGN
19	1.0	no	long	no				XRB	AGN
20	1.0	yes	long	no				ABS	HMXB
21	1.0	yes	long	no				SNR	SNR
22	9.1	no	long	no				SOFT	AGN
23	0.1	no	long	no				ABS	AGN
24	10.2	no	rapid	no				SNR	FS?
25	0.9	no	none	no				XRB	AGN
26	6.1	no	none	no				ABS	AGN

Continued on next page

Table 4.2 – continued from previous page

Source No.	r^a (kpc)	Assoc. with galaxy?	Variability[b]	In *HST* footprint?	# Optical Counterparts	Location on CMD	Location on XCMD	ID. from HRs	Final ID
(1)	(2)	(3)	(4)	(5)	(6)	(7)	(8)	(9)	(10)
27	0.9	no	long	no				XRB	AGN
28	0.9	no	long	no				XRB	AGN
29	1.1	no	long	no				XRB	AGN
30	8.1	no	long	no				SOFT	AGN
31	0.1	yes	long	no				SNR	SNR
32	1.2	no	none	no				XRB	AGN
33	7.0	no	long	no				XRB	AGN
34	2.2	no	none	no				XRB	AGN
35	1.5	no	long	no				XRB	AGN
36	1.2	no	long	no				XRB	AGN
37	4.0	no	long	no				ABS	AGN
38	2.8	no	long	no				XRB	AGN
39	3.3	no	long	no				ABS	AGN
40	0.6	no	none	no				XRB	AGN
41	2.9	no	long	no				XRB	AGN
42	3.1	yes	none	no				SOFT	SNR
43	3.4	no	long	no				ABS	AGN
44	3.8	no	none	yes	0		AGN	SOFT	AGN
45	0.1	yes	none	no				XRB	HMXB
46	0.4	no	none	yes	31	MS	HMXB	XRB	HMXB?
47	4.7	no	none	yes	0		AGN	XRB	AGN
48	2.2	no	long	yes	15	RGB	AGN	XRB	AGN
49	3.6	no	none	yes	0		AGN	ABS	AGN
50	1.8	no	none	yes	0		AGN	SNR	FS?
51	2.3	yes	none	no				ABS	HMXB
52	1.4	no	none	no				XRB	AGN
53	4.2	no	long	yes	74	MS	HMXB	SOFT	HMXB?
54	6.3	no	none	no				XRB	AGN
55	0.4	yes	none	no				SOFT	HMXB?
56	1.0	no	long	no				XRB	AGN
57	2.2	no	long	yes	36	MS	AGN	SNR	FS?
58	0.4	yes	long	no				SNR	SNR
59	0.5	yes	none	no				SNR	SNR
60	9.1	no	none	no				XRB	AGN
61	4.2	no	long	no				XRB	AGN
62	0.2	yes	none	no				XRB	HMXB
63	4.6	no	long	no				XRB	AGN

Continued on next page

Table 4.2 – continued from previous page

Source No. (1)	r^a (kpc) (2)	Assoc. with galaxy? (3)	Variability^b (4)	In *HST* footprint? (5)	# Optical Counterparts (6)	Location on CMD (7)	Location on XCMD (8)	ID. from HRs (9)	Final ID (10)
64	2.5	no	none	no				SNR	FS?
65	2.1	no	long	no				ABS	AGN
66	4.3	no	long	no				ABS	AGN
67	0.6	no	none	no				XRB	AGN
68	4.6	no	none	no				SOFT	FS
69	3.7	no	long	no				HARD	AGN
70	3.4	no	none	no				XRB	AGN
71	2.1	no	none	no				XRB	AGN
72	3.5	no	none	no				SOFT	AGN
73	4.8	no	none	no				XRB	AGN
74	7.1	no	none	no				XRB	AGN
75	3.5	yes	long	no				XRB	LMXB?
76	9.2	no	none	no				XRB	AGN
77	0.5	no	none	no				XRB	AGN
78	16.5	no	long	no				SOFT	FS?
79	14.2	no	rapid	no				SNR	FS?
80	7.8	no	none	no				SOFT	AGN
81	2.8	no	long	no				XRB	AGN
82	2.5	yes	none	no				ABS	HMXB
83	6.7	no	none	no				SOFT	FS?
84	4.2	no	none	no				ABS	AGN
85	1.6	no	long	no				ABS	AGN
86	2.7	yes	long	no				SNR	SNR
87	2.5	no	long	no				XRB	AGN
88	5.4	no	long	no				XRB	AGN
89	4.0	no	none	no				SOFT	AGN
90	8.5	no	none	no				XRB	AGN
91	2.7	no	none	no				SOFT	AGN
92	0.3	yes	long	no				SNR	SNR
93	0.1	yes	none	no				ABS	HMXB
94	1.2	yes	long	no				XRB	HMXB
95	0.3	no	none	no				XRB	AGN
96	4.5	no	none	no				XRB	AGN
97	0.1	yes	none	no				XRB	HMXB
98	2.9	no	none	no				ABS	AGN
99	2.8	no	none	no				SNR	AGN
100	4.3	no	long	no				HARD	AGN

Continued on next page

Table 4.2 – continued from previous page

Source No. (1)	r^a (kpc) (2)	Assoc. with galaxy? (3)	Variability[b] (4)	In *HST* footprint? (5)	# Optical Counterparts (6)	Location on CMD (7)	Location on XCMD (8)	ID. from HRs (9)	Final ID (10)
101	1.4	yes	none	no				ABS	HMXB
102	0.7	no	none	no				XRB	AGN
103	4.0	no	none	no				SNR	FS?
104	8.4	no	none	no				XRB	AGN
105	6.6	no	none	no				XRB	AGN
106	1.4	no	none	no				XRB	AGN
107	1.9	yes	none	no				XRB	HMXB
108	7.5	no	none	no				XRB	AGN
109	3.0	no	long	no				XRB	AGN
110	3.4	no	long	no				XRB	AGN
111	5.9	no	none	no				HARD	AGN
112	13. 0	no	none	no				HARD	AGN
113	11.2	no	none	no				SOFT	AGN
114	3.6	no	none	no				ABS	FS?
115	2.9	no	long	no				XRB	AGN
116	1.6	yes	none	no				SNR	SNR

[a]Inclination-corrected galactocentric radius.

[b]Variability is classified as 'long'-term, 'rapid,' or 'none.'

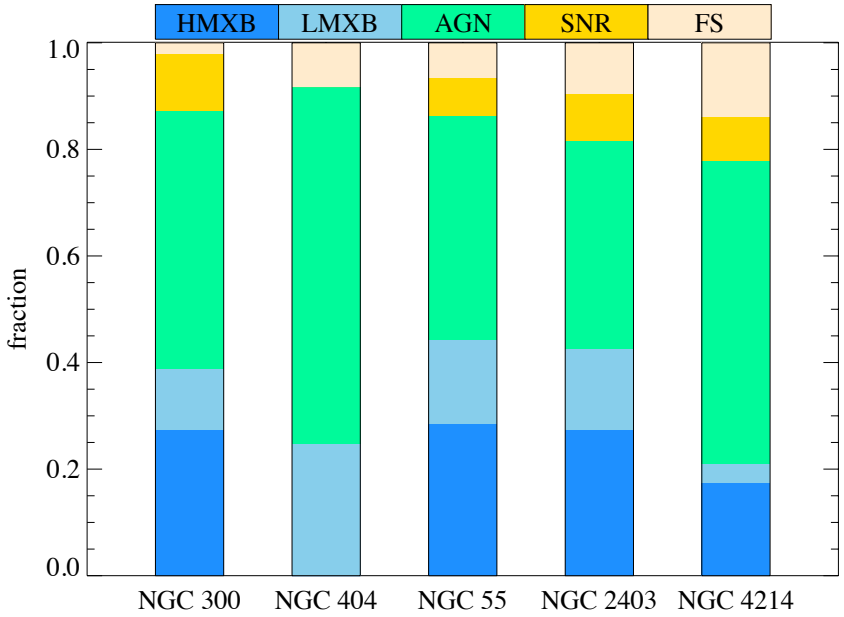

Figure 4.9: The fraction of X-ray sources classified as HMXBs, LMXBs, background AGN, foreground stars ('FS'), and SNRs in each galaxy.

Chapter 5

X-RAY LUMINOSITY FUNCTIONS AND IMPLICATIONS FOR BINARY EVOLUTION

In this chapter, I present the construction and analysis of the HMXB X-ray luminosity functions (XLFs) for each galaxy. The overall shape of the XLF is a useful tool for constraining HMXB formation and evolution models.

5.1 X-ray Luminosity Functions

For a survey covering a total geometric area A, the cumulative number of sources $N(>S)$ (in deg^{-2}) can be evaluated by summing over all sources with fluxes exceeding S (in units of erg s^{-1} cm^{-2}), weighted by the survey area, $A(S)$, over which a source with flux S could have been detected:

$$N(>S) = \sum_{i,S_i>S} \frac{1}{A(S_i)}. \tag{5.1}$$

The factor $A(S)$ accounts for survey completeness for sources distributed uniformly over the survey area. Although there is no reason to assume that sources associated with each galaxy follow a uniform distribution (and we expect a higher source density near the galaxy center), we note that the radial source distributions presented in Chapter 3 did not reveal any major features. Uncertainties in the completeness over the survey area are likely to be small (less than $\sim$10%). The sensitivity maps allow the area function $A(S)$ to be evaluated by summing the sensitivity map over the regions where a source with flux S would be detectable.

Although our point source detection strategy and subsequent source analysis was performed over the full 0.35-8 keV energy range, we restrict our XLF analysis to the 2-8 keV energy band. The hard band reduces contamination from foreground sources and does not suffer from absorption to the same degree as the softer bands, leading to lower uncertainties

in each source's hard X-ray luminosity. Each galaxy had 2-8 keV images, exposure maps, and sensitivity maps separately from the 0.35-8 keV analysis (see Chapter 2). The completeness levels of the luminosity functions is different for each galaxy, owing to different exposure times and distances, ranging from a few $\times 10^{35}$ erg s^{-1} to $\sim 10^{36}$ erg s^{-1}. Four of the five galaxies have 90% limiting completeness levels of at least 10^{36} erg s^{-1} in the 2-8 keV band, with the exception of NGC 300 having a limiting luminosity of 3×10^{36} erg s^{-1}. For easy cross-comparison between the galaxies in our sample, the low-luminosity end is terminated at 3×10^{36} erg s^{-1}.

From $N(> S)$, the differential log$N$-log$S$ distribution can be computed:

$$N(S)\Delta S = \frac{N(> [S + \Delta S]) - N(> S)}{\Delta S}. \tag{5.2}$$

Using the X-ray source classifications determined in Chapter 4, we construct XLFs for the strong HMXB candidates in each galaxy. Since NGC 404 has no evidence for a HMXB population due to its lack of recent star formation, we construct the 2-8 keV XLF using the LMXB candidates. Although we do not expect the NGC 404 LMXBs to follow the same trends as the HMXBs identified for the star-forming galaxies, the multiwavelength approach utilizing the resolved stellar populations to select LMXB candidates has never been performed outside of the Milky Way. Given the resolved nature of the NGC 404 stellar populations, it is interesting to compare the LMXB and HMXB populations selected using the same classification method. We note that uncertainties inherent in our X-ray source classification scheme will dominate the standard deviations of our XLF best fit parameters, and these uncertainties are going to be higher at lower luminosities (where contamination from background AGN will be the highest).

5.1.1 XLFs of Individual Galaxies

We fit the differential 2-8 keV XLFs of individual galaxies constructed from the HMXB candidates with a single-slope power law:

$$\frac{dN}{dL_{36}} = A_d L_{36}^{-\gamma_d} \tag{5.3}$$

where $L_{36} = L_X/10^{36}$ erg s^{-1}. We only fit the portion of the XLFs with luminosities greater than 3×10^{36} erg s^{-1} (roughly the 90% limiting luminosity for all of our sample galaxies). Other authors have reported a high-luminosity break in the XLF near $\sim10^{40-41}$ erg s^{-1} [161, 204, 275]. However, none of the galaxies targeted in our study contain such luminous X-ray sources, so we therefore do not impose a high-luminosity cutoff in our power law model. We note that for NGC 404, the dwarf S0 galaxy with no HMXBs, we construct the XLF from the LMXB candidates only. The NGC 404 XLF is used for comparison purposes only, and not for determining properties of HMXB populations.

Table 5.1: X-ray Luminosity Function Fits

Galaxy	A_d	γ_d	# HMXBs[a]
(1)	(2)	(3)	(4)
NGC 300	48±7	1.58±0.18	14
NGC 404	70±21	$1.73^{+0.23}_{-0.18}$	0[b]
NGC 55	55±21	$2.03^{+0.30}_{-0.22}$	21
NGC 2403	70±6	$1.56^{+0.11}_{-0.10}$	36
NGC 4214	42±10	1.54±0.17	13

[a] The number of HMXB candidates with $L > 3 \times 10^{36}$ erg s^{-1} used for our XLF fitting.

[b] For NGC 404, 16 LMXB candidates were used to construct the differential XLF.

The differential XLFs are fit using a Markov Chain Monte Carlo (MCMC) method. We use the sampler `emcee`[1] [157, 130], written in Python. Our approach is similar to that described in [440]; we provide a brief summary of the method here and refer the reader to the other cited papers for further details. `emcee` explores parameter space utilizing a set

[1] See `dan.iel.fm/emcee`.

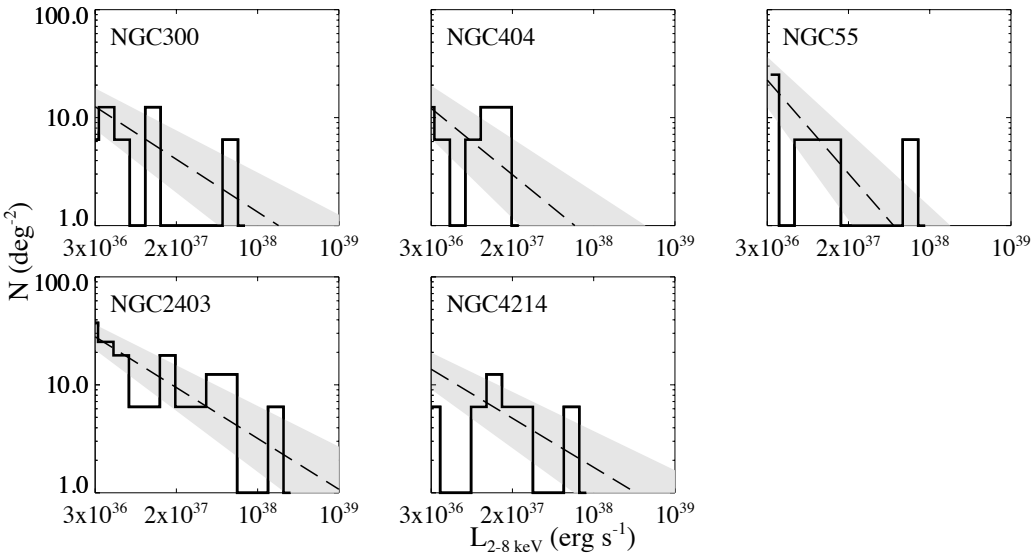

Figure 5.1: The differential 2-8 keV XLFs for each galaxy, with the best-fit power law superimposed. The gray shading shows the 1σ uncertainty in our XLF fits.

of "walkers" which, for each MCMC increment, takes a step in parameter space towards another walker. The step size is selected stochastically, and after each step the posterior probability distribution function is evaluated using Bayes' theorem. Steps in parameter space that increase the probability are always accepted, whereas steps resulting in a lower probability are only sometimes accepted. In order to ensure we sufficiently explored the parameter space for each XLF, we chose 32 walkers and random (valid) values for each walker's starting point. We used 750 burn-in steps and 500 chain steps per walker. The best fit parameters for each galaxy are listed in Table 5.1. The differential XLFs, with the best-fit power-laws superimposed, are shown in Figure 5.1.

Some previous works report the slope of the *cumulative* XLF. Integrating the differential XLF in Equation 5.3 results in a cumulative XLF of the form

$$N(> 10^{36}\text{erg s}^{-1}) = \frac{A_d}{(\gamma_d - 1)} L_{36}^{-(\gamma_d - 1)}. \tag{5.4}$$

We can define the cumulative XLF normalization $A_c = A_d/(\gamma_d - 1)$ and the cumulative slope $\gamma_c = \gamma_d - 1$. We fit the cumulative XLF of each galaxy using our MCMC method to ensure that this approximation was a reasonable one: the best-fit cumulative XLF slopes agreed with our γ_c prediction to within $\sim 2\sigma$ for all five galaxies. However, the correlated errors present in each bin of the cumulative XLF, along with the low number of data points used to derive each XLF, make the cumulative fit parameters less reliable and harder to interpret than the differential XLF. For the remainder of this work, we use all fit quantities derived or approximated from the differential XLF.

A linear relationship has been observed between the cumulative XLF normalization, A, and the SFR [275]. Figure 5.2 shows the cumulative XLF normalization as a function of SFR over the last 100 Myr (the dwarf S0 galaxy NGC 404, in cyan, is shown for contrast). We additionally show the previously-obtained best-fitting linear relationship [275], which was derived for galaxies with typically higher SFRs than we observe in our sample. NGC 55 falls marginally above this relationship, while NGC 2403 falls slightly below it. However, none of the star forming galaxies deviate from the observed relationship by a large factor.

Earlier works have utilized different approaches for identifying which X-ray sources are

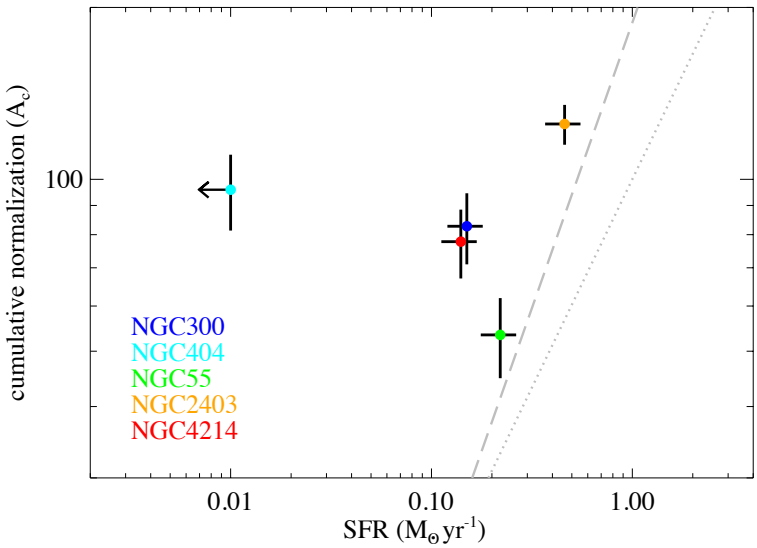

Figure 5.2: The cumulative XLF normalization versus SFR for the CLVS galaxies, compared to the best-fitting linear (dashed gray line) and logarithmic (dotted gray line) relationships found by [275].

to be used in the construction of the XLFs [216, 275], including differences in determining the regions used to measure source counts and covering only select portions of each galaxy. It is therefore possible that the XLFs are contaminated by a residual LMXB contribution from the bulges of galaxies in some studies [216], while other studies neglect the central region of the host galaxy entirely [275]. In contrast, the multiwavelength analysis of the *resolved* stellar populations associated with each individual X-ray source has enabled us to identify the strong individual HMXB candidates in each galaxy from which our XLFs are constructed.

Models of the XLF evolution have revealed that the slope of the cumulative XLF in the hard X-ray band correlates with the time elapsed since a nearly-instantaneous burst of star formation [with a SFR of 10 $M_{\odot}$ yr^{-1} and lasting 20 Myr 120]. The models predict that the "universal" HMXB XLF index of $\sim$1.6 is achieved at $\sim$50–90 Myr after the burst. The *HST* images of NGC 300 and NGC 2403 have been used to examine the SFHs of the resolved (coeval) stellar populations in the immediate vicinity of our HMXB candidates [444], allowing the approximate ages of the HMXBs to be determined. The typical HMXB age was found to be to be $\sim$40-55 Myr, consistent with HMXB evolution models [332]. Despite having SFHs very different from those typically examined in models [e.g., 120], the CLVS star-forming galaxies are consistent with the universal HMXB XLF and predictions of the age at which X-ray production by HMXBs peaks.

5.2 Star Formation Histories

The exquisite *HST* imaging and deep *Chandra* imaging presented in this thesis make an ideal data set through which the L_X–SFR relationship can be investigated in the low-SFR regime. Previous studies of the L_X–SFR relationship (especially important for high-z AGN studies) have depended on estimates of the SFR from various multiwavelength analyses. The key advantage of our study is the use of resolved stellar photometry from *HST* to calculate the SFHs of each galaxy. *HST* imaging of all five galaxies in our sample were obtained through the ANGST survey [87]. Detailed analyses of the SFHs are available in the literature: NGC 300 [153], NGC 404 [447], NGC 2403 [448], NGC 4214 [446]. The SFH of NGC 55 was examined as part of a study of Local Group dwarf galaxies [439].

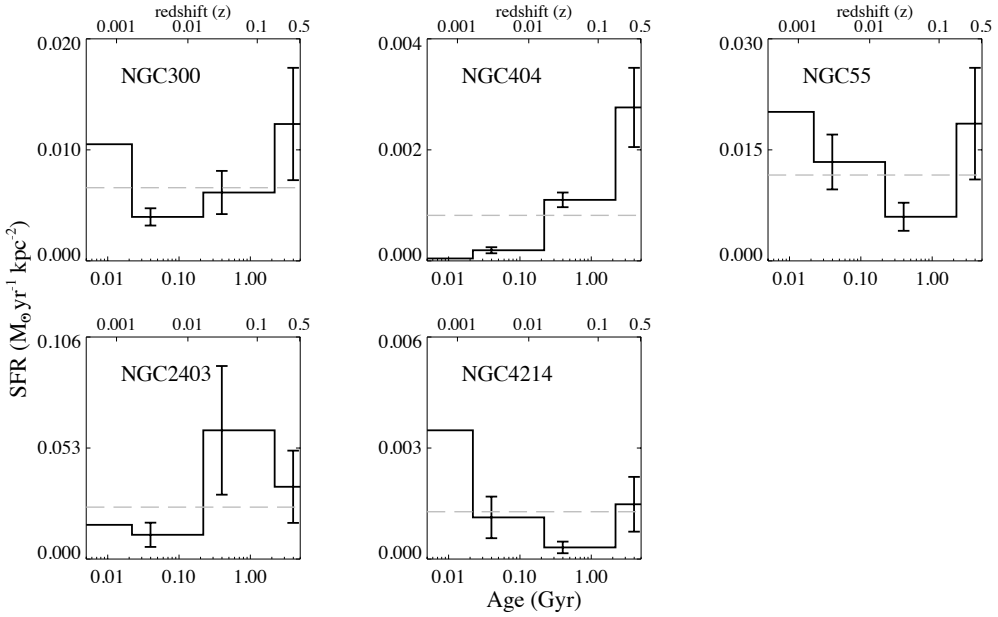

Figure 5.3: The SFHs of each of the five CLVS galaxies. The dashed gray lines indicate the lifetime average SFH.

The SFHs of each galaxy are shown in Figure 5.3, showing the SFR over the entire lifetime of the galaxy (back to 14 Gyr). We define the birthrate parameter, b, as the ratio of the total SFR in the last 100 Myr to the average SFR over the lifetime of the galaxy:

$$b = \frac{\sum \mathrm{SFR}(< 100\mathrm{Myr})}{\langle \mathrm{SFR} \rangle}, \tag{5.5}$$

Figure 5.4 compares the total SFR over the last 100 Myr to the birthrate parameter b for each galaxy. All four of the star-forming galaxies in our sample show vigorous ongoing star formation, with b parameters ranging from ∼3–5, while NGC 404 has a very low value of b (∼0.15) as expected for an early-type galaxy. It is interesting to note that NGC 4214 is classified as a "Wolf-Rayet" galaxy due to the high level of *relatively* recent star formation over the last 100 Myr, despite the fact that the majority of the NGC 4214 stellar population is old [∼74% of the stellar population has ages >8 Gyr 446].

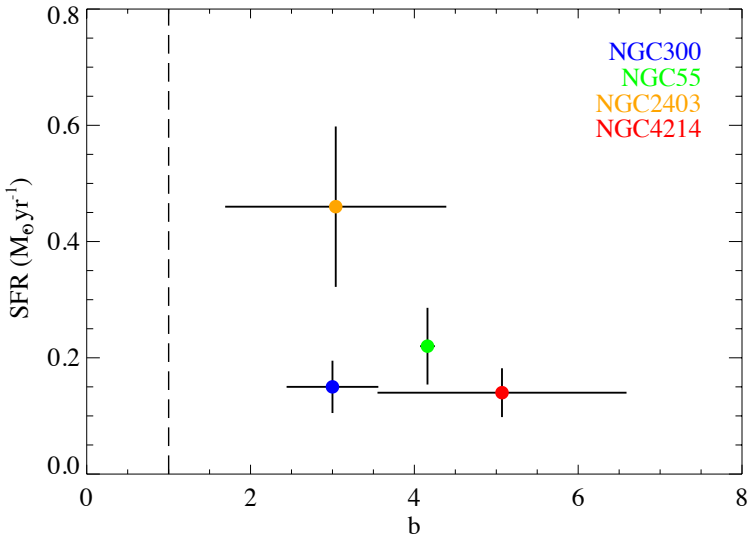

Figure 5.4: The SFR as a function of the 100 Myr birthrate parameter, b, for the four star-forming galaxies in this survey. The vertical dashed line shows where $b = 1$; i.e., where the SFR rate over the last 100 Myr is equal to the SFR over the lifetime of the galaxy.

To determine the current SFR for each galaxy, flux measurements were made using public *GALEX* FUV and *Spitzer* 24μ images from the Local Volume Legacy survey [LVL; 88, 239]. We utilize a hybrid FUV+24μ SFR calibration [170], which uses the 24μ flux to make a dust correction to the FUV flux using the following relation:

$$L_{FUV}^{corr} = L_{FUV}^{obs} + (3.89 \times L_{24\mu})\,\mathrm{erg\ s^{-1}}. \tag{5.6}$$

FUV fluxes are corrected for Galactic foreground extinction [359] and $E(B-V)$ values [239]. The corrected FUV luminosity is then converted to a SFR using the following relation [also from 170],

$$SFR_{FUV}(M_\odot\ \mathrm{yr}^{-1}) = L_{FUV}^{corr}\left(\mathrm{erg\ s^{-1}}\right) \times 10^{-43.35}, \tag{5.7}$$

which assumes a Kroupa IMF over a mass range of 0.1–100 $M_\odot$ [228], solar metallicity, and a constant SFH over the past 100 Myr. Relative SFR fractions are calculated by comparing

the integrated SF found within the *HST* footprints to the total SFR found within the galaxy-wide LVL apertures.

The values of b and and the global SFRs for each galaxy are listed in Table 5.2.

Table 5.2: Galaxy Sample, Star Formation Rates, and Birthrate Parameters

Galaxy	Obs ID	SFR ($M_\odot$ yr^{-1})	b
(1)	(2)	(3)	(4)
NGC 300	12238	0.15	3.00±0.56
NGC 404	384, 870, 12239	<0.01	0.15±0.09
NGC 55	2255, 4744	0.22	4.16±1.35
NGC 2403	2014, 4627, 4628, 4629, 4630	0.46	3.04±1.52
NGC 4214	2030, 4743, 5197	0.14	5.07±2.54

5.3 Observed Correlations with Star Formation

Although the CLVS galaxies span a similar range of stellar mass as previous studies of the L_X-SFR relationship, all five galaxies have low SFRs compared to the galaxies examined in earlier studies. We illustrate this in Figure 5.5, where the cumulative distributions of star forming galaxies analyzed in the literature (black, [275]; gray, [161]) are shown compared to the CLVS galaxies. We have highlighted the locations of the five galaxies considered in this work. All of our galaxies have significantly lower SFRs than other galaxies studied. The CLVS galaxies additionally represent a significantly lower rate of specific star formation (sSFR): SFR/M_* (in units of 10^{-10} yr^{-1}) for our star-forming galaxy sample is 0.45, while the average for the literature data is an order of magnitude larger, at 4.2 [275].

Figure 5.6 shows the cumulative XLF slope as a function of SFR for both our sample and the sample of star-forming galaxies [216] . For the star-forming sample, we estimate the SFR of each galaxy using empirical cross-calibration of SFR indicators [350] for either *IRAS* 60μ emission [283] or *GALEV* NUV emission [89]. The individual XLFs of the CLVS

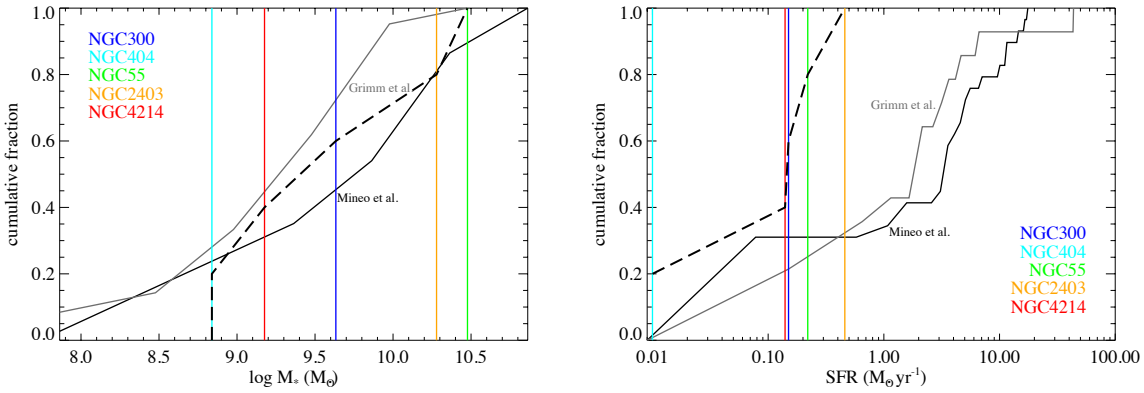

Figure 5.5: Cumulative distributions of the stellar masses *(left)* and SFR *(right)* of galaxies examined in three L_X-SFR studies. In both panels, the [275] sample is shown in black and the [161] sample is shown in gray. The cumulative distribution of the CLVS galaxies are shown by the dashed line, with the individual galaxies shown by the colored vertical lines. Although the CLVS galaxies span a comparable range in stellar masses compared to earlier studies (left), our sample is at the low-SFR end when compared to these other studies.

star-forming galaxies have a mean γ_d of 1.7 with a standard deviation of ± 0.2, corresponding to a cumulative slope of $\sim$0.7. This value is consistent with the "universal" XLF reported in previous studies [161, 68, 275], and somewhat flatter ($\sim 2\sigma$) than the average observed for the star-forming sample [216] sample ($\gamma_c \sim 0.97 \pm 0.13$). The only galaxy in our sample that deviates from the "universal" slope is NGC 55, which may suffer from increased contamination in the HMXB candidate sample due to the edge-on nature of the galaxy.

The addition of the CLVS galaxies to the star-forming sample [216] shows evidence in a decreasing trend in γ_c with SFR. This trend is consistent with theoretical models and earlier observations: initially, star-forming galaxies produce both bright and faint HMXBs, resulting in a relatively flat XLF [416, 120]. As the HMXB populations age, the brightest (i.e., most massive) Roche lobe-overflowing systems evolve faster, resulting in a steepening of the XLF slope. We find the best-fit linear relationship between the cumulative XLF slope γ_c and SFR to be:

$$\gamma_c = (0.59 \pm 0.12) - (0.25 \pm 0.10)\log SFR\left(M_{\odot}\mathrm{yr}^{-1}\right) \tag{5.8}$$

We performed a Spearman rank correlation to determine the probability that this correlation is genuine. We find this probability to be less than $\sim$5%, providing marginal ($\sim 2\sigma$) evidence of a correlation. We additionally perform a two-sided KS test to determine the probability that the observed values of γ_c were drawn from a uniform distribution with a mean value of 0.97. We find this probability to be $\sim$2%, providing marginal evidence that the observed values of γ_c were not drawn from a uniform distribution.

In Figure 5.7, we compare the relationship between the number of HMXBs with 2-10 keV luminosities above 10^{38} erg s^{-1} and the recent SFR for the CLVS galaxies and a literature study of star-forming galaxies [161]. We note that sources above this luminosity threshold, which was chosen based on the completeness limits of the galaxies in the literature sample, will be dominated by HMXBs with X-ray production driven by Roche lobe overflow. Additionally, this luminosity cutoff is approximately at the Eddington limit of a NS, implying that systems with BH primaries may contribute significantly to the observed relationship. Both previous studies found linear relationships between the number of HMXBs above 10^{38}

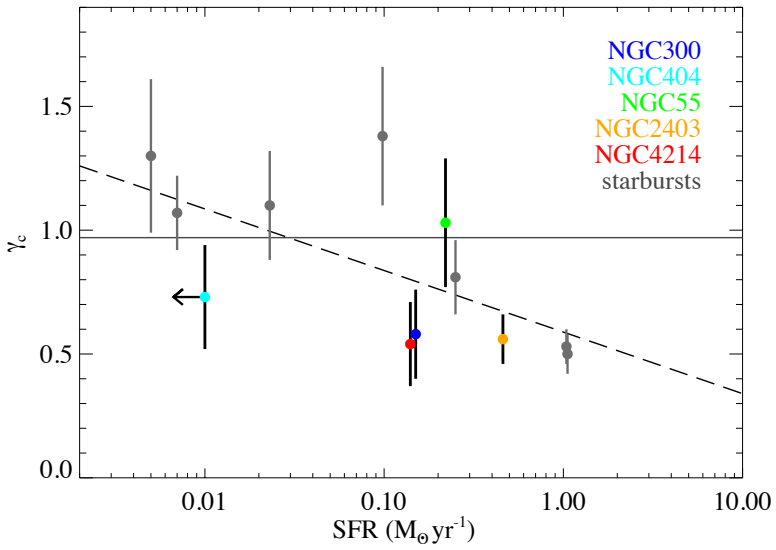

Figure 5.6: The slope of the cumulative XLF as a function of SFR for the CLVS galaxies (approximated at $\gamma_c \approx \gamma_d - 1$) and the [216] starburst sample (gray). The SFR shown for NGC 404 is an upper limit. The addition of the CLVS galaxies suggests a trend of decreasing γ_c with SFR.

erg s^{-1} and the SFR [161, 275], with slopes of 2.9±0.2 and 3.2±0.3, respectively. When we add the CLVS galaxies, which have significantly lower SFRs, to their samples, we find a best-fit relationship with a slope of 3.0±0.4, in agreement with both previous studies. Fitting to CLVS galaxies alone yields a slope of 3.3±0.6.

The simplest assumption concerning the connection of HMXBs and SFR is that the number of X-ray sources with a high-mass companion is directly proportional to the recent SFR of the host galaxy. When the XLF is not very steep (i.e., $\gamma < 1$), this assumption is easily justified. Using the differential XLF of the form presented in Equation 5.3, the $n = 0$ and 1 moments can be computed:

$$N_{\rm tot} = I_0 \approx \frac{AL_0}{1-\gamma}\left(\frac{L_{\rm max}}{L_0}\right)^{1-\gamma} \tag{5.9}$$

and

$$L_{\rm tot} = I_1 \approx \frac{AL_0^2}{2-\gamma}\left(\frac{L_{\rm max}}{L_0}\right)^{2-\gamma} \tag{5.10}$$

where $N_{\rm tot}$ is the total number of HMXBs, $L_{\rm tot}$ is the total X-ray luminosity produced by the HMXBs, and $L_{\rm max}$ is the highest observed luminosity. Dividing equation 5.10 by equation 5.9 results in a relationship between $L_{\rm tot}$ and $N_{\rm tot}$:

$$L_{\rm tot} = \left(\frac{1-\gamma}{2-\gamma}\right) L_{\rm max} N_{\rm tot}. \tag{5.11}$$

Therefore, if the total luminosity is proportional to the SFR of the galaxy (e.g., SFR = $\alpha L_{\rm tot}$), then the total number of HMXBs must also scale proportionally with the SFR. This relationship, however, is also dependent on $L_{\rm max}$. The SFR of a galaxy may drastically under-predict the observed X-ray luminosity if that galaxy hosts a rare, luminous HMXB.

5.3.1 The L_X-SFR Relation in the Low-SFR Regime

Understanding the L_X–SFR relation is important not only for the study of HMXBs, but also for studies of AGN at high redshift. To accurately separate the X-ray luminosity associated with star formation from that produced by a central AGN, the L_X–SFR for HMXBs must be constrained down to modest SFRs. The collective HMXB luminosity was computed by

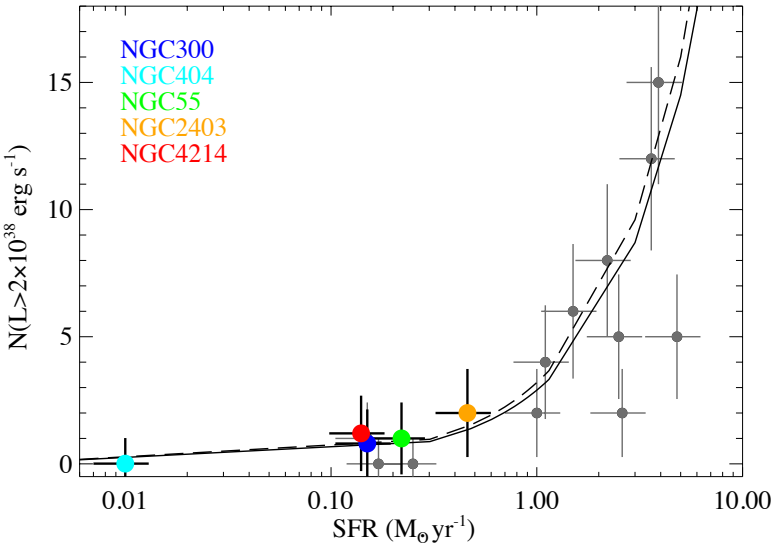

Figure 5.7: The number of sources with a 2-10 keV luminosity above 2×10^{38} erg s^{-1} as a function of the SFR of the host galaxy. The gray points show the sample from [161], and the CLVS galaxies are shown by the colored points. The solid line is the best-fit relationship found in [161], while the dashed line shows the best-fit relation obtained in [275]; our low-SFR sample is consistent with both relationships. NGC 300 and NGC 4214 are shown with an arbitrary y-axis offset of 0.2 for clarity.

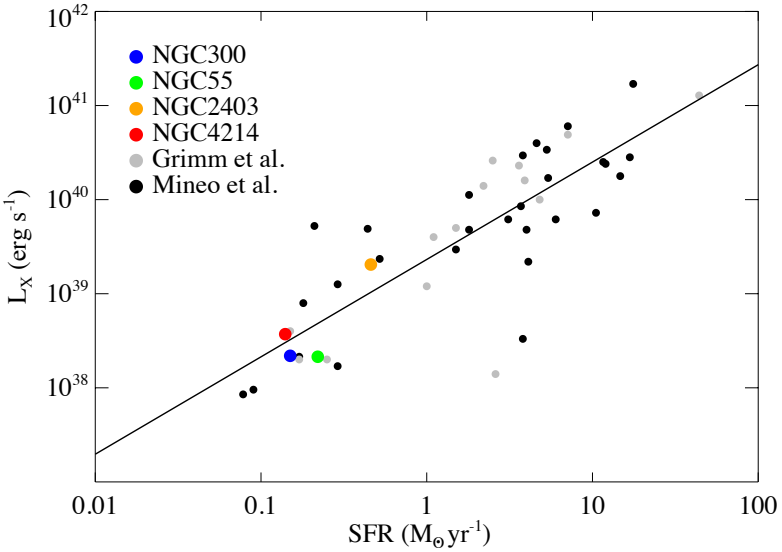

Figure 5.8: The L_X–SFR relation. The star-forming CLVS galaxies are shown by the colored points, while the galaxies from [275] are shown in black and the [161] primary sample is shown in gray. The solid line shows the best-fit relationship.

Table 5.3: HMXB-SFR Relation Data

Galaxy	M_*	SFR/M_*	$N_{\rm HMXB}$	$N_{\rm HMXB}$	$N_{\rm HMXB}$	logL_X^a
	(10^9 $M_\odot$)	(10^{-10} yr^{-1})		($L > 10^{37}$)	($L > 10^{38}$)	(erg s^{-1})
(1)	(2)	(3)	(4)	(5)	(6)	(7)
NGC 300	4.3[b]	0.35	57	2	1	38.34
NGC 404[c]	0.69[d]	<0.01	21	13	0	38.73
NGC 55	30[e]	0.07	42	2	1	38.33
NGC 2403	19[f]	0.24	54	37	2	39.31
NGC 4214	1.5 [g]	0.93	16	9	1	38.57
CLVS average[h]	13.7	0.40	42	12.5	1.3	38.85

[a]The total X-ray luminosity in the 0.35-8 keV energy band of the HMXB candidates; [b][327]; [c]For NGC 404 we report the number and luminosity of LMXB candidates; [d][400]; [e][99]; [f][95]; [g][210]; [h]Average values are reported for the star-forming galaxies only (excluding NGC 404).

summing the luminosities of our individual HMXB candidates. Because of our efforts to reach similar depths for all galaxies, the limiting luminosities only vary by a factor of ∼5. Since this difference in limiting luminosity affects only the faintest detectable sources, the contribution to the collective HMXB luminosity will be small, $< 2\%$.

Figure 5.8 shows the L_X–SFR relation for the CLVS galaxies compared to the literature samples (gray points, [161]; black points, [275]). We derived best-fit L_X–SFR relationships using our sample combined with the star-forming galaxies from the literature. In both cases, the value of the power law index is consistent with unity; we therefore fix the index at 1 and obtain the best-fitting linear relation:

$$L_X = (2.3 \pm 0.3) \times 10^{39} \text{ erg s}^{-1} \times \text{SFR}/(\text{M}_\odot \text{ yr}^{-1}). \quad (5.12)$$

When we fit the CLVS galaxies alone, the luminosity factor is $(2.7\pm0.5)\times10^{39}$ erg s^{-1}. These results are consistent with that found in previous studies, including the relations found by including galaxies with AGN components and higher redshifts than we considered here [190,

and references therein].

This result is notable for two reasons. First, unlike previous studies, our SFRs were derived from resolved stellar photometry and detailed SFHs for each galaxy, as compared to the star formation indicators used in other works. Second, our relationship was derived using only the strong individual HMXB candidates. The fact that our L_X–SFR relation agrees so well with that found in other works, where the contribution from contaminants (background AGN, foreground stars, etc.) were subtracted out in a statistical sense only, suggests that our X-ray source classification scheme is recovering a significant fraction of HMXBs in each galaxy (and that the statistical corrections work reasonably well for high-SFR galaxies).

Although it has been noted [161, 152] that the L_X–SFR may be non-linear in the low-SFR regime (i.e., SFR$<$ a few $M_\odot$ yr^{-1}), we do not observe any evidence for this in our sample (with SFRs down to $\sim$0.1 $M_\odot$ yr^{-1}). The non-linearity of the L_X–SFR relation is likely the result of small number statistics and observer bias, suggesting that statistical corrections are less reliable in the low-SFR regime. Furthermore, previous studies have utilized the *Chandra* archive to obtain data, and these observations may have been selectively performed because the host galaxies were known to have high SFRs and high X-ray luminosities. In contrast, our survey is volume-limited and designed to match existing *HST* observations. As a result, the CLVS galaxies are significantly less X-ray luminous and have lower SFRs when compared to earlier studies, thereby providing a useful probe of the L_X–SFR relation in the low L_X and low SFR regime.

As evidenced by Figure 5.7, only a small number of X-ray sources are responsible for the observed L_X–SFR relationship in star forming galaxies. We have investigated at what level the lower-luminosity XRBs, which form the dominant population by number, contribute to this relationship. For each galaxy, we compute the luminosities for which 90% of the XRB populations are fainter than (which we refer to as $L_{90\%}$) and which 50% of XRBs fall below, $L_{50\%}$. The percentile luminosities are defined by

$$\int_{L_{\rm min}}^{L_{p\%}} f(L){\rm d}L = p\% \int_{L_{\rm min}}^{L_{\rm max}} f(L){\rm d}L, \tag{5.13}$$

where $f(L)$ are the XLFs constructed in Section 5.1.1. We assume $L_{\rm min} = 3 \times 10^{36}$ erg

s^{-1} (roughly the 90% completeness limit for all five galaxies), $L_{\rm max}$ was set to the highest luminosity observed in each galaxy's HMXB population (typically a few 10^{38} erg s^{-1}).

There is a slight trend towards higher percentile luminosities with SFR, shown in Figure 5.9, although it is not significant (a Spearman rank test yields $\rho = 0.5$). The average values of $L_{90\%}$ and $L_{50\%}$ are 9×10^{37} erg s^{-1} and 3×10^{37} erg s^{-1}, respectively. Qualitatively, these estimates support the theoretical prediction that the formation of bright HMXBs (with L_X greater than a few 10^{38} erg s^{-1}) is uncommon in galaxies [195, 20, 29], and illustrates that the observed L_X–SFR relationship is being driven by less than 10% of the host galaxy's HMXB population. However, the uncertainties in the percentile luminosities are quite large ($\log L_{\rm err} \sim 0.5$), as they depend sensitively on number of sources observed.

5.4 X-ray Binary Formation and Evolution

5.4.1 HMXB Formation Efficiency

HMXBs are a ubiquitous feature of recent star formation. More specifically, HMXBs are the direct result of massive star formation, which have a significantly higher rate of forming in binaries or multiple star systems than solar-type stars [see 469, 265, and references therein]. However, in order to form an HMXB, the progenitor binary must survive the SN explosion that occurs when the more massive companion dies and maintain orbital parameters conducive to mass transfer onto the resulting compact object. Constraining the efficiency of HMXB formation (e.g., the probability that a given massive binary will produce an HMXB) can therefore provide useful insight into the evolutionary pathways that must be taken by a progenitor massive binary in order to form an HMXB.

Simultaneously measuring the number of HMXBs and OBs stars in a given galaxy is highly challenging, as deep multiwavelength observations of the resolved stellar population are required. To date, such studies have focused only on the Milky Way [247, 248] and the Magellanic Clouds [166, 259, 73, 4]. A correlation between the ratio of the number of HMXBs to OB stars and the SFR at the age of maximum Be-star production (~ 42 Myr) was directly observed in the SMC [6], as well as in NGC 300 and NGC 2403 [444].

In addition to being able to identify strong HMXB candidates down to a limiting lumi-

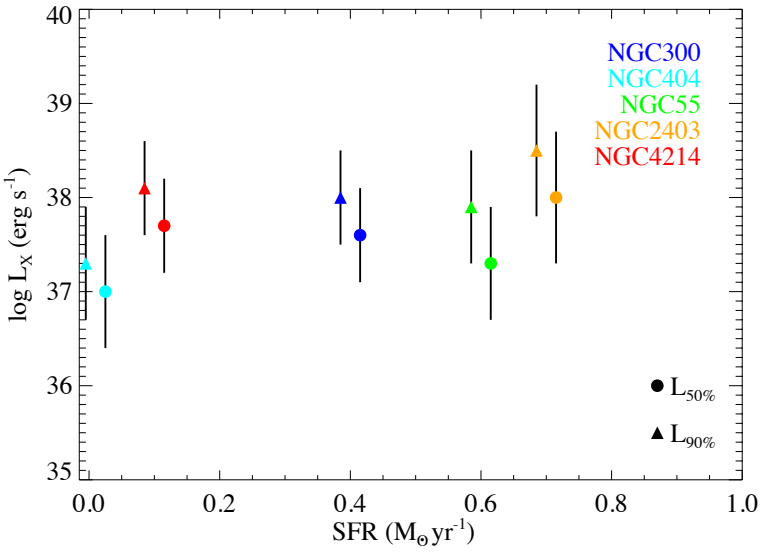

Figure 5.9: The 90% and 50% X-ray luminosities as a function of SFR. There is a slight trend towards higher percentile luminosities at higher SFRs, although it is not statistically significant. Values of $L_{90\%}$ for each galaxy are shown by triangles, and $L_{50\%}$ values are shown by circles; symbols are offset by ± 0.015 $M_\odot$ yr^{-1} for clarity.

nosity of $L_X \sim 10^{36}$ erg s^{-1} with *Chandra*, our *HST* observations reach a depth of $M_V \sim 0$ for each galaxy, making it possible to resolve individual O and B-type main sequence stars. To estimate the number of OB stars present in each *HST* field, we select stars with $V - I <$ the reddening of each galaxy, typically ∼0.03-0.11 (corresponding approximately to the $V - R$ color of an A0 main sequence star) and absolute magnitudes $F555W < -1$ in each *HST* exposure for the four star-forming galaxies in our sample. This cut corresponds to a minimum detectable stellar mass of ∼3 $M_\odot$ in each galaxy. We then count the number of HMXB candidates present within each *HST* field. The relationship between the number of HMXBs and number of OB stars is shown in Figure 5.10.

The number of observed HMXBs increases with the number of OB stars present in each field. We fit a linear relationship to this trend:

$$n_{HMXB} = (0.4 \pm 0.1) \times \left(\frac{n_{OB}}{10^3}\right). \tag{5.14}$$

This relationship provides an estimate of the efficiency at which OB stars form HMXBs: only ∼1 HMXB (with $L_X > 10^{36}$ erg s^{-1}) forms for every ∼3,800 OB stars that form. We note that the observed OB stars in our observations are *not* the direct progenitors of the observed HMXBs (although some of the observed systems may potentially form HMXBs later in their evolution). Instead, the observed OB stars are likely *less* massive than those that formed the HMXBs. A true HMXB efficiency factor must include the shape of the IMF at high stellar masses (e.g., for our observations, above ∼3 $M_\odot$) as well as the IMF of the secondary star in the massive binary.

Nonetheless, the SFRs of our sample galaxies over the last ∼100 Myr (from the resolved star formation histories) indicate that these galaxies have been actively forming massive stars over a time period which we would expect to see HMXB formation. Given equation 5.14, we can roughly estimate the formation fraction of bright HMXBs from primordial massive binaries to be ∼0.03%.

We note that our HMXB candidates all have X-ray luminosities greater than ∼10^{36} erg s^{-1}. We therefore attempt to estimate the efficiency at which lower-luminosity HMXBs form from primordial OB binaries. HMXBs in the SMC follow a single, unbroken power law down

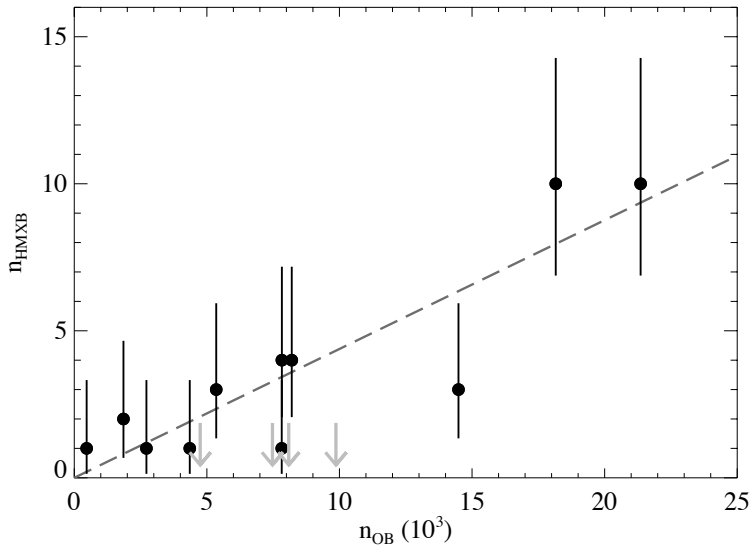

Figure 5.10: The number of HMXBs observed by *Chandra* as a function of the number of OB stars observed in each *HST* field. *HST* fields that did not contain any strong HMXB candidates are shown by the gray upper limits. The dark gray dashed line shows the best-fit linear relationship between the number of OB stars to HMXB candidates.

to $L_X \sim 10^{34}$ erg s^{-1} with a differential index of $\sim$0.50, still roughly consistent with the universal XLF slope [374], although binary simulations suggest the XLF may flatten at very low X-ray luminosities [$<10^{33}$ erg s^{-1}; 29]. If we assume the "universal" XLF extends down to $\sim 10^{34}$ erg s^{-1}, we find the number of predicted HMXBs increases by a factor of $\sim$16. We therefore expect 1 HMXB (with $L_X > 10^{34}$ erg s^{-1}) to form for every 240 primordial OB binaries, or $\sim$0.4% of the time.

5.4.2 Timescale of the X-ray Luminous Phase

We can use our cumulative HMXB XLFs of the star-forming galaxies in our sample to estimate the fraction of compact objects that went through an "X-ray luminous" phase ($L_X > 10^{35}$ erg s^{-1}). Past attempts to measure this quantity have relied on indirect measurements of the SFR and the number of HMXBs with luminosities $> 10^{38}$ erg s^{-1} [275]. The SFRs of the low mass galaxies considered here is low compared to these earlier studies, resulting in fewer HMXBs with luminosities above 10^{38} erg s^{-1}. However, our survey is sensitive to much lower limiting luminosities than previously accessible. We therefore chose to use the average cumulative XLF of the star-forming galaxies to constrain the fraction of binaries that underwent an HMXB phase.

To construct the average cumulative XLF, we weighted the two fit parameters (normalization A and slope γ) by the SFR of each galaxy, so that

$$\langle A \rangle = \frac{\sum_i \mathrm{SFR}_i A_i}{\sum_i \mathrm{SFR}_i} \tag{5.15}$$

and

$$\langle \gamma \rangle = \frac{\sum_i \mathrm{SFR}_i \gamma_i}{\sum_i \mathrm{SFR}_i}. \tag{5.16}$$

We find average differential XLF parameters $\langle \gamma_d \rangle = 1.67 \pm 0.11$ and $\langle A_d \rangle = 59 \pm 6$. Integrating Equation 5.3 yields the number of HMXBs N_X, for four galaxies, with X-ray luminosities greater than 10^{35} erg s^{-1}:

$$N_X(> 10^{35} \mathrm{erg\ s^{-1}}) \approx 410 \pm 50. \tag{5.17}$$

This value corresponds to ∼103 HMXBs per galaxy. The corresponding relationship in [275] predicts ∼32 HMXBs (assuming a mean SFR of 0.24 $M_{\odot}$ yr^{-1} for our sample) per galaxy. Our estimate of the number of HMXBs with a luminosity $>10^{35}$ erg s^{-1} is 2.4σ higher than predicted in [275].

The total number of luminous HMXBs present at any given time depends on four parameters: the fraction of the birth rate of compact objects ($\dot{N}_{\rm co}$), the fraction of compact objects that are in massive binaries ($f_{\rm bin}$), the fraction of binaries that undergo an X-ray luminous phase (f_X), and the average duration of the X-ray luminous phase (τ_X). We therefore can write:

$$N_X \sim \dot{N}_{\rm co} f_{\rm bin} f_X \tau_X. \tag{5.18}$$

We can assume the birth rate of compact objects is roughly equal to the birth rate of massive stars (i.e., those stars with $m \geq 8\ M_{\odot}$). A Kroupa IMF [228] predicts ∼1% of stars form with masses sufficient to form a compact object; therefore, the birth rate of compact objects is:

$$\dot{N}_{\rm co} \sim 10^{-2} \times {\rm SFR}\ (M_{\odot}{\rm yr}^{-1}). \tag{5.19}$$

Using the mean SFR from our galaxy sample (0.24 $M_{\odot}$ yr^{-1}), we estimate $\dot{N}_{\rm co} \sim 2.4 \times 10^{-3}$ compact objects per year.

The duration of the X-ray luminous phase depends on the nature of the HMXB components and the accretion mechanism. Observations of the Milky Way and Magellanic Clouds suggest HMXBs can be separated into two broad classes: those with supergiant OB-type companions, and those with a rapidly rotating Be companion [BeXBs; 248]. Approximately $^2/_3$ of HMXBs are BeXBs [309]. While the most luminous HMXBs are powered by Roche-lobe overflow from the stellar companion into an accretion disk around the compact object [i.e., NGC 300 X-1, 37], the compact objects in a vast majority of lower-luminosity sources ($<10^{37}$ erg s^{-1}) are accreting material directly from the stellar winds of their companion [309, 341]. Theoretical models suggest that the HMXB phase lasts $\sim 10^{4-5}$ years [418, 29].

We can now use our estimates for the number of X-ray luminous HMXBs N_X, the birth

rate of compact objects $\dot{N}_{\rm co}$, and the the typical SFR for galaxies in our sample to find the fraction of binaries that experience an X-ray luminous phase:

$$f_{\rm bin} f_X \sim (0.4 \pm 0.1) \left(\frac{\tau_X}{10^5 \text{ yr}} \right)^{-1}. \tag{5.20}$$

In other words, we find that 30–50% of evolved massive binaries become X-ray sources with $L_X > 10^{35}$ erg s^{-1}, with a characteristic lifetime of 10^5 years.

In Section 5.4.1, we utilized our matched *HST* observations to directly measure $f_{\rm bin} f_X$ in each field containing an HMXB candidate down to $\sim 10^{36}$ erg s^{-1}. When we repeat the above exercise for a limiting lower luminosity of 10^{36} erg s^{-1}, the factor in equation 5.20 becomes 0.3±0.1, consistent with our result here.

We would like to stress that the OB stars observed in our *HST* imaging are *not* the progenitors of the observed HMXBs, with the exception of a small handful of optical counterpart candidates. The observed OB stars either formed at the same time as the HMXB progenitors, but with a mass too low to form an HMXB, or have formed more recently. In this section, we considered only stars born with a mass sufficient to form a compact object (>8 $M_\odot$), while our *HST* observations are capable of detecting individual stars down to ~ 3 $M_\odot$. A Kroupa IMF predicts $\sim$1% of stars will form with a mass >8 $M_\odot$, while $\sim$3.5% of stars will form with >3 $M_\odot$.

We therefore estimate that 1 HMXB (with $L_X > 10^{36}$ erg s^{-1}) forms for every 3800 stars with a companion of mass $> 3 M_\odot$, while $\sim$40% of evolved massive binaries experience a luminous HMXB phase at some point during their evolution.

5.4.3 The Mass Distribution of the Stellar Companions

Observations of HMXB populations can be used to place constraints on the mass ratio distribution of evolved massive binaries. The fraction of X-ray luminous systems (which we here define as $L_X > 10^{35}$ erg s^{-1}) must be less than or equal to the fraction of binary systems with a compact object and a massive stellar companion [typically $\geq 5 M_\odot$; 167].

The Kroupa IMF [228] over a mass range of 0.1–120 $M_\odot$ predicts $\sim$2% of stars have masses greater than 5 $M_\odot$. However, in Section 5.4.2 we estimated $\sim$40% of massive binaries

capable of forming an HMXB will produce X-rays at some point in their lives. Thus, the measured fraction of X-ray producing HMXBs is larger than the predicted fraction of binaries with stellar companions capable of powering this X-ray emission by a factor of ∼20. This discrepancy suggests that the mass distribution of the HMXB secondary stars is significantly different from a Kroupa IMF, which is not surprising since the masses of the secondaries increase as they accrete from their more massive companion.

If we assume a general power law model for the mass distribution of the stellar companions, $\phi(m_2) \propto m_2^{-a}$, we can estimate the power law index required by our X-ray observations. Setting the fraction of HMXB stellar companions $\phi(m_2 > 5\ M_\odot)$ equal to the X-ray luminous fraction derived in equation 5.20, we can constrain the power law index $a < 0.3$. This is significantly flatter than the high-mass power law index of the Kroupa IMF. Our observations strongly exclude the possibility that the masses of the stars in HMXBs are independently drawn from a Kroupa IMF. This result is comparable to the direct measurements of the companion mass distribution observed in star clusters and associations, where $a = 0.4$–0.5 [272, 339].

5.4.4 Duty Cycle of X-ray Variability

With the exception of NGC 300, for which we have only a single "snapshot" observation, all XLFs discussed in this work were created from the merged image of multiple *Chandra* observations. Since compact X-ray sources are known to be variable, especially at luminosities below $\sim 10^{37}$ erg s^{-1}, the faint end of the XLFs could be affected by the fraction of time each X-ray source spends in a high-luminosity or "burst" phase (i.e., the duty cycle). More formally, the duty cycle (DC) is defined as:

$$\mathrm{DC} = \frac{T_b}{T_b + T_q}, \tag{5.21}$$

where T_b is the total time the system spends bursting and T_q is the total time spent in quiescence.

We searched our catalog for HMXB candidates that exhibited a change in flux of an order of magnitude or more over multiple observations. We found five such objects from NGC 2403

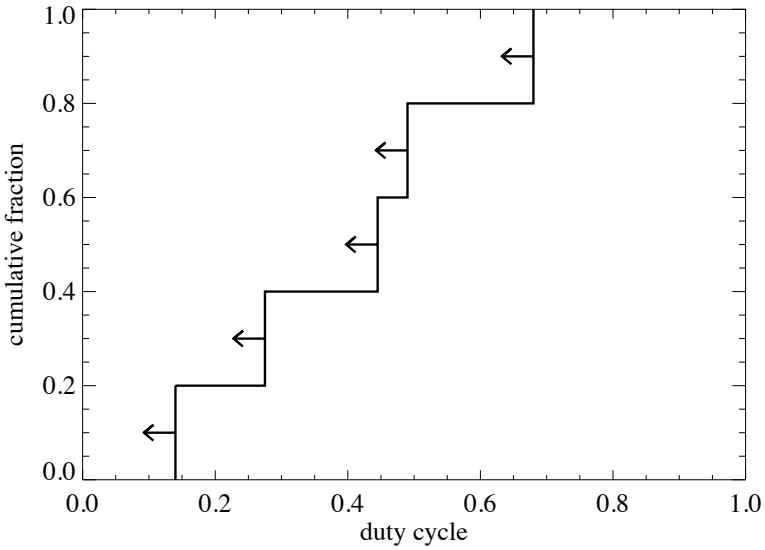

Figure 5.11: Cumulative histogram of the duty cycle upper limits for HMXBs exhibiting a change in flux greater than an order of magnitude.

and NGC 55, with a total of seven *Chandra* fields and five *XMM-Newton* fields, for which we were able to estimate an upper limit on the DC. This estimate assumes that the observed "burst" lasted the duration of the exposure where the flux was elevated (T_b). Although it is likely that these "bursts" occurred over some fraction of the exposure time, for our low-count data we were not able to reliably determine if an outburst occurred for only a portion of a given observation. All exposures during which the source was either not detected, or detected to be a least an order of magnitude fainter than the peak luminosity, were taken to be the quiescent time (T_q). If we assumed that all the time between observations was spent in quiescence, the DC becomes $\sim$0.2%. The cumulative distribution of DC upper limits is shown in Figure 5.11. The median value of DC for our (albeit small) sample is <41%.

Observations suggest that DC$\sim$ 3–10% for many subclasses of variable XRB systems [100, 132, 349]. In both HMXBs and LMXBs, outbursts are thought to originate from thermal disk instabilities when the mass transfer (MT) rate is lower than the critical rate, $\dot{M}_{\rm crit}$ [423, 219, 111, 271]. Unfortunately, the details of these models are not well under-

stood, making it impossible to directly calculate the DC from first principles. Studies of dwarf novae [107] undergoing similar outbursts due to disk instability have resulted in an approximate equation for the DC,

$$\mathrm{DC} \approx \left(\dot{M}_d/\dot{M}_{crit}\right)^2, \tag{5.22}$$

where $\dot{M}_{\rm d}$ is the mass loss rate from the donor star. Our median DC implies a mass-loss rate from the companion star is <64% the critical rate.

We next expanded our analysis to include all HMXB candidates showing evidence for long-term variability. The majority (∼82%) of these sources have luminosities in the range of 10^{36-37} erg s^{-1}, as is expected for Type I outbursts from HMXBs containing a NS primary and a rapidly rotating Be companion [309, 341]. BeXBs are the most common variety of HMXB, making up $\sim$ 70% of all HMXB systems [309]. Since the X-ray production is caused by the periastron passage of a NS in a moderately eccentric orbit ($e \sim 0.3$), this variability occurs on timescales comparable to the orbital period of the system (usually tens to hundreds of days). We therefore consider it likely that the majority of the variable HMXB candidates are BeXBs undergoing a Type I outburst.

The low DC implies that only a small fraction of the X-ray-variable XRB population is expected to be represented in a single "snapshot" XLF. Ideally, the DC of the XRBs detected in the CLVS galaxies and their effect on the XLFs could be constrained by constructing XLFs from individual exposures. The effects of variability on the shape of the XLF have been investigated for the Antennae [466] and for the starburst galaxy M82 [68], but have only reached a limiting luminosity of a few $\times 10^{37}$ erg s^{-1}. Although there is some indication that shorter exposures (e.g., with a higher limiting luminosity of $\sim 10^{38}$ erg s^{-1}) yield steeper XLFs, this result is not statistically significant. Unfortunately, the individual observations for the CLVS galaxies span a wide range of exposure times (and, correspondingly, limiting luminosities), making it impossible to construct homogeneous individual XLFs that probe the luminosity regime in which we are interested ($< 10^{37}$ erg s^{-1}).

Chapter 6

INDIVIDUAL X-RAY SOURCES OF INTEREST

In this chapter, I present a summary of three interesting, individual objects that resulted from the *Chandra* Local Volume Survey. These studies were made possible by obtaining the two new *Chandra* observations of NGC 404 and NGC 300 for the CLVS.

First, I will discuss the NGC 404 central engine. Then, I will describe two off-nuclear point sources in NGC 300: SN 2010da and NGC 300 X-1.

6.1 The NGC 404 Central Engine

NGC 404 is the nearest S0 type galaxy to the Milky Way and the closest galactic nucleus to be classified as a low-ionization nuclear emission-line region [LINER, 180]. Many recent studies have successfully linked LINERs to AGN activity; for example, the detections of X-ray cores [112, 128, 156, 467, 155], radio cores [287], and mid-IR coronal lines [356] are all indicative of an accreting black hole (BH) energy source.

It is well established that the nuclei of active galaxies exhibit a broad range of luminosities, from the most energetic quasars to more modest Seyferts. AGN with nuclear X-ray luminosities below $\sim 10^{41}$ erg s^{-1} are classified as low luminosity AGNs [LLAGNs, 226], and are the most common variety of AGN observed in the local universe. About 30% of all nearby bright galaxies exhibit LLAGN activity, and many host LINERs [180].

While the observed nuclear X-ray luminosity of NGC 404 is low, only a few times 10^{37} erg s^{-1} [119], the presence of a LLAGN in NGC 404 remains ambiguous. At low nuclear luminosities, several alternative explanations for the power source have been investigated, such as circumnuclear starbursts [154, 76], shock heating by supernovae (SNe) in a high-density environment [3, 300], and photoionization by very hot O stars [398]. Moreover, a number of studies of the SEDs of weak AGNs in LINERs find that the AGN does not produce enough photons to power the emission lines [e.g., 179, 118, and references therein].

The nuclear X-ray luminosity of NGC 404 is consistent with that of a single high mass X-ray binary (HMXB) or a giant star-forming region such as 30 Doradus [432], and the soft X-ray emission is consistent with a hot gas origin, potentially blown out by a compact starburst or SNe. No radio core has been observed in NGC 404 at 15 GHz [to a limiting flux of 1.4 mJy, 287], however an unresolved 3 mJy continuum source is detected at 1.4 GHz [101], comparable in luminosity to the Crab Nebula. A compact X-ray source was previously detected in the central region of NGC 404 [246, 119], but its low luminosity and soft thermal spectrum indicate a possible starburst event origin. Mid-IR observations of the NGC 404 nuclear region show high ionization lines consistent with AGNs [356]; however, the [Ne V] lines (a more reliable indicator of AGN activity) are not detected [1].

Additionally, *HST* observations show Hα emission occurring in both a compact source $0\farcs16$ north of the nucleus and in structures reminiscent of supernova remnants [318], and [O III] emission originates from a double-lobed structure along the major axis of the galaxy [315] with a higher velocity dispersion than the central Hα emission [45]. While the UV spectrum of the nucleus reveals signatures of O stars, the dilution of the lines suggest that $\sim$60% of the UV flux may originate from a non-thermal source [262]. The observed level of UV variability [the UV emission declined by a factor of three between 1993 and 2002, 263] provides the strongest evidence for the existence of an accreting, massive black hole in the NGC 404 nucleus.

Analysis of NICMOS data [335] reveals a nuclear star cluster (NSC) within the central arcsecond of NGC 404. NSCs are present in $\sim$70% of galaxies [158, 285], independent of the host galaxy morphology [41, 57, 81], and are considered to be the foundation of circumnuclear starbursts and supernovae that could drive LINER activity [273, 403, 63]. However, if NGC 404 is dominated by star formation, the rate is exceptionally low, with only two to six O stars being sufficient to explain the observed luminosity [101]. Dynamical modeling of stellar and gas kinematics in the nucleus [363] provide mixed evidence for the presence of a SMBH. They derive a firm upper limit of $\sim 10^6\ M_\odot$, and a best fitting gas dynamical mass of $4.5^{+3.0}_{-2.5}\times10^5\ M_\odot$ (3σ errors). Although other low-mass galaxies have been identified as candidate IMBH hosts through reverberation mapping [i.e., NGC 4395; 311] and indirect mass measurements [i.e., by narrow optical line measurements; 159], NGC 404

could be, if confirmed, the lowest-mass central BH ever dynamically detected in the center of a galaxy.

With both a NSC and possible IMBH, the nuclear region of NGC 404 is a complicated environment. However, NGC 404 provides an ideal test case to address several key questions relating to LLAGN activity: is there an intrinsic lower limit to the luminosity of the AGN phenomenon, and what fraction of LINERs are powered by stellar processes versus those that host a dwarf version of more powerful Seyferts and quasars? Deep, high spatial resolution X-ray observations can potentially resolve many ambiguities surrounding the NGC 404 nucleus, such as the morphology of the X-ray emission, the shape of the X-ray spectrum, and the variability properties of the source.

6.1.1 Imaging

We searched for potential optical counterparts using optical observations in the *Hubble* Legacy Archive, but were unable to unambiguously identify any optical sources within the *HST* field of view coincident with our X-ray point sources. The nuclear region of NGC 404 has been detected with 2MASS ($J = 11.5$, $H = 10.6$, $K = 10.6$), which was used to align the X-ray and optical images (see Chapter 2). We thus conclude that our residual systematic uncertainty in absolute pointing is conservatively $0\farcs4$.

We co-added the available *Chandra* observations to investigate the morphology of the NGC 404 X-ray emission. Earlier work [119] saw evidence for extended soft X-ray emission as far out as $10''$ ($\sim$0.15 kpc) from the nucleus, with potential shell-like structures suggestive of a hot gas superbubble (see the discussion by Chu & Mac Low 1990).

We divided our *Chandra* image into three energy bands: soft (0.3-1 keV), medium (1-2 keV), and hard (2-7 keV). Each image was adaptively smoothed using `csmooth`[1]. Figure 6.1 shows a smoothed RGB rendering of the NGC 404 nucleus. The image shows a hard core, coincident with the optical and radio center of the galaxy, and soft surrounding emission. Extended X-ray emission is detected out to $\sim15''$ ($\sim$0.2 kpc). We additionally see a soft source not detected in optical images, $\sim10''$ northeast of the nucleus. For comparison, the

[1]See `http://cxc.harvard.edu/ciao/ahelp/csmooth.html`

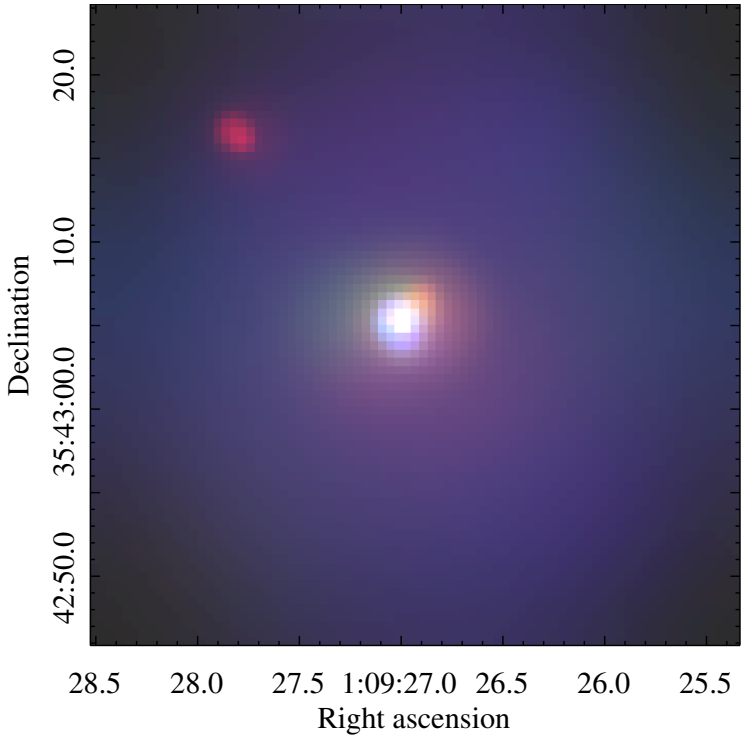

Figure 6.1: Adaptively smoothed image of our *Chandra* observation of the NGC 404 nuclear region. This rendering emphasizes the hard nuclear point source and the soft extended region in the center of the galaxy, as well as a super-soft X-ray source $\sim 10''$ to the northeast of the nucleus and low levels of diffuse emission out to $\sim 15''$. Red = 0.3-1 keV, green = 1-2 keV, and blue = 2-7 keV.

NSC extends out to $0\farcs7$ [$\sim$10 pc; 363], and the disk scale length of NGC 404 is $\sim 130''$ [$\sim$2 kpc; 11]. The adaptively smoothed 0.3-1 keV and 2-7 keV images, with contours superimposed, are shown in Figure 6.2 to emphasize the compact nature of the hard central source.

We next used the smoothed soft and hard energy images to construct a hardness ratio map of the NGC 404 nuclear region (Figure 6.3). We define a hardness ratio HR = (hard-soft)/(hard+soft); dark areas in the hardness ratio map correspond to softer X-ray emission, while light regions indicate hard emission. There is clearly a point-like region of hard emission, coincident with the location of the NSC, surrounded by an extended area of predominantly soft X-ray emission.

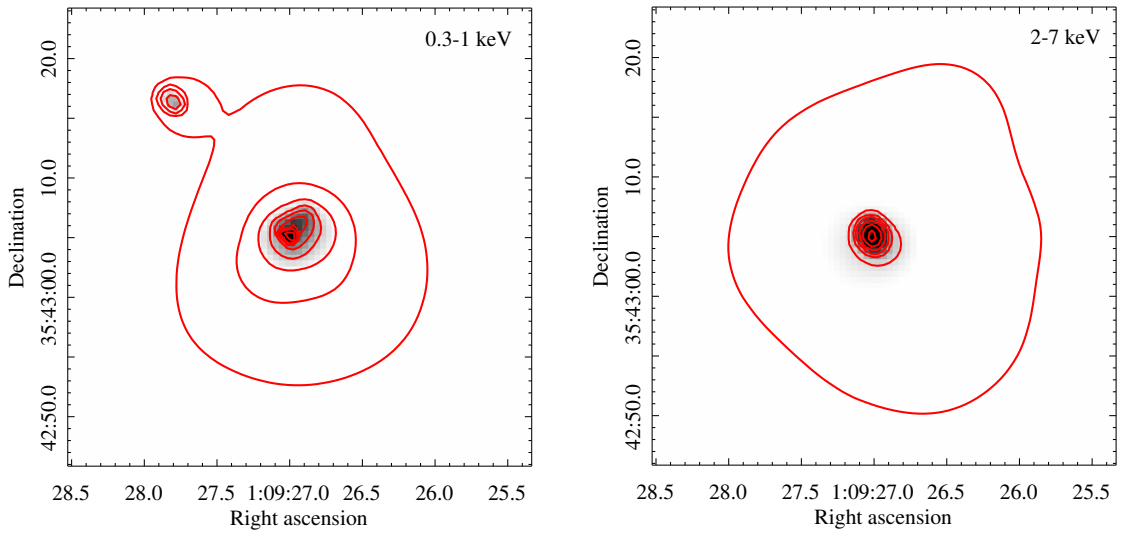

Figure 6.2: The left panel shows the smoothed 0.3-1 keV emission, and the right panel shows the smoothed 2-7 keV emission. The red contours are set to the same levels for both images. The soft, 0.3-1 keV contours show extended, asymmetric emission, while the hard 2-7 keV contours are consistent with a point source origin.

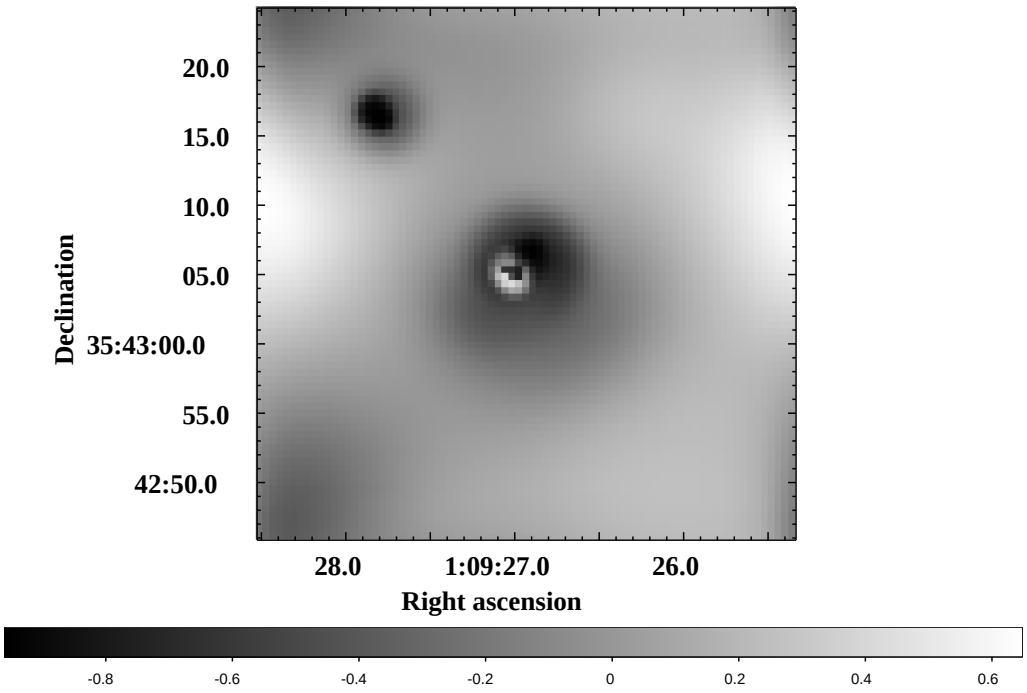

Figure 6.3: The smoothed hardness map of the NGC404 nuclear X-ray emission. Dark regions indicate soft emission, while light regions indicate hard emission. A hard point source is clearly visible within a region of extended soft emission.

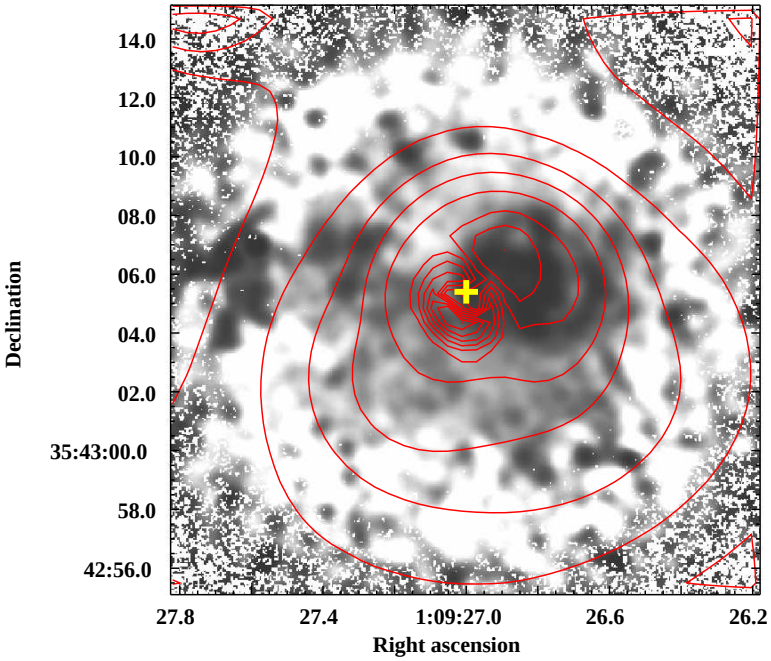

Figure 6.4: The *HST* Hα-*I* color map of the NGC 404 nucleus with HR map contours superimposed (red). Dark regions in the map are likely associated with areas of younger stars, and appear to coincide with the soft, extended X-ray emission region seen in our HR map and RGB rendering. The center of the radio emission is shown by the yellow cross, and coincides with the center of the hard nuclear point source.

In Figure 6.4, we show a Hα-*I* color map of the NGC 404 nuclear region [363], with contours from our HR map overlaid. Dark regions on the Hα-*I* color map correspond to regions with high Hα flux, likely associated with young stars. We find one such region is coincident with soft, extended X-ray emission seen in our RGB rendering.

6.1.2 Timing

We find no evidence for long-term ($\sim$10 year) variability; our best-fit 0.5-2 keV luminosity ($\sim 10^{37}$ erg s^{-1}, see next section) agrees with previous observations [119]. We generated light curves in four energy ranges (the total 0.3-10 keV band, and the soft, medium, and hard bands described above) to search for short-term variability over the course of our 97

ks observation. We generated cumulative arrival time distributions of counts for each light curve, then ran a two-sided KS test against the expected cumulative arrival time distribution for a constant count rate.

Figure 6.5 shows the cumulative arrival time distributions for our total 0.3-8 keV light curve and the hard 2-7 keV light curve. As summarized in Table 6.1, we found no evidence from our KS tests for variability at energies softer than 2 keV; however, our hard light curve yields a KS chance probability of 5.8×10^{-4}. Both AGNs and XRBs exhibit strong and rapid variability; the apparent detection of hard X-ray variability on time scales of $\sim$1 day therefore lends support to the idea that the NGC 404 nucleus hosts an accreting object. Detailed spectral fitting (described in the next section) is needed to constrain the nature of the compact accreting object further.

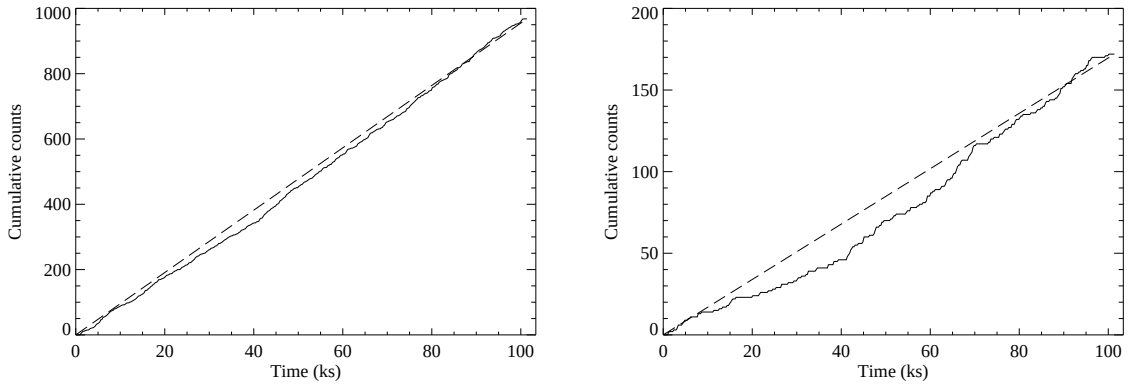

Figure 6.5: Cumulative arrival time of counts during the observation. The dashed lines represent the predicted arrival times assuming a constant count rate. The left panel is for the total 0.3-8 keV light curve, and is consistent with a constant count rate. The *right* panel is for the hard 2-7 keV light curve, and shows evidence for variability.

Table 6.1: NGC 404 Temporal Variability as a Function of Energy

Energy range (keV)	Net Counts	K-S chance probability
(1)	(2)	(3)
0.3-10	1237	0.756
0.3-1	487	0.811
1-2	261	0.365
2-7	220	5.8×10^{-4}

6.1.3 X-ray Spectral Fitting

Hard X-ray spectra of LLAGNs in LINERs are typically well represented by a two-component model: a power-law component plus soft thermal emission [399], and the Hα luminosities of LINERs are positively correlated with the X-ray luminosities in the 2-10 keV band (Ho 2001). To test whether the NGC 404 nucleus is consistent with being a LLAGN, we use our observation with archival *Chandra* ACIS-S observations to perform spectral fitting in the 0.3-8 keV energy band. The total nuclear region ($<17''$) of NGC 404 contained $\sim$1200 counts.

Our imaging analysis of the NGC 404 nuclear region indicated the presence of two distinct regions within the nucleus: a hard point source coincident with the optical and radio center of the galaxy, and a soft, extended region likely associated with an area of recent star formation. Using our HR contours and Hα-I color map, we extracted spectra using elliptical regions for each of the two distinct sources, with an elliptical area of 11 square arcseconds for the hard point source and 27 square arcseconds for the soft extended source. The hard nuclear point source contained $\sim$500 counts, and our soft, extended region contained $\sim$90 counts.

All our models fix an absorption component due to the Galactic column and an intrinsic absorption inferred from optical extinction [359]. We find no evidence in our spectral fitting for additional absorption, and we find no evidence for the presence of a reflection component in any of the 0.3-8 keV spectra. We use the mass-metallicity relation derived in [404] to estimate the NGC 404 metallicity to be 12 + log(O/H) $\sim$8.6-9 (i.e., near solar abundances).

We first attempted to model the soft, diffuse emission as a power law, a disk blackbody, and a thermal plasma. We find the thermal plasma model provides the best fit, with C/dof = 5.5/4 and a goodness of 51% for $kT = 0.67 \pm 0.11$ keV and abundances fixed at their solar values. The 0.3-10 keV luminosity of the soft X-ray emission is $(2.5 \pm 0.2) \times 10^{36}$ erg s^{-1}, with an estimated 2-10 keV luminosity of $8.8^{+0.4}_{-3.8} \times 10^{34}$ erg s^{-1}. Our data are consistent with the idea of gas being ejected from the central region in a superbubble.

We attempted to model the hard, nuclear point-source as a simple power law, but were unable to obtain an acceptable fit (C/dof = 33/25 and a goodness of 76%). Single-temperature thermal plasma models, with abundances either fixed at their solar values or allowed to vary, additionally did not result in acceptable fits (C/dof = 68/25 for $Z/Z_{\odot}$ fixed at solar, and C/dof = 42/24 with $Z/Z_{\odot}$ <0.05). Two-temperature thermal plasma models, with abundances fixed at solar values or allowed to vary, severely over-parameterized the data. We find a goodness of 0.4% with C/dof = 11/23 for our model with $Z/Z_{\odot} = 1$, and a goodness of 0.3% with C/dof = 11/22 for $Z/Z_{\odot}$ <0.06.

We next attempted to model the hard, nuclear point source as a power law contaminated by thermal emission from the soft, diffuse X-ray source. For each fit, we fixed the thermal plasma temperature to be within the 90% confidence interval of our best-fit model to the soft, diffuse source. Abundances were kept fixed at solar values. We find the hard, nuclear point source to be best described by $kT = 0.78$ keV, with a power law photon index $\Gamma = 1.88^{+0.28}_{-0.32}$ contributing to ∼72% of the total 0.3-8 keV photon flux and C/dof = 21/24. We find a 0.3-10 keV luminosity of $2.4^{+0.7}_{-0.4} \times 10^{37}$ erg s^{-1} and a 2-10 keV luminosity of $1.2^{+0.7}_{-0.4} \times 10^{37}$ erg s^{-1}. Although the fit moderately over-parameterizes the data (the `goodness` command yields 21%), this model produces our best fitting parameters and is consistent with our imaging analysis.

Finally, we applied the results of our spectral fitting to the soft, diffuse emission and the hard, nuclear point source to model the entire nuclear region of NGC 404 as a power law contaminated by thermal plasma emission. We assume the best-fit thermal plasma temperature (0.67 keV) from the soft, diffuse emission and the best-fit power law photon index ($\Gamma = 1.88$) from the hard nuclear point source. We find the power law component contributes ∼55% of the 0.3-8 keV photon flux, with C/dof = 124/126 (`goodness` = ∼30%).

Table 6.2: Best-Fit Spectral Models for the NGC 404 Central Engine

Region	Best-Fit Model	Parameter	Best-Fit Value
(1)	(2)	(3)	(4)
		kT	0.67±0.11 keV
		C/dof	5.5/4
soft, diffuse emission	thermal plasma	`goodness`	51%
		$L_{0.3-10}$	$(2.5\pm0.2)\times10^{36}$ erg s^{-1}
		L_{2-10}	$8.8^{+0.4}_{-3.8}\times10^{34}$ erg s^{-1}
		kT	0.78 keV (fixed)
		Γ	$1.88^{+0.28}_{-0.32}$
		frac. PL	72%
hard, nuclear point source	power law + thermal plasma	C/dof	21/24
		`goodness`	21%
		$L_{0.3-10}$	$2.4^{+0.7}_{-0.4}\times10^{37}$ erg s^{-1}
		L_{2-10}	$1.2^{+0.7}_{-0.4}\times10^{37}$ erg s^{-1}
		kT	0.67 keV (fixed)
		Γ	$1.85^{+0.31}_{-0.30}$
		frac. PL	55%
total nuclear region	power law + thermal plasma	C/dof	124/126
		`goodness`	30%
		$L_{0.3-10}$	$3.0^{+0.7}_{-0.5}\times10^{37}$ erg s^{-1}
		L_{2-10}	$1.3^{+0.8}_{-0.5}\times10^{37}$ erg s^{-1}

To estimate the errors on the power law photon index, we find the best-fit value of Γ when the thermal plasma temperature is set at our 90% confidence interval lower limit (0.56 keV) and upper limit (0.78 keV). We find a best-fit photon index $\Gamma = 1.85^{+0.31}_{-0.30}$ using this approach. We calculate the 0.3-10 keV luminosity to be $3.0^{+0.7}_{-0.5} \times 10^{37}$ erg s^{-1} and a 2-10 keV luminosity of $1.3^{+0.8}_{-0.5} \times 10^{37}$ erg s^{-1}.

The results of our spectral fitting are summarized in Table 6.2. Figure 6 shows the 0.3-8 keV spectra for the soft, diffuse emission, the hard nuclear point source, and the total nuclear region (with our best-fit models superimposed). The presence of a power law component in the NGC 404 nucleus, in addition to variability in the 2-7 keV emission, lends support to the idea that the NGC 404 nucleus hosts an accreting black hole, but its low luminosity (on the order of a few times 10^{37} erg s^{-1}) is comparable to that of a single XRB.

6.1.4 Discussion

By modeling the hard nuclear point source and diffuse soft emission found in the NGC 404 nucleus separately, we are able to resolve the ambiguity of the X-ray emission: a hard point source provides a power law component, and extended, diffuse gas supplies the thermal plasma emission.

The Eddington luminosity is defined as $L_{\rm Edd} = 1.3{\times}10^{38}$ $(M_{\rm BH}/M_{\odot})$ erg s^{-1}, and the Eddington ratio ξ is commonly defined as $\xi = \log_{10}(L/L_{\rm Edd})$, where the bolometric luminosity L is typically estimated as $L/L_{0.2-25{\rm keV}} = 16$ for AGNs (Ho 2008), whereas the bolometric correction factor for XRBs is roughly 2-5 times lower than for AGN [457]. The relationship between the X-ray power law photon index Γ and Eddington ratio has been investigated for XRBs [457] and LLAGNs [78]. An anticorrelation is found for LLAGNs, whereas a positive correlation is observed for XRBs and luminous AGNs [431, 370].

We estimate ξ for NGC 404 assuming the black hole is an XRB, with $M_{\rm BH}$ $\sim$10 $M_{\odot}$, and an IMBH AGN, with $M_{\rm BH} \sim 10^5$ $M_{\odot}$. In Figure 6.6, we use our best-fit photon index for the hard nuclear point source and estimates of ξ to compare our NGC 404 data to the observed relationships for both XRBs and LLAGNs from [457] and C+09, respectively. The errors in ξ indicate a factor of three change in BH mass (i.e., an AGN ranging from $3.3{\times}10^4$

$M_\odot$ to 3×10^5 $M_\odot$ and an XRB ranging from 3.3 $M_\odot$ to 30 $M_\odot$). We find that while our data fall well below the relationship for a high/soft state XRB [457], our data are consistent with the anticorrelation found for the LLAGN sample [78]. However, due to the large scatter observed in the LLAGN sample and the errors in our observed photon index, we cannot decisively rule out the possibility that the NGC 404 central engine is powered by an XRB in the low/hard state. Our data moderately favor the IMBH AGN interpretation; however, the UV spectrum and nuclear star cluster still allow the possibility of an XRB component.

In Table 6.3, we summarize the observed multiwavelength properties of NGC 404, found in both the literature and presented in this work, and indicate if the origin is likely to be an AGN or XRB. Additionally, the upper limits on the radio core [287] and the detection of an unresolved radio continuum [101] can be combined with our deep X-ray observations to place upper limits on the central BH mass of NGC 404 – a correlation has been established relating the radio luminosity L_R and X-ray luminosity L_X [79, 142, 141] over many orders of magnitude in BH mass and luminosity, forming the "fundamental plane of black hole activity." We use the best-fit BH "fundamental plane" [23] and the upper limit on the radio core flux of NGC 404 to estimate $M_{\rm BH} < 2\times10^6$ $M_\odot$. If the unresolved 3 mJy continuum source is indeed powered by an accreting BH, it would imply $M_{\rm BH} \sim 3\times10^5$ $M_\odot$.

Additionally, we use the following relation between radio luminosity and star formation rate [77],

$$\left(\frac{L_{\rm N}}{\rm WHz^{-1}}\right) \sim 5.3\times10^{21}\left(\frac{\nu}{\rm GHz}\right)^{-\alpha}\left[\frac{SFR(M\geq5M_\odot)}{M_\odot{\rm yr}^{-1}}\right], \tag{6.1}$$

where $\alpha \sim 0.8$ is the nonthermal spectral index and SFR is the star formation rate (in $M_\odot$ yr^{-1}), to test whether the observed radio luminosity is consistent with the observed low star formation rate. Using the SFR upper limit [$\sim 10^{-3}$ $M_\odot$ yr^{-1}, 363], we predict an upper limit on the radio luminosity at 1.4 GHz to be $\sim4\times10^{25}$ erg s^{-1}. This upper limit is roughly eight orders of magnitude below the observed 1.4 GHz upper limit for the NGC 404 nucleus. We therefore conclude the observed radio luminosity cannot be explained by star formation alone, and is evidence for the presence of an AGN in the NGC 404 nucleus.

The X-ray luminosity of the AGN in NGC 404 bears directly on the question of whether

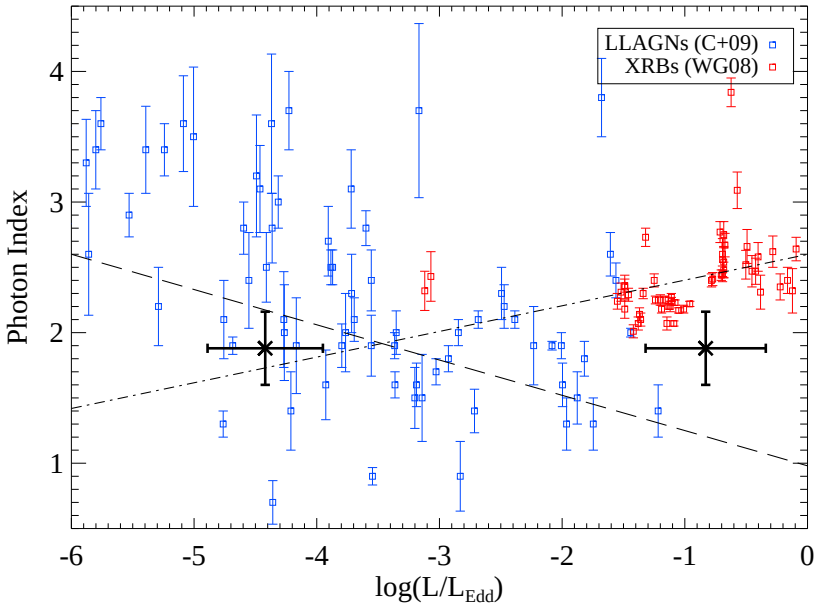

Figure 6.6: The observed relationship between power law photon index and Eddington ratio for LLAGNs (C+09, blue points) and XRBs (WG08, red points). The dashed line shows the best-fitting anticorrelation to the LLAGN sample, and the dot-dashed line shows the best-fitting correlation for the XRB sample. The estimated Eddington ratio for NGC 404, assuming a 10 $M_{\odot}$ and 10^5 $M_{\odot}$ central black hole, along with the best-fit photon index from our spectral fitting, is shown by the black crosses. Assuming a low Eddington ratio places NGC 404 well within the typical values for LLAGNs, while assuming a high Eddington ratio places NGC 404 in a vacant part of the diagram. Our data are consistent with an IMBH central engine powering the X-ray emission from the NGC 404 nucleus.

Table 6.3: AGN vs. XRB Properties Exhibited by the NGC 404 Central Engine

Property or Observation	AGN	XRB
(1)	(2)	(3)
Radio fluxes and upper limits	X	
Soft X-ray emission[a]		X
Supernova remnant-like optical Hα emission[a]		X
Mid-IR high ionization lines; hot dust	X	
UV spectrum	X	X
UV variability	X	
Dynamical BH estimates	X	
Nuclear star cluster		X
X-ray 2-10 keV variability	X	X
X-ray power law emission ($\Gamma \sim$1.9)	X	

[a]Observations are *not* associated with the hard nuclear point source.

accretion power can account for the observed luminosities of the optical emission lines, whose relative intensities are the defining characteristic of LINERs. In a recent study of the energy budgets of three dozen LINERs, including NGC 404, it was found that in the majority of cases the weak AGN does not provide enough ionizing photons to account for the observed luminosities of the hydrogen recombination lines [118]. This conclusion is in general agreement with previous studies. In the particular case of NGC 404 the number of ionizing photons was found to be deficient by a factor of $\approx$60. The X-ray luminosity of NGC 404 measured here is only $\approx$25% higher than that measured previously [119], after accounting for the different distance used in that paper, and is consistent (within errors) with the result obtained here. Therefore, the situation regarding the ionizing photon output of the AGN remains the same. However, the estimated ionizing luminosity of hot stars in the nucleus of NGC 404 [based on measurements of the UV spectrum with *HST*, 262] is adequate to power the emission lines. This conclusion was re-iterated in [363]; a relatively small number of O stars in the nuclear star cluster could provide enough ionizing luminosity. Therefore, the LINER in NGC 404 appears to be powered by stellar processes.

Summary

The new 99 ks exposure of NGC 404 obtained as part of the *Chandra* Local Volume Survey has allowed us to critically test several forms for the 0.3-10 keV spectrum, and the excellent spatial resolution has enabled us to investigate the X-ray morphology of the NGC 404 nuclear region. The presence of a power law component and a moderate level of variability in the hard emission is indicative of X-ray emission powered by accretion onto a BH. The estimated 0.3-10 keV luminosity ($\sim$2-3$\times10^{37}$ erg s^{-1}) is both comparable to that of a single Galactic XRB and is also consistent with a IMBH accreting at extremely low levels, on the order of a few times 10^{-9} $M_{\odot}$ yr^{-1}. We find the NGC 404 X-ray spectral shape and luminosity to be consistent with observed LLAGNs, and inconsistent with observed XRBs. We therefore favor the scenario in which the NGC 404 nucleus is powered by an IMBH, with a mass on the order of 10^5 $M_{\odot}$ as dynamically estimated in [363]. Such a weak AGN does not produce a sufficient quantity of ionizing photons necessary to power a LINER – we therefore conclude that the LINER in NGC 404 is powered by stellar processes.

Very low accretion rates are common in nearby galaxies with BH masses less than a few times 10^6 $M_{\odot}$ [143, 10, 181]. Additional, multiwavelength observations of the NGC 404 nucleus are required to robustly determine the mass of the central BH – for example, resolved stellar populations within the nucleus would enable a robust dynamical mass determination, and a radio detection of the compact source would verify the location of NGC 404 on the fundamental plane of BH activity.

6.2 SN 2010da: The "Supernova Impostor" in NGC 300

Supernova (SN) 2010da was first detected as an optical transient on 24 May 2010 in NGC 300 [281]. Within hours of the initial optical detection, SN 2010da was observed by the *Swift* X-ray Telescope [XRT, 199], and an X-ray point source with a 0.2-10 keV luminosity of $(4.5^{+0.9}_{-2.1}) \times 10^{38}$ erg s^{-1} was found to be coincident with the optical outburst. Such optical transients are commonly assigned an official SN designation only to be later recognized as "impostors," and frequently result from the outbursts of massive stars. However, the brightest stellar X-ray emitters have outburst luminosities on the order of 10^{35} erg s^{-1}

[165], three orders of magnitude lower than what was observed by *Swift*.

Such high X-ray luminosities are observed in high mass X-ray binaries (HMXBs), consisting of a compact object primary with a secondary massive star, typically either a Be (non-supergiant, fast rotating B-type stars with spectral lines in emission) or an OB supergiant. Known Be/X-ray binaries (BeXBs) contain a neutron star in a wide, moderately eccentric orbit and undergo X-ray outbursts during periastron passage of the compact object. The majority of known HMXBs are BeXBs [$\sim$60%; see 248, and references therein], although the true fraction of BeXBs may be higher owing to the transient nature of the sources. Somewhat less numerous are supergiant X-ray binaries (SGXBs), consisting of a compact object orbiting within the wind of a supergiant OB star. These systems show persistent X-ray emission (with X-ray luminosities of 10^{35-36} erg s^{-1}) either from direct accretion of the stellar wind or from Roche-lobe overflow via an accretion disk. Only a few dozen confirmed or suspected SGXBs are known in the Milky Way [248, 429], although this number is increasing with higher energy surveys [64]. The relatively low number of SGXB systems is naturally explained by the short lifetimes of the supergiant companion stars.

During the new CLVS observation of NGC 300, SN 2010da was detected at $\sim 7\sigma$ significance RA (J2000) = $00^{\rm h}55^{\rm m}04.^{\rm s}85$ and Dec (J2000) = -37°41′ 43.″5, in excellent agreement (within 0.″2) with the position of the optical outburst [281]. The source is 3.8′ off-axis from the *Chandra* aim point. We detect a net 71 source counts in the 0.5-8 keV band. The background was estimated using an annular region, centered on the source position, extending from a radius of 25″ to 30″ away from the source. The 0.5-8 keV background count rate was found to be $\sim 2 \times 10^{-6}$ ct s^{-1} arcsec^{-2}.

6.2.1 Imaging and Hardness Ratios

Our *Chandra* observation was divided into three images consisting of different energy bands: "soft" (0.5-1 keV), "medium" (1-2 keV), and "hard" (2-8 keV). Each image was adaptively smoothed. Figure 6.7 shows a raw RGB image, a smoothed RGB rendering, and the radial counts distributions for both our detection and the *Chandra* PSF. The `AE` extraction region is shown in both images, and the surface brightness profile shows emission in excess of

the PSF out to a radius $\sim 8''$ ($\sim$70 pc) at $\sim 4\sigma$ significance. The largest possible sphere of influence of the outburst would have a radius of only $\sim$0.1 pc, indicating the diffuse emission, if associated with the SN 2010da system, is the result of earlier activity in the system's history.

The size and shell-shaped structure of the extended emission is reminiscent of a supernova remnant (SNR). We therefore calculate the hardness ratio of the diffuse emission, using the definition from the catalog of SNRs in M 33 [322, 316]: $HR = (M - S)/(S + M + H)$, where S is the soft 0.35-1.1 keV band, M is the medium 1.1-2.6 keV band, and H is the hard 2.6-8.0 keV band. The diffuse emission has a $HR = -0.4$; using the best-fit temperature of SNRs in M 33 ($kT \sim 0.6$ keV), we estimate a 0.35-2 keV luminosity of $\sim 6 \times 10^{35}$ erg s^{-1}. All these quantities are consistent with being a SNR; however, with only $\sim$10 net counts, we are unable to perform detailed spectral fitting to confirm this interpretation. We examined public Hα imaging of NGC 300 and find a low significance Hα knot coincident with the northern tip of the shell. We find no obvious, bright Hα emission coincident with the soft X-ray shell, making the source of the soft X-ray emission difficult to reliably classify.

We estimate the probability of a SNR falling within $\sim 8''$ of the X-ray and optical outburst location. Due to its similarities in stellar mass, morphology, and star formation histories to NGC 300, we use the M 33 catalog of 137 SNRs (Long et al. 2010) in our estimate. NGC 300 covers an area of $\sim$270 arcmin^2 (from the optical D_{25} isophote), implying a density of ~ 0.5 SNRs per arcmin^2 or 1.4×10^{-4} SNRs per arcsec^2. Within a search area of 200 arcsec^2 (the size of the SN 2010da region considered in this work), this produces a probability of $\sim$3%. This probability is likely a lower limit, since HMXBs and SNRs are preferentially found in star forming regions.

The detection of diffuse emission surrounding the central X-ray point source has potentially interesting implications. If the emission is indeed a SNR, it may be the remains of the SN that produced the compact companion and would provide useful constraints on HMXB evolution models. Alternatively, ejecta from an earlier outburst event may interact with the surrounding ISM, producing shock-heated gas that radiates as soft X-rays. Assuming an outflow velocity of $\sim$1000 km s^{-1}, we can roughly estimate the time since the last outburst to be $\sim$20,000 years.

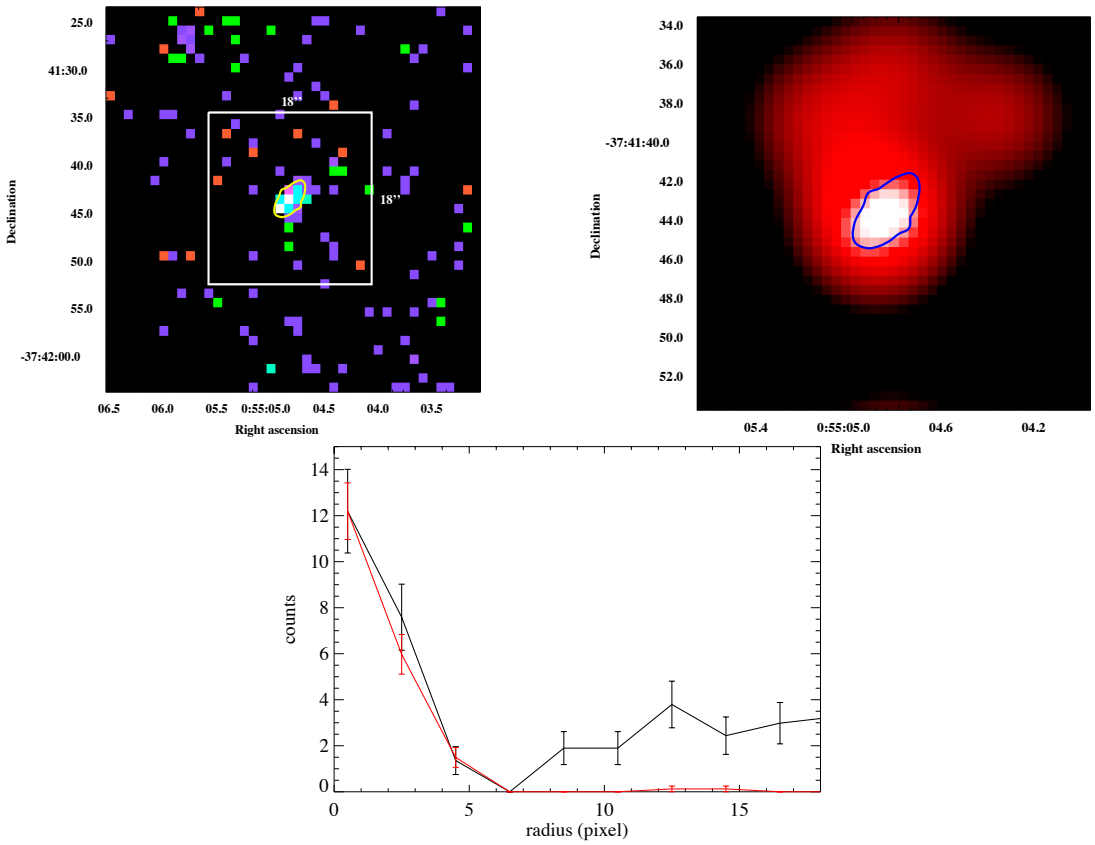

Figure 6.7: The top left panel shows a raw RGB image of our observation; the extraction region determined by `AE` is shown in yellow. The while 18″ by 18″ box shows the same region as the adaptively smoothed RGB image in the top right panel. The same extraction region is shown in blue in our smoothed imaged. In both cases, red = 0.5-1 keV, green = 1-2 keV, and blue = 2-8 keV. The bottom panel shows a radial profile of the counts in our SN 2010da detection (black) and the *Chandra* PSF (red). A clear excess is seen past ~ 6 pixels, corresponding to the diffuse emission in the top left and right panels.

6.2.2 Spectral Fitting

Soft, thermal X-ray emission (such as from a stellar origin) does not provide an acceptable fit to our 0.5-6 keV spectrum. Allowing the temperature, abundances, or both to vary does not improve the goodness of the fit, and all two-temperature thermal plasma models over-parameterize the data. Similarly, all models that included an absorption component beyond the Galactic column over-parameterize the data.

The best-fit *Swift* spectral model is a power law with Γ = -0.03$^{+0.11}_{-0.08}$, an unabsorbed 0.3-10 keV flux of $8.6^{+1.6}_{-4.0} \times 10^{-13}$ erg s^{-1} cm^{-2}, and a corresponding unabsorbed 0.3-10 keV luminosity of $4.5^{+0.9}_{-2.1} \times 10^{38}$ erg s^{-1}. This luminosity implies a super-Eddington outburst, assuming a 1.4 $M_{\odot}$ neutron star. To directly compare our observation with the *Swift* spectrum, we model the 0.5-6 keV spectrum with a power law. We find a statistically acceptable fit for $\Gamma = 0.15 \pm 0.42$, with $C/dof = 276/511$ (the `goodness` command yields 58%). We next use a blackbody model, which yields a temperature of $kT = 1.75^{+0.94}_{-0.44}$ keV with $C/dof = 242/373$ and a goodness of 67%. Both cases yield a 0.3-10 keV luminosity of 1.6-2.4$\times 10^{37}$ erg s^{-1} details of our spectral fitting are summarized in Table 6.4. Our best-fit blackbody spectral model and residuals are shown in Figure 6.8. In both cases, adding an additional absorbing column does not improve the quality of the fit; we therefore find no evidence for absorption beyond the Galactic column.

Continuum (2-100 keV) spectral fitting of several Galactic XRBs containing NS primaries was performed in [72]; in particular, two HMXB cases (Vela X-1 and GX 301-2) show continuum Γ consistent with zero. Alternatively, some Galactic SGXBs have shown the spectra to be consistent with a black body, with typical temperatures ranging from 1.6-1.9 keV [377].

6.2.3 Time Evolution

We attempt to further constrain the nature of the SN 2010da X-ray source using its time evolution. Figure 6.9 shows the cumulative photon arrival time distribution. While short-term variability is a common feature of HMXB systems, a two-sided K-S test against a constant count rate source yields a probability of 0.85. While we do not detect rapid X-ray

Table 6.4: SN 2010da Spectral Fits

Model	Parameter	Best-Fit Value	Units
(1)	(2)	(3)	(4)
Swift power law, during outburst	Γ	$-0.03^{+0.11}_{-0.08}$	
	unabs. flux	$8.6^{+1.6}_{-4.0}$	10^{-13} erg s^{-1} cm^{-2}
	unab. luminosity	$4.5^{+0.9}_{-2.1}$	10^{38} erg s^{-1}
	C/dof	255/237	
Chandra power law, post-outburst	$N_{\rm H}$	4.09×10^{20} (fixed)	cm^{-2}
	Γ	0.15±0.15	
	unabs. flux	4.5±2.5	10^{-14} erg s^{-1} cm^{-2}
	unabs. luminosity	2.4±1.3	10^{37} erg s^{-1}
	C/dof	276/511	
	`goodness`	58.14%	
Chandra blackbody, post-outburst	$N_{\rm H}$	4.09×10^{20} (fixed)	cm^{-2}
	kT	$1.75^{+0.94}_{-0.44}$	keV
	unabs. flux	$3.1^{+0.4}_{-1.1}$	10^{-14} erg s^{-1} cm^{-2}
	unabs. luminosity	$1.6^{+0.2}_{-0.6}$	10^{37} erg s^{-1}
	C/dof	242/373	
	`goodness`	67.29%	

All reported fluxes and luminosities are unabsorbed, and correspond to a 0.3-10 keV energy range.

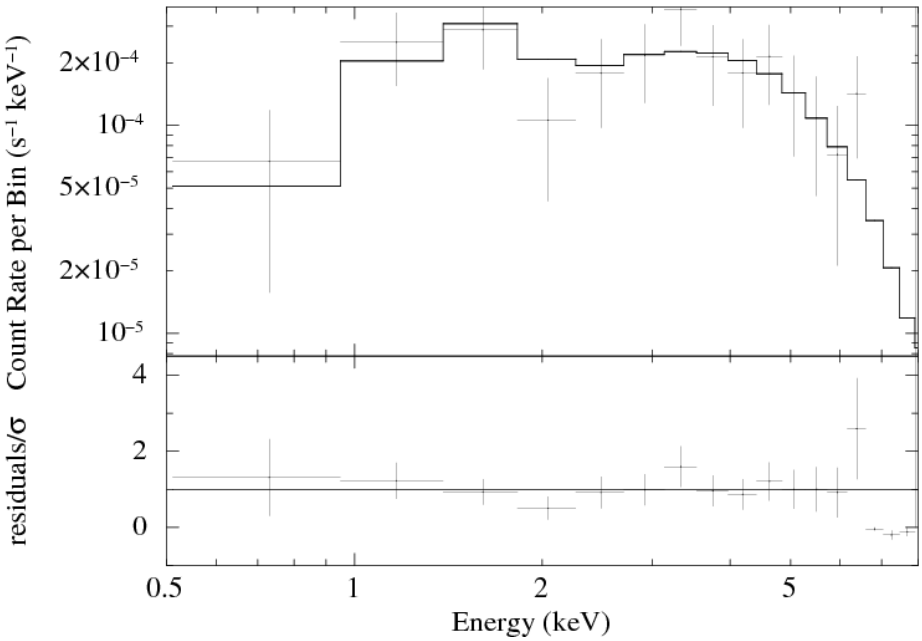

Figure 6.8: The *Chandra* 0.5-6 keV spectrum of SN 2010da. Our best-fit spectral model, a blackbody emitter ($kT = 1.75^{+0.94}_{-0.44}$ keV) with no evidence for absorption beyond the Galactic column, is superimposed.

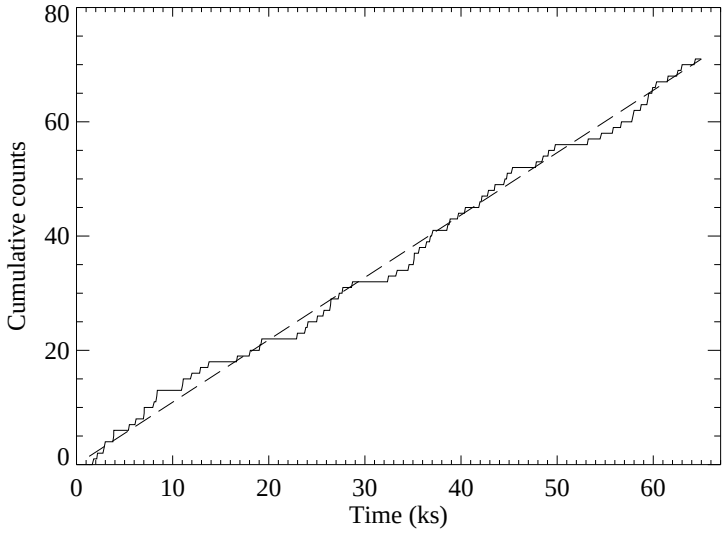

Figure 6.9: The cumulative arrival time distribution of counts during our observation (solid line). The dashed line shows the expected distribution for a constant count rate. A two-sided K-S test against a constant count rate source yields a probability of 0.85, indicating our observation is consistent with a constant count rate.

variability in our observation, we note that the low number of source counts makes our observation relatively insensitive to strong, rapid variability.

The long-term X-ray emission from SN 2010da can be constrained using four archival *XMM-Newton* observations (taken on 2000 Dec. 26, 2001 Jan. 1, 2005 May 22, and 2005 Nov. 25) which contain the position of the SN 2010da progenitor within the field of view. During all four observations, the 3σ upper limit of the unabsorbed 0.3-10 keV luminosity is estimated to be $\sim 3 - 9 \times 10^{36}$ erg s^{-1}, two orders of magnitude lower than the observed outburst X-ray luminosity and $\sim$3 times lower than its current luminosity. These estimates are relatively insensitive to our choice of spectral model, and including heavy absorption as observed in the progenitor system changes our luminosity estimates by less than 20%. Figure 6.10 shows luminosity estimates from all available X-ray data for SN 2010da and the

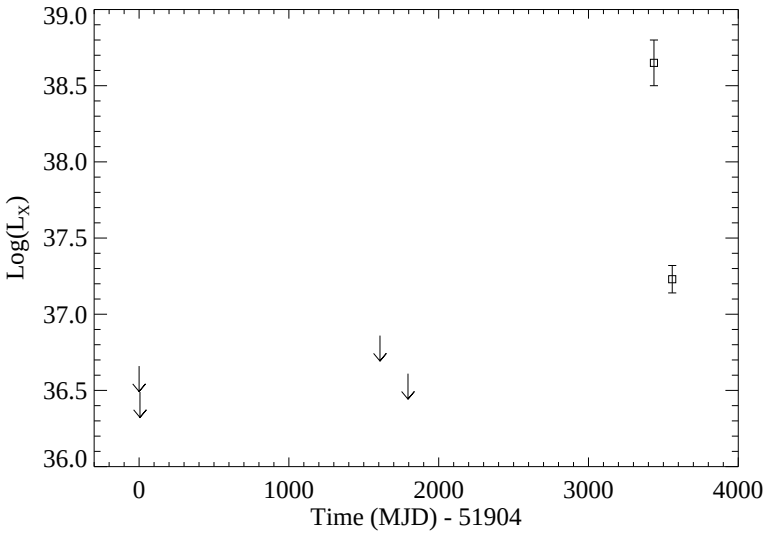

Figure 6.10: The long-term X-ray luminosity of SN 2010da, relative to the date of the outburst. Downward arrows indicate 3σ upper limits derived from archival *XMM-Newton* images.

progenitor system.

We additionally compare the decay rate of the SN 2010da X-ray emission to decay of optical brightness. Multicolor optical photometry of SN 2010da in B, V , R, and I filters was obtained during the outburst [42] and nine days later [324] on the SMARTS 1.3m telescope at Cerro Tololo using the ANDICAM camera. We calculate the e-folding time for each optical filter and the X-ray emission. We use the X-ray luminosity derived from the unabsorbed $\Gamma \sim 0$ spectral model for both the *Swift* and *Chandra* observations to ensure the luminosity change is not due to a change in assumed spectral model between observations. We find e-folding times for X-ray, B, V, R, and I bands to be 41, 13, 18, 20, and 11 days, respectively. Compared to the decay rates of the optical magnitudes, the X-ray emission decay rate is $\sim 2-4$ times slower.

6.2.4 SN 2010da: A High Mass X-ray Binary?

The 0.5-6 keV spectrum of SN 2010da is well described by either a $\Gamma \sim 0$ power law or a blackbody with $kT \sim 1.8$ keV, both of which are used in the literature to describe known HMXB systems. The X-ray hardness and peak luminosity are consistent with the system possessing a neutron star primary. The X-ray luminosity of the progenitor ($< 8 \times 10^{36}$ erg s^{-1}) and sharp increase in X-ray emission coincident with an increased mass-loss rate of the secondary further supports the HMXB scenario. Both the *Chandra* and *Swift* X-ray detections suggest that the X-ray outburst may have been fueled by a mass loss event from the secondary, or that the optical outburst originated from an accretion event onto the primary.

We estimate the mass of the progenitor star using a luminosity of 1.3×10^4 $L_\odot$ as estimated from the SED of the progenitor system [324] and the mass-luminosity relation of main sequence stars [above ~ 1 $M_\odot$, 103], we estimate the mass of the SN 2010da progenitor to be $\sim$11 $M_\odot$. Although many ATels have referred to this source as an "LBV outburst," our low mass estimate combined with the low luminosity (assuming all optical luminosity originated from the secondary) suggest a different class of star; for example, a Be-type star.

Be type stars show line emission and excess infrared emission attributed to a circumstellar envelope [452], both which were observed in SN 2010da [214, 69]. Mass loss from the Be star changes the density of the surrounding disk, and drives the disk to become optically thick at optical/IR wavelengths [292, 277]; BeXBs are therefore observed to brighten in the IR prior to outburst events, as was observed in the SN 2010da progenitor [235]. Additionally, the optical outburst spectrum of SN 2010da showed a He II λ4686 emission feature, often used as a signature of accretion around neutron stars [i.e., where streams impact the accretion disk or from disk winds, 389, 414, 310].

X-ray variability in BeXBs can occur on timescales of seconds to years. Two types of outbursting activity are observed in these systems: the lower-luminosity, (quasi)periodic Type I outbursts, and the more luminous, longer-lived Type II outbursts, which show a 3-4 order of magnitude increase in X-ray luminosity (reaching the Eddington limit of a neutron star) and remaining luminous for months or longer [340], as in SN 2010da. While BeXB

outbursts are characterized by their X-ray properties, optical spectroscopic surveys of the Be companions have been undertaken in both the Milky Way [341] and the SMC [73, 4]. The optical magnitudes of the Be companions is roughly four orders of magnitude lower than the observed SN 2010da outburst. Such an extreme optical outburst that coincides with an X-ray outburst has not been observed in nearby BeXBs, and may be indicative of a giant stellar eruption of the secondary, a flaring event originating in the accretion disk around the neutron star, or some other related phenomenon. Additional optical and infrared photometric and spectroscopic monitoring of this system is required to confirm the theory of a Be companion star, and to better constrain the origin of the unusually luminous optical outburst that SN 2010da exhibited.

Deep follow-up X-ray observations, sensitive to a limiting luminosity of a few 10^{35} erg s^{-1}, would be capable of verifying the quiescent X-ray luminosity of this system and would monitor the SN 2010da system for future outburst events that may strengthen the case for a BeXB origin. Additional sensitive observations may provide further evidence for a supernova remnant origin of the diffuse emission. Time-resolved optical spectroscopy of the massive star may confirm the presence of a compact object primary and provide constraints on the masses and orbital parameters of this system.

6.3 NGC 300 X-1: a Wolf Rayet + Black Hole Binary

If a merger between the compact object and stellar companion is avoided, the OB star can potentially evolve through a Wolf-Rayet (WR) phase [410]. Such systems are expected to be exceedingly rare: population synthesis [250] suggests that only ∼1 WR+BH binary and ∼1 WR+NS binary may exist as bright X-ray sources in a Milky Way-like galaxy. To date, only two extragalactic X-ray bright WR+BH binaries are known: IC 10 X-1 in the dwarf irregular galaxy IC 10 [71, 16] and NGC 300 X-1 [59, 83, 82], while Cyg X-3 in the Milky Way [250] is also a WR+BH candidate. While other systems with BH primaries and massive, main-sequence companions (i.e., M 33 X-7, LMC X-1, LMC X-3, and Cyg X-1 in the Milky Way, [268]) may also be the direct progenitors of BH-BH or BH-NS binaries, WR stars represent an advanced stage of stellar evolution, making WR+BH binaries close to their end state.

X-1 has been observed four times with *XMM-Newton*, and the X-ray spectra were found to be consistent with two distinct spectral states: a high state and a steep power law (SPL) state [14]. Radial velocity measurements of the X-1 secondary [82] have established a physical link between the compact object and massive star. The orbital period was found to be ∼32 hours, consistent with the X-ray period observed in *Swift* measurements [58]. The orbital inclination angle was found to be $i = 60^\circ - 75^\circ$, although this value was obtained through geometrical arguments and not formal dynamical modeling of the system. The BH mass has been constrained to be ∼13-30 $M_\odot$ using optical and X-ray observations [58, 82]. It has been proposed that heavy stellar-mass BHs may correspond to regions of low metallicity, where the progenitor star experienced a lower mass-loss rate. The metallicity of NGC 300 has been found to exhibit metallicity gradients [413]; at the location of X-1, the metallicity is log(O/H)+12≈8.44, corresponding to $Z = 0.6Z_\odot$ [82]. Thus, X-1 is comparable in mass and metallicity to M 33 X-7 [with a best-fit mass of 15.65±1.45 $M_\odot$; 415].

The short orbital period of X-1 (also comparable to the ∼35 hour period observed for IC 10 X-1) indicates that the BH progenitor was larger than the present separation between the BH and the WR companion, and thus underwent extreme mass loss via a Roche-lobe overflow [280, 22]. Studies of systems with high BH masses and close orbital separations are of paramount importance for binary evolution models, as they provide clues to how extreme mass-loss proceeds and how massive binaries survive the initial SN during BH formation. Such systems are the direct progenitors of BH-BH binaries, predicted to be the first detectable sources for gravitational radiation instruments such as LIGO and VIRGO [18, 19].

X-1 was detected at R.A. (J2000) = 00:55:10.00, decl. (J2000) = -37:42:12.2 (Figure 6.11), in excellent agreement with the position reported in SIMBAD, 4′.8 off-axis from the *Chandra* aim point for the observation. We detect a total of 1957 net counts, corresponding to a source significance of ∼43σ. The 0.5-8 keV background count rate was low, $\sim 7 \times 10^{-7}$ counts s^{-1} arcsec^{-2}, throughout the observation. We estimate the level of pile-up suffered during the observation to be <5% using PIMMs8 v4.2[2]. Less than 2% of

[2]See `http://cxc.harvard.edu/toolkit/pimms.jsp`

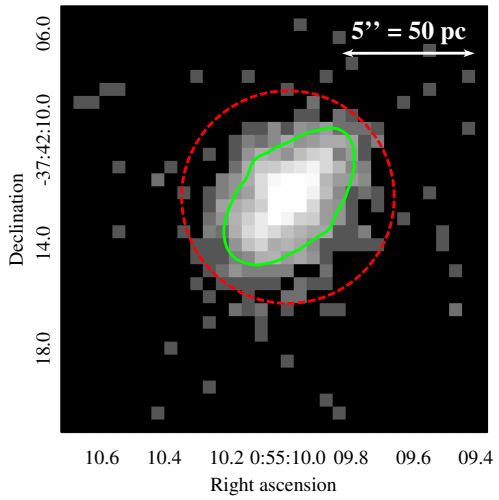

Figure 6.11: The *Chandra* 0.35-8 keV image of NGC 300 X-1. The green polygon is the `AE` source extraction region, and the dashed red circle shows the `AE` determined background region. The elongation of the green extraction region reflects the shape of the *Chandra* off-axis PSF at the source position.

the total source counts have energies above 5.0 keV, and we find no evidence for diffuse or extended emission in our observation. Figure 6.11 shows our *Chandra* 0.35-8 keV detection of X-1, with the source extraction region (green) and background region (red) found by `AE` superimposed.

6.3.1 Variability

Timing studies have been used to isolate the fast X-ray variability of X-ray binaries (XRBs) containing NSs and BHs. Many systems containing a NS exhibit rapid periodic X-ray pulsations indicative of magnetically channeled accretion, whereas BH primaries (lacking a material surface) cannot sustain a magnetic field anchored to them. Thus, while many systems containing a BH are observed to be rapidly variable, they do not exhibit periodic

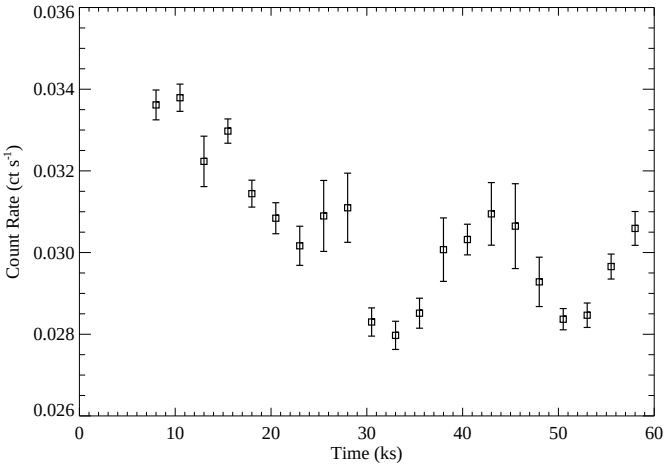

Figure 6.12: The *Chandra* 0.5-8 keV light curve of NGC 300 X-1, binned to 3 ks with 1σ error bars.

X-ray pulsations. We first investigate the short-term X-ray variability of X-1. The 0.35-8 keV light curve (shown binned to ∼3 ks in Figure 6.12) was extracted as part of the `AE` timing analysis stage, and a two-sided K-S test was performed to determine the probability of the X-ray source showing significant variability during the observations. We find the K-S probability of a constant count rate to be 0.08, and fitting a constant count rate (equal to the mean count rate of the observation, 0.031 ct s^{-1}) to the observed light curve yields a reduced χ^2 of 4.53. The X-1 light curve exhibits rapid low amplitude ($\leq$30%) variability, with a clear secular decline during the first ∼30 ks of the observation.

We searched for evidence of short-term, periodic X-ray pulsations using a periodogram analysis [188]. We calculated the 68%, 90%, and 99% confidence levels using Monte Carlo simulations assuming a null hypothesis of a constant count rate dominated by white noise; the periodogram and confidence levels are shown in Figure 6.13. While we find no obvious peaks in the X-1 periodogram above 99%, there is one peak at 0.785 hours (corresponding to ∼2.8 ks or 47 minutes) that exceeds the 90% confidence level. To determine if this peak is a genuine signal, we fold the 0.35-8 keV light curve on a 0.785 hour period for multiple

time binning schemes. The resulting folded light curves do not show evidence for variability with phase over this period. We additionally evaluate the likelihood that some peaks will appear significant by chance: the expectation value of a peak at a given significance can be evaluated by $\langle N \rangle = N_P \times P$, where N_P is the number of points in the periodogram and P is the chance probability. For the ∼2000 points in our periodogram, we would expect to recover at least one peak with a chance probability of 0.05% (i.e., at the 99.95% confidence level). We therefore find no evidence that the peak at 0.785 hours corresponds to a real periodic signal.

Studies of XRBs containing both Bondi-Hoyle accreting NSs and disk-accreting BHs have found their power density spectra (PDS) to be remarkably similar [420], consistent with a power law with a spectra index $\gamma \sim 1$; i.e., power $\propto \nu^{-\gamma}$, where ν is the frequency [288, 24, 421] . We use the IDL routine `psd.pro` (a routine which computes the power density spectrum using the appropriate Fourier transforms and offers options for plotting) to construct a PDS of X-1, shown in Figure 6.14. We measure the spectral index to be $\gamma = 1.02 \pm 0.15$ with χ^2/dof =14/25, consistent with previous PDS measurements derived from *XMM-Newton* observations of X-1 (Barnard et al. 2008) and typical of BHs in either the thermal or SPL state [420, 25]. Although the *Chandra* ACIS read-out time does not allow us to measure the X-1 PDS out to 10 Hz, we can use the observed 0.1-1 Hz power and the slope γ to estimate the integrated power continuum r. We find $r \sim 0.1$, significantly higher than expected for a high/soft state XRB. To measure the PDS above 1 Hz, observations with higher time resolution (i.e., $\sim 1\mu$s time resolution with *RXTE*) would be required. However, the relative softness of the spectrum (*RXTE* operates over an energy range of 2–200 keV) and distance to NGC 300 make it implausible for such observations to currently be performed.

Quasi-periodic oscillations (QPOs) are typically observed in low/hard and intermediate state XRBs [usually at 4-10 Hz 84, 268]. When coupled with the X-ray spectroscopic photon index [426] QPOs have been used by some authors to constrain the mass of the accreting BH [373, 369], although this approach depends on knowing the origin and nature of the QPO – for example, resonances in the disk due to relativistic effects or "trapping" of oscillations in the inner accretion disk [343, 9]. We find no evidence for QPOs for the duration of our

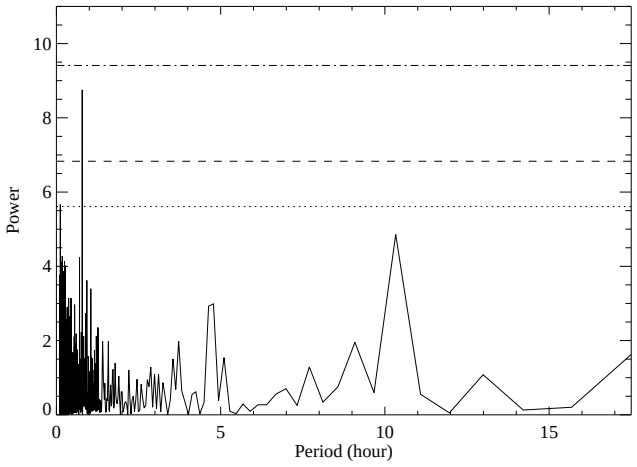

Figure 6.13: Searching for periodicities in the *Chandra* light curve of NGC 300 X-1 using a periodogram analysis. The dotted, dashed, and dot-dashed lines represent the 68%, 90%, and 99% confidence levels, respectively.

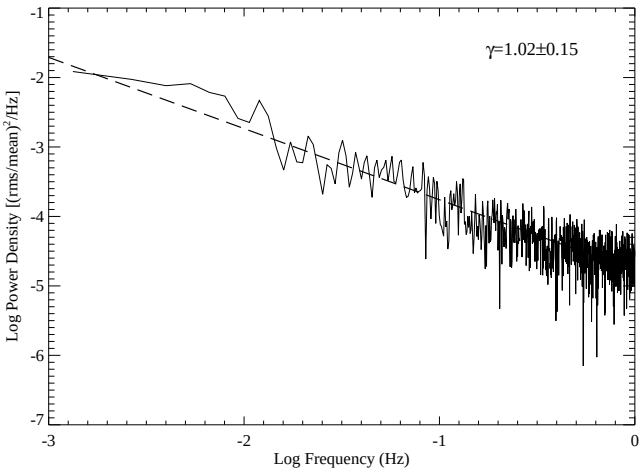

Figure 6.14: The power density spectrum for our observation of NGC 300 X-1. We find the slope $\gamma = 1.02 \pm 0.15$, consistent with an accreting black hole in the steep power law state, and find no evidence for QPOs at our observed frequencies.

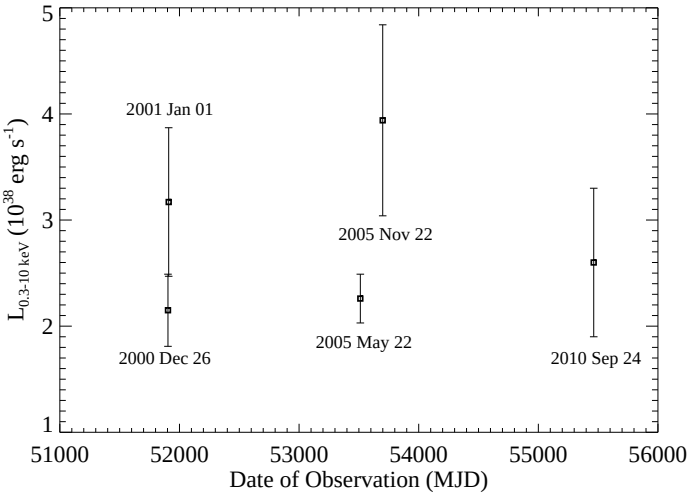

Figure 6.15: The long-term (∼10 years) 0.3-10 keV luminosity of NGC 300 X-1 from *XMM-Newton* [14] observations and our new *Chandra* observation.

observation; however, our data are sensitive only to frequencies lower than ∼1 Hz.

A long-term (∼10 year) light curve of X-1 was constructed using the *XMM-Newton* 0.3-10 keV luminosities [14], corrected for the different distance to NGC 300 used in that work. We supplement the existing *XMM-Newton* luminosities with the 0.3-10 keV luminosity found during the spectral fitting of our *Chandra* observation (see next subsection). The long-term light curve is shown in Figure 6.15. We find the 0.3-10 keV *Chandra* luminosity to be comparable to the luminosities found in the *XMM-Newton* observations, which showed a factor of ∼3 variability in the long-term luminosity of X-1. Persistent X-ray emission within a factor of a few is a signature of BH HMXBs and ULXs [for example, the most luminous sources in M 101; 205], with the notable exception of HLX-1 ESO 243-49 [observed to vary by up to a factor of ∼50; 236]. The accretion mechanism, however, may be different for normal BH HMXBs and ULXs: mass transfer in known HMXBs with BH primaries occurs via wind accretion or Roche lobe overflow, whereas ULXs may be undergoing a different phase of mass transfer which occurs on the thermal timescale [see 268, and references therein].

6.3.2 Spectral Fitting

Previous *XMM-Newton* observations of NGC 300 X-1 [14] have shown the X-ray spectra of two observations to be consistent with that of a HMXB in a high/soft state. The other two observations yielded spectra that were not consistent with such a model, providing the first evidence that X-1 may undergo X-ray state changes analogous to a typical XRB. In general, the *XMM-Newton* spectra have a photon index Γ ∼2.4–4.1, with a blackbody disk temperature $kT_{\rm in}$ ranging from 1.5-2.0 keV [14]. The power law component was estimated to contribute ∼60-90% of the total X-ray flux. They concluded that, over the ∼5 years spanned by the *XMM-Newton* observations, X-1 exhibited qualities of either being in a soft thermal state or a very high (i.e., steep power law) state.

We extracted the *Chandra* 0.5-5 keV spectrum of X-1. Due to the high number of source counts, we grouped the spectrum to contain at least 20 counts per energy bin and evaluated the goodness of our fits using χ^2 statistics and standard weighting. All models include a column of neutral absorption fixed at the Galactic column $N_{\rm H,Gal}$ of 4.09×10^{20} cm^{-2} [208], and we find no evidence for absorption beyond the Galactic column. We fit the spectrum using two models: a simple power law and a power law with a disk blackbody.

The normalization of the `diskbb` model is defined as:

$$L = \frac{(R_{\rm in}/{\rm km})}{(D/10\ {\rm kpc})^2} \cos\theta, \tag{6.2}$$

where $R_{\rm in}$ is the innermost disk radius, D is the distance to the source, and θ is the inclination angle of the disk. The innermost disk radius is in turn dependent on the BH mass via $R_{\rm in} = 6GM_{\rm BH}/c^2$; however, the normalization suffers from severe limitations that make it an unreliable estimator of BH mass. For example, the `diskbb` model does not adequately capture all the physics of disk emission, nor does it include relativistic effects [93, 94] and does not correctly treat the inner disk boundary [468]. Moreover, uncertainties in the distance to NGC 300 [on the order of ∼2% 87] and the inclination of the system will introduce additional error into any mass estimates. However, due to the limited number of photons originating from the thermal component, our model fits do not improve when using more sophisticated disk models. Therefore, we make our best interpretation of the physical

properties of X-1 using the `diskbb` model.

The 0.5-5 keV spectrum was found to be well described by both a simple power law with $\Gamma = 2.5 \pm 0.1$ ($\chi^2/dof = 66/72$) and a two-component model with $\Gamma = 2.0 \pm 0.3$ and $kT_{\rm in} = 0.23^{+0.04}_{-0.05}$ keV ($\chi^2/dof = 56/70$ with a disk normalization of $3.7^{+5.8}_{-2.1}$) and is shown in Figure 6.16. We performed an F-test to evaluate the significance of the fit improvement when adding the second component; we find the probability of the two models being drawn from the same underlying spectrum to be less than 1%, strongly indicating the need for the disk component. The unabsorbed 0.3-10 keV luminosity is found to be $2.6^{+0.8}_{-1.0} \times 10^{38}$ erg s^{-1}, with 74% of the luminosity originating in the power-law component. We therefore find that the addition of a disk component significantly improves the quality of our spectral fit.

Due to the rapid variability displayed in the light curve and the change in spectral state between the *XMM-Newton* and *Chandra* observations, we next split the X-1 spectrum in three time intervals: (1) from the start of our observation through 20 ks, (2) from 20 ks to 40 ks, and (3) from 40 ks until the end of the observation. We modeled each spectrum as a single power law and as a power law with a disk blackbody component. The total spectrum and the spectrum for the three time intervals are shown in Figure 6.16. The results of our spectral fitting are summarized in Table 6.5, and our best-fit models are shown in boldface. The best-fit model for each time interval was determined by which model yielded the lowest reduced χ^2. We initially allowed the normalization of the disk blackbody component to vary between the three periods, but this resulted in poorly constrained model parameters. Since neither the mass of the black hole, the spin, nor the inclination of the disk can vary over the timescales probed by our observation, we chose to fix the disk normalization parameter to the best-fit value found for the total time-averaged spectrum.

For the first time 20 ks, we favor the simple power law-only spectral model, with $\Gamma = 2.6 \pm 0.2$ (unabsorbed 0.3-10 keV luminosity of $2.4^{+0.4}_{-0.3} \times 10^{38}$ erg s^{-1}). For the middle time interval, ranging from 20-40 ks, we find the power law-only fit is improved by adding a disk blackbody component with a disk temperature of 0.26 ± 0.02 keV. However, our model is relatively insensitive to the value of the power law photon index: we find $\Delta\chi^2/dof \sim 0.1$ over a range of Γ from 0.9-2.4; we therefore only constrain $\Gamma < 2.4$. The two-component model model yields an unabsorbed 0.3-10 keV luminosity of $3.1^{+1.0}_{-0.6} \times 10^{38}$ erg s^{-1}, with 55%

Table 6.5: NGC 300 X-1 0.5-5 keV Spectral Fitting

Model	Parameter	Units	0-20 ks	20-40 ks	40-60 ks	Total
(1)	(2)	(3)	(4)	(5)	(6)	(7)
po	Γ		**2.6**±0.2	2.6±0.2	2.3±0.1	2.5±0.1
	χ^2/dof		**29/26**	31/25	27/35	66/72
	$L_{0.3-10}{}^a$	10^{38} erg s^{-1}	$\mathbf{2.4}^{+0.4}_{-0.3}$	$2.7^{+0.1}_{-0.7}$	$3.2^{+0.1}_{-0.6}$	2.6±0.5
diskbb+po	$kT_{\rm in}$	keV	$0.2^{+0.1}_{-0.2}$	**0.26**±0.02	**<0.24**	$\mathbf{0.23}^{+0.04}_{-0.05}$
	Γ		$2.4^{+0.3}_{-0.5}$	< 2.4	$\mathbf{2.1}^{+0.3}_{-0.5}$	**2.0**±0.3
	disk norm.		3.7 (fixed)	**3.7 (fixed)**	**3.7 (fixed)**	$\mathbf{3.7}^{+5.8}_{-2.1}$
	Frac. PL^b		84%	**55%**	**87%**	**74%**
	χ^2/dof		28/25	**19/24**	**25/34**	**56/70**
	$L_{0.3-10}{}^a$	10^{38} erg s^{-1}	$2.6^{+2.1}_{-0.5}$	$\mathbf{3.1}^{+1.0}_{-0.6}$	$\mathbf{3.2}^{+0.3}_{-0.6}$	$\mathbf{2.6}^{+0.8}_{-1.0}$

The favored spectral model for each spectrum is shown in boldface. All spectral models include an absorbing column fixed at the Galactic value, $N_{\rm H,Gal} = 4.09 \times 10^{20}$ cm^{-2}.

[a] The total unabsorbed 0.3-10 keV luminosity predicted from the spectral model.

[c]The fraction of the unabsorbed model luminosity originating from the power law spectral component.

of the 0.3-10 keV luminosity originating from the power law component. The fit for the final time interval, lasting from 40 ks until the end of the observation, is not statistically improved when a disk component is added, however the fit residuals at higher energies are improved with the second component. We constrain the disk temperature to be < 0.24 keV, with a photon index $\Gamma = 2.1^{+0.3}_{-0.5}$, yielding an unabsorbed 0.3-10 keV luminosity of $3.2^{+0.3}_{-0.6} \times 10^{38}$ erg s^{-1} (with 87% of the luminosity originating from the power law component). Figure 6.16 shows the time-averaged and time-resolved spectra of X-1, with the best-fit models superimposed.

We find the luminosity of X-1 to be comparable to those reported by [14], although our spectral models yield disk temperatures roughly an order of magnitude lower (∼0.2 keV, compared to 1.5-2.0 keV) and a moderately harder photon index (Γ ∼2.0-2.6, compared to 3.1-4.1). Despite this, the fraction of the luminosity originating from the power law component (∼55-87%) is similar to what was previously observed.

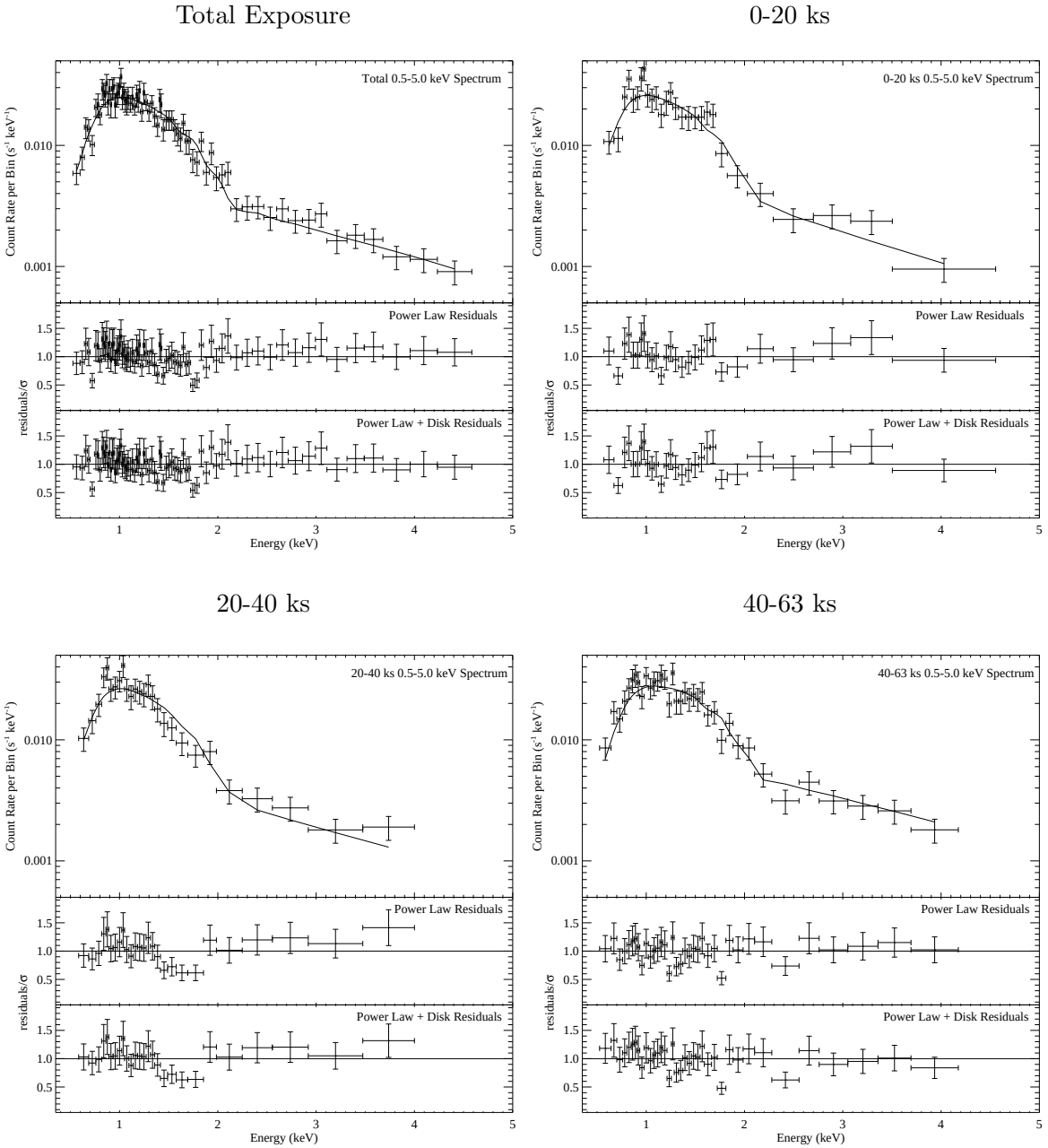

Figure 6.16: In each figure, the top panel shows the 0.5-5 keV spectrum with the best-fit model superimposed. The middle panel shows the fit residuals for a power law-only spectral model, and the bottom panel shows the fit residuals when a disk blackbody model is included. The top row shows the time-averaged spectrum for the entire observation (left) and the first 20 ks (right), while the bottom row shows the middle 20-40 ks (left) and the final portion of the exposure from 40-63 ks (right).

Table 6.6: X-ray Spectral and Timing Characteristics of BH XRBs and NGC 300 X-1[a]

Parameter	Thermal	Hard	Steep Power Law	NGC 300 X-1
(1)	(2)	(3)	(4)	(5)
Γ	2.1-4.8	1.4-2.1	>2.4	2.0-2.6
$kT_{\rm in}$ (keV)	0.7-1.5	0.1-0.2	0.1-1.5	0.20-0.26
PL frac.	<25%	>80%	>20% (>50%)	∼55-87%
r[b]	<0.075	>0.1	< 0.15	∼ 0.1
rms of QPOs	<0.005 (or absent)	present	> 0.01 (absent)	none at < 1 Hz
γ	∼ 1	Lorentzian	∼ 1	1.02±0.15

[a] Compiled from van der Klis (1994) and McClintock & Remillard (2006).

[b] Integrated power continuum over 0.1-10 Hz.

6.3.3 Summary and Discussion

In Table 6.6, we list six parameters (both spectroscopic and timing) commonly used to identify X-ray spectral states in BH XRBs compiled from van der Klis (1994) and McClintock & Remillard (2006), and list the quantities derived for X-1 in this work. The best-fit power law photon index for our full time-averaged spectrum ($\Gamma = 2.0\pm0.3$) lies near the boundary between the hard state and the thermal/SPL states; however, our shorter time period spectra favor moderately steeper values of Γ, and may be as steep as $\Gamma = 2.6\pm0.2$. All other parameters listed in Table 6.6 are consistent with a SPL interpretation of the *Chandra* spectrum of X-1.

The physical origin of the SPL state is commonly explained by stable disk accretion with inverse Compton scattering in a corona providing a nonthermal component [463, 151]. In this scenario, a large fraction of the accretion power is emitted in the stable accretion disk which produces a soft, multicolor disk blackbody-type spectrum. Models involving more complicated geometry and feedback have been developed to explain the origin of the Comptonizing electrons, and typically involve magnetic activity at the surface of the disk and may be related to jet formation [320, 96, 151]. This interpretation was favored to explain the earlier *XMM-Newton* observations of the NGC 300 X-1 spectrum [14], and it is

estimated that a small fraction of the $\sim 10^{-5} - 10^{-4}$ $M_{\odot}$ yr^{-1} wind from the Wolf-Rayet companion would provide a sufficient amount of mass and angular momentum to sustain an accretion disk around the NGC 300 X-1 BH. This scenario predicts that NGC 300 X-1, and other HMXBs containing BH primaries, would remain in a persistently high state, and is supported by observations: other known extragalactic HMXB systems with BH primaries have never been observed to enter a low/hard state (i.e., LMC X-1, [451, 298, 460]; M 33 X-1, [313]).

We compare X-1 with other subpopulations of HMXBs: those containing BH primaries, NS primaries, and ULXs. While ULXs are statistically consistent with representing a subpopulation of HMXBs [394], no known Galactic BH XRB has been observed to possess both an Eddington (or higher) X-ray luminosity *and* a hard power law-dominated spectrum (with $1.5 < \Gamma < 2.5$; [200, 247, 392]. ULXs appear to exist in a persistent high/hard state, requiring both a high mass accretion rate ($\dot{m}$) and either a strong corona or jet. Studies of HMXBs (especially those in the SMC) containing NS primaries find X-ray spectra that are significantly harder, with $\Gamma \sim 0.7-1.3$ [166, 238]. In Figure 6.17, we compare the 0.3-10 keV luminosities and photon indices of well-studied HMXBs systems (observed to be only in the high or SPL states), including those containing BH primaries (M 33 X-7, [313]; IC 10 X-1, [16]; and LMC X-1 and X-3, [460]), ULXs (NGC 1365 X-1 and X-2, [385]; Holmberg II X-1, [164]), and HMXBs powered by NSs in the SMC [166]. The three classes of HMXB clearly occupy distinct regions of the plot, and X-1 is only consistent with known BH-HMXBs in either the high or SPL states.

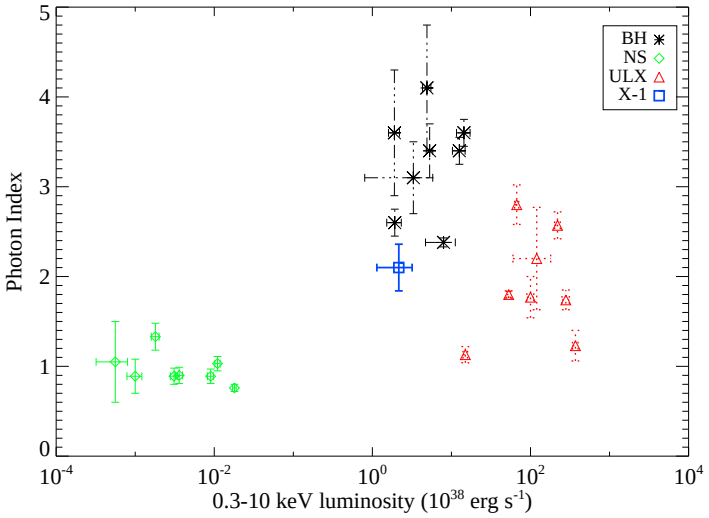

Figure 6.17: We compare the 0.3-10 keV luminosities and photon indices for known, well-studied HMXBs with BH primaries (black stars, dot-dashed error bars) in the high or steep power law state, NS primaries (green diamonds, solid error bars), and ULXs (red triangles, dotted error bars). X-1 (blue square with thick solid error bars) is consistent with other known BH HMXB systems.

Chapter 7

SUMMARY AND FUTURE WORK

7.1 The Impact of the Chandra Local Volume Survey

The *Chandra* Local Volume Survey has examined the resolved X-ray point source populations of five nearby galaxies using matched *Chandra* and *HST* imaging. A total of 629 highly significant X-ray sources were detected between the five galaxies, of which ∼140 are strong HMXB candidates. The remaining sources are a mix of background AGN, foreground stars, and bright SNRs. XLFs of the HMXB candidates were constructed for the four star-forming galaxies in our sample. For comparison, the XLF of the LMXB population of the dwarf S0 galaxy NGC 404 was also examined. The normalization of the XLF is known to correlate with the SFR of the host galaxy, and the four star-forming galaxies in our sample follow this trend while the early-type NGC 404 clearly deviates. For the four star-forming galaxies in our sample, we find an average differential XLF slope of 0.7 ± 0.2, consistent with the "universal" XLF of HMXBs.

The power of the CLVS comes from the resolved stellar populations accessible through the *HST* imaging. This thesis represented the first time that extragalactic HMXB populations can be *directly* studied. Previous studies of the XLFs of different classes of XRBs have been performed in a statistical sense only – that is, the expected contribution from contaminating source (i.e., background AGN) has been subtracted only statistically. For the CLVS galaxies, individual X-ray sources that are highly likely to be XRBs were extracted from the rest of the catalog and used for analysis – no statistical estimation of background contamination is required. Additionally, previous studies of HMXBs and their relationship to the SFR of the host galaxy have relied on various indirect methods of determining SFRs. With the available *HST* imaging, complete star formation histories can be constructed, even for different regions within the same galaxy, giving an unprecedented view into the L_X–SFR relationship.

The CLVS galaxies are somewhat lower-mass than previously studied galaxies, and have much more modest SFRs. This sample of HMXBs therefore allows us to probe a region of the L_X–SFR relation that has not been well-vetted in the literature. The fact that our *Chandra* and *HST* analysis of these galaxies produces results that are consistent with previous studies is evidence that (1) the statistical corrections to the shape of the XLF applied in previous works are reasonably reliable when resolved imaging of the stellar populations is not possible, and (2) that our multiwavelength source classification scheme is capturing a large fraction of HMXBs while rejecting a large fraction of contaminating sources. Additionally, the L_X–SFR relationship has been shown to be valid over nearly two orders of magnitude in SFR. While there is a correlation between the X-ray luminosity and the specific SFR of each galaxy, it is significantly weaker. Despite some contribution to X-ray emission from LMXBs, L_X alone is not a useful proxy for the host galaxy's SFR and stellar mass simultaneously.

Using our deep optical imaging (capable of detecting late-B/early-A main sequence stars), we have examined the number ratio of HMXBs to OB stars in each galaxy. We estimate the fraction of compact objects that are X-ray bright ($>10^{36}$ erg s^{-1}) due to accretion from a massive companion at least once in their lifetimes is $\sim$60–80%. This fraction can be used to constrain the mass distribution of the stellar companions in HMXBs, which is significantly flatter than a Kroupa IMF, consistent with optical observations of massive binaries.

This dissertation has provided a rigorous test of correlations between the star formation of a galaxy and its resulting HMXB populations. In the next section, I will summarize some of the possible future research that can be conducted in the area of XLF modeling, massive binary star evolution, and the effects of XRBs on galaxy formation and evolution.

7.2 Future Research

7.2.1 The Effect of Intermediate-Luminosity Transients on the X-ray Luminosity Function

The XLFs that are used to characterize a galaxy's XRB population are typically constructed from a single "snapshot" exposure of a galaxy. Aside from the XLFs presented in this thesis, most XLFs of extragalactic point source populations do not extend below of 10^{37}

erg s^{-1} [150, 161, 162, 275], and attempts to observationally constrain theoretical models [29, 131, 344] are incomplete at low- and intermediate-luminosities.

These snapshot XLFs are likely to contain many varieties of X-ray variable sources, some of which may change in luminosity by an order of magnitude or more. We will refer to these objects as "X-ray transients" (XRTs), and a brief summary of their properties (e.g., their quiescent and burst luminosities, and burst timescales) are presented in Table **??**. While these sources enter the measured XLF, their duty cycles are relatively uncertain. The consistency of the XLF across multiple epochs is therefore poorly constrained, especially at low- and intermediate-luminosities.

Galactic XRTs exhibit a wide range in variability characteristics, and studies of Galactic sources have been extremely useful because much information can be gleaned about individual sources with very low luminosities. For example, the burst luminosities of nearly all XRTs reaches 10^{36} erg s^{-1}, and only the very brightest reach $>10^{37}$ erg s^{-1}. However, the large angular extent of the Galaxy, the often (highly) uncertain distances to Galactic X-ray sources, and potentially severe levels of obscuration along Galactic lines of sight make it difficult to learn about entire *populations* of X-ray–variable sources. By targeting nearby galaxies, we overcome all of these obstacles. The entire XRT population can be observed, all the X-ray sources are essentially equidistant, and galaxies located far from the Galactic plane will have low foreground absorbing column.

The majority of Galactic XRTs are detected *below* the typical 10^{37} erg s^{-1} limit of extragalactic studies [29, 268], however studies of Galactic sources suffer from uncertain distance measurements, obscuration along the Galactic plane, and do not provide a global view of the XRT population. To put the Milky Way's faint- and intermediate-luminosity XRT population into context requires a temporal study of external disk galaxies to lower X-ray luminosities. To that end, we have successfully proposed for a deep, multi-epoch survey of NGC 300 to study the global intermediate-luminosity XRT demographics in detail, and their impact on the shape of the XLF down to $\sim 5\times10^{35}$ erg s^{-1}.

For reasons that are not yet clear, *bright* XRTs do not appear to make a substantial contribution to the shape of the *high-luminosity* end of the observed XLF [466]; however, this low contribution is likely because very few XRTs reach these high luminosities. Previous

Table 7.1: Summary of X-ray Transient Properties

Class	Quiescent L_X (erg s^{-1})	Burst L_X (erg s^{-1})	Burst timescale	References
(1)	(2)	(3)	(4)	(5)
bLMXB[a]	$<10^{33}$	$\sim10^{38}$	year	[405]
fLMXB[b]	$<10^{33}$	$\sim10^{36}$	year	[405]
SFXT	10^{32}	10^{35-37}	minutes	[365, 376]
BeXB	$<10^{33-35}$	Type I: $<10^{37}$ Type II: 10^{38}	hours days	[309, 341]

[a] "Bright" LMXBs; [b] "Faint" LMXBs

snapshot and archival X-ray observing programs have not had the sensitivity to detect sources below $\sim10^{37}$ erg s^{-1}, where the majority of XRTs are detected in the Milky Way. The effect of these low- and intermediate-luminosity sources on the shape of the XLF is almost completely unknown, and cannot be accurately determined from Galactic sources alone.

A pair of new *Chandra* exposures (130 ks in total) and four new optical and UV *HST* pointings will be obtained in 2014, which will be used to address this issue.

7.2.2 X-ray Binary Feedback

Feedback processes are vital in regulating the baryonic content of dark matter haloes, and it is generally accepted that these feedback processes are required to produce the observed properties of galaxies [26, 46, 211]. Star formation, SNe, and irradiation and winds from massive stars are believed to be the dominant feedback processes, especially in dwarf galaxies [66, 234, 269, 386]. Recently, XRB feedback (XBF) has been shown to be important in low-mass, low-metallicity environments, and hence in early epochs of galaxy formation [207, 276, 321]. With their low masses and metallicities, dwarf galaxies are the best available analogs to the proto-galaxies responsible for hierarchical galaxy formation in the early universe.

HMXBs, especially those with BH primaries, are capable of depositing a large fraction

of their energy output into the surrounding interstellar medium [ISM; 307]. For example, the jets of the Galactic HMXB Cyg X-1 provide kinetic energy equivalent to the bolometric X-ray luminosity of the system [140], while a single microquasar can provide a kinetic energy output up to $\sim 10^4$ times its X-ray power [306, 384]. XBF from XRBs can last up to $\sim 10^8$ yr after the formation of the relevant stellar population, and may be capable of keeping gas hot in non-star forming regions of galaxies [207]. Additionally, the low cross section for photon absorption by neutral hydrogen (which decreases with energy as E_γ^{-3}) means that X-rays can diffuse through the *intergalactic* medium and deposit energy far from their parent stellar populations, thereby influencing galaxy evolution over large distances [321]. If such output due to XRBs is common, it would suggest XBF is a significant – and overlooked – contributor to galaxy evolution and the reionization of the early Universe.

XBF is anticipated to be most significant in galaxies with stellar masses of 10^{7-8} $M_\odot$ [207], making dwarf galaxies uniquely suited for studying XBF. Models suggest XBF may dominate in some systems even *before* SN feedback begins. The strongest drivers of XBFs are HMXBs, but predicting the number of HMXBs in a dwarf galaxy cannot be done with any great accuracy. If one assumes the X-ray luminosity function of HMXBs in massive star-forming galaxies [161, 275] remains valid down to a few $\times 10^{35}$ erg s^{-1}, the SFR of the SMC predicts $\sim$20 HMXBs, a factor of 3 lower than observed [6, 5, 73]. For the LMC, the relationship predicts $\sim$30 HMXBs compared to the 36 currently known [247]. In comparison, the lower-mass Phoenix dwarf galaxy, which has a similar SFH to the SMC, does not appear to host any HMXBs [15].

Very bright HMXBs (i.e., those with X-ray luminosities above 10^{38} erg s^{-1}) likely possessing BH primaries. The ratio of BH to NS systems is expected to increase with redshift [276], and the number of HMXBs formed is strongly metallicity dependent [243]. With their higher mass compact objects, BH-HMXBs are capable of injecting larger quantities of energy into the surrounding ISM than their NS-counterpart systems, making the ratio of BH to NS systems an important parameter of XBF models.

Since multiple low-mass galaxies are expected to merge and form a single massive galaxy, it is interesting to ask the question: *Do the combined HMXB populations of multiple dwarf galaxies resemble that of a single massive galaxy?* While no BH-HMXBs are currently known

in the SMC [6, 5], several have been found in the LMC [247]. Differences in the BH-NS ratios of dwarf galaxies and massive galaxies throughout cosmic time may have important consequences for the effectiveness of XBF in regulating the baryonic content of galaxies.

7.2.3 Accurate Models of Binary Star Evolution

Entire populations of XRBs provide a useful diagnostic for galaxy evolution. While individual XRBs are excellent laboratories for studying stellar evolution, simply understanding the orbital mechanics and mass transfer mechanisms at work in a single XRB is not enough — one *must* consider the larger environment in which the XRB lives. X-ray population synthesis (XPS) attempts to simulate the evolution of XRBs and predict the resulting XLF given the star formation history, metallicity, and stellar mass of the host galaxy. The ultimate goal of XPS is to create a coherent picture of XRB formation and evolution within the larger context of galaxy evolution, where results of detailed theoretical modeling can be calibrated against a large sample of well-studied galaxies. At present, there is no one "industry standard" XPS code readily available with the required capabilities [194, 195, 21, 253, 471], and model comparisons to observational data have typically been limited to only one or two galaxies at a time. For our understanding of XRB evolution in the context of galaxy-wide star formation to progress, an easily accessible XPS code that has been rigorously calibrated against observational data is needed.

HMXBs follow a "universal" XLF (with a slope of 0.6), and LMXBs in elliptical galaxies show a significantly steeper XLF slope [$\sim$1.2; 150]. While the slope of the XLF is dependent on the age of the underlying X-ray source population [21, 120, 29], the relationship is non-monotonic with age when traced over a few hundred million years [21]. About 20 Myr after a star formation event, mostly bright HMXBs have formed, leading to a rather flat XLF. After $\sim$70 Myr, the most massive stellar companions have ended their lives, allowing fainter HMXBs to dominate the X-ray emission and causing the observed XLF to steepen. As the stellar population continues to age past $\sim$170 Myr, lower mass stars begin to undergo mass transfer to their compact companions and begin to contribute to the high-luminosity end of the XLF, once again flattening the slope. The ages of HMXBs in NGC 300 and NGC 2403

have been estimated using color magnitude diagrams to be ∼40–60 Myr [444], and other age have been estimated for HMXBs in the LMC and SMC [374, 5].

With the wealth of observational data about the XRB-host galaxy connection available, the typical approach to XPS has been the following: make some reasonable assumptions about initial mass function of the parent stellar population, the binary mass ratio distribution, and mass loss prescriptions during different phases of stellar evolution, then produce XLFs with varying metallicities and find the range of star formation histories that best reproduces the observed XLF. The converse approach, however, has *not* been explored in detail: use the star formation history and metallicity evolution of the host galaxy (both of which can be measured to an accuracy of better than ∼20% using *HST* observations) to find which initial assumptions need to be modified to re-create the observed XLF. For example, the fraction of stars that are a part of a binary or multiple-star system can only be measured for either very luminous or very nearby stars [115, 114], and may not be representative of all stars in all environments; additionally, some X-ray observations of stellar clusters hint at a top-heavy initial mass function [e.g., a higher fraction high-mass stars in clusters than low density environments, 70]. The number of stars that exist at each mass, the fraction of stars that form in binary systems, the mass ratio between binary companions, and prescriptions for stellar mass loss or tidal interactions are difficult to directly measure but will have a profound influence on a galaxys XRB population. The XPS technique offers a tantalizing new approach to investigating such open questions.

The Need for an "Industry Standard" XPS Code

The theoretical foundation on which XPS is built is relatively young. Two existing binary evolution codes dominate XPS studies: StarTrack [21] and Binary Star Evolution [BSE, 194, 195]. StarTrack was originally developed for modeling binary compact objects [17], but was later updated to treat the formation and evolution of XRBs for a given star formation history or metallicity of the host galaxy [21]. BSE, initially developed by [194, 195], is easily available and has been utilized by many authors, but it lacks some critical features necessary for XLF analysis. Most importantly, it fails to compute the X-ray luminosity

generated by the binary systems it creates. Thus, authors must modify BSE using their own prescription for estimating X-ray luminosities and producing XLFs [249, 472]. A great deal of the literature on XPS studies is spent "reinventing the wheel," and a thorough, rigorous comparison between StarTrack and the many varieties of BSE is lacking. The theoretical results of XRB evolutionary studies must therefore be regarded with some skepticism, and comparisons to observations are typically limited to only one or two galaxies [131, 132].

Both BSE and StarTrack treat major physical processes operating in binary systems, including: tidal interactions, which act to synchronize the spins of the stars and circularize the binary orbit [196]; mass transfer from stellar companion to compact object, both through stellar winds and through the formation of accretion disks; the common envelope phase, in which the outer atmosphere of the evolving stellar companion encompasses the orbit of the stellar remnant and may lead to a coalescence of the two stars or a tightening of the binary orbit [305]; evolution of the binary orbit due to magnetic breaking and the generation of gravitational radiation; and supernova explosions and compact object formation. Despite their outward similarities, BSE and StarTrack have some critical differences. StarTrack is capable of forming black holes reaching $\sim$10–20 $M_{\odot}$ [consistent with observed Galactic populations, 301], while the compact objects formed by BSE all have masses below $\sim$2.5 $M_{\odot}$. StarTrack additionally uses more recent supernova kick distributions [motivated by observations, 8, 182] than BSE, which affects the post-supernova binary orbit. StarTracks ability to directly produce XLFs resembling observations has been demonstrated for galaxies with dominant LMXB populations [21, 131, 132]. However, because BSE is faster than StarTrack it is better suited for simulating XRBs from large stellar populations, and BSE follows in detail the evolution of binary components.

As shown in this thesis, the data needed to guide the construction of a new XPS code already exists. A natural path for future research involves developing an "industry standard" XPS code, includes the most up-to-date formalisms of tidal interactions, mass transfer, magnetic and gravitational braking, compact object formation, and X-ray luminosity production. The code should be easily accessible through a web interface and will include tools to help astronomers plan observations of X-ray point source populations. A thorough comparison of the model XLFs to the high quality, resolved observations of X-ray and stellar

populations in dozens of nearby galaxies should also be performed. Once an XPS code has been properly calibrated, observational data can be used as input and the validity of traditional assumptions and prescriptions will be tested.

BIBLIOGRAPHY

[1] N. P. Abel and S. Satyapal. [Ne V] Emission in Optically Classified Starbursts. *Astrophysical Journal*, 678:686–692, May 2008.

[2] M. A. Agüeros, S. F. Anderson, K. R. Covey, S. L. Hawley, B. Margon, E. R. Newsom, B. Posselt, N. M. Silvestri, P. Szkody, and W. Voges. X-Ray-Emitting Stars Identified from the ROSAT All-Sky Survey and the Sloan Digital Sky Survey. *Astrophysical Journal Supplements*, 181:444–465, April 2009.

[3] A. Alonso-Herrero, M. J. Rieke, G. H. Rieke, and J. C. Shields. The Nature of LINERS. *Astrophysical Journal*, 530:688–703, February 2000.

[4] V. Antoniou, D. Hatzidimitriou, A. Zezas, and P. Reig. Optical Spectroscopy of 20 Be/X-ray Binaries in the Small Magellanic Cloud. *Astrophysical Journal*, 707:1080–1097, December 2009.

[5] V. Antoniou, A. Zezas, D. Hatzidimitriou, and V. Kalogera. Star Formation History and X-ray Binary Populations: The Case of the Small Magellanic Cloud. *Astrophysical Journal Letters*, 716:L140–L145, June 2010.

[6] V. Antoniou, A. Zezas, D. Hatzidimitriou, and J. C. McDowell. The Chandra Survey of the Small Magellanic Cloud "Bar". II. Optical Counterparts of X-ray Sources. *Astrophysical Journal*, 697:1695–1716, June 2009.

[7] W. D. Arnett. Gravitational collapse and weak interactions. *Canadian Journal of Physics*, 44:2553–2594, 1966.

[8] Z. Arzoumanian, D. F. Chernoff, and J. M. Cordes. The Velocity Distribution of Isolated Radio Pulsars. *Astrophysical Journal*, 568:289–301, March 2002.

[9] B. Aschenbach. Measuring mass and angular momentum of black holes with high-frequency quasi-periodic oscillations. *Astronomy & Astrophysics*, 425:1075–1082, October 2004.

[10] F. K. Baganoff, M. W. Bautz, W. N. Brandt, G. Chartas, E. D. Feigelson, G. P. Garmire, Y. Maeda, M. Morris, G. R. Ricker, L. K. Townsley, and F. Walter. Rapid X-ray flaring from the direction of the supermassive black hole at the Galactic Centre. *Nature*, 413:45–48, September 2001.

[11] W. E. Baggett, S. M. Baggett, and K. S. J. Anderson. Bulge-Disk Decomposition of 659 Spiral and Lenticular Galaxy Brightness Profiles. *Astronomical Journal*, 116:1626–1642, October 1998.

[12] C. D. Bailyn and J. E. Grindlay. Compact X-ray binaries in hierarchical triples. I - Tidal angular momentum loss and GX 17 + 2. *Astrophysical Journal*, 312:748–754, January 1987.

[13] M. K. Barker, A. M. N. Ferguson, M. J. Irwin, N. Arimoto, and P. Jablonka. Quantifying the faint structure of galaxies: the late-type spiral NGC 2403. *Monthly Notices of the Royal Astronomical Society*, 419:1489–1506, January 2012.

[14] R. Barnard, J. S. Clark, and U. C. Kolb. NGC 300 X-1 and IC 10 X-1: a new breed of black hole binary? *Astronomy & Astrophysics*, 488:697–703, September 2008.

[15] E. S. Bartlett, M. J. Coe, F. Haberl, V. A. McBride, and R. H. D. Corbet. The search for high-mass X-ray binaries in the Phoenix dwarf galaxy. *Monthly Notices of the Royal Astronomical Society*, 422:2302–2313, May 2012.

[16] F. E. Bauer and W. N. Brandt. Chandra and Hubble Space Telescope Confirmation of the Luminous and Variable X-Ray Source IC 10 X-1 as a Possible Wolf-Rayet, Black Hole Binary. *Astrophysical Journal Letters*, 601:L67–L70, January 2004.

[17] K. Belczynski and T. Bulik. Formation and Evolution of Microquasar GRS 1915+105. *Astrophysical Journal Letters*, 574:L147–L150, August 2002.

[18] K. Belczynski, T. Bulik, C. L. Fryer, A. Ruiter, F. Valsecchi, J. S. Vink, and J. R. Hurley. On the Maximum Mass of Stellar Black Holes. *Astrophysical Journal*, 714:1217–1226, May 2010.

[19] K. Belczynski, M. Dominik, T. Bulik, R. O'Shaughnessy, C. Fryer, and D. E. Holz. The Effect of Metallicity on the Detection Prospects for Gravitational Waves. *Astrophysical Journal Letters*, 715:L138–L141, June 2010.

[20] K. Belczynski, V. Kalogera, F. A. Rasio, R. E. Taam, A. Zezas, T. Bulik, T. J. Maccarone, and N. Ivanova. Compact Object Modeling with the StarTrack Population Synthesis Code. *Astrophysical Journal Supplements*, 174:223–260, January 2008.

[21] K. Belczynski, V. Kalogera, A. Zezas, and G. Fabbiano. X-Ray Binary Populations: The Luminosity Function of NGC 1569. *Astrophysical Journal Letters*, 601:L147–L150, February 2004.

[22] K. Belczynski and J. Ziolkowski. On the Apparent Lack of Be X-Ray Binaries with Black Holes. *Astrophysical Journal*, 707:870–877, December 2009.

[23] M. E. Bell, T. Tzioumis, P. Uttley, R. P. Fender, P. Arévalo, E. Breedt, I. McHardy, D. E. Calvelo, O. Jamil, and E. Körding. X-ray and radio variability in the low-luminosity active galactic nucleus NGC 7213. *Monthly Notices of the Royal Astronomical Society*, 411:402–410, February 2011.

[24] T. Belloni and G. Hasinger. An atlas of aperiodic variability in HMXB. *Astronomy & Astrophysics*, 230:103–119, April 1990.

[25] T. M. Belloni. States and Transitions in Black Hole Binaries. In T. Belloni, editor, *Lecture Notes in Physics, Berlin Springer Verlag*, volume 794 of *Lecture Notes in Physics, Berlin Springer Verlag*, page 53, March 2010.

[26] A. J. Benson, R. G. Bower, C. S. Frenk, C. G. Lacey, C. M. Baugh, and S. Cole. What Shapes the Luminosity Function of Galaxies? *Astrophysical Journal*, 599:38–49, December 2003.

[27] R. J. Beswick, T. W. B. Muxlow, M. K. Argo, A. Pedlar, J. M. Marcaide, and K. A. Wills. Monitoring of the Prompt Radio Emission from the Unusual Supernova SN 2004dj in NGC 2403. *Astrophysical Journal Letters*, 623:L21–L24, April 2005.

[28] H. A. Bethe and J. R. Wilson. Revival of a stalled supernova shock by neutrino heating. *Astrophysical Journal*, 295:14–23, August 1985.

[29] H. Bhadkamkar and P. Ghosh. Collective Properties of X-Ray Binary Populations of Galaxies. I. Luminosity and Orbital Period Distributions of High-mass X-Ray Binaries. *Astrophysical Journal*, 746:22, February 2012.

[30] V. B. Bhalerao, M. H. van Kerkwijk, and F. A. Harrison. Constraints on the Compact Object Mass in the Eclipsing High-mass X-Ray Binary XMMU J013236.7+303228 in M 33. *Astrophysical Journal*, 757:10, September 2012.

[31] D. Bhattacharya and E. P. J. van den Heuvel. Formation and evolution of binary and millisecond radio pulsars. *Physics Reports*, 203:1–124, 1991.

[32] L. Bildsten, D. Chakrabarty, J. Chiu, M. H. Finger, D. T. Koh, R. W. Nelson, T. A. Prince, B. C. Rubin, D. M. Scott, M. Stollberg, B. A. Vaughan, C. A. Wilson, and R. B. Wilson. Observations of Accreting Pulsars. *Astrophysical Journal Supplements*, 113:367, December 1997.

[33] B. Binder, B. F. Williams, M. Eracleous, T. J. Gaetz, A. K. H. Kong, E. D. Skillman, and D. R. Weisz. The Chandra Local Volume Survey: The X-Ray Point-source Population of NGC 404. *Astrophysical Journal*, 763:128, February 2013.

[34] B. Binder, B. F. Williams, M. Eracleous, T. J. Gaetz, P. P. Plucinsky, E. D. Skillman, J. J. Dalcanton, S. F. Anderson, D. R. Weisz, and A. K. H. Kong. The Chandra Local Volume Survey: The X-Ray Point-source Catalog of NGC 300. *Astrophysical Journal*, 758:15, October 2012.

[35] B. Binder, B. F. Williams, M. Eracleous, M. R. Garcia, S. F. Anderson, and T. J. Gaetz. A Deep Chandra Observation of the Wolf-Rayet + Black Hole Binary NGC 300 X-1. *Astrophysical Journal*, 742:128, December 2011.

[36] B. Binder, B. F. Williams, M. Eracleous, A. C. Seth, J. J. Dalcanton, E. D. Skillman, D. R. Weisz, S. F. Anderson, T. J. Gaetz, and P. P. Plucinsky. A Deep Chandra View of the NGC 404 Central Engine. *Astrophysical Journal*, 737:77, August 2011.

[37] B. Binder, B. F. Williams, A. K. H. Kong, T. J. Gaetz, P. P. Plucinsky, J. J. Dalcanton, and D. R. Weisz. Chandra Detection of SN 2010da Four Months After Outburst: Evidence for a High-mass X-Ray Binary in NGC 300. *Astrophysical Journal Letters*, 739:L51, October 2011.

[38] A. Blaauw. On the origin of the O- and B-type stars with high velocities (the "runaway" stars), and some related problems. *Bulletin of the Astronomical Institutes of the Netherlands*, 15:265, May 1961.

[39] J. M. Blondin. The shadow wind in high-mass X-ray binaries. *Astrophysical Journal*, 435:756–766, November 1994.

[40] J. M. Blondin, A. Mezzacappa, and C. DeMarino. Stability of Standing Accretion Shocks, with an Eye toward Core-Collapse Supernovae. *Astrophysical Journal*, 584:971–980, February 2003.

[41] T. Böker, S. Laine, R. P. van der Marel, M. Sarzi, H.-W. Rix, L. C. Ho, and J. C. Shields. A Hubble Space Telescope Census of Nuclear Star Clusters in Late-Type Spiral Galaxies. I. Observations and Image Analysis. *Astronomical Journal*, 123:1389–1410, March 2002.

[42] H. E. Bond. Optical Photometry of the New Optical Transient SN 2010da in NGC 300. *The Astronomer's Telegram*, 2640:1, May 2010.

[43] H. Bondi. On spherically symmetrical accretion. *Monthly Notices of the Royal Astronomical Society*, 112:195, 1952.

[44] H. Bondi and F. Hoyle. On the mechanism of accretion by stars. *Monthly Notices of the Royal Astronomical Society*, 104:273, 1944.

[45] A. Bouchard, P. Prugniel, M. Koleva, and M. Sharina. Stellar population and kinematics of NGC 404. *Astronomy & Astrophysics*, 513:A54, April 2010.

[46] R. G. Bower, A. J. Benson, R. Malbon, J. C. Helly, C. S. Frenk, C. M. Baugh, S. Cole, and C. G. Lacey. Breaking the hierarchy of galaxy formation. *Monthly Notices of the Royal Astronomical Society*, 370:645–655, August 2006.

[47] E. Bozzo, M. Falanga, and L. Stella. Are There Magnetars in High-Mass X-Ray Binaries? The Case of Supergiant Fast X-Ray Transients. *Astrophysical Journal*, 683:1031–1044, August 2008.

[48] A. Bressan, F. Fagotto, G. Bertelli, and C. Chiosi. Evolutionary sequences of stellar models with new radiative opacities. II - Z = 0.02. *Astronomy & Astrophysics Supplements*, 100:647–664, September 1993.

[49] P. S. Broos, L. K. Townsley, E. D. Feigelson, K. V. Getman, F. E. Bauer, and G. P. Garmire. Innovations in the Analysis of Chandra-ACIS Observations. *Astrophysical Journal*, 714:1582–1605, May 2010.

[50] S. W. Bruenn. Stellar core collapse - Numerical model and infall epoch. *Astrophysical Journal Supplements*, 58:771–841, August 1985.

[51] S. W. Bruenn, A. Mezzacappa, W. R. Hix, J. M. Blondin, P. Marronetti, O. E. B. Messer, C. J. Dirk, and S. Yoshida. Mechanisms of Core-Collapse Supernovae Simulation Results from the CHIMERA Code. In G. Giobbi, A. Tornambe, G. Raimondo, M. Limongi, L. A. Antonelli, N. Menci, and E. Brocato, editors, *American Institute of Physics Conference Series*, volume 1111 of *American Institute of Physics Conference Series*, pages 593–601, May 2009.

[52] A. Burrows, J. Hayes, and B. A. Fryxell. On the Nature of Core-Collapse Supernova Explosions. *Astrophysical Journal*, 450:830, September 1995.

[53] A. Burrows and J. M. Lattimer. The prompt mechanism of Type II supernovae. *Astrophysical Journal Letters*, 299:L19–L22, December 1985.

[54] A. Burrows, E. Livne, L. Dessart, C. D. Ott, and J. Murphy. An acoustic mechanism for core-collapse supernova explosions. *New Astronomy Review*, 50:487–491, October 2006.

[55] A. Burrows, E. Livne, L. Dessart, C. D. Ott, and J. Murphy. Features of the Acoustic Mechanism of Core-Collapse Supernova Explosions. *Astrophysical Journal*, 655:416–433, January 2007.

[56] N. Cappelluti, M. Brusa, G. Hasinger, A. Comastri, G. Zamorani, A. Finoguenov, R. Gilli, S. Puccetti, T. Miyaji, M. Salvato, C. Vignali, T. Aldcroft, H. Böhringer, H. Brunner, F. Civano, M. Elvis, F. Fiore, A. Fruscione, R. E. Griffiths, L. Guzzo, A. Iovino, A. M. Koekemoer, V. Mainieri, N. Z. Scoville, P. Shopbell, J. Silverman, and C. M. Urry. The XMM-Newton wide-field survey in the COSMOS field. The point-like X-ray source catalogue. *Astronomy & Astrophysics*, 497:635–648, April 2009.

[57] C. M. Carollo, I. J. Danziger, R. M. Rich, and X. Chen. Nuclear Properties of Kinematically Distinct Cores. *Astrophysical Journal*, 491:545, December 1997.

[58] S. Carpano, A. M. T. Pollock, A. Prestwich, P. Crowther, J. Wilms, L. Yungelson, and M. Ehle. A 33 hour period for the Wolf-Rayet/black hole X-ray binary candidate NGC 300 X-1. *Astronomy & Astrophysics*, 466:L17–L20, May 2007.

[59] S. Carpano, A. M. T. Pollock, J. Wilms, M. Ehle, and M. Schirmer. A Wolf-Rayet/black-hole X-ray binary candidate in NGC 300. *Astronomy & Astrophysics*, 461:L9–L12, January 2007.

[60] S. Carpano, J. Wilms, M. Schirmer, and E. Kendziorra. X-ray properties of NGC 300. I. Global properties of X-ray point sources and their optical counterparts. *Astronomy & Astrophysics*, 443:103–114, November 2005.

[61] W. Cash. Parameter estimation in astronomy through application of the likelihood ratio. *Astrophysical Journal*, 228:939–947, March 1979.

[62] B. Cester, S. Ferluga, and C. Boehm. The empirical mass-luminosity relation. *Astrophysics and Space Science*, 96:125–140, October 1983.

[63] R. Chandar, C. Leitherer, C. A. Tremonti, D. Calzetti, A. Aloisi, G. R. Meurer, and D. de Mello. The Stellar Content of Nearby Star-forming Galaxies. III. Unravelling the Nature of the Diffuse Ultraviolet Light. *Astrophysical Journal*, 628:210–230, July 2005.

[64] S. Chaty, J. A. Zurita Heras, and A. Bodaghee. The INTEGRAL legacy on High Mass X-ray Binaries. In *Eighth Integral Workshop. The Restless Gamma-ray Universe (INTEGRAL 2010)*, 2010.

[65] W. Chen and R. L. White. Nonthermal X-ray emission from winds of OB supergiants. *Astrophysical Journal*, 366:512–528, January 1991.

[66] R. A. Chevalier. The interaction of supernovae with the interstellar medium. *Annual Review of Astronomy & Astrophysics*, 15:175–196, 1977.

[67] R. A. Chevalier. Evolution of the Crab Nebula. In M. C. Kafatos and R. B. C. Henry, editors, *The Crab Nebula and Related Supernova Remnants*, pages 63–72, 1985.

[68] Y.-K. Chiang and A. K. H. Kong. The long-term variability of the X-ray sources in M82. *Monthly Notices of the Royal Astronomical Society*, 414:1329–1338, June 2011.

[69] R. Chornock and E. Berger. Spectroscopy of SN 2010da in NGC 300. *The Astronomer's Telegram*, 2637:1, May 2010.

[70] D. M. Clark, S. S. Eikenberry, B. R. Brandl, J. C. Wilson, J. C. Carson, C. P. Henderson, T. L. Hayward, D. J. Barry, A. F. Ptak, and E. J. M. Colbert. A First Estimate of the X-Ray Binary Frequency as a Function of Star Cluster Mass in a Single Galactic System. *Astrophysical Journal*, 678:798–803, May 2008.

[71] J. S. Clark and P. A. Crowther. On the Wolf-Rayet counterpart to IC 10 X-1. *Astronomy & Astrophysics*, 414:L45–L48, January 2004.

[72] W. Coburn, W. A. Heindl, R. E. Rothschild, D. E. Gruber, I. Kreykenbohm, J. Wilms, P. Kretschmar, and R. Staubert. Magnetic Fields of Accreting X-Ray Pulsars with the Rossi X-Ray Timing Explorer. *Astrophysical Journal*, 580:394–412, November 2002.

[73] M. J. Coe, W. R. T. Edge, J. L. Galache, and V. A. McBride. Optical properties of Small Magellanic Cloud X-ray binaries. *Monthly Notices of the Royal Astronomical Society*, 356:502–514, January 2005.

[74] E. J. M. Colbert, T. M. Heckman, A. F. Ptak, D. K. Strickland, and K. A. Weaver. Old and Young X-Ray Point Source Populations in Nearby Galaxies. *Astrophysical Journal*, 602:231–248, February 2004.

[75] S. A. Colgate. Radio frequency emission from supernova ejecta. *Astronomical Journal*, 71:850, February 1966.

[76] L. Colina, R. Gonzalez Delgado, J. M. Mas-Hesse, and C. Leitherer. Detection of a Super-Star Cluster as the Ionizing Source in the Low-Luminosity Active Galactic Nucleus NGC 4303. *Astrophysical Journal*, 579:545–553, November 2002.

[77] J. J. Condon. Radio emission from normal galaxies. *Annual Review of Astronomy and Astrophysics*, 30:575–611, 1992.

[78] A. Constantin, P. Green, T. Aldcroft, D.-W. Kim, D. Haggard, W. Barkhouse, and S. F. Anderson. Probing the Balance of AGN and Star-forming Activity in the Local Universe with ChaMP. *Astrophysical Journal*, 705:1336–1355, November 2009.

[79] S. Corbel, M. A. Nowak, R. P. Fender, A. K. Tzioumis, and S. Markoff. Radio/X-ray correlation in the low/hard state of GX 339-4. *Astronomy & Astrophysics*, 400:1007–1012, March 2003.

[80] R. H. D. Corbet, J. J. M. in't Zand, A. M. Levine, and F. E. Marshall. Rossi X-Ray Timing Explorer and BeppoSAX Observations of the Transient X-Ray Pulsar XTE J1859+083. *Astrophysical Journal*, 695:30–35, April 2009.

[81] P. Côté, S. Piatek, L. Ferrarese, A. Jordán, D. Merritt, E. W. Peng, M. Haşegan, J. P. Blakeslee, S. Mei, M. J. West, M. Milosavljević, and J. L. Tonry. The ACS Virgo Cluster Survey. VIII. The Nuclei of Early-Type Galaxies. *Astrophysical Journal Supplements*, 165:57–94, July 2006.

[82] P. A. Crowther, R. Barnard, S. Carpano, J. S. Clark, V. S. Dhillon, and A. M. T. Pollock. NGC 300 X-1 is a Wolf-Rayet/black hole binary. *Monthly Notices of the Royal Astronomical Society*, 403:L41–L45, March 2010.

[83] P. A. Crowther, S. Carpano, L. J. Hadfield, and A. M. T. Pollock. On the optical counterpart of NGC 300 X-1 and the global Wolf-Rayet content of NGC 300. *Astronomy & Astrophysics*, 469:L31–L34, July 2007.

[84] W. Cui, S. N. Zhang, W. Focke, and J. H. Swank. Temporal Properties of Cygnus X-1 during the Spectral Transitions. *Astrophysical Journal*, 484:383, July 1997.

[85] M. Dahlem, K. A. Weaver, and T. M. Heckman. An X-Ray Minisurvey of Nearby Edge-on Starburst Galaxies. I. The Data. *Astrophysical Journal Supplements*, 118:401–453, October 1998.

[86] S. E. Dahm, T. Simon, E. M. Proszkow, and B. M. Patten. X-Ray Observations of the Young Cluster NGC 2264. *Astronomical Journal*, 134:999–1018, September 2007.

[87] J. J. Dalcanton, B. F. Williams, A. C. Seth, A. Dolphin, J. Holtzman, K. Rosema, E. D. Skillman, A. Cole, L. Girardi, S. M. Gogarten, I. D. Karachentsev, K. Olsen, D. Weisz, C. Christensen, K. Freeman, K. Gilbert, C. Gallart, J. Harris, P. Hodge, R. S. de Jong, V. Karachentseva, M. Mateo, P. B. Stetson, M. Tavarez, D. Zaritsky, F. Governato, and T. Quinn. The ACS Nearby Galaxy Survey Treasury. *Astrophysical Journal*, 183:67–108, July 2009.

[88] D. A. Dale, S. A. Cohen, L. C. Johnson, M. D. Schuster, D. Calzetti, C. W. Engelbracht, A. Gil de Paz, R. C. Kennicutt, J. C. Lee, A. Begum, M. Block, J. J. Dalcanton, J. G. Funes, K. D. Gordon, B. D. Johnson, A. R. Marble, S. Sakai, E. D. Skillman, L. van Zee, F. Walter, D. R. Weisz, B. Williams, S.-Y. Wu, and Y. Wu. The Spitzer

Local Volume Legacy: Survey Description and Infrared Photometry. *Astrophysical Journal*, 703:517–556, September 2009.

[89] D. A. Dale, J. D. T. Smith, L. Armus, B. A. Buckalew, G. Helou, R. C. Kennicutt, Jr., J. Moustakas, H. Roussel, K. Sheth, G. J. Bendo, D. Calzetti, B. T. Draine, C. W. Engelbracht, K. D. Gordon, D. J. Hollenbach, T. H. Jarrett, L. J. Kewley, C. Leitherer, A. Li, S. Malhotra, E. J. Murphy, and F. Walter. Mid-Infrared Spectral Diagnostics of Nuclear and Extranuclear Regions in Nearby Galaxies. *Astrophysical Journal*, 646:161–173, July 2006.

[90] T. J. Davidge and S. Courteau. Near-Infrared Adaptive Optics Imaging of the Central Regions of Nearby Sc Galaxies. II. NGC 247 and NGC 2403. *Astronomical Journal*, 123:1438–1453, March 2002.

[91] K. Davidson, T. R. Gull, S. P. Maran, T. P. Stecher, R. A. Fesen, R. A. Parise, C. A. Harvel, M. Kafatos, and V. L. Trimble. The ultraviolet spectrum of the Crab Nebula. *Astrophysical Journal*, 253:696–706, February 1982.

[92] K. Davidson and J. P. Ostriker. Neutron-Star Accretion in a Stellar Wind: Model for a Pulsed X-Ray Source. *Astrophysical Journal*, 179:585–598, January 1973.

[93] S. W. Davis, C. Done, and O. M. Blaes. Testing Accretion Disk Theory in Black Hole X-Ray Binaries. *Astrophysical Journal*, 647:525–538, August 2006.

[94] S. W. Davis and I. Hubeny. A Grid of Relativistic, Non-LTE Accretion Disk Models for Spectral Fitting of Black Hole Binaries. *Astrophysical Journal Supplements*, 164:530–535, June 2006.

[95] W. J. G. de Blok, F. Walter, E. Brinks, C. Trachternach, S.-H. Oh, and R. C. Kennicutt, Jr. High-Resolution Rotation Curves and Galaxy Mass Models from THINGS. *Astronomical Journal*, 136:2648–2719, December 2008.

[96] E. M. de Gouveia Dal Pino, P. P. Piovezan, and L. H. S. Kadowaki. The role of magnetic reconnection on jet/accretion disk systems. *Astronomy & Astrophysics*, 518:A5, July 2010.

[97] G. de Vaucouleurs. Southern Galaxies. I. Luminosity, Rotation, and Mass of the Magellanic System NGC 55. *Astrophysical JournalMonthly Notices of the Royal Astronomical Society*, 133:405, March 1961.

[98] G. de Vaucouleurs, A. de Vaucouleurs, H. G. Corwin, Jr., R. J. Buta, G. Paturel, and P. Fouque. *Third Reference Catalogue of Bright Galaxies*. 1991.

[99] G. de Vaucouleurs, A. de Vaucouleurs, H. G. Corwin, Jr., R. J. Buta, G. Paturel, and P. Fouqué. *Third Reference Catalogue of Bright Galaxies. Volume I: Explanations and references. Volume II: Data for galaxies between 0^h and 12^h. Volume III: Data for galaxies between 12^h and 24^h.* 1991.

[100] N. Degenaar and R. Wijnands. The behavior of subluminous X-ray transients near the Galactic center as observed using the X-ray telescope aboard Swift. *Astronomy & Astrophysics*, 495:547–559, February 2009.

[101] M. S. del Río, E. Brinks, and J. Cepa. High-Resolution H I Observations of the Galaxy NGC 404: A Dwarf S0 with Abundant Interstellar Gas. *Astronomical Journal*, 128:89–102, July 2004.

[102] A. T. Deller, A. M. Archibald, W. F. Brisken, S. Chatterjee, G. H. Janssen, V. M. Kaspi, D. Lorimer, A. G. Lyne, M. A. McLaughlin, S. Ransom, I. H. Stairs, and B. Stappers. A Parallax Distance and Mass Estimate for the Transitional Millisecond Pulsar System J1023+0038. *Astrophysical Journal Letters*, 756:L25, September 2012.

[103] O. Demircan and G. Kahraman. Stellar mass-luminosity and mass-radius relations. *Astrophysics and Space Science*, 181:313–322, July 1991.

[104] P. B. Demorest, T. Pennucci, S. M. Ransom, M. S. E. Roberts, and J. W. T. Hessels. A two-solar-mass neutron star measured using Shapiro delay. *Nature*, 467:1081–1083, October 2010.

[105] J. D. M. Dewi. CXOU J121538.2+361921 in the galaxy NGC 4214: a double neutron star in the making? *Monthly Notices of the Royal Astronomical Society*, 372:L1–L4, October 2006.

[106] J. D. M. Dewi and T. M. Tauris. On the energy equation and efficiency parameter of the common envelope evolution. *Astronomy & Astrophysics*, 360:1043–1051, August 2000.

[107] A. Dobrotka, M. Friedjung, A. Retter, L. Hric, and R. Novak. The possible orbital period of the nova V1493 Aquilae. *Astronomy & Astrophysics*, 448:1107–1110, March 2006.

[108] A. E. Dolphin. WFPC2 Stellar Photometry with HSTPHOT. *Publicatins of the Astronomical Society of the Pacific*, 112:1383–1396, October 2000.

[109] A. E. Dolphin. Numerical methods of star formation history measurement and applications to seven dwarf spheroidals. *Monthly Notices of the Royal Astronomical Society*, 332:91–108, May 2002.

[110] L. Drissen, J.-R. Roy, A. F. J. Moffat, and M. M. Shara. The Ionizing Star Clusters of Giant H II Regions in NGC 2403. *Astronomical Journal*, 117:1249–1274, March 1999.

[111] G. Dubus, J.-P. Lasota, J.-M. Hameury, and P. Charles. X-ray irradiation in low-mass binary systems. *Monthly Notices of the Royal Astronomical Society*, 303:139–147, February 1999.

[112] R. P. Dudik, S. Satyapal, M. Gliozzi, and R. M. Sambruna. A Chandra Snapshot Survey of Infrared-bright LINERs: A Possible Link Between Star Formation, Active Galactic Nucleus Fueling, and Mass Accretion. *Astrophysical Journal*, 620:113–125, February 2005.

[113] A. S. Eddington. On the relation between the masses and luminosities of the stars. *Monthly Notices of the Royal Astronomical Society*, 84:308–332, March 1924.

[114] P. P. Eggleton. Towards multiple-star population synthesis. *Monthly Notices of the Royal Astronomical Society*, 399:1471–1481, November 2009.

[115] P. P. Eggleton and A. A. Tokovinin. A catalogue of multiplicity among bright stellar systems. *Monthly Notices of the Royal Astronomical Society*, 389:869–879, September 2008.

[116] P. P. Eggleton and F. Verbunt. Triple star evolution and the formation of short-period, low mass X-ray binaries. *Monthly Notices of the Royal Astronomical Society*, 220:13P–18P, May 1986.

[117] C. W. Engelbracht, K. D. Gordon, G. J. Bendo, P. G. Pérez-González, K. A. Misselt, G. H. Rieke, E. T. Young, D. C. Hines, D. M. Kelly, J. A. Stansberry, C. Papovich, J. E. Morrison, E. Egami, K. Y. L. Su, J. Muzerolle, H. Dole, A. Alonso-Herrero, J. L. Hinz, P. S. Smith, W. B. Latter, A. Noriega-Crespo, D. L. Padgett, J. Rho, D. T. Frayer, and S. Wachter. Far-Infrared Imaging of NGC 55. *Astrophysical Journal SupplementsAstrophysical Journal*, 154:248–252, September 2004.

[118] M. Eracleous, J. A. Hwang, and H. M. L. G. Flohic. An Assessment of the Energy Budgets of Low-Ionization Nuclear Emission Regions. *Astrophysical Journal*, 711:796–807, March 2010.

[119] M. Eracleous, J. C. Shields, G. Chartas, and E. C. Moran. Three LINERs under the Chandra X-Ray Microscope. *Astrophysical Journal*, 565:108–124, January 2002.

[120] M. Eracleous, M. S. Sipior, and S. Sigurdsson. Models for the Evolution of X-Ray Binaries in a Young Stellar Population. In E. J. A. Meurs & G. Fabbiano, editor, *Populations of High Energy Sources in Galaxies*, volume 230 of *IAU Symposium*, pages 417–422, 2006.

[121] A. A. Esin, J. E. McClintock, and R. Narayan. Advection-dominated Accretion and the Spectral States of Black Hole X-Ray Binaries: Application to Nova MUSCAE 1991. *Astrophysical Journal*, 489:865, November 1997.

[122] G. Fabbiano, D.-W. Kim, and G. Trinchieri. An X-ray catalog and atlas of galaxies. *Astrophysical Journal Supplements*, 80:531–644, June 1992.

[123] G. Fabbiano and G. Trinchieri. X-ray observations of spiral galaxies. II - Images and spectral parameters of 13 galaxies. *Astrophysical Journal*, 315:46–67, April 1987.

[124] G. Fabbiano and N. E. White. *Compact stellar X-ray sources in normal galaxies*, pages 475–506. April 2006.

[125] A. C. Fabian and K. Iwasawa. The mass density in black holes inferred from the X-ray background. *Monthly Notices of the Royal Astronomical Society*, 303:L34–L36, February 1999.

[126] H. Feng and P. Kaaret. XMM-Newton Observations of Ultraluminous X-Ray Sources in Nearby Galaxies. *Astrophysical Journal*, 633:1052–1063, November 2005.

[127] A. M. N. Ferguson, R. F. G. Wyse, and J. S. Gallagher. The Spectacular Ionized Interstellar Medium of NGC 55. *Astronomical Journal*, 112:2567, December 1996.

[128] H. M. L. G. Flohic, M. Eracleous, G. Chartas, J. C. Shields, and E. C. Moran. The Central Engines of 19 LINERs as Viewed by Chandra. *Astrophysical Journal*, 647:140–160, August 2006.

[129] T. Foglizzo. A Simple Toy Model of the Advective-Acoustic Instability. I. Perturbative Approach. *Astrophysical Journal*, 694:820–832, April 2009.

[130] D. Foreman-Mackey, D. W. Hogg, D. Lang, and J. Goodman. emcee: The MCMC Hammer. *Publications of the Astronomical Society of the Pacific*, 125:306–312, March 2013.

[131] T. Fragos, V. Kalogera, K. Belczynski, G. Fabbiano, D.-W. Kim, N. J. Brassington, L. Angelini, R. L. Davies, J. S. Gallagher, A. R. King, S. Pellegrini, G. Trinchieri, S. E. Zepf, A. Kundu, and A. Zezas. Models for Low-Mass X-Ray Binaries in the Elliptical Galaxies NGC 3379 and NGC 4278: Comparison with Observations. *Astrophysical Journal*, 683:346–356, August 2008.

[132] T. Fragos, V. Kalogera, B. Willems, K. Belczynski, G. Fabbiano, N. J. Brassington, D.-W. Kim, L. Angelini, R. L. Davies, J. S. Gallagher, A. R. King, S. Pellegrini,

G. Trinchieri, S. E. Zepf, and A. Zezas. Transient Low-mass X-ray Binary Populations in Elliptical Galaxies NGC 3379 and NGC 4278. *Astrophysical Journal Letters*, 702:L143–L147, September 2009.

[133] W. L. Freedman and B. F. Madore. Distances to the galaxies M81 and NGC 2403 from CCD I band photometry of Cepheids. *Astrophysical Journal Letters*, 332:L63–L66, September 1988.

[134] P. E. Freeman, V. Kashyap, R. Rosner, and D. Q. Lamb. A Wavelet-Based Algorithm for the Spatial Analysis of Poisson Data. *Astrophysical Journal*, 138:185–218, January 2002.

[135] P. C. C. Freire. Eclipsing Binary Pulsars. In F. A. Rasio and I. H. Stairs, editors, *Binary Radio Pulsars*, volume 328 of *Astronomical Society of the Pacific Conference Series*, page 405, July 2005.

[136] P. C. C. Freire, A. Wolszczan, M. van den Berg, and J. W. T. Hessels. A Massive Neutron Star in the Globular Cluster M5. *Astrophysical Journal*, 679:1433–1442, June 2008.

[137] C. L. Fryer, A. L. Hungerford, and G. Rockefeller. Supernova Explosions:. Understanding Mixing. *International Journal of Modern Physics D*, 16:941–981, 2007.

[138] C. L. Fryer and M. S. Warren. Modeling Core-Collapse Supernovae in Three Dimensions. *Astrophysical Journal Letters*, 574:L65–L68, July 2002.

[139] C. L. Fryer and M. S. Warren. The Collapse of Rotating Massive Stars in Three Dimensions. *Astrophysical Journal*, 601:391–404, January 2004.

[140] E. Gallo, R. Fender, C. Kaiser, D. Russell, R. Morganti, T. Oosterloo, and S. Heinz. A dark jet dominates the power output of the stellar black hole Cygnus X-1. *Nature*, 436:819–821, August 2005.

[141] E. Gallo, R. P. Fender, J. C. A. Miller-Jones, A. Merloni, P. G. Jonker, S. Heinz, T. J. Maccarone, and M. van der Klis. A radio-emitting outflow in the quiescent state

of A0620-00: implications for modelling low-luminosity black hole binaries. *Monthly Notices of the Royal Astronomical Society*, 370:1351–1360, August 2006.

[142] E. Gallo, R. P. Fender, and G. G. Pooley. A universal radio-X-ray correlation in low/hard state black hole binaries. *Monthly Notices of the Royal Astronomical Society*, 344:60–72, September 2003.

[143] M. R. Garcia, S. S. Murray, F. A. Primini, W. R. Forman, J. E. McClintock, and C. Jones. A First Look at the Nuclear Region of M31 with Chandra. *Astrophysical Journal Letters*, 537:L23–L26, July 2000.

[144] K. G. Gayley. An Improved Line-Strength Parameterization in Hot-Star Winds. *Astrophysical Journal*, 454:410, November 1995.

[145] N. Gehrels. Confidence limits for small numbers of events in astrophysical data. *Astrophysical Journal*, 303:336–346, April 1986.

[146] A. Georgakakis, K. Nandra, E. S. Laird, J. Aird, and M. Trichas. A new method for determining the sensitivity of X-ray imaging observations and the X-ray number counts. *Monthly Notices of the Royal Astronomical Society*, 388:1205–1213, August 2008.

[147] K. K. Ghosh, S. Rappaport, A. F. Tennant, D. A. Swartz, D. Pooley, and N. Madhusudhan. Discovery of a 3.6 hr Eclipsing Luminous X-Ray Binary in the Galaxy NGC 4214. *Astrophysical Journal*, 650:872–878, October 2006.

[148] R. Giacconi, H. Gursky, F. R. Paolini, and B. B. Rossi. Evidence for x Rays From Sources Outside the Solar System. *Physical Review Letters*, 9:439–443, December 1962.

[149] R. Giacconi, E. Kellogg, P. Gorenstein, H. Gursky, and H. Tananbaum. An X-Ray Scan of the Galactic Plane from UHURU. *Astrophysical Journal Letters*, 165:L27, April 1971.

[150] M. Gilfanov. Low-mass X-ray binaries as a stellar mass indicator for the host galaxy. *Monthly Notices of the Royal Astronomical Society*, 349:146–168, March 2004.

[151] M. Gilfanov. X-Ray Emission from Black-Hole Binaries. In T. Belloni, editor, *Lecture Notes in Physics, Berlin Springer Verlag*, volume 794 of *Lecture Notes in Physics, Berlin Springer Verlag*, page 17, March 2010.

[152] M. Gilfanov, H.-J. Grimm, and R. Sunyaev. L_X-SFR relation in star-forming galaxies. *Monthly Notices of the Royal Astronomical Society*, 347:L57–L60, January 2004.

[153] S. M. Gogarten, J. J. Dalcanton, B. F. Williams, R. Roškar, J. Holtzman, A. C. Seth, A. Dolphin, D. Weisz, A. Cole, V. P. Debattista, K. M. Gilbert, K. Olsen, E. Skillman, R. S. de Jong, I. D. Karachentsev, and T. R. Quinn. The Advanced Camera for Surveys Nearby Galaxy Survey Treasury. V. Radial Star Formation History of NGC 300. *Astrophysical Journal*, 712:858–874, April 2010.

[154] R. M. González Delgado, R. Cid Fernandes, E. Pérez, L. P. Martins, T. Storchi-Bergmann, H. Schmitt, T. Heckman, and C. Leitherer. The Stellar Populations of Low-Luminosity Active Galactic Nuclei. II. Space Telescope Imaging Spectrograph Observations. *Astrophysical Journal*, 605:127–143, April 2004.

[155] O. González-Martín, J. Masegosa, I. Márquez, and M. Guainazzi. Fitting Liner Nuclei within the Active Galactic Nucleus Family: A Matter of Obscuration? *Astrophysical Journal*, 704:1570–1585, October 2009.

[156] O. González-Martín, J. Masegosa, I. Márquez, M. A. Guerrero, and D. Dultzin-Hacyan. X-ray nature of the LINER nuclear sources. *Astronomy & Astrophysics*, 460:45–57, December 2006.

[157] J. Goodman and J. Weare. Ensemble samplers with affine invariance. *Commun. Appl. Math. Comput. Sci.*, 2010.

[158] A. W. Graham and R. Guzmán. HST Photometry of Dwarf Elliptical Galaxies in Coma, and an Explanation for the Alleged Structural Dichotomy between Dwarf and Bright Elliptical Galaxies. *Astronomical Journal*, 125:2936–2950, June 2003.

[159] J. E. Greene and L. C. Ho. A New Sample of Low-Mass Black Holes in Active Galaxies. *Astrophysical Journal*, 670:92–104, November 2007.

[160] H.-J. Grimm, M. Gilfanov, and R. Sunyaev. The Milky Way in X-rays for an outside observer. Log(N)-Log(S) and luminosity function of X-ray binaries from RXTE/ASM data. *Astronomy & Astrophysics*, 391:923–944, September 2002.

[161] H.-J. Grimm, M. Gilfanov, and R. Sunyaev. High-mass X-ray binaries as a star formation rate indicator in distant galaxies. *Monthly Notices of the Royal Astronomical Society*, 339:793–809, March 2003.

[162] H.-J. Grimm, J. McDowell, A. Zezas, D.-W. Kim, and G. Fabbiano. The X-Ray Binary Population in M33. I. Source List and Luminosity Function. *Astrophysical Journal Supplements*, 161:271–303, December 2005.

[163] J. E. Grindlay. Globular cluster origin of X-ray bursters. *Advances in Space Research*, 3:19–27, 1984.

[164] F. Grisé, P. Kaaret, H. Feng, J. J. E. Kajava, and S. A. Farrell. X-ray Spectral State is not Correlated with Luminosity in Holmberg II X-1. *Astrophysical Journal Letters*, 724:L148–L152, December 2010.

[165] M. A. Guerrero and Y.-H. Chu. An X-Ray Survey of Wolf-Rayet Stars in the Magellanic Clouds. I. The Chandra ACIS Data Set. *Astrophysical Journal Supplements*, 177:216–237, July 2008.

[166] F. Haberl and W. Pietsch. X-ray observations of Be/X-ray binaries in the SMC. *Astronomy & Astrophysics*, 414:667–676, February 2004.

[167] G. M. H. J. Habets and J. R. W. Heintze. Empirical bolometric corrections for the main-sequence. *Astronomy & Astrophysics Supplements*, 46:193–237, November 1981.

[168] Z. Han, P. Podsiadlowski, and P. P. Eggleton. A Possible Criterion for Envelope Ejection in Asymptotic Giant Branch or First Giant Branch Stars. *Monthly Notices of the Royal Astronomical Society*, 270:121, September 1994.

[169] Z. Han, P. Podsiadlowski, and P. P. Eggleton. The formation of bipolar planetary nebulae and close white dwarf binaries. *Monthly Notices of the Royal Astronomical Society*, 272:800–820, February 1995.

[170] C.-N. Hao, R. C. Kennicutt, B. D. Johnson, D. Calzetti, D. A. Dale, and J. Moustakas. Dust-corrected Star Formation Rates of Galaxies. II. Combinations of Ultraviolet and Infrared Tracers. *Astrophysical Journal*, 741:124, November 2011.

[171] J. M. Hartwell, I. R. Stevens, D. K. Strickland, T. M. Heckman, and L. K. Summers. Chandra and XMM-Newton observations of NGC 4214: the hot interstellar medium and the luminosity function of dwarf starbursts. *Monthly Notices of the Royal Astronomical Society*, 348:406–420, February 2004.

[172] M. Hashimoto, K. Iwamoto, and K. Nomoto. Type II supernovae from 8-10 solar mass asymptotic giant branch stars. *Astrophysical Journal Letters*, 414:L105–L108, September 1993.

[173] K. Hebeler, J. M. Lattimer, C. J. Pethick, and A. Schwenk. Constraints on Neutron Star Radii Based on Chiral Effective Field Theory Interactions. *Physical Review Letters*, 105(16):161102, October 2010.

[174] D. J. Helfand and E. C. Moran. The Hard X-Ray Luminosity of OB Star Populations: Implications for The Contribution of Star Formation to the Cosmic X-Ray Background. *Astrophysical Journal*, 554:27–42, June 2001.

[175] M. Herant, W. Benz, W. R. Hix, C. L. Fryer, and S. A. Colgate. Inside the supernova: A powerful convective engine. *Astrophysical Journal*, 435:339–361, November 1994.

[176] W. Hillebrandt, K. Nomoto, and R. G. Wolff. Supernova explosions of massive stars - The mass range 8 to 10 solar masses. *Astronomy & Astrophysics*, 133:175–184, April 1984.

[177] W. Hillebrandt, M. Reinecke, and J. C. Niemeyer. Thermonuclear supernovae. *Computer Physics Communications*, 127:53–58, May 2000.

[178] S. Hirose, J. H. Krolik, and O. Blaes. Radiation-Dominated Disks are Thermally Stable. *Astrophysical Journal*, 691:16–31, January 2009.

[179] L. C. Ho. Nuclear Activity in Nearby Galaxies. *Annual Review of Astronomy and Astrophysics*, 46:475–539, September 2008.

[180] L. C. Ho, A. V. Filippenko, W. L. W. Sargent, and C. Y. Peng. A Search for "Dwarf" Seyfert Nuclei. IV. Nuclei with Broad H alpha Emission. *Astrophysical Journal*, 112:391–+, October 1997.

[181] L. C. Ho, Y. Terashima, and J. S. Ulvestad. Detection of the "Active" Nucleus of M32. *Astrophysical Journal*, 589:783–789, June 2003.

[182] G. Hobbs, D. R. Lorimer, A. G. Lyne, and M. Kramer. A statistical study of 233 pulsar proper motions. *Monthly Notices of the Royal Astronomical Society*, 360:974–992, July 2005.

[183] E. Høg, C. Fabricius, V. V. Makarov, S. Urban, T. Corbin, G. Wycoff, U. Bastian, P. Schwekendiek, and A. Wicenec. The Tycho-2 catalogue of the 2.5 million brightest stars. *Astronomy & Astrophysics*, 355:L27–L30, March 2000.

[184] J. A. Holtzman, C. Afonso, and A. Dolphin. The Local Group Stellar Populations Archive from the Hubble Space Telescope WFPC2. *Astrophysical Journal Supplements*, 166:534–548, October 2006.

[185] J. A. Holtzman, C. J. Burrows, S. Casertano, J. J. Hester, J. T. Trauger, A. M. Watson, and G. Worthey. The Photometric Performance and Calibration of WFPC2. *Publications of the Astronomical Society of the Pacific*, 107:1065, November 1995.

[186] T. E. Holzer and W. I. Axford. The Theory of Stellar Winds and Related Flows. *Annual Review of Astronomy and Astrophysics*, 8:31, 1970.

[187] C. G. Hoopes, R. A. M. Walterbos, and B. E. Greenwalt. Diffuse Ionized Gas in Three Sculptor Group Galaxies. *Astronomical Journal*, 112:1429, October 1996.

[188] J. H. Horne and S. L. Baliunas. A prescription for period analysis of unevenly sampled time series. *Astrophysical Journal*, 302:757–763, March 1986.

[189] A. E. Hornschemeier, W. N. Brandt, G. P. Garmire, D. P. Schneider, A. J. Barger, P. S. Broos, L. L. Cowie, L. K. Townsley, M. W. Bautz, D. N. Burrows, G. Chartas, E. D. Feigelson, R. E. Griffiths, D. Lumb, J. A. Nousek, L. W. Ramsey, and W. L. W. Sargent. The Chandra Deep Survey of the Hubble Deep Field-North Area. II. Results from the Caltech Faint Field Galaxy Redshift Survey Area. *Astrophysical Journal*, 554:742–777, June 2001.

[190] A. E. Hornschemeier, T. M. Heckman, A. F. Ptak, C. A. Tremonti, and E. J. M. Colbert. Chandra-SDSS Normal and Star-Forming Galaxies. I. X-Ray Source Properties of Galaxies Detected by the Chandra X-Ray Observatory in SDSS DR2. *Astronomical Journal*, 129:86–103, January 2005.

[191] J. P. Huchra, M. J. Geller, J. Gallagher, D. Hunter, L. Hartmann, G. Fabbiano, and M. Aaronson. Star formation in blue galaxies. I - Ultraviolet, optical, and infrared observations of NGC 4214 and NGC 4670. *Astrophysical Journal*, 274:125–135, November 1983.

[192] P. J. Humphrey, W. Liu, and D. A. Buote. χ^2 and Poissonian Data: Biases Even in the High-Count Regime and How to Avoid Them. *Astrophysical Journal*, 693:822–829, March 2009.

[193] R. M. Humphreys, J. L. Prieto, P. Rosenfield, L. A. Helton, C. S. Kochanek, K. Z. Stanek, R. Khan, D. Szczygiel, K. Mogren, R. A. Fesen, D. Milisavljevic, B. Williams, J. Murphy, J. Dalcanton, and K. Gilbert. SN 2010U: A Luminous Nova in NGC 4214. *Astrophysical Journal LettersAstrophysical Journal Supplements*, 718:L43–L47, July 2010.

[194] J. R. Hurley, O. R. Pols, and C. A. Tout. Comprehensive analytic formulae for stellar evolution as a function of mass and metallicity. *Monthly Notices of the Royal Astronomical Society*, 315:543–569, July 2000.

[195] J. R. Hurley, C. A. Tout, and O. R. Pols. Evolution of binary stars and the effect of tides on binary populations. *Monthly Notices of the Royal Astronomical Society*, 329:897–928, February 2002.

[196] P. Hut. Tidal evolution in close binary systems. *Astronomy & Astrophysics*, 99:126–140, June 1981.

[197] I. Iben, Jr. and M. Livio. Common envelopes in binary star evolution. *Astronomical Society Pacific Publications*, 105:1373–1406, December 1993.

[198] I. Iben, Jr. and A. Renzini. Asymptotic giant branch evolution and beyond. *Annual Review of Astronomy and Astrophysics*, 21:271–342, 1983.

[199] S. Immler, P. Brown, and B. R. Russell. Swift XRT Detection of Supernova 2010da in X-Rays. *The Astronomer's Telegram*, 2639:1, May 2010.

[200] J. A. Irwin, J. N. Bregman, and A. E. Athey. The Lack of Very Ultraluminous X-Ray Sources in Early-Type Galaxies. *Astrophysical Journal Letters*, 601:L143–L146, February 2004.

[201] N. Isobe, K. Makishima, H. Takahashi, T. Mizuno, R. Miyawaki, P. Gandhi, M. Kawaharada, A. Senda, T. Yoshida, A. Kubota, and H. Kobori. Spectral Transitions of an Ultraluminous X-Ray Source, NGC 2403 Source 3. *Astronomical Society Japan Publications*, 61:279, January 2009.

[202] H.-T. Janka and E. Mueller. Neutrino heating, convection, and the mechanism of Type-II supernova explosions. *Astronomy & Astrophysics*, 306:167, February 1996.

[203] H.-T. Janka, B. Müller, F. S. Kitaura, and R. Buras. Dynamics of shock propagation and nucleosynthesis conditions in O-Ne-Mg core supernovae. *Astronomy & Astrophysics*, 485:199–208, July 2008.

[204] T. E. Jeltema, C. R. Canizares, D. A. Buote, and G. P. Garmire. X-Ray Source Population in the Elliptical Galaxy NGC 720 with Chandra. *Astrophysical Journal*, 585:756–766, March 2003.

[205] L. P. Jenkins, T. P. Roberts, R. S. Warwick, R. E. Kilgard, and M. J. Ward. An XMM-Newton view of M101 - I. The luminous X-ray source population. *Monthly Notices of the Royal Astronomical Society*, 349:404–424, April 2004.

[206] A. Jordán, P. Côté, M. J. West, R. O. Marzke, D. Minniti, and M. Rejkuba. Hubble Space Telescope Observations of cD Galaxies and Their Globular Cluster Systems. *Astronomical Journal*, 127:24–47, January 2004.

[207] S. Justham and K. Schawinski. Another thread in the tapestry of stellar feedback: X-ray binaries. *Monthly Notices of the Royal Astronomical Society*, 423:1641–1651, June 2012.

[208] P. M. W. Kalberla, W. B. Burton, D. Hartmann, E. M. Arnal, E. Bajaja, R. Morras, and W. G. L. Pöppel. The Leiden/Argentine/Bonn (LAB) Survey of Galactic HI. Final data release of the combined LDS and IAR surveys with improved stray-radiation corrections. *Astronomy & Astrophysics*, 440:775–782, September 2005.

[209] I. D. Karachentsev, A. E. Dolphin, D. Geisler, E. K. Grebel, P. Guhathakurta, P. W. Hodge, V. E. Karachentseva, A. Sarajedini, P. Seitzer, and M. E. Sharina. The M 81 group of galaxies: New distances, kinematics and structure. *Astronomy & Astrophysics*, 383:125–136, January 2002.

[210] I. D. Karachentsev, V. E. Karachentseva, W. K. Huchtmeier, and D. I. Makarov. A Catalog of Neighboring Galaxies. *Astronomical Journal*, 127:2031–2068, April 2004.

[211] G. Kauffmann, J. M. Colberg, A. Diaferio, and S. D. M. White. Clustering of galaxies in a hierarchical universe - II. Evolution to high redshift. *Monthly Notices of the Royal Astronomical Society*, 307:529–536, August 1999.

[212] R. Kaur, B. Paul, B. Kumar, and R. Sagar. A Study of the Long-Term Evolution of Quasi-Periodic Oscillations in the Accretion-Powered X-Ray Pulsar 4U 1626-67. *Astrophysical Journal*, 676:1184–1188, April 2008.

[213] R. C. Kennicutt, Jr. Star Formation in Galaxies Along the Hubble Sequence. *Annual Review of Astronomy and Astrophysics*, 36:189–232, 1998.

[214] R. Khan, K. Z. Stanek, C. S. Kochanek, T. A. Thompson, and J. L. Prieto. Mid-IR progenitor of SN 2010da in NGC 300. *The Astronomer's Telegram*, 2632:1, May 2010.

[215] R. E. Kilgard, J. J. Cowan, M. R. Garcia, P. Kaaret, M. I. Krauss, J. C. McDowell, A. H. Prestwich, F. A. Primini, C. J. Stockdale, G. Trinchieri, M. J. Ward, and A. Zezas. A Chandra Survey of Nearby Spiral Galaxies. I. Point Source Catalogs. *Astrophysical Journal*, 159:214–241, August 2005.

[216] R. E. Kilgard, P. Kaaret, M. I. Krauss, A. H. Prestwich, M. T. Raley, and A. Zezas. A Minisurvey of X-Ray Point Sources in Starburst and Nonstarburst Galaxies. *Astrophysical Journal*, 573:138–143, July 2002.

[217] D.-W. Kim and G. Fabbiano. Chandra X-Ray Observations of NGC 1316 (Fornax A). *Astrophysical Journal*, 586:826–849, April 2003.

[218] D.-W. Kim and G. Fabbiano. X-Ray Luminosity Function and Total Luminosity of Low-Mass X-Ray Binaries in Early-Type Galaxies. *Astrophysical Journal*, 611:846–857, August 2004.

[219] A. R. King, J. Frank, U. Kolb, and H. Ritter. Global Analysis of Mass Transfer Cycles in Cataclysmic Variables. *Astrophysical Journal*, 467:761, August 1996.

[220] F. S. Kitaura, H.-T. Janka, and W. Hillebrandt. Explosions of O-Ne-Mg cores, the Crab supernova, and subluminous type II-P supernovae. *Astronomy & Astrophysics*, 450:345–350, April 2006.

[221] T. Klähn, D. Blaschke, S. Typel, E. N. E. van Dalen, A. Faessler, C. Fuchs, T. Gaitanos, H. Grigorian, A. Ho, E. E. Kolomeitsev, M. C. Miller, G. Röpke, J. Trümper, D. N. Voskresensky, F. Weber, and H. H. Wolter. Constraints on the high-density nuclear equation of state from the phenomenology of compact stars and heavy-ion collisions. *Physical Review C*, 74(3):035802, September 2006.

[222] C. S. Kochanek, J. F. Beacom, M. D. Kistler, J. L. Prieto, K. Z. Stanek, T. A. Thompson, and H. Yüksel. A Survey About Nothing: Monitoring a Million Supergiants for Failed Supernovae. *Astrophysical Journal*, 684:1336–1342, September 2008.

[223] A. M. Koekemoer, A. S. Fruchter, R. N. Hook, and W. Hack. MultiDrizzle: An Integrated Pyraf Script for Registering, Cleaning and Combining Images. In S. Arribas, A. Koekemoer, and B. Whitmore, editors, *HST Calibration Workshop : Hubble after the Installation of the ACS and the NICMOS Cooling System*, page 337, 2003.

[224] A. K. H. Kong and R. Di Stefano. A Luminous Recurrent Supersoft X-Ray Source in NGC 300. *Astrophysical Journal Letters*, 590:L13–L16, June 2003.

[225] A. K. H. Kong, M. R. Garcia, F. A. Primini, S. S. Murray, R. Di Stefano, and J. E. McClintock. X-Ray Point Sources in the Central Region of M31 as Seen by Chandra. *Astrophysical Journal*, 577:738–756, October 2002.

[226] A. Koratkar, S. E. Deustua, T. Heckman, A. V. Filippenko, L. C. Ho, and M. Rao. Low-luminosity active galaxies: Are they similar to Seyfert galaxies? *Astrophysical Journal*, 440:132–140, February 1995.

[227] J. Kotoku, T. Mizuno, A. Kubota, and K. Makishima. ASCA Observation of Ultra-Luminous X-Ray Sources in the Nearby Spiral Galaxy NGC 2403. *Astronomical Society Japan Publications*, 52:1081–, December 2000.

[228] P. Kroupa. The Initial Mass Function of Stars: Evidence for Uniformity in Variable Systems. *Science*, 295:82–91, January 2002.

[229] J. Krtička and J. Kubát. The winds of hot massive first stars. *Astronomy & Astrophysics*, 446:1039–1049, February 2006.

[230] J. Krtička, S. P. Owocki, and G. Meynet. Mass and angular momentum loss via decretion disks. *Astronomy & Astrophysics*, 527:A84, March 2011.

[231] A. Kundu, T. J. Maccarone, and S. E. Zepf. The Low-Mass X-Ray Binary-Globular Cluster Connection in NGC 4472. *Astrophysical Journal Letters*, 574:L5–L9, July 2002.

[232] F. K. Lamb, C. J. Pethick, and D. Pines. A Model for Compact X-Ray Sources:

Accretion by Rotating Magnetic Stars. *Astrophysical Journal*, 184:271–290, August 1973.

[233] S. S. Larsen and T. Richtler. Young massive star clusters in nearby spiral galaxies. III. Correlations between cluster populations and host galaxy properties. *Astronomy & Astrophysics*, 354:836–846, February 2000.

[234] R. B. Larson. Effects of supernovae on the early evolution of galaxies. *Monthly Notices of the Royal Astronomical Society*, 169:229–246, November 1974.

[235] T. Laskar, E. Berger, and R. Chornock. Significant brightening of the progenitor of SN2010da at 3.6 micron 6 months prior to the eruption. *The Astronomer's Telegram*, 2648:1, May 2010.

[236] J.-P. Lasota, T. Alexander, G. Dubus, D. Barret, S. A. Farrell, N. Gehrels, O. Godet, and N. A. Webb. The Origin of Variability of the Intermediate-mass Black-hole ULX System HLX-1 in ESO 243-49. *Astrophysical Journal*, 735:89, July 2011.

[237] J. M. Lattimer and M. Prakash. Neutron Star Structure and the Equation of State. *Astrophysical Journal*, 550:426–442, March 2001.

[238] S. Laycock, A. Zezas, J. Hong, J. J. Drake, and V. Antoniou. Exploring the Small Magellanic Cloud to the Faintest X-ray Fluxes: Source Catalog, Timing, and Spectral Analysis. *Astrophysical Journal*, 716:1217–1240, June 2010.

[239] J. C. Lee, A. Gil de Paz, R. C. Kennicutt, Jr., M. Bothwell, J. Dalcanton, J. José G. Funes S., B. D. Johnson, S. Sakai, E. Skillman, C. Tremonti, and L. van Zee. A GALEX Ultraviolet Imaging Survey of Galaxies in the Local Volume. *Astrophysical Journal Supplements*, 192:6, January 2011.

[240] C. Leitherer, W. D. Vacca, P. S. Conti, A. V. Filippenko, C. Robert, and W. L. W. Sargent. Hubble Space Telescope Ultraviolet Imaging and Spectroscopy of the Bright Starburst in the Wolf-Rayet Galaxy NGC 4214. *Astrophysical Journal*, 465:717, July 1996.

[241] D. C. Leonard. On the progenitors of core-collapse supernovae. *Astrophysics & Space Science*, 336:117–122, November 2011.

[242] A. P. Lightman and D. M. Eardley. Black Holes in Binary Systems: Instability of Disk Accretion. *Astrophysical Journal Letters*, 187:L1, January 1974.

[243] T. Linden, V. Kalogera, J. F. Sepinsky, A. Prestwich, A. Zezas, and J. S. Gallagher. The Effect of Starburst Metallicity on Bright X-ray Binary Formation Pathways. *Astrophysical Journal*, 725:1984–1994, December 2010.

[244] T. Linden, F. Valsecchi, and V. Kalogera. On the Rarity of X-Ray Binaries with Naked Helium Donors. *Astrophysical Journal*, 748:114, April 2012.

[245] B. Link. Constraining Hadronic Superfluidity with Neutron Star Precession. *Physical Review Letters*, 91(10):101101, September 2003.

[246] P. Lira, A. Lawrence, and R. A. Johnson. Multiwavelength study of the nuclei of a volume-limited sample of galaxies - I. X-ray observations. *Monthly Notices of the Royal Astronomical Society*, 319:17–42, November 2000.

[247] Q. Z. Liu, J. van Paradijs, and E. P. J. van den Heuvel. High-mass X-ray binaries in the Magellanic Clouds. *Astronomy & Astrophysics*, 442:1135–1138, November 2005.

[248] Q. Z. Liu, J. van Paradijs, and E. P. J. van den Heuvel. Catalogue of high-mass X-ray binaries in the Galaxy (4th edition). *Astronomy & Astrophysics*, 455:1165–1168, September 2006.

[249] Q. Z. Liu, J. van Paradijs, and E. P. J. van den Heuvel. A catalogue of low-mass X-ray binaries in the Galaxy, LMC, and SMC (Fourth edition). *Astronomy & Astrophysics*, 469:807–810, July 2007.

[250] D. Lommen, L. Yungelson, E. van den Heuvel, G. Nelemans, and S. Portegies Zwart. Cygnus X-3 and the problem of the missing Wolf-Rayet X-ray binaries. *Astronomy & Astrophysics*, 443:231–241, November 2005.

[251] D. R. Lorimer, F. Camilo, and M. A. McLaughlin. Timing of pulsars found in a deep Parkes multibeam survey. *Monthly Notices of the Royal Astronomical Society*, 434:347–351, September 2013.

[252] A. J. Loveridge, M. V. van der Sluys, and V. Kalogera. Analytical Expressions for the Envelope Binding Energy of Giants as a Function of Basic Stellar Parameters. *Astrophysical Journal*, 743:49, December 2011.

[253] G.-L. Lü, C.-H. Zhu, and Z.-J. Wang. Population synthesis of high mass X-ray binaries. *Research in Astronomy and Astrophysics*, 11:327–334, March 2011.

[254] S. H. Lubow and F. H. Shu. Gas dynamics of semidetached binaries. *Astrophysical Journal*, 198:383–405, June 1975.

[255] J. W. MacKenty, J. Maíz-Apellániz, C. E. Pickens, C. A. Norman, and N. R. Walborn. Hubble Space Telescope/WFPC2 and VLA Observations of the Ionized Gas in the Dwarf Starburst Galaxy NGC 4214. *Astronomical Journal*, 120:3007–3026, December 2000.

[256] A. Maeder and G. Meynet. Massive Star Evolution with Mass Loss and Rotation. In *Revista Mexicana de Astronomia y Astrofisica Conference Series*, volume 33 of *Revista Mexicana de Astronomia y Astrofisica Conference Series*, pages 38–43, August 2008.

[257] J. Maíz-Apellániz, H. E. Bond, M. H. Siegel, Y. Lipkin, D. Maoz, E. O. Ofek, and D. Poznanski. The Progenitor of the Type II-P SN 2004dj in NGC 2403. *Astrophysical Journal Letters*, 615:L113–L116, November 2004.

[258] J. Maíz-Apellániz, L. Cieza, and J. W. MacKenty. Tip of the Red Giant Branch Distances to NGC 4214, UGC 685, and UGC 5456. *Astronomical Journal*, 123:1307–1315, March 2002.

[259] W. A. Majid, R. C. Lamb, and D. J. Macomb. X-Ray Pulsars in the Small Magellanic Cloud. *Astrophysical Journal*, 609:133–143, July 2004.

[260] K. Makishima, A. Kubota, T. Mizuno, T. Ohnishi, M. Tashiro, Y. Aruga, K. Asai, T. Dotani, K. Mitsuda, Y. Ueda, S. Uno, K. Yamaoka, K. Ebisawa, Y. Kohmura, and K. Okada. The Nature of Ultraluminous Compact X-Ray Sources in Nearby Spiral Galaxies. *Astrophysical Journal*, 535:632–643, June 2000.

[261] K. Makishima, Y. Maejima, K. Mitsuda, H. V. Bradt, R. A. Remillard, I. R. Tuohy, R. Hoshi, and M. Nakagawa. Simultaneous X-ray and optical observations of GX 339-4 in an X-ray high state. *Astrophysical Journal*, 308:635–643, September 1986.

[262] D. Maoz, A. Koratkar, J. C. Shields, L. C. Ho, A. V. Filippenko, and A. Sternberg. The Ultraviolet Spectra of LINERs: A Comparative Study. *Astronomical Journal*, 116:55–67, July 1998.

[263] D. Maoz, N. M. Nagar, H. Falcke, and A. S. Wilson. The Murmur of the Sleeping Black Hole: Detection of Nuclear Ultraviolet Variability in LINER Galaxies. *Astrophysical Journal*, 625:699–715, June 2005.

[264] A. Marek and H.-T. Janka. Delayed Neutrino-Driven Supernova Explosions Aided by the Standing Accretion-Shock Instability. *Astrophysical Journal*, 694:664–696, March 2009.

[265] B. D. Mason, W. I. Hartkopf, D. R. Gies, T. J. Henry, and J. W. Helsel. The High Angular Resolution Multiplicity of Massive Stars. *Astronomical Journal*, 137:3358–3377, February 2009.

[266] D. M. Matonick, R. A. Fesen, W. P. Blair, and K. S. Long. An Optical Search for Supernova Remnants in NGC 2403. *Astrophysical Journal Supplements*, 113:333, December 1997.

[267] R. Mayle and J. R. Wilson. Supernovae from collapse of oxygen-magnesium-neon cores. *Astrophysical Journal*, 334:909–926, November 1988.

[268] J. E. McClintock and R. A. Remillard. *Black hole binaries*, pages 157–213. April 2006.

[269] R. McCray and T. P. Snow, Jr. The violent interstellar medium. *Annual Review of Astronomy & Astrophysics*, 17:213–240, 1979.

[270] K. E. McGowan, M. J. Coe, M. P. E. Schurch, V. A. McBride, J. L. Galache, W. R. T. Edge, R. H. D. Corbet, S. Laycock, and D. A. H. Buckley. The Chandra Small Magellanic Cloud Wing Survey - the search for X-ray binaries. *Monthly Notices of the Royal Astronomical Society*, 383:330–338, January 2008.

[271] K. Menou, J.-M. Hameury, J.-P. Lasota, and R. Narayan. Disc instability models for X-ray transients: evidence for evaporation and low α-viscosity? *Monthly Notices of the Royal Astronomical Society*, 314:498–510, May 2000.

[272] S. A. Metchev and L. A. Hillenbrand. The Palomar/Keck Adaptive Optics Survey of Young Solar Analogs: Evidence for a Universal Companion Mass Function. *Astrophysical Journal Supplements*, 181:62–109, March 2009.

[273] G. R. Meurer, T. M. Heckman, C. Leitherer, A. Kinney, C. Robert, and D. R. Garnett. Starbursts and Star Clusters in the Ultraviolet. *Astronomical Journal*, 110:2665, December 1995.

[274] G. Micela, S. Sciortino, V. Kashyap, F. R. Harnden, Jr., and R. Rosner. ROSAT Observations of the Pleiades. I. X-Ray Characteristics of a Coeval Stellar Population. *Astrophysical Journal Supplements*, 102:75, January 1996.

[275] S. Mineo, M. Gilfanov, and R. Sunyaev. X-ray emission from star-forming galaxies - I. High-mass X-ray binaries. *Monthly Notices of the Royal Astronomical Society*, 419:2095–2115, January 2012.

[276] I. F. Mirabel, M. Dijkstra, P. Laurent, A. Loeb, and J. R. Pritchard. Stellar black holes at the dawn of the universe. *Astronomy & Astrophysics*, 528:A149, April 2011.

[277] A. S. Miroshnichenko, J. Fabregat, K. S. Bjorkman, D. C. Knauth, N. D. Morrison, A. E. Tarasov, P. Reig, I. Negueruela, and P. Blay. Spectroscopic observations of the δ Scorpii binary during its recent periastron passage. *Astronomy & Astrophysics*, 377:485–495, October 2001.

[278] S. Miyaji. The neutron star in 4U 1820-30 and X-ray bursts. In Y. Tanaka, editor, *Physics of Neutron Stars and Black Holes*, pages 269–272, 1988.

[279] S. Miyaji, K. Nomoto, K. Yokoi, and D. Sugimoto. Supernova Triggered by Electron Captures. *Publications of the Astronomical Society of Japan*, 32:303, 1980.

[280] M. R. Mokiem, A. de Koter, J. S. Vink, J. Puls, C. J. Evans, S. J. Smartt, P. A. Crowther, A. Herrero, N. Langer, D. J. Lennon, F. Najarro, and M. R. Villamariz. The empirical metallicity dependence of the mass-loss rate of O- and early B-type stars. *Astronomy & Astrophysics*, 473:603–614, October 2007.

[281] L. A. G. Monard. Supernova 2010da in NGC 300. *Central Bureau Electronic Telegrams*, 2289:1, May 2010.

[282] D. G. Monet, S. E. Levine, B. Canzian, H. D. Ables, A. R. Bird, C. C. Dahn, H. H. Guetter, H. C. Harris, A. A. Henden, S. K. Leggett, H. F. Levison, C. B. Luginbuhl, J. Martini, A. K. B. Monet, J. A. Munn, J. R. Pier, A. R. Rhodes, B. Riepe, S. Sell, R. C. Stone, F. J. Vrba, R. L. Walker, G. Westerhout, R. J. Brucato, I. N. Reid, W. Schoening, M. Hartley, M. A. Read, and S. B. Tritton. The USNO-B Catalog. *Astronomical Journal*, 125:984–993, February 2003.

[283] M. Moshir and et al. IRAS Faint Source Catalogue, version 2.0. In *IRAS Faint Source Catalogue, version 2.0 (1990)*, page 0, 1990.

[284] D. J. Muñoz, D. Mardones, G. Garay, D. Rebolledo, K. Brooks, and S. Bontemps. Massive Clumps in the NGC 6334 Star-forming Region. *Astrophysical Journal*, 668:906–917, October 2007.

[285] V. M. Muñoz Marín, R. M. González Delgado, H. R. Schmitt, R. Cid Fernandes, and E. Pérez. Stellar clusters in the nuclear regions of AGN with the Advanced Camera for Surveys. *Astrophysics and Space Science*, 324:253–258, December 2009.

[286] J. C. Muñoz-Mateos, A. Gil de Paz, S. Boissier, J. Zamorano, T. Jarrett, J. Gallego, and B. F. Madore. Specific Star Formation Rate Profiles in Nearby Spiral Galaxies:

Quantifying the Inside-Out Formation of Disks. *Astrophysical Journal*, 658:1006–1026, April 2007.

[287] N. M. Nagar, H. Falcke, and A. S. Wilson. Radio sources in low-luminosity active galactic nuclei. IV. Radio luminosity function, importance of jet power, and radio properties of the complete Palomar sample. *Astronomy & Astrophysics*, 435:521–543, May 2005.

[288] F. Nagase. Accretion-powered X-ray pulsars. *Publications of the Astronomical Society of Japan*, 41:1–79, 1989.

[289] S. Nakano and K. Itagaki. Supernova 2004dj in NGC 2403. *Central Bureau Electronic Telegrams*, 74:1, August 2004.

[290] K. Nandra, E. S. Laird, K. Adelberger, J. P. Gardner, R. F. Mushotzky, J. Rhodes, C. C. Steidel, H. I. Teplitz, and K. A. Arnaud. A deep Chandra survey of the Groth Strip - I. The X-ray data. *Monthly Notices of the Royal Astronomical Society*, 356:568–586, January 2005.

[291] R. Narayan and I. Yi. Advection-dominated Accretion: Underfed Black Holes and Neutron Stars. *Astrophysical Journal*, 452:710, October 1995.

[292] I. Negueruela, A. T. Okazaki, J. Fabregat, M. J. Coe, U. Munari, and T. Tomov. The Be/X-ray transient 4U 0115+63/V635 Cassiopeiae. II. Outburst mechanisms. *Astronomy & Astrophysics*, 369:117–131, April 2001.

[293] K. Nomoto. Evolutionary models of the Crab Nebula's progenitor. In M. C. Kafatos and R. B. C. Henry, editors, *The Crab Nebula and Related Supernova Remnants*, pages 97–113, 1985.

[294] K. Nomoto and M. Hashimoto. Presupernova evolution of massive stars. *Physics Reports*, 163:13–36, 1988.

[295] K. Nomoto, D. Sugimoto, W. M. Sparks, R. A. Fesen, T. R. Gull, and S. Miyaji. The Crab Nebula's progenitor. *Nature*, 299:803–805, October 1982.

[296] J. Nordhaus, A. Burrows, A. Almgren, and J. Bell. Dimension as a Key to the Neutrino Mechanism of Core-collapse Supernova Explosions. *Astrophysical Journal*, 720:694–703, September 2010.

[297] I. D. Novikov and Y. B. Zel'dovich. Physical Processes Near Cosmological Singularities. *Annual Review of Astronomy and Astrophysics*, 11:387, 1973.

[298] M. A. Nowak, J. Wilms, W. A. Heindl, K. Pottschmidt, J. B. Dove, and M. C. Begelman. A good long look at the black hole candidates LMC X-1 and LMC X-3. *Monthly Notices of the Royal Astronomical Society*, 320:316–326, January 2001.

[299] K. A. G. Olsen, B. W. Miller, N. B. Suntzeff, R. A. Schommer, and J. Bright. The Globular Cluster Systems of the Sculptor Group. *Astronomical Journal*, 127:2674–2693, May 2004.

[300] E. Olsson, S. Aalto, M. Thomasson, R. Beswick, and S. Hüttemeister. NGC 5218 - a starburst driven LINER galaxy? High resolution CO, radio continuum and H i-absorption. *Astronomy & Astrophysics*, 473:389–398, October 2007.

[301] J. A. Orosz. Inventory of black hole binaries. In K. van der Hucht, A. Herrero, and C. Esteban, editors, *A Massive Star Odyssey: From Main Sequence to Supernova*, volume 212 of *IAU Symposium*, page 365, 2003.

[302] J. Ostriker. Compact X-ray Sources. In *Bulletin of the American Astronomical Society*, volume 8 of *Bulletin of the American Astronomical Society*, page 438, June 1976.

[303] B. Otte and R.-J. Dettmar. Long slit spectroscopy of diffuse ionized gas in NGC 55. *Astronomy & Astrophysics*, 343:705–712, March 1999.

[304] S. P. Owocki and A. ud-Doula. The Effect of Magnetic Field Tilt and Divergence on the Mass Flux and Flow Speed in a Line-driven Stellar Wind. *Astrophysical Journal*, 600:1004–1015, January 2004.

[305] B. Paczynski. Common Envelope Binaries. In P. Eggleton, S. Mitton, and J. Whe-

lan, editors, *Structure and Evolution of Close Binary Systems*, volume 73 of *IAU Symposium*, page 75, 1976.

[306] M. W. Pakull and L. Mirioni. Counterparts of Super-Eddington X-Ray Sources in Nearby Galaxies. In E. R. Schielicke, editor, *Astronomische Gesellschaft Meeting Abstracts*, volume 18 of *Astronomische Gesellschaft Meeting Abstracts*, page 112, 2001.

[307] M. W. Pakull and L. Mirioni. Bubble Nebulae around Ultraluminous X-Ray Sources. In J. Arthur and W. J. Henney, editors, *Revista Mexicana de Astronomia y Astrofisica Conference Series*, volume 15 of *Revista Mexicana de Astronomia y Astrofisica, vol. 27*, pages 197–199, January 2003.

[308] T. Park, V. L. Kashyap, A. Siemiginowska, D. A. van Dyk, A. Zezas, C. Heinke, and B. J. Wargelin. Bayesian Estimation of Hardness Ratios: Modeling and Computations. *Astrophysical Journal*, 652:610–628, November 2006.

[309] B. Paul and S. Naik. Transient High Mass X-ray Binaries. *Bulletin of the Astronomical Society of India*, 39:429–449, September 2011.

[310] K. J. Pearson, R. I. Hynes, D. Steeghs, P. G. Jonker, C. A. Haswell, A. R. King, K. O'Brien, G. Nelemans, and M. Méndez. Multiwavelength Observations of EXO 0748-676. II. Emission-Line Behavior. *Astrophysical Journal*, 648:1169–1180, September 2006.

[311] B. M. Peterson, M. C. Bentz, L.-B. Desroches, A. V. Filippenko, L. C. Ho, S. Kaspi, A. Laor, D. Maoz, E. C. Moran, R. W. Pogge, and A. C. Quillen. Multiwavelength Monitoring of the Dwarf Seyfert 1 Galaxy NGC 4395. I. A Reverberation-based Measurement of the Black Hole Mass. *Astrophysical Journal*, 632:799–808, October 2005.

[312] A. Pickles and É. Depagne. All-Sky Spectrally Matched UBVRI-ZY and u'g'r'i'z' Magnitudes for Stars in the Tycho2 Catalog. *Publications of the Astronomical Society of the Pacific*, 122:1437–1464, December 2010.

[313] W. Pietsch, F. Haberl, M. Sasaki, T. J. Gaetz, P. P. Plucinsky, P. Ghavamian, K. S.

Long, and T. G. Pannuti. M33 X-7: ChASeM33 Reveals the First Eclipsing Black Hole X-Ray Binary. *Astrophysical Journal*, 646:420–428, July 2006.

[314] T. Piran. Gamma-Ray Bursts as Probes for Quantum Gravity. In J. Kowalski-Glikman and G. Amelino-Camelia, editors, *Lecture Notes in Physics, Berlin Springer Verlag*, volume 669 of *Lecture Notes in Physics, Berlin Springer Verlag*, page 351, 2005.

[315] H. Plana, J. Boulesteix, P. Amram, C. Carignan, and C. Mendes de Oliveira. Extended ionized gas in elliptical galaxies. II. Velocity and monochromatic maps of 11 elliptical and lenticular galaxies. *Astronomy & Astrophysicss*, 128:75–109, February 1998.

[316] P. P. Plucinsky, B. Williams, K. S. Long, T. J. Gaetz, M. Sasaki, W. Pietsch, R. Tüllmann, R. K. Smith, W. P. Blair, D. Helfand, J. P. Hughes, P. F. Winkler, M. de Avillez, L. Bianchi, D. Breitschwerdt, R. J. Edgar, P. Ghavamian, J. Grindlay, F. Haberl, R. Kirshner, K. Kuntz, T. Mazeh, T. G. Pannuti, A. Shporer, and D. A. Thilker. Chandra ACIS Survey of M33 (ChASeM33): A First Look. *Astrophysical Journal*, 174:366–378, February 2008.

[317] A. J. T. Poelarends, F. Herwig, N. Langer, and A. Heger. The Supernova Channel of Super-AGB Stars. *Astrophysical Journal*, 675:614–625, March 2008.

[318] R. W. Pogge, D. Maoz, L. C. Ho, and M. Eracleous. The Narrow-Line Regions of LINERS as Resolved with the Hubble Space Telescope. *Astrophysical Journal*, 532:323–339, March 2000.

[319] A. M. T. Pollock. The Einstein view of the Wolf-Rayet stars. *Astrophysical Journal*, 320:283–295, September 1987.

[320] J. Poutanen and A. C. Fabian. Spectral evolution of magnetic flares and time lags in accreting black hole sources. *Monthly Notices of the Royal Astronomical Society*, 306:L31–L37, July 1999.

[321] C. Power, G. James, C. Combet, and G. Wynn. Feedback from High-mass X-Ray

Binaries on the High-redshift Intergalactic Medium: Model Spectra. *Astrophysical Journal*, 764:76, February 2013.

[322] A. H. Prestwich, J. A. Irwin, R. E. Kilgard, M. I. Krauss, A. Zezas, F. Primini, P. Kaaret, and B. Boroson. Classifying X-Ray Sources in External Galaxies from X-Ray Colors. *Astrophysical Journal*, 595:719–726, October 2003.

[323] A. H. Prestwich, R. E. Kilgard, F. Primini, J. C. McDowell, and A. Zezas. The Luminosity Function of X-ray Sources in Spiral Galaxies. *Astrophysical Journal*, 705:1632–1636, November 2009.

[324] J. L. Prieto, H. E. Bond, C. S. Kochanek, R. Khan, K. Z. Stanek, and T. A. Thompson. Optical and Near-IR Follow-up of SN 2010da: Evidence for Warm Dust. *The Astronomer's Telegram*, 2660:1, June 2010.

[325] J. E. Pringle and M. J. Rees. Accretion Disc Models for Compact X-Ray Sources. *Astronomy & Astrophysics*, 21:1, October 1972.

[326] C. F. Prosser, S. Randich, J. R. Stauffer, J. H. M. M. Schmitt, and T. Simon. ROSAT Pointed Observations of the Alpha Persei Cluster. *Astronomical Journal*, 112:1570, October 1996.

[327] D. Puche, C. Carignan, and A. Bosma. H I studies of the Sculptor group galaxies. VI - NGC 300. *Astronomical Journal*, 100:1468–1476, November 1990.

[328] D. Puche, C. Carignan, and R. J. Wainscoat. H I studies of the Sculptor group galaxies. III - NGC 55. *Astronomical Journal*, 101:447–455, February 1991.

[329] J. Puls, U. Springmann, and M. Lennon. Radiation driven winds of hot luminous stars. XIV. Line statistics and radiative driving. *Astronomy & Astrophysics Supplements*, 141:23–64, January 2000.

[330] J. Puls, J. S. Vink, and F. Najarro. Mass loss from hot massive stars. *Astronomy & Astrophysicsr*, 16:209–325, December 2008.

[331] M. L. Pumo, M. Turatto, M. T. Botticella, A. Pastorello, S. Valenti, L. Zampieri, S. Benetti, E. Cappellaro, and F. Patat. EC-SNe from Super-Asymptotic Giant Branch Progenitors: Theoretical Models Versus Observations. *Astrophysical Journal Letters*, 705:L138–L142, November 2009.

[332] A. C. Quillen and J. Bland-Hawthorn. When is star formation episodic? A delay differential equation 'negative feedback' model. *Monthly Notices of the Royal Astronomical Society*, 386:2227–2234, June 2008.

[333] N. V. Raguzova and S. B. Popov. Be X-ray binaries and candidates. *Astronomical and Astrophysical Transactions*, 24:151–185, June 2005.

[334] F. A. Rasio and M. Livio. On the Formation and Evolution of Common Envelope Systems. *Astrophysical Journal*, 471:366, November 1996.

[335] S. Ravindranath, L. C. Ho, C. Y. Peng, A. V. Filippenko, and W. L. W. Sargent. Central Structural Parameters of Early-Type Galaxies as Viewed with Nicmos on the Hubble Space Telescope. *Astronomical Journal*, 122:653–678, August 2001.

[336] A. M. Read and W. Pietsch. X-ray emission from the Sculptor galaxy NGC 300. *Astronomy & Astrophysics*, 373:473–484, July 2001.

[337] A. M. Read, T. J. Ponman, and D. K. Strickland. ROSAT PSPC observations of nearby spiral galaxies - I. The data. *Monthly Notices of the Royal Astronomical Society*, 286:626–668, April 1997.

[338] M. J. Rees, M. C. Begelman, R. D. Blandford, and E. S. Phinney. Ion-supported tori and the origin of radio jets. *Nature*, 295:17–21, January 1982.

[339] M. M. Reggiani and M. R. Meyer. Binary Formation Mechanisms: Constraints from the Companion Mass Ratio Distribution. *Astrophysical Journal*, 738:60, September 2011.

[340] P. Reig. Rapid spectral and timing variability of Be/X-ray binaries during type ;II outbursts. *Astronomy & Astrophysics*, 489:725–740, October 2008.

[341] P. Reig. Be/X-ray binaries. *Astrophysics and Space Science*, 332:1–29, March 2011.

[342] D. Reimers and D. Koester. Spectroscopic identification of white dwarfs in galactic clusters. IV - NGC 2168. *Astronomy & Astrophysics*, 202:77–80, August 1988.

[343] R. A. Remillard, M. P. Muno, J. E. McClintock, and J. A. Orosz. Evidence for Harmonic Relationships in the High-Frequency Quasi-periodic Oscillations of XTE J1550-564 and GRO J1655-40. *Astrophysical Journal*, 580:1030–1042, December 2002.

[344] M. Revnivtsev, K. Postnov, A. Kuranov, and H. Ritter. On the nature of the break in the X-ray luminosity function of low-mass X-ray binaries. *Astronomy & Astrophysics*, 526:A94, February 2011.

[345] P. M. Ricker and R. E. Taam. The Interaction of Stellar Objects within a Common Envelope. *Astrophysical Journal Letters*, 672:L41–L44, January 2008.

[346] B. J. Robinson and K. J. van Damme. 21 cm observations of NGC 55. *Australian Journal of Physics*, 19:111, February 1966.

[347] J. Rodriguez, J. A. Tomsick, and A. Bodaghee. Swift follow-up observations of 13 INTEGRAL sources. *Astronomy & Astrophysics*, 517:A14, July 2010.

[348] J. Rodriguez, J. A. Tomsick, and S. Chaty. Swift follow-up observations of 17 INTEGRAL sources of uncertain or unknown nature. *Astronomy & Astrophysics*, 494:417–428, January 2009.

[349] P. Romano, V. La Parola, S. Vercellone, G. Cusumano, L. Sidoli, H. A. Krimm, C. Pagani, P. Esposito, E. A. Hoversten, J. A. Kennea, K. L. Page, D. N. Burrows, and N. Gehrels. Two years of monitoring supergiant fast X-ray transients with Swift. *Monthly Notices of the Royal Astronomical Society*, 410:1825–1836, January 2011.

[350] D. Rosa-González, E. Terlevich, and R. Terlevich. An empirical calibration of star formation rate estimators. *Monthly Notices of the Royal Astronomical Society*, 332:283–295, May 2002.

[351] M. F. Ryba and J. H. Taylor. High-precision timing of millisecond pulsars. I - Astrometry and masses of the PSR 1855 + 09 system. *Astrophysical Journal*, 371:739–748, April 1991.

[352] E. E. Salpeter. The Luminosity Function and Stellar Evolution. *Astrophysical Journal*, 121:161, January 1955.

[353] E. L. Sandquist, R. E. Taam, and A. Burkert. On the Formation of Helium Double Degenerate Stars and Pre-Cataclysmic Variables. *Astrophysical Journal*, 533:984–997, April 2000.

[354] C. L. Sarazin, J. A. Irwin, and J. N. Bregman. Resolving the Mystery of X-Ray-faint Elliptical Galaxies: Chandra X-Ray Observations of NGC 4697. *Astrophysical Journal Letters*, 544:L101–L105, December 2000.

[355] W. L. W. Sargent and A. V. Filippenko. Luminous clusters of Wolf-Rayet stars in the SBmIII galaxy NGC 4214. *Astronomical Journal*, 102:107–112, July 1991.

[356] S. Satyapal, R. M. Sambruna, and R. P. Dudik. A joint mid-infrared spectroscopic and X-ray imaging investigation of LINER galaxies. *Astronomy & Astrophysics*, 414:825–838, February 2004.

[357] S. Sazonov, M. Revnivtsev, M. Gilfanov, E. Churazov, and R. Sunyaev. X-ray luminosity function of faint point sources in the Milky Way. *Astronomy & Astrophysics*, 450:117–128, April 2006.

[358] L. Scheck, H.-T. Janka, T. Foglizzo, and K. Kifonidis. Multidimensional supernova simulations with approximative neutrino transport. II. Convection and the advective-acoustic cycle in the supernova core. *Astronomy & Astrophysics*, 477:931–952, January 2008.

[359] D. J. Schlegel, D. P. Finkbeiner, and M. Davis. Maps of Dust Infrared Emission for Use in Estimation of Reddening and Cosmic Microwave Background Radiation Foregrounds. *Astrophysical Journal*, 500:525, June 1998.

[360] E. M. Schlegel, P. Barrett, and K. P. Singh. A ROSAT PSPC Study of NGC 55. *Astronomical Journal*, 113:1296–1309, April 1997.

[361] E. M. Schlegel and T. G. Pannuti. Chandra-detected X-Ray Sources in the Nearby Spiral Scd Galaxy NGC 2403. *Astronomical Journal*, 125:3025–3036, June 2003.

[362] K.-H. Schmidt and T. Boller. Nearby galaxies. 3: Gas-to-dust ratio in the interstellar medium of spiral and dwarf irregular galaxies. *Astronomische Nachrichten*, 314:361–370, September 1993.

[363] A. C. Seth, M. Cappellari, N. Neumayer, N. Caldwell, N. Bastian, K. Olsen, R. D. Blum, V. P. Debattista, R. McDermid, T. Puzia, and A. Stephens. The NGC 404 Nucleus: Star Cluster and Possible Intermediate-mass Black Hole. *Astrophysical Journal*, 714:713–731, May 2010.

[364] A. C. Seth, J. J. Dalcanton, and R. S. de Jong. A Study of Edge-On Galaxies with the Hubble Space Telescope Advanced Camera for Surveys. II. Vertical Distribution of the Resolved Stellar Population. *Astronomical Journal*, 130:1574–1592, October 2005.

[365] V. Sguera, E. J. Barlow, A. J. Bird, D. J. Clark, A. J. Dean, A. B. Hill, L. Moran, S. E. Shaw, D. R. Willis, A. Bazzano, P. Ubertini, and A. Malizia. INTEGRAL observations of recurrent fast X-ray transient sources. *Astronomy & Astrophysics*, 444:221–231, December 2005.

[366] N. Shakura, K. Postnov, A. Kochetkova, and L. Hjalmarsdotter. Theory of quasi-spherical accretion in X-ray pulsars. *Monthly Notices of the Royal Astronomical Society*, 420:216–236, February 2012.

[367] N. I. Shakura and R. A. Sunyaev. Black holes in binary systems. Observational appearance. *Astronomy & Astrophysics*, 24:337–355, 1973.

[368] S. L. Shapiro, S. A. Teukolsky, and I. Wasserman. Implications of the millisecond pulsar for neutron star models. *Astrophysical Journal*, 272:702–707, September 1983.

[369] N. Shaposhnikov and L. Titarchuk. Comprehensive Analysis of RXTE Data from Cygnus X-1: Spectral Index-Quasi-Periodic Oscillation Frequency-Luminosity Correlations. *Astrophysical Journal*, 643:1098–1113, June 2006.

[370] O. Shemmer, W. N. Brandt, H. Netzer, R. Maiolino, and S. Kaspi. The Hard X-Ray Spectral Slope as an Accretion Rate Indicator in Radio-quiet Active Galactic Nuclei. *Astrophysical Journal Letters*, 646:L29–L32, July 2006.

[371] G. A. Shields, C. F. McKee, D. N. C. Lin, and M. C. Begelman. Compton-heated winds and coronae above accretion disks. II - Instability and oscillations. *Astrophysical Journal*, 306:90–106, July 1986.

[372] I. S. Shklovsky. On the Nature of the Source of X-Ray Emission of SCO XR-1. *Astrophysical Journal Letters*, 148:L1, April 1967.

[373] C. R. Shrader and L. Titarchuk. A Method for Black Hole Mass Determination in Accretion-powered X-Ray Sources. *Astrophysical Journal*, 598:168–177, November 2003.

[374] P. Shtykovskiy and M. Gilfanov. High-mass X-ray binaries in the Small Magellanic Cloud: the luminosity function. *Monthly Notices of the Royal Astronomical Society*, 362:879–890, September 2005.

[375] P. E. Shtykovskiy and M. R. Gilfanov. High-mass X-ray binaries and recent star formation history of the Small Magellanic Cloud. *Astronomy Letters*, 33:437–454, July 2007.

[376] L. Sidoli. Supergiant Fast X-ray Transients as transient sources in High Mass X-ray Binaries. *ArXiv e-prints*, November 2011.

[377] L. Sidoli, P. Romano, L. Ducci, A. Paizis, G. Cusumano, V. Mangano, H. A. Krimm, S. Vercellone, D. N. Burrows, J. A. Kennea, and N. Gehrels. Supergiant Fast X-ray Transients in outburst: new Swift observations of XTE J1739-302, IGR J17544-2619 and IGR J08408-4503. *Monthly Notices of the Royal Astronomical Society*, 397:1528–1538, August 2009.

[378] L. Siess. Evolution of massive AGB stars. II. model properties at non-solar metallicity and the fate of Super-AGB stars. *Astronomy & Astrophysics*, 476:893–909, December 2007.

[379] M. Sirianni, M. J. Jee, N. Benítez, J. P. Blakeslee, A. R. Martel, G. Meurer, M. Clampin, G. De Marchi, H. C. Ford, R. Gilliland, G. F. Hartig, G. D. Illingworth, J. Mack, and W. J. McCann. The Photometric Performance and Calibration of the Hubble Space Telescope Advanced Camera for Surveys. *Publications of the Astronomical Society of the Pacific*, 117:1049–1112, October 2005.

[380] S. L. Skinner, S. A. Zhekov, M. Güdel, W. Schmutz, and K. R. Sokal. New X-Ray Detections of WNL Stars. *Astronomical Journal*, 143:116, May 2012.

[381] M. F. Skrutskie, R. M. Cutri, R. Stiening, M. D. Weinberg, S. Schneider, J. M. Carpenter, C. Beichman, R. Capps, T. Chester, J. Elias, J. Huchra, J. Liebert, C. Lonsdale, D. G. Monet, S. Price, P. Seitzer, T. Jarrett, J. D. Kirkpatrick, J. E. Gizis, E. Howard, T. Evans, J. Fowler, L. Fullmer, R. Hurt, R. Light, E. L. Kopan, K. A. Marsh, H. L. McCallon, R. Tam, S. Van Dyk, and S. Wheelock. The Two Micron All Sky Survey (2MASS). *Astronomical Journal*, 131:1163–1183, February 2006.

[382] R. K. Smith, N. S. Brickhouse, D. A. Liedahl, and J. C. Raymond. Collisional Plasma Models with APEC/APED: Emission-Line Diagnostics of Hydrogen-like and Helium-like Ions. *Astrophysical Journal Letters*, 556:L91–L95, August 2001.

[383] R. Soria and A. K. H. Kong. XMM-Newton Observations of the Spiral Galaxy M74 (NGC 628). *Astrophysical Journal Letters*, 572:L33–L37, June 2002.

[384] R. Soria, M. W. Pakull, J. W. Broderick, S. Corbel, and C. Motch. Radio lobes and X-ray hotspots in the microquasar S26. *Monthly Notices of the Royal Astronomical Society*, 409:541–551, December 2010.

[385] R. Soria, G. Risaliti, M. Elvis, G. Fabbiano, S. Bianchi, and Z. Kuncic. The XMM-NEWTON Long Look of NGC 1365: Lack of a High/Soft State in its Ultraluminous X-Ray Sources. *Astrophysical Journal*, 695:1614–1622, April 2009.

[386] L. Spitzer, Jr. Theories of the hot interstellar gas. *Annual Review of Astronomy & Astrophysics*, 28:71–101, 1990.

[387] A. W. Steiner, J. M. Lattimer, and E. F. Brown. The Equation of State from Observed Masses and Radii of Neutron Stars. *Astrophysical Journal*, 722:33–54, October 2010.

[388] J. F. Steiner, R. C. Reis, A. C. Fabian, R. A. Remillard, J. E. McClintock, L. Gou, R. Cooke, L. W. Brenneman, and J. S. Sanders. A broad iron line in LMC X-1. *Monthly Notices of the Royal Astronomical Society*, 427:2552–2561, December 2012.

[389] M. D. Still, H. Quaintrell, P. D. Roche, and A. P. Reynolds. Spectral signatures of reprocessing on the companion and accretion disc of Hercules X-1. *Monthly Notices of the Royal Astronomical Society*, 292:52, November 1997.

[390] A.-M. Stobbart, T. P. Roberts, and R. S. Warwick. A dipping black hole X-ray binary candidate in NGC 55. *Monthly Notices of the Royal Astronomical Society*, 351:1063–1070, July 2004.

[391] A.-M. Stobbart, T. P. Roberts, and R. S. Warwick. The X-ray properties of the dwarf Magellanic-type galaxy NGC 55. *Monthly Notices of the Royal Astronomical Society*, 370:25–42, July 2006.

[392] A.-M. Stobbart, T. P. Roberts, and J. Wilms. XMM-Newton observations of the brightest ultraluminous X-ray sources. *Monthly Notices of the Royal Astronomical Society*, 368:397–413, May 2006.

[393] R. A. Sunyaev, B. M. Tinsley, and D. L. Meier. Observable properties of primeval giant elliptical galaxies or ten million Orions at high redshift. *Comments on Astrophysics*, 7:183–195, 1978.

[394] D. A. Swartz, K. K. Ghosh, A. F. Tennant, and K. Wu. The Ultraluminous X-Ray Source Population from the Chandra Archive of Galaxies. *Astrophysical Journal Supplements*, 154:519–539, October 2004.

[395] R. E. Taam and P. M. Ricker. Common Envelope Evolution. *ArXiv Astrophysics e-prints*, November 2006.

[396] R. E. Taam and E. L. Sandquist. Common Envelope Evolution of Massive Binary Stars. *Annual Review of Astronomy & Astrophysics*, 38:113–141, 2000.

[397] T. Takiwaki and K. Kotake. Gravitational Wave Signatures of Magnetohydrodynamically Driven Core-collapse Supernova Explosions. *Astrophysical Journal*, 743:30, December 2011.

[398] Y. Terashima, L. C. Ho, and A. F. Ptak. Hard X-Ray Emission and the Ionizing Source in LINERS. *Astrophysical Journal*, 539:161–165, August 2000.

[399] Y. Terashima, N. Iyomoto, L. C. Ho, and A. F. Ptak. X-Ray Properties of LINERs and Low-Luminosity Seyfert Galaxies Observed with ASCA. I. Observations and Results. *Astrophysical Journal Supplements*, 139:1–36, March 2002.

[400] D. A. Thilker, L. Bianchi, D. Schiminovich, A. Gil de Paz, M. Seibert, B. F. Madore, T. Wyder, R. M. Rich, S. Yi, T. Barlow, T. Conrow, K. Forster, P. Friedman, C. Martin, P. Morrissey, S. Neff, and T. Small. NGC 404: A Rejuvenated Lenticular Galaxy on a Merger-induced, Blueward Excursion Into the Green Valley. *Astrophysical Journal*, 714:L171–L175, May 2010.

[401] S. E. Thorsett and D. Chakrabarty. Neutron Star Mass Measurements. I. Radio Pulsars. *Astrophysical Journal*, 512:288–299, February 1999.

[402] N. A. Tikhonov, O. A. Galazutdinova, and I. O. Drozdovsky. Thick disks and halos of spiral galaxies M 81, NGC 55 and NGC 300. *Astronomy & Astrophysics*, 431:127–142, February 2005.

[403] C. A. Tremonti, D. Calzetti, C. Leitherer, and T. M. Heckman. Star Formation in the Field and Clusters of NGC 5253. *Astrophysical Journal*, 555:322–337, July 2001.

[404] C. A. Tremonti, T. M. Heckman, G. Kauffmann, J. Brinchmann, S. Charlot, S. D. M. White, M. Seibert, E. W. Peng, D. J. Schlegel, A. Uomoto, M. Fukugita, and

J. Brinkmann. The Origin of the Mass-Metallicity Relation: Insights from 53,000 Star-forming Galaxies in the Sloan Digital Sky Survey. *Astrophysical Journal*, 613:898–913, October 2004.

[405] S. Trudolyubov and W. Priedhorsky. M31 Globular Cluster X-Ray Sources: XMM-Newton and Chandra Results. *Astrophysical Journal*, 616:821–844, December 2004.

[406] S. P. Trudolyubov, K. N. Borozdin, W. C. Priedhorsky, K. O. Mason, and F. A. Cordova. On the X-Ray Source Luminosity Distributions in the Bulge and Disk of M31: First Results from the XMM-Newton Survey. *Astrophysical Journal Letters*, 571:L17–L21, May 2002.

[407] R. Tüllmann, T. J. Gaetz, P. P. Plucinsky, K. D. Kuntz, B. F. Williams, W. Pietsch, F. Haberl, K. S. Long, W. P. Blair, M. Sasaki, P. F. Winkler, P. Challis, T. G. Pannuti, R. J. Edgar, D. J. Helfand, J. P. Hughes, R. P. Kirshner, T. Mazeh, and A. Shporer. The Chandra ACIS Survey of M33 (ChASeM33): The Final Source Catalog. *Astrophysical Journal*, 193:31–+, April 2011.

[408] R. Tüllmann and M. R. Rosa. An unusual high-ionization nebula in ¡ASTROBJ¿NGC 55¡/ASTROBJ¿. *Astronomy & Astrophysics*, 416:243–250, March 2004.

[409] R. Tüllmann, M. R. Rosa, T. Elwert, D. J. Bomans, A. M. N. Ferguson, and R.-J. Dettmar. Star formation in gaseous galaxy halos. VLT-spectroscopy of extraplanar H II-regions in ¡ASTROBJ¿NGC 55¡/ASTROBJ¿. *Astronomy & Astrophysics*, 412:69–80, December 2003.

[410] A. Tutukov and L. Yungelson. Evolution of close binaries and wolf-rayet stars. *Nauchnye Informatsii*, 27:58, 1973.

[411] L. Úbeda, J. Maíz-Apellániz, and J. W. MacKenty. The Young Stellar Population of NGC 4214 as Observed with the Hubble Space Telescope. I. Data and Methods. *Astronomical Journal*, 133:917–931, March 2007.

[412] L. Úbeda, J. Maíz-Apellániz, and J. W. MacKenty. The Young Stellar Population of

NGC 4214 as Observed with the Hubble Space Telescope. II. Results. *Astronomical Journal*, 133:932–951, March 2007.

[413] M. A. Urbaneja, A. Herrero, F. Bresolin, R.-P. Kudritzki, W. Gieren, J. Puls, N. Przybilla, F. Najarro, and G. Pietrzyński. On the α-Element Abundance Gradients in the Disk of the Sculptor Spiral Galaxy NGC 300. *Astrophysical Journal*, 622:862–877, April 2005.

[414] A. K. F. Val Baker, A. J. Norton, and H. Quaintrell. The mass of the neutron star in SMC X-1. *Astronomy & Astrophysics*, 441:685–688, October 2005.

[415] F. Valsecchi, E. Glebbeek, W. M. Farr, T. Fragos, B. Willems, J. A. Orosz, J. Liu, and V. Kalogera. Formation of the black-hole binary M33 X-7 through mass exchange in a tight massive system. *Nature*, 468:77–79, November 2010.

[416] J. Van Bever and D. Vanbeveren. Hard X-rays emitted by starbursts as predicted by population synthesis models including a realistic fraction of interacting binaries. *Astronomy & Astrophysics*, 358:462–470, June 2000.

[417] E. P. J. van den Heuvel. Quasi-Conservative Evolution - Formation of the Massive X-Ray Binaries. In W. H. G. Lewin and E. P. J. van den Heuvel, editors, *Accretion-Driven Stellar X-ray Sources*, page 316, 1983.

[418] E. P. J. van den Heuvel. Information on Stellar Black Hole Formation Derived from X-ray Binaries and Gamma Ray Bursts. In P. Podsiadlowski, S. Rappaport, A. R. King, F. D'Antona, and L. Burderi, editors, *Evolution of Binary and Multiple Star Systems*, volume 229 of *Astronomical Society of the Pacific Conference Series*, page 525, 2001.

[419] E. P. J. van den Heuvel and J. Heise. Centaurus X-3, Possible Reactivation of an Old Neutron Star by Mass Exchange in a Close Binary. *Nature Physical Science*, 239:67–69, October 1972.

[420] M. van der Klis. Similarities in neutron star and black hole accretion. *Astrophysical Journal Supplements*, 92:511–519, June 1994.

[421] M. van der Klis. Quasi-periodic Oscillations and Noise in Accreting Black Holes and Low-Magnetic Field Neutron Stars. In J. Greiner, H. W. Duerbeck, and R. E. Gershberg, editors, *IAU Colloq. 151: Flares and Flashes*, volume 454 of *Lecture Notes in Physics, Berlin Springer Verlag*, page 321, 1995.

[422] M. H. van Kerkwijk, P. A. Charles, T. R. Geballe, D. L. King, G. K. Miley, L. A. Molnar, E. P. J. van den Heuvel, M. van der Klis, and J. van Paradijs. Infrared helium emission lines from Cygnus X-3 suggesting a Wolf-Rayet star companion. *Nature*, 355:703–705, February 1992.

[423] J. van Paradijs. On the Accretion Instability in Soft X-Ray Transients. *Astrophysical Journal Letters*, 464:L139, June 1996.

[424] S. Vaughan, R. Edelson, R. S. Warwick, and P. Uttley. On characterizing the variability properties of X-ray light curves from active galaxies. *Monthly Notices of the Royal Astronomical Society*, 345:1271–1284, November 2003.

[425] F. Verbunt. Origin and evolution of X-ray binaries and binary radio pulsars. *Annual Review of Astronomy & Astrophysics*, 31:93–127, 1993.

[426] F. Vignarca, S. Migliari, T. Belloni, D. Psaltis, and M. van der Klis. Tracing the power-law component in the energy spectrum of black hole candidates as a function of the QPO frequency. *Astronomy & Astrophysics*, 397:729–738, January 2003.

[427] J. Vinkó, K. Takáts, K. Sárneczky, G. M. Szabó, S. Mészáros, R. Csorvási, T. Szalai, A. Gáspár, A. Pál, S. Csizmadia, A. Kóspál, M. Rácz, M. Kun, B. Csák, G. Fürész, H. DeBond, J. Grunhut, J. Thomson, S. Mochnacki, and T. Koktay. The first year of SN 2004dj in NGC 2403. *Monthly Notices of the Royal Astronomical Society*, 369:1780–1796, July 2006.

[428] R. Voss and M. Gilfanov. A study of the population of LMXBs in the bulge of M 31. *Astronomy & AstrophysicsAstronomical Journal*, 468:49–59, June 2007.

[429] R. Walter, J. Zurita Heras, L. Bassani, A. Bazzano, A. Bodaghee, A. Dean, P. Dubath, A. N. Parmar, M. Renaud, and P. Ubertini. XMM-Newton and INTEGRAL

observations of new absorbed supergiant high-mass X-ray binaries. *Astronomy & Astrophysics*, 453:133–143, July 2006.

[430] S. Wanajo, M. Tamamura, N. Itoh, K. Nomoto, Y. Ishimaru, T. C. Beers, and S. Nozawa. The r-Process in Supernova Explosions from the Collapse of O-Ne-Mg Cores. *Astrophysical Journal*, 593:968–979, August 2003.

[431] J.-M. Wang, K.-Y. Watarai, and S. Mineshige. The Hot Disk Corona and Magnetic Turbulence in Radio-quiet Active Galactic Nuclei: Observational Constraints. *Astrophysical Journal Letters*, 607:L107–L110, June 2004.

[432] Q. Wang and D. J. Helfand. An X-ray image of the violent interstellar medium in 30 Doradus. *Astrophysical Journal*, 370:541–550, April 1991.

[433] X. Wang, Y. Yang, T. Zhang, J. Ma, X. Zhou, W. Li, Y.-Q. Lou, and Z. Li. The Progenitor of SN 2004dj in a Star Cluster. *Astrophysical Journal Letters*, 626:L89–L92, June 2005.

[434] M. G. Watson. The Milky way in X-Rays. In G. Fabbiano, J. S. Gallagher, and A. Renzini, editors, *Windows on Galaxies*, volume 160 of *Astrophysics and Space Science Library*, page 177, 1990.

[435] R. F. Webbink. Double white dwarfs as progenitors of R Coronae Borealis stars and Type I supernovae. *Astrophysical Journal*, 277:355–360, February 1984.

[436] A. E. Wehrle, E. Pian, C. M. Urry, L. Maraschi, I. M. McHardy, A. J. Lawson, G. Ghisellini, R. C. Hartman, G. M. Madejski, F. Makino, A. P. Marscher, S. J. Wagner, J. R. Webb, G. S. Aldering, M. F. Aller, H. D. Aller, D. E. Backman, T. J. Balonek, P. Boltwood, J. Bonnell, J. Caplinger, A. Celotti, W. Collmar, J. Dalton, A. Drucker, R. Falomo, C. E. Fichtel, W. Freudling, W. K. Gear, N. Gonzalez-Perez, P. Hall, H. Inoue, W. N. Johnson, D. Kazanas, M. R. Kidger, T. Kii, R. I. Kollgaard, Y. Kondo, J. Kurfess, Y. C. Lin, B. McCollum, K. McNaron-Brown, F. Nagase, A. D. Nair, S. Penton, J. E. Pesce, M. Pohl, C. M. Raiteri, M. Renda, E. I. Robson, R. M. Sambruna, A. F. Schirmer, C. Shrader, M. Sikora, A. Sillanpaeae, P. S. Smith, J. A.

Stevens, J. Stocke, L. O. Takalo, H. Teraesranta, D. J. Thompson, R. Thompson, M. Tornikoski, G. Tosti, A. Treves, P. Turcotte, S. C. Unwin, E. Valtaoja, M. Villata, W. Xu, A. Yamashita, and A. Zook. Multiwavelength Observations of a Dramatic High-Energy Flare in the Blazar 3C 279. *Astrophysical Journal*, 497:178, April 1998.

[437] V. Weidemann. Masses and evolutionary status of white dwarfs and their progenitors. *Annual Review of Astronomy & Astrophysics*, 28:103–137, 1990.

[438] M. Weisskopf. The Chandra X-Ray Observatory Overview. In *APS April Meeting Abstracts*, page J8001, April 2000.

[439] D. R. Weisz, J. J. Dalcanton, B. F. Williams, K. M. Gilbert, E. D. Skillman, A. C. Seth, A. E. Dolphin, K. B. W. McQuinn, S. M. Gogarten, J. Holtzman, K. Rosema, A. Cole, I. D. Karachentsev, and D. Zaritsky. The ACS Nearby Galaxy Survey Treasury. VIII. The Global Star Formation Histories of 60 Dwarf Galaxies in the Local Volume. *Astrophysical Journal*, 739:5, September 2011.

[440] D. R. Weisz, M. Fouesneau, D. W. Hogg, H.-W. Rix, A. E. Dolphin, J. J. Dalcanton, D. T. Foreman-Mackey, D. Lang, L. C. Johnson, L. C. Beerman, E. F. Bell, K. D. Gordon, D. Gouliermis, J. S. Kalirai, E. D. Skillman, and B. F. Williams. The Panchromatic Hubble Andromeda Treasury. IV. A Probabilistic Approach to Inferring the High-mass Stellar Initial Mass Function and Other Power-law Functions. *Astrophysical Journal*, 762:123, January 2013.

[441] P. Wellmann. Die Supernova in NGC 4214. Mit 3 Textabbildungen. *Zeitschrift fuer Astrophysik*, 35:205, 1955.

[442] N. E. White, F. Nagase, and A. N. Parmar. The properties of X-ray binaries. *X-ray Binaries*, pages 1–57, 1995.

[443] R. E. White, III, C. L. Sarazin, and S. R. Kulkarni. X-Ray Binaries and Globular Clusters in Elliptical Galaxies. *Astrophysical Journal Letters*, 571:L23–L26, May 2002.

[444] B. F. Williams, B. A. Binder, J. J. Dalcanton, M. Eracleous, and A. Dolphin. The

Ages of High-mass X-Ray Binaries in NGC 2403 and NGC 300. *Astrophysical Journal*, 772:12, July 2013.

[445] B. F. Williams, J. J. Dalcanton, A. E. Dolphin, J. Holtzman, and A. Sarajedini. The Detection of Inside-Out Disk Growth in M33. *Astrophysical Journal Letters*, 695:L15–L19, April 2009.

[446] B. F. Williams, J. J. Dalcanton, K. M. Gilbert, A. C. Seth, D. R. Weisz, E. D. Skillman, and A. E. Dolphin. The ACS Nearby Galaxy Survey Treasury. VII. The NGC 4214 Starburst and the Effects of Star Formation History on Dwarf Morphology. *Astrophysical Journal*, 735:22, July 2011.

[447] B. F. Williams, J. J. Dalcanton, K. M. Gilbert, A. Stilp, A. Dolphin, A. C. Seth, D. Weisz, and E. Skillman. The Advanced Camera for Surveys Nearby Galaxy Survey Treasury. VI. The Ancient Star-forming Disk of NGC 404. *Astrophysical Journal*, 716:71–83, June 2010.

[448] B. F. Williams, J. J. Dalcanton, A. Stilp, A. Dolphin, E. D. Skillman, and D. Radburn-Smith. The ACS Nearby Galaxy Survey Treasury. XI. The Remarkably Undisturbed NGC 2403 Disk. *Astrophysical Journal*, 765:120, March 2013.

[449] B. F. Williams, T. J. Gaetz, F. Haberl, W. Pietsch, A. Shporer, P. Ghavamian, P. P. Plucinsky, T. Mazeh, M. Sasaki, and T. G. Pannuti. The Chandra ACIS Survey of M33 (ChASeM33): Transient X-Ray Sources Discovered in M33. *Astrophysical Journal*, 680:1120–1131, June 2008.

[450] J. Wilms, A. Allen, and R. McCray. On the Absorption of X-Rays in the Interstellar Medium. *Astrophysical Journal*, 542:914–924, October 2000.

[451] J. Wilms, M. A. Nowak, K. Pottschmidt, W. A. Heindl, J. B. Dove, and M. C. Begelman. Discovery of recurring soft-to-hard state transitions in LMC X-3. *Monthly Notices of the Royal Astronomical Society*, 320:327–340, January 2001.

[452] C. A. Wilson, M. H. Finger, and A. Camero-Arranz. Outbursts Large and Small from EXO 2030+375. *Astrophysical Journal*, 678:1263–1272, May 2008.

[453] L. M. Winter, R. F. Mushotzky, and C. S. Reynolds. XMM-Newton Archival Study of the Ultraluminous X-Ray Population in Nearby Galaxies. *Astrophysical Journal*, 649:730–752, October 2006.

[454] S. E. Woosley. Nucleosynthesis and Stellar Evolution. In J. Audouze, C. Chiosi, and S. E. Woosley, editors, *Saas-Fee Advanced Course 16: Nucleosynthesis and Chemical Evolution*, page 1, 1986.

[455] S. E. Woosley, A. Heger, and T. A. Weaver. The evolution and explosion of massive stars. *Reviews of Modern Physics*, 74:1015–1071, November 2002.

[456] S. E. Woosley and T. A. Weaver. The Evolution and Explosion of Massive Stars. II. Explosive Hydrodynamics and Nucleosynthesis. *Astrophysical Journal Supplements*, 101:181, November 1995.

[457] Q. Wu and M. Gu. The X-Ray Spectral Evolution in X-Ray Binaries and Its Application to Constrain the Black Hole Mass of Ultraluminous X-Ray Sources. *Astrophysical Journal*, 682:212–217, July 2008.

[458] F. Xia and Y.-N. Fu. The V-band Empirical Mass-luminosity Relation for Main Sequence Stars. *Chinese Astronomy and Astrophysics*, 34:277–287, July 2010.

[459] H. Yamaoka. Supernova 2004dj in NGC 2403. *IAU Circulars*, 8385:1, August 2004.

[460] Y. Yao, Q. D. Wang, and S. Nan Zhang. Black hole X-ray binaries LMC X-1 and X-3: observations confront spectral models. *Monthly Notices of the Royal Astronomical Society*, 362:229–234, September 2005.

[461] M. Yukita, D. A. Swartz, R. Soria, and A. F. Tennant. Discovery of a Transient X-Ray Source in the Compact Stellar Nucleus of NGC 2403. *Astrophysical Journal*, 664:277–283, July 2007.

[462] M. Yukita, D. A. Swartz, A. F. Tennant, and R. Soria. An X-Ray View of Star Formation in the Central 3 kpc of NGC 2403. *Astronomical Journal*, 139:1066–1088, March 2010.

[463] A. A. Zdziarski and M. Gierliński. Radiative Processes, Spectral States and Variability of Black-Hole Binaries. *Progress of Theoretical Physics Supplement*, 155:99–119, 2004.

[464] Y. B. Zeldovich and O. H. Guseynov. Collapsed Stars in Binaries. *Astrophysical Journal*, 144:840, May 1966.

[465] A. Zezas and G. Fabbiano. Chandra Observations of "The Antennae" Galaxies (NGC 4038/4039). IV. The X-Ray Source Luminosity Function and the Nature of Ultraluminous X-Ray Sources. *Astrophysical Journal*, 577:726–737, October 2002.

[466] A. Zezas, G. Fabbiano, A. Baldi, F. Schweizer, A. R. King, A. H. Rots, and T. J. Ponman. Chandra Monitoring Observations of the Antennae Galaxies. II. X-Ray Luminosity Functions. *Astrophysical Journal*, 661:135–148, May 2007.

[467] W. M. Zhang, R. Soria, S. N. Zhang, D. A. Swartz, and J. F. Liu. A Census of X-ray Nuclear Activity in Nearby Galaxies. *Astrophysical Journal*, 699:281–297, July 2009.

[468] E. R. Zimmerman, R. Narayan, J. E. McClintock, and J. M. Miller. Multitemperature Blackbody Spectra of Thin Accretion Disks with and without a Zero-Torque Inner Boundary Condition. *Astrophysical Journal*, 618:832–844, January 2005.

[469] H. Zinnecker and H. W. Yorke. Toward Understanding Massive Star Formation. *Annual Review of Astronomy & Astrophysics*, 45:481–563, September 2007.

[470] J. Ziolkowski. Population of Galactic black holes. *Mem. Societa Astronomica Italiana*, 81:294, 2010.

[471] Z.-Y. Zuo and X.-D. Li. The Contribution of X-ray Binaries to the Evolution of Late-type Galaxies: Evolutionary Population Synthesis Simulations. *Astrophysical Journal*, 733:5, May 2011.

[472] Z.-Y. Zuo, X.-D. Li, and X.-W. Liu. Spatial distribution of luminous X-ray binaries in spiral galaxies. *Monthly Notices of the Royal Astronomical Society*, 387:121–127, June 2008.

VITA

The author was born on November 29, 1985 in West Covina, California. She attended the University of California, San Diego, where she received a Bachelor of Science degree in physics with a specialization in astrophysics in 2008. She subsequently attended the University of Washington for her graduate studies in 2008. She completed her Master of Science degree in 2010.